



**DNA-TEMPLATED
POLY(*N*-SUBSTITUTED PYRROLE)BIPYRIDINIUM
NANOWIRES:
PREPARATION AND CHARACTERIZATION**

MAHDI M. ALMAKY

A thesis submitted for the degree of

Doctor of Philosophy

Newcastle University

School of Chemistry

Chemical Nanoscience Laboratories

Newcastle upon Tyne, UK.

February 2013

Abstract

Conductive polymers nanowires have been prepared using DNA-templating methods from monomer units designed in modular form. The monomer units comprise a polymerisable, pyrrolyl group, and a flexible alkyl linker attached to bipyridine groups in order to provide a metal-binding functionality within the polymers. The possibility for these DNA/polymer nanowires to act as templates for deposition of metal with enhanced electrical conductivity was also explored.

Pyrrole with a flexible alkyl linker was combined with; pyridine (mono-I) as a control experiment, 2,2' bipyridyl (mono-II) and 4,4' bipyridyl (mono-III) with a metal ion binding site (nitrogen atom). This was in order to provide the metal-binding functionality for metal deposition to improve the conductivity as well as the morphology of the aimed hybrid templated nanowires. This series of pyrrole-pyridine derivatives were characterised using a range of techniques such as Proton Nuclear Magnetic Resonance (^1H NMR) spectroscopy, Fourier Transform Infrared (FTIR) spectroscopy, Mass Spectroscopy (MS) and Elemental Analysis.

Prior to the nanowires fabrication, pyrrole, as a control, and the prepared monomer units (mono-I, mono-II and mono-III) were chemically polymerised in a bulk scale using FeCl_3 as an oxidant, then spectroscopic data and electrical conductivity of the resulting polymers were measured. A significant decrease in conductivity of poly-I, poly-II and poly-III compared to PPy, but was especially observed for the bipyridinium derivatives. This was suggested to be due to the steric hindrance of the alkyl side chain in the polymer backbone, in addition, the involvement of the non-quaternised pyridyl nitrogen in poly-II and poly-III by the nucleophilic attack on pyrrolyl groups in the polymerisation reaction.

DNA-templated poly(N-substituted pyrrole)bipyridinium nanowires were synthesised at room temperature using the chemical oxidation method. The resulting CPs/DNA hybrids have been characterised using electronic and vibrational spectroscopic methods especially Ultraviolet-Visible (UV-Vis) spectroscopy and FTIR spectroscopy. The nanowires morphology was characterised using Atomic Force Microscopy (AFM). The electrical properties of the prepared nanowires were characterised using Electrostatic Force Microscopy (EFM), and measured using conductive AFM (c-AFM) and two

terminal I/V technique, where the temperature dependence of the conductivity was probed. The conductivities of the prepared CPs/DNA nanowires are generally lower than PPy/DNA nanowires showing the large effect on N-alkylation in decreasing the conductivity of the polymer, but these are higher than the conductivity of their corresponding bulk films. This enhancement in conductivity could be attributed to the ordering of the polymer chains on DNA during the templating process.

Finally, the prepared CPs/DNA nanowires were used as templates for the growth of copper nanowires at room temperature using aqueous solution of $\text{Cu}(\text{NO}_3)_2$ as a source of Cu^{2+} and ascorbic acid as reducing agent. AFM images showed that these nanowires were uniform and continuous compared to copper nanowires prepared using the templating method directly onto DNA. Electrical characterization of the nanowires by c-AFM revealed slight improvement in conductivity of these nanowires (Cu-CPs/DNA) compared to CPs/DNA nanowires before metallisation.

Using similar preparation method, Poly-II/DNA nanostructures were also used as templates to direct the formation of Pd nanowires. An aqueous solution of PdCl_2 was used as a source of Pd^{2+} ions and NaBH_4 solution was used as reducing agent. AFM studies show that the resulting Pd-poly-II/DNA nanowires exhibit continuous and smooth morphology. Electrostatic Force Microscopy showed that these nanowires are electrically conductive.

Dedication

This thesis is dedicated to all those who believe in the richness of learning.

Mahdi Almaky

Feb. 2013

Acknowledgements

I would like to offer my sincerest thanks and gratitude to my supervisor, Prof. Andrew Houlton, for his continuous guidance, encouragement, advice and feedback through all the stages of this project since the beginning of my studies. This thesis would not have been possible without his patience, help and support. I also thank my second supervisor, Dr. Benjamin Horrocks, for his steadfast scientific support and advice during the years of my study.

I would like to acknowledge the academic and technical support to all friendly and cheerful doctors, technicians and students in Chemical Nanoscience Laboratories and all staff, technicians and administration members in the School of Chemistry for all their help, services and support throughout the course of this thesis. My thanks and gratitude extended to all the members of staff and administrators at Newcastle University.

My gratitude and thanks to my wife, daughters and sons, who offered me continued patience, encouragement and unlimited motivation and inspiration at all times. I also must express my deep gratitude to my parents, brothers, sisters and all family in Libya for their moral and spiritual support and prayers throughout all my life.

Finally, I would like to thank my sponsor, the Libyan government, for providing the funding which allowed me to undertake this research.

Table of contents

Chapter 1. Introduction	1
1.1. Nanomaterials – Definition and examples	1
1.2. Nanowires	5
1.3. Nanowires fabrication methods	8
1.4. DNA-based nano-technology	12
1.4.1. DNA structure	12
1.4.2. DNA as a template for nanowires fabrication	14
1.5. Conducting polymers	16
1.6. Substituted polypyrrole	24
1.7. Conductive polymers nanowires	28
1.8. Objective	35
1.9. References	35
Chapter 2. Experimental techniques used in nanowires characterisation	50
2.1. Alignment of DNA-templated Nanowires	50
2.2. Spectroscopic techniques used for the characterisation of nanowires	53
2.2.1. Fourier transformer Infrared (FTIR) spectroscopy	53
2.2.2. Ultraviolet-Visible (UV-Vis) absorption spectroscopy	56
2.2.3. X-ray photoelectron spectroscopy (XPS)	59
2.3. Scanning probe microscopic techniques used for the characterisation of nanowires	64
2.3.1. The atomic force microscopy (AFM)	64
2.3.2. Electrostatic force microscopy (EFM)	66
2.3.3. Conductive atomic force microscopy (C-AFM)	69
2.3.4. The two terminal I-V measurements	72
2.4. References	75
Chapter 3. Preparation and chemical polymerisation of substituted pyrrole derivatives	80
3.1. Introduction	80
3.2. Experimental	87
3.2.1. Materials and instruments	87

3.2.2. Synthesis of 1-(3-chloropropyl)pyrrole.....	88
3.2.3. Synthesis of N-(3-Pyrrol-1-yl-propyl)pyridine hexafluoro- phosphate (Mono-I).....	89
3.2.4. Synthesis of N-(3-Pyrrol-1-yl-propyl)-2,2`-bipyridinium hexafluorophosphate (mono-II).....	89
3.2.5. Synthesis of N-(3-Pyrrol-1-yl-propyl)-4,4`-bipyridinium hexafluorophosphate (mono-III).....	90
3.2.6. Chemical polymerisation.....	91
3.2.7. Electrochemical polymerisation.....	92
3.2.8. Two-terminal current – voltage measurements.....	92
3.3. Results and discussion.....	94
3.3.1. Synthesis of 1-(3-chloropropyl)pyrrole.....	94
3.3.2. Synthesis of Mono-I.....	96
3.3.3. Synthesis of Mono-II.....	98
3.3.4. Synthesis of mono-III.....	100
3.3.5. Chemical Polymerisation of monomers and characterisation.....	100
3.3.6. Electrochemical Polymerisation of monomers.....	105
3.3.7. Electrical characterisation using two terminal I/V measurements...	107
3.4. Summary.....	114
3.5. References.....	115
Chapter 4. Polymer nanowire synthesis and characterisation.....	121
4.1. Introduction.....	121
4.2. Experimental.....	124
4.2.1. Materials.....	124
4.2.2. Preparation of polymer/DNA nanowires.....	124
4.2.3. Preparation of substrates for AFM studies.....	124
4.2.4. Deposition of DNA-templated nanowires on substrates.....	125
4.2.5. FTIR spectroscopy.....	125
4.2.6. Atomic Force Microscopy (AFM).....	126
4.2.7. Electrostatic Force Microscopy (EFM).....	126
4.2.8. Conductive AFM (c-AFM).....	127
4.2.9. Two-Terminal Current-Voltage (I-V) measurements.....	127
4.3. Results and discussion.....	128
4.3.1. Nanowires synthesis.....	128

4.3.2. Fourier transform infrared spectroscopy investigation.....	129
4.3.3. AFM characterisation of poly-I/DNA nanowires:.....	134
4.3.4. Electrostatic force microscopy (EFM) investigation of poly-I/DNA nanowires:.....	141
4.3.5. Conductive atomic force microscopy (c-AFM) of poly- I/DNA nanowires.....	144
4.3.6. Two terminal I-V measurements of ppy/DNA and poly- I/DNA nanowires.....	149
4.3.7. AFM characterisation of poly-II/DNA and poly-III/DNA nanowires.....	155
4.3.8. Electrical characterisation of poly-II/DNA and poly-III/DNA nanowires using EFM.....	161
4.3.9. Conductive atomic force microscopy (c-AFM) for poly-II/DNA and poly-III/DNA nanowires.....	164
4.4. Summary.....	167
4.5. References.....	168
Chapter 5. Metallization of CPs/DNA Nanowires.....	173
5.1. Introduction.....	173
5.2. Experimental.....	177
5.2.1. Materials.....	177
5.2.2. Templating Copper nanoparticles on Poly-II/DNA and poly- III/DNA hybrids nanowires.....	177
5.2.3. Templating Pd nanoparticles on Poly-II/DNA and poly-III/DNA hybrids nanowires.....	177
5.2.4. FTIR spectroscopy:.....	178
5.2.5. Uv-Vis Absorption spectroscopy:.....	178
5.2.6. X-ray Photoelectron Spectroscopy (XPS).....	179
5.2.7. Atomic Force Microscopy (AFM)and Electrostatic Force Microscopy (EFM):.....	179
5.2.8. Conductive AFM (c-AFM):.....	179
5.3. Results and discussion.....	180
5.3.1. Templating Copper nanostructures on Poly-II/DNA and poly- III/DNA hybrids nanowires.....	180
5.3.2. FTIR spectroscopy:.....	181

5.3.3. <i>UV-Vis Absorption Spectroscopy</i>	184
5.3.4. <i>X-ray Photoelectron Spectroscopy</i>	186
5.3.5. <i>AFM characterisation of Cu-poly-II/DNA and Cu-poly-III/ DNA nanowires</i>	192
5.3.6. <i>EFM characterisation of Cu-poly-II/DNA and Cu-poly-III/ DNA nanowires</i>	199
5.3.7. <i>Conductive AFM of Cu-poly-II/DNA and Cu-poly-III/ DNA nanowires</i>	203
5.4. Templating palladium nanoparticles on Poly-II/DNA hybrids nanowires	208
5.4.1. <i>UV-Vis absorption spectra of Pd-poly-II/DNA nanostructures</i>	208
5.4.2. <i>X-ray photoelectron spectroscopy (XPS)</i>	209
5.4.3. <i>Pd-poly-II/DNA nanowires assembly: AFM characterization</i>	211
5.4.4. <i>Electrical characterisation of Pd-poly-II/DNA nanowires by Electrostatic Force Microscopy (EFM)</i>	214
5.5. Summary.....	216
5.6. References.....	217
Chapter 6. Overall conclusion and future work	223
6.1. Achievements.....	223
6.2. Future work.....	227
6.3. References.....	228
Chapter 7. Appendix	229

List of Figures

Figure 1. Schematic diagram shows the classification of nanostructures.....	1
Figure 2. “Moore’s Law” plot of transistor size versus year.....	2
Figure 3. Melting temperature for Au particles of different sizes.....	3
Figure 4. Photograph of the emission of different sizes of CdSe nanoparticles in solution.....	4
Figure 5. Schematic diagram of (a) a single wall carbon nanotube, (b) a double wall carbon nanotube, and (c) a multi-wall carbon nanotube.....	5
Figure 6. Nanowire nanosensor for pH detection. (A) Schematic illustrating the conversion of a NW FET into NW nanosensors for pH sensing.....	6
Figure 7. Schematic procedure for making stable Cu nanowires and then using it to sense molecules adsorbed onto them.....	7
Figure 8. Schematic illustration of a typical nanowire synthesis process using a catalyst driven VLS process including the initial nucleation and the continued growth.....	9
Figure 9. showing the fabrication of PPy nanotubes using AAO membrane.....	10
Figure 10. Casting of silver nanowires with the peptide nanotubes.....	12
Figure 11. The four bases that compose DNA.....	13
Figure 12. The polymeric scheme of DNA.....	12
Figure 13. Schematic diagram of the structure of double-stranded DNA.....	14
Figure 14. The chemical structure of polypyrrole.....	18
Figure 15. General structure types of polaron and bipolaron forms.....	22
Figure 16: Ideal structure of neutral (non-conducting) polypyrrole (a) and oxidized (conducting) polypyrrole: polaron (b) and bipolaron (c) structures upon doping....	23
Figure 17. Electronic structure diagrams for a polymer chain containing polaron and bipolaron.....	24
Figure 18. Chemical structure of: a) Poly(3-methylpyrrole-4-carboxylic acid), and b) alkylsulfonic acid 3-substituted pyrrole.....	25
Figure 19. Chemical structure of: Pyrrole-substituted metallic porphyrins (a), metallated cyclam complexes (b), and 4-methyl-4’(2-pyrrol-1ylethyl)-2,2’-bipyridine (c).....	27
Figure 20. Proposed mechanism of self-assembly DNA/PPy nanowires.....	30

Figure 21. Tapping mode AFM images of nanowires on SiO ₂ /Si substrate. (a) Ag/DNA; (b) Ag/poly(alkynyl-TP)/DNA; and (c) Ag/poly(TP)/DNA.....	32
Figure 22. Synthesis of DNA-templated nanowires functionalised for enhanced deposition of metals.....	33
Figure 23. Construction of a silver wire connecting two gold electrodes.....	50
Figure 24. Schematic mechanism of the DNA combing method.....	51
Figure 25. Schematic showing the pipette method for nanowires combing by droplet suction.....	52
Figure 26. Tapping Mode AFM image of DNA/polyTPT nanowire aligned across a 2.5 mm gap between two Au microelectrodes. The Au electrodes are embedded in a 200 nm thick insulating SiO layer on a Si substrate.....	52
Figure 27. a schematic diagram of the FTIR instrument.....	54
Figure 28. FTIR spectra of DNA, DNA/PPy, PPy and the difference spectrum (DNA/PPY)-(DNA).....	55
Figure 29. FTIR spectra of DNA vs the Cu ²⁺ /DNA complex in the 600 - 2000 cm ⁻¹ region.....	55
Figure 30. Possible electronic transitions of π , σ , and n electrons.....	56
Figure 31. Schematic diagram of double beam UV-visible absorption spectrometer.....	57
Figure 32. UV-Vis spectra of Cu ₂ O/Ct–DNA nanowires (black), Ct-DNA solution (blue) and Benedict’s solution (Purple), by hassanien et al.....	58
Figure 33. Schematic of principle of X-ray photoelectron spectroscopy.....	59
Figure 34. Schematic overview of the photo-excitation processes in atoms.....	60
Figure 35. Survey XPS spectrum of F-DWNTs.....	61
Figure 36. The XPS Si 2p spectrum of silicon dioxide overlayer on silicon substrate.....	62
Figure 37. Schematic of electrons from the near surface region and from the bulk.....	63
Figure 38. Schematic diagram of the essential components of an XPS instrument...63	63
Figure 39. schematic showing principle of atomic force microscopy.....	65
Figure 40. Schematic diagram of the main components of the AFM, adopted from.....	66
Figure 41. Principles of scanned conductance microscopy operation and its use to detect conductive objects (e.g. nanowires) on a dielectric film (e.g. SiO ₂).....	67
Figure 42. (a) AFM image of PIn/DNA nanowire with a diameter of 5 nm, EFM	

phase image of the same nanowire at a tip/sample bias of -6 V, and (c) Phase shift as a function of applied voltage of PIn/DNA nanowire with a diameter of 28 nm on a SiO ₂ /Si surface.....	69
Figure 43. Schematic diagram of C-AFM technique for electrical characterisation. Measurements are recorded upon individual nanowires located at the periphery of a dense network of the nanowires deposited upon the substrate support.....	70
Figure 44. (a) schematic diagram shows the measurement of changes in resistance with distance (length) Using C-AFM, the I-V curves should be recorded at different points along the nanowire. (b) DNA-PIm-Pd nanowires resistance as a function of tip-contact relative distance for different applied forces in c-AFM I-V measurements. The inset shows the current map of the nanowires, and several I-V measurement positions are indicated by red crosses.....	71
Figure 45. a) Probe station used in the electrical measurements. b) Au electrodes inside the probe station. c) AFM image of PPy-DNA nanowire aligned across Au electrodes.....	72
Figure 46. Examples of pyrrole-containing natural products and materials.....	80
Figure 47. Substituted pyrrole derivatives that have been prepared as conducting polymers.....	81
Figure 48. N-substituted pyrrole-pyridine derivatives that have: (1) monodentate, (2) bidentate and (3) tridentate.....	84
Figure 49. Suggested monomers for the conductive templated nanowires.....	85
Figure 50. ¹ H NMR spectrum of 1-(3-chloropropyl)pyrrole.....	95
Figure 51. FTIR spectrum of 1-(3-chloropropyl)pyrrole.....	95
Figure 52. Molecular structure of one independent molecule of N-(3-Pyrrol-1-yl-propyl)pyridinium hexafluoro-phosphate.....	97
Figure 53. Molecular structure of one independent molecule of mono-II.....	99
Figure 54. Uv-Vis spectra of poly-I prepared by chemical polymerisation using FeCl ₃ as oxidising agent.....	102
Figure 55. FTIR spectra of: (a) mono-I and chemically prepared poly-I in the range (600 cm ⁻¹ -4000 cm ⁻¹), (b) Chemically prepared PPy using FeCl ₃ as oxidizing agent in the range (600 cm ⁻¹ -4000 cm ⁻¹), (c) mono I and poly-I in the range (1400 cm ⁻¹ – 1800 cm ⁻¹) and (d) mono-I and poly-I in the range (2750 cm ⁻¹ -3400 cm ⁻¹).....	103
Figure 56. FTIR spectra of mono-II and chemically prepared poly-II in the range (1300 cm ⁻¹ -1700 cm ⁻¹).....	104

Figure 57. FTIR spectra of mono-III and chemically prepared poly-III in the range (1300 cm ⁻¹ -1700 cm ⁻¹).....	104
Figure 58. Consecutive cyclicvoltammograms for a platinum electrode in contact with a 50 mM of LiClO ₄ /AN solution containing 0.05 M of (a) mono-I (b) mono-II and (c) mono-III at a scan rate of 100 mV s ⁻¹	105
Figure 59. Temperature dependence of I-V curves of chemically prepared PPy film.....	106
Figure 60. Cyclicvoltammograms for a platinum electrode in contact with a 50 mM of LiClO ₄ /AN solution containing 0.05 M of (a) mono-I (b) mono-II and (c) mono-III at a scan rate of 100 mV s ⁻¹	110
Figure 61. XPS N1s spectrum of poly-II (A) and poly-III (B) with contributions of pyridinic nitrogen, pyrrolic nitrogen, and quaternary nitrogen.....	112
Figure 62. (a) AFM image of DNA immobilised on mica after polymerisation of pyrrole. Bar, 200 nm, height scale is 4 nm. (b) AFM image showing that material isolated from the reaction contains both bare DNA molecules (white arrow) and thicker DNA/PPy nanowire (black arrow).....	123
Figure 63. Monomers for the conductive templated nanowires.....	128
Figure 64. FTIR spectra of poly-I / DNA complex vs. controls. Infrared spectra of polyI, ct- DNA, poly-I / DNA complex and the difference spectrum (poly-I / DNA- DNA).....	130
Figure 65. FTIR spectra of DNA and poly-I/DNA complex in the 600 - 1800 cm ⁻¹ region.....	131
Figure 66. FTIR spectra of DNA vs the poly-II/DNA complex in the 600 - 1800 cm ⁻¹ region.....	132
Figure 67. FTIR spectra of DNA vs the poly-III/DNA complex in the 600 - 1800 cm ⁻¹ region.....	133
Figure 68. AFM image of ct-DNA deposited onto TMS-modified Si/SiO ₂ surface. Blue and green crosses highlight DNA strands with heights of 1.0 nm and 2.0 nm respectively. Red cross highlights an example of some larger structure heights, up to 8.0 nm. Scale bar = 500 nm, height scale = 20 nm. The inset shows a typical height cross section at various points in the image.....	135
Figure 69. Tapping Mode AFM height image of a section of poly-I/DNA nanowires aligned on Si/SiO ₂ substrate modified with TMS, observed 2 hrs after preparation, Scale bar = 1 μm, height scale = 20 nm, and inset shows a typical height cross section of the nanowires.....	136

Figure 70. Height distribution of 100 λ -DNA molecules before and after treatment with polyI, measured after 2 hours of reaction time. The heights were determined from Tapping Mode AFM images.....	137
Figure 71. Tapping Mode AFM height image of a section of poly-I/DNA nanowires aligned on TMS modifide Si/SiO ₂ substrate modified with TMS, observed 24 hrs after initiation of rection, Scale bar = 1 μ m, height scale = 20 nm, and inset shows a typical height cross section of the nanowires.....	137
Figure 72. Tapping Mode AFM height image of a section of a polyI/DNA nanowires aligned on Si/SiO ₂ substrate modified with TMS, observed 15 days after initiation of the reaction, Scale bar =200 nm, height scale = 20 nm.....	138
Figure 73. Tapping Mode AFM height images of (a) poly-I/DNA and (b) ppy/DNA nanowires immobilized upon a Si/SiO ₂ substrate, modified with a TMS. Scale bar= 1 μ m, height scale=20 nm. (c) and (d) showing the corresponding surface plot of (a) and (b) respectively. (e) and (f) are the corresponding line trace of particular nanowires in (a) and (b) respectively.....	139
Figure 74. (a) AFM image of poly-I/DNA nanowires on SiO ₂ /Si surface, observed 24 hrs after preparation, scale bar is 500 nm, height scale=20 nm. (b) EFM phase image of the same nanowires at a tip/sample bias of +6 V and lift height of 60 nm. (c) The corresponding profile of the phase shift along a cross section of the nanowire at a diameter of 17 nm.....	143
Figure 75. Phase shift versus tip sample bias of poly-I/DNA nanowires with different diameters 17, 13, and 4.5 nm.....	144
Figure 76. Optical image of AFM cantilever and nanowires. Inset; Schematic illustration of the experimental C-AFM set-up.....	145
Figure 77. C-AFM of ppy/DNA nanowire aligned on a Si/SiO ₂ (200nm) substrate (a) Contact mode image, the datascale corresponds to a height of 60 nm; (b) Deflection error image (the data scale corresponds to a height of 20 nm) and (c) c-AFM current image (the datascale corresponds to a current of 100 nA). The tip-sample bias was 7.0V; the images (a)-(c) were acquired simultaneously. Scale bar 500 nm (a-c).....	146
Figure 78. PPy/DNA nanowire resistance as a function of tip-contact relative distance in c-AFM measurements. Sample bias = 7.0 V at 0.5 deflection set point.....	147
Figure 79. C-AFM of poly-I/DNA nanowire aligned on a Si/SiO ₂ (200nm) substrate (a) Contact mode image, the datascale corresponds to a height of	

60 nm; (b) Deflection error image (the data scale corresponds to a height of 20 nm) and (c) c-AFM current image (the data scale corresponds to a current of 100 nA). The tip-sample bias was 7.0V; the images (a)-(c) were acquired simultaneously. Scale bar 500 nm (a-c).....	148
Figure 80. Poly-I/DNA nanowire resistance as a function of tip-contact relative distance in c-AFM measurements. Sample bias = 7.0 V at 0.5 deflection set point.	148
Figure 81. Schematic diagram of Two-terminal conductivity measurements apparatus.....	149
Figure 82. Tapping mode AFM image of a PPy/DNA nanowire aligned across Au microelectrodes. The mean nanowire diameter is 25 nm, and the interelectrode gap is 8.0 μm . The scale bar is 2.0 μm	150
Figure 83. Current-voltage curves for the ppy/DNA nanowire of Figure x. Each curve was recorded at a fixed temperature covers the range of 293 - 373K.....	151
Figure 84. Conductance vs temperature for a single ppy/DNA nanowire over two cycles of heating and cooling.....	152
Figure 85. Arrhenius plot for the zero-bias conductance of single PPy/DNA nanowire.....	152
Figure 86. AFM tapping Mode image of single poly-I/DNA nanowire aligned across two Au electrodes. Length of the nanowire (L)=6.5 μm and average diameter (D)=30 nm. Scale bar 1.0 μm and height scale 20 nm.....	153
Figure 87. Current-voltage curves for the poly-I/DNA nanowire of figure 86. Each curve was recorded at a fixed temperature covers the range of 293 - 373 K.	154
Figure 88. Conductance vs temperature for a single poly-I/DNA nanowire aligned across two Au electrodes.....	154
Figure 89. Arrhenius plot for the zero-bias conductance of single Poly-I/DNA nanowire.....	155
Figure 90. AFM images of poly-II/DNA (a) and poly-III/DNA nanowires (b), observed 2 h after preparation on a SiO ₂ / Si surface. The red arrows indicate the bare DNA molecules, where the blue arrows indicate the poly-II/DNA nanowires. These images were taken in tapping mode. Data scales correspond to height range of 10 nm. The scale bar of all images is 1.0 μm	156
Figure 91. Height distribution of ~100 ct-DNA molecules before treatment with polymers. The heights were determined from Tapping Mode AFM images.....	157
Figure 92. Height distribution of ~100 λ -DNA molecules after treatment with poly-II (a) and poly-III (b). The heights were determined from Tapping Mode AFM	

images 2 hours after preparation.....	158
Figure 93. (a):Tapping mode AFM image of poly-II/DNA nanorope observed 24 h after preparation aligned on a Si/SiO ₂ substrate. The data scale is 20 nm, and the scale bar is 2.0 μm. (b): The corresponding surface plots. (c): showing the corresponding line trace of (a).....	159
Figure 94. Tapping mode AFM image of poly-III/DNA nanorope observed 24 h after preparation aligned on a Si/SiO ₂ substrate. The data scale is 20 nm, and the scale bar is 1.0 μm.....	160
Figure 95. (a) EFM phase image of poly-II/DNA nanowires at a tip/sample bias of +6 V and lift height of 60 nm. The red arrow indicates a DNA molecule with positive phase shift. Scale bare = 500 nm. (b) The corresponding profile of the phase shift along a cross section of the nanowire at a diameter of 10 nm. (c) The phase shift of poly-II/DNA nanowires as a function of applied voltage between -10and +10 V at diameter of 10 nm.....	162
Figure 96. (a) EFM phase image of poly-III/DNA nanowires at a tip/sample bias of +6 V and lift height of 60 nm. The red arrows indicate non-covered parts of nanowires with positive phase shift. Scale bare = 500 nm. (b) The corresponding profile of the phase shift along a cross section of the nanowire at a diameter of 20 nm. (c) The phase shift of poly-III/DNA nanowires as a function of applied voltage between -10 and +10 V for different nanowires with different diameters.....	163
Figure 97. C-AFM of poly-II/DNA nanowire aligned on a Si/SiO ₂ (200nm) substrate (a) Contact mode image, the datascale corresponds to a height of 60 nm; (b) Deflection error image (the data scale corresponds to a height of 20 nm) and (c) c-AFM current image (the data scale corresponds to a current of 100 nA). The tip-sample bias was 7.0V; the images (a)-(c) were acquired simultaneously. Scale bar 500 nm (a-c).....	164
Figure 98. Poly-II/DNA nanowire resistance as a function of tip-contact relative distance in c-AFM measurements. Sample bias = 7.0 V at 0.5 deflection set point.	165
Figure 99. Poly-III/DNA nanowire resistance as a function of tip-contact relative distance in c-AFM measurements. Sample bias = 7.0 V at 0.5 deflection set point.	166
Figure 100. Tapping Mode AFM height image of a section of a λ-DNA molecule following solution treatments with Cu(NO ₃) ₂ and ascorbic acid, highlighting the “beads-on-a-string” morphology associated with Cu ⁰ material deposited along the DNA. The arrows highlight regions between Cu ⁰ nanoparticles on the DNA	

template, where less substantial Cu ⁰ deposition has taken place. Scale bar=200 nm, height scale=8 nm.....	174
Figure 101. EFM phase images. (b) poly(alkynyl-TP)/DNA; (c) Ag/DNA and (e) Ag/poly(alkynyl-TP)/DNA.....	175
Figure 102. FTIR spectra of ct-DNA(a) poly-II/DNA (b) and Cu-poly-II/DNA hybrid (c).....	181
Figure 103. FTIR spectra of poly-III/DNA (a) and Cu-poly-III/DNA hybrid (b)....	183
Figure 104. UV-Vis absorption spectra of 3.0 mM mono-II (MII), poly-II (PII), CT-DNA (CT-DNA), poly-II/DNA (PII/DNA), Cu(II)-poly-II/DNA (Cu(II)-PII/DNA) and Cu ⁰ -poly-II/DNA (Cu-PII/DNA/AA).....	185
Figure 105. UV-Vis absorption spectra of poly-III/DNA(PIII/DNA), Cu(II)-poly-III/DNA (Cu(II)-PIII/DNA) and Cu ⁰ -poly-III/DNA (Cu-PIII/DNA/AA). 187	187
Figure 106. XPS Fe 2p spectra of poly-II sample on Si/SiO ₂ substrate, prepared using FeCl ₃ as oxidising agent (a) before washing with DI water, (b) after washing with DI water.....	187
Figure 107. XPS survey spectrum of Cu-poly-II/DNA nanowires sample.....	188
Figure 108. XPS spectra of (a) C1s spectrum of Cu-poly-II/DNA and (b) C1s spectrum of Cu poly III/DNA. Peak positions of the fitted components are indicated. The binding energies are reported after calibration of the energy scale so that the main C1s binding energy is 284.6 eV.....	189
Figure 109. A representative fit of copper (2p _{3/2} and 2p _{1/2}) spectra for Cu-poly-II/DNA nanowires. The binding energies are reported after calibration of the energy scale so that the main C1s binding energy is 284.6 eV.....	190
Figure 110. A representative fit of copper (2p _{3/2} and 2p _{1/2}) spectra for Cu-poly-III/DNA nanowires. The binding energies are reported after calibration of the energy scale so that the main C 1s binding energy is 284.6 eV.....	191
Figure 111. Tapping Mode AFM height image of Cu-poly-II/DNA nanowires aligned on Si/SiO ₂ substrate, observed 1 hour after preparation. Scale bar = 500 nm, height scale = 20 nm.....	193
Figure 112. Tapping Mode AFM height image of Cu-poly-II/DNA nanowires aligned on Si/SiO ₂ substrate, observed 24 hours after preparation. Scale bar = 1 μm, height scale = 20 nm.....	194
Figure 113. Tapping Mode AFM height image of Cu-poly-II/DNA nanowires deposited on Si/SiO ₂ substrate, observed 48 hours after preparation. Scale bar = 1 μm, height scale = 20 nm.....	195

Figure 114. Tapping Mode AFM height images of Cu-poly-II/DNA nanowires deposited on Si/SiO ₂ substrate, observed 2 hours (a) and 48 hours (b) after preparation combined with their line traces referenced against the substrate.....	196
Figure 115. Tapping Mode AFM height image of Cu-poly-III/DNA nanowires deposited on Si/SiO ₂ substrate, observed 24 hours after preparation. Scale bar = 1 μm, height scale = 20 nm.....	197
Figure 116. Tapping Mode AFM height images of (A-a) poly-II/DNA nanowires before metallisation immobilized upon a Si/SiO ₂ substrate, modified with a TMS, (B-a) Cu-poly-II/DNA nanowires after Cu ⁰ metallisation, with (A-b) and (B-b) showing the corresponding line trace of (A-a) and (B-a) respectively. (A-c) and (B-c) showing the corresponding surface plot of (A-a) and (B-a) respectively. Scale bar= 1 μm, height scale=20 nm.....	198
Figure 117. Tapping Mode AFM height images show a comparison between the morphology of : (a) Cu/DNA nanowire, scale bar=200 nm, height scale=8 nm, with permission from reference. And (b) Cu-poly-II/DNA nanowire, 48 hours after preparation, scale bar=200 nm, height scale=20 nm, using Cu(NO ₃) ₂ as a source of Cu ²⁺ and ascorbic acid as a reducing agent in both methods.....	199
Figure 118. (a) AFM image of Cu-poly-II/DNA nanowires observed 1 hour after preparation on SiO ₂ /Si surface with a SiO ₂ thickness of 200 nm with various nanostructures morphologies and diameters, grayscale 20 nm. (b) Correspondent EFM Phase image of the same nanowires at a tip/sample bias of +6 V and lift height of 60 nm. Scale bar of both images = 500 nm.....	200
Figure 119. (a) AFM phase image of Cu-poly-II/DNA nanowire on SiO ₂ /Si surface with a SiO ₂ thickness of 200 nm observed 24 hours after preparation. (b) The correspondent EFM phase image at a tip/sample bias of +6 V and lift height of 60 nm. The inset shows the corresponding profile of the phase shift along a cross section of the nanowire. (c) inset of the AFM image shows the height cross section of the nanowire at a diameter of ~17 nm, (d) shows the phase shift as a function of applied voltage of the same nanowire at a diameter of 17 nm, scale bar of both images = 500 nm.....	201
Figure 120. (a): AFM image of Cu-poly-III/DNA nanowires on SiO ₂ /Si surface with a SiO ₂ thickness of 200 nm observed 24 hours after preparation. (b): The correspondent EFM Phase image at a tip/sample bias of +6 V and lift height of 60 nm Scale bar of both images= 500 nm. (c): Inset of the AFM image shows the height cross section of the nanowire at a diameter of ~16 nm, (d): shows the inset	

of the corresponding profile of the phase shift along a cross section of the nanowire at a diameter of 16 nm. (d): The phase shift as a function of applied voltage of the same nanowire on bias between -10V and +10V.....	203
Figure 121. C-AFM measurements of Cu-poly-II/DNA nanowires aligned on a 200 nm SiO ₂ /Si substrate. a) Contact mode image the grayscale corresponds to a height of 13 nm; b) Deflection error image (the grayscale corresponds to a height of 10 nm) and c) c-AFM current image (the grayscale corresponds to a current of 100 nA). The tip-sample bias was 0.5V; the images (a)-(c) were acquired simultaneously. Scale bars (a-c)=1.5 μm.....	204
Figure 122. Cu-poly-II/DNA nanowire resistance at zero bias as a function of tip-contact relative distance for different applied forces in single-point c-AFM I-V measurements.....	205
Figure 123. C-AFM measurements of Cu-poly-III/DNA nanowires aligned on a 200 nm SiO ₂ /Si substrate. a) Contact mode image the grayscale corresponds to a height of 13 nm; b) Deflection error image (the grayscale corresponds to a height of 10 nm) and c) cAFM current image (the grayscale corresponds to a current of 100 nA). The tip-sample bias was 0.5V; the images (a)-(c) were acquired simultaneously. Scale bars (a-c)=1.0 μm.....	206
Figure 124. Cu-poly-III/DNA nanowire resistance at zero bias as a function of tip-contact relative distance for different applied forces in single-point c-AFM I-V measurements.....	207
Figure 125. UV-Vis absorption spectra of mono-II (Mono-II), poly-II/DNA (Poly-II/DNA) and Pd poly II/DNA (Pd-poly-II/DNA).....	209
Figure 126. A representative fit of Pd 3d _{5/2} and Pd 3d _{3/2} spectra for Cu-poly-III/DNA nanowires. The binding energies are reported after calibration of the energy scale so that the main C 1s binding energy is 284.6 eV.....	210
Figure 127. Tapping Mode AFM height images of (a) poly-II/DNA nanowires before metallisation immobilized upon a Si/SiO ₂ substrate, modified with a TMS, (b) Pd- poly-II/DNA nanowires after metallisation. (c) and (d) are the corresponding line trace of (a) and (b) respectively. Scale bar= 1 μm, height scale=20 nm.....	212
Figure 128. (a): Height distribution of ~100 poly-II/DNA templates before metallization, determined from Tapping Mode AFM images 2 hours after preparation. (b): The height distribution of ~100 Pd poly II/DNA nanowires determined from Tapping Mode AFM images after 24 hours of reaction time.....	213

Figure 129. (a): AFM image of Pd-poly-II/DNA nanowires on SiO₂/Si surface with a SiO₂ thickness of 200 nm observed 24 hours after preparation. (b): The correspondent EFM Phase image at a tip/sample bias of +6 V and lift height of 60 nm Scale bar of both images = 300 nm. (c): Inset of the AFM image shows the height cross section of the nanowire at a diameter of ~25 nm, (d): shows the inset of the corresponding profile of the phase shift along a cross section of the nanowire at a diameter of 25 nm. (e): The phase shift as a function of applied voltage of the same nanowire on bias between -10V and +10V.....215

List of Schemes

Scheme 1. The mechanism for pyrrole oxidative polymerization.....	20
Scheme 2. The reduced (a) and oxidized (b) forms of the polymer.....	21
Scheme 3. polymerisation of N-vinylpyrrole.....	25
Scheme 4. Schematic of oxidative polymerisation of 2,5-di(2-thienyl)-pyrrole (TPT).....	31
Scheme 5. DNA-templated synthesis of poly(alkynyl-TP) nanowires and deposition of Ag nanocrystals.....	32
Scheme 6. Reaction mechanism for the Clauson-Kaas synthesis of N-substituted pyrrole derivatives.....	82
Scheme 7. The mechanism for the N-alkylation of pyrrole by nucleophilic substitution reaction.....	82
Scheme 8. Proposed products of the chemical polymerisation of mono-I, mono-II and mono-III.....	86
Scheme 9. Synthesis of 1-(3-chloropropyl) pyrrole.....	94
Scheme 10. Synthesis of mono-I.....	96
Scheme 11. Synthesis of mono-II.....	98
Scheme 12. Synthesis of Mono-III.....	100
Scheme 13. Proposed mechanism for the polymerization reaction of N-(3-Pyrrol-1-yl)-4,4'-bipyridinium (mono-III).....	109
Scheme 14. Generalised reaction sequence for the growth of nanoscale conducting polymers at a DNA template.....	122
Scheme 15. Formation of Polymer/DNA nanowires by self-assembly.....	129
Scheme 16. TMS modification of silicon substrates.....	134
Scheme 17. Diagram shows the higher cationic charge of poly-I compared to equivalently oxidized PPy. These stronger interactions produce less non-specific polymer formation as judged by AFM.....	141
Scheme 18. DNA-templated synthesis of poly(alkynyl-TP) nanowires and deposition of Ag nanocrystals.....	175
Scheme 19. Synthesis of poly-II/DNA nanowires and deposition of metal nanocrystals.....	176
Scheme 20. DNA-templated synthesis of poly-II nanowires and deposition of metal nanocrystals, where M= the targeted metal and L= Ligand.....	180
Scheme 21. DNA-templated synthesis of poly-II nanowires and deposition of Pd nanocrystals. Where L= Ligand, x= number of ligands.....	208

List of Tables

Table 1.	Structure and conductivities range (in $S\text{ cm}^{-1}$) of some of conducting polymers.....	17
Table 2.	Chemical shifts in different oxidation states of Si.....	62
Table 3.	Electrical conductivity of chemically prepared polymers.....	108
Table 4.	Selected bands in positions and assignments in the FTIR spectrum of DNA and poly-I/DNA spectra and their assignments.....	131
Table 5.	selected bands in DNA and poly-II/DNA spectra and their assignments.....	132
Table 6.	Selected bands in DNA and poly-III/DNA spectra and their assignments.....	133
Table 7.	The main bands observed in the FTIR spectra of ct-DNA, Poly-II/DNA and Cu Poly II/DNA in the region of 2000-600 cm^{-1}	182
Table 8.	The main bands observed in the FTIR spectra of ct-DNA, Poly-III/DNA and Cu Poly III/DNA in the region of 2000-600 cm^{-1}	183
Table 9.	Electrical conductivity at room temperature of DNA template polymers nanowires and their corresponding bulk polymer films.....	224
Table 10.	Electrical conductivity at room temperature, using c-AFM, of DNA templated polymers nanostructures and their corresponding copper metallised nanowires.....	226

1. Introduction

1.1. Nanomaterials – Definition and examples

“*There is plenty of room at the bottom*”, was the title of the lecture given by R. Feynman in 1959.[1] That lecture is considered the starting pointing of research in nanomaterials science and technology.[2] However, the word ‘nanotechnology’ was not used until 15 years later by the Japanese scientist, Norio Taniguchi, when discussing the ability to precisely engineer materials at the nanometre scale ($1 \text{ nm} = 10^{-9}$ meters). The word “Nano” comes from the Greek word “nanos”, meaning dwarf.

Nanostructures have been defined as materials that have at least one of its dimensions in the range of 1-100 nanometre. [3-8] This leads to different types of structured material based on the number of nanoscale dimensions. Zero dimensional (0-D) include nanocluster and nanoparticles, while one dimensional (1-D) include nanofibers, nanowires, nanotubes and nanorods. Example for two dimensional nanostructures (2-D) are sheets and films with nanometer thickness. Three dimensional (3-D) nanostructure materials are those in which the 0D, 1D and 2D structural elements are in close contact with each other to form larger structures such as polycrystals and multilayer nanomaterial.[5] Figure 1 illustrates different categories of nanostructures according to their dimensions.

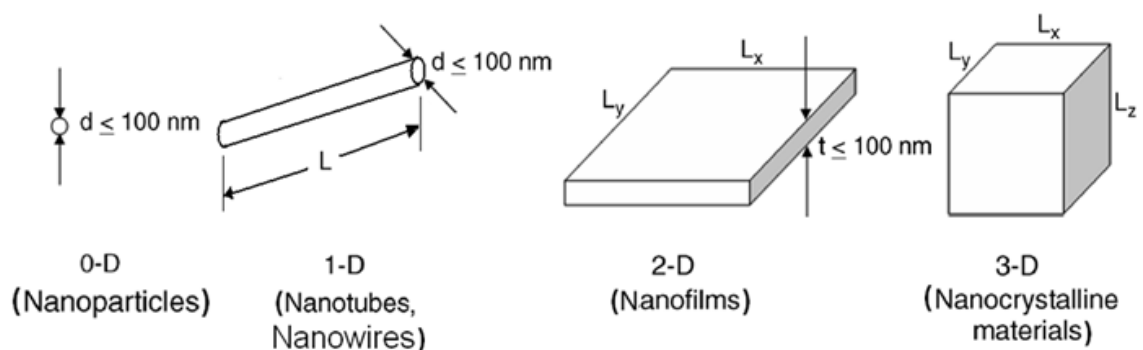


Figure 1. Schematic diagram shows the classification of nanostructures.

The study of chemistry, engineering and biological systems of many materials was in the nanometer regime for decades. More recently, electronic devices with features in the nanometers (nm) size range have been reached. The continued decrease in device dimensions has followed the well-known Moore's law predicted in 1965.[9-11] This law is now used in the semiconductor industry to guide long-term planning and to set targets for research and development. Figure 2 shows that the dimension of a device halves approximately every eighteen months and today's transistors are well within the nanometer range.

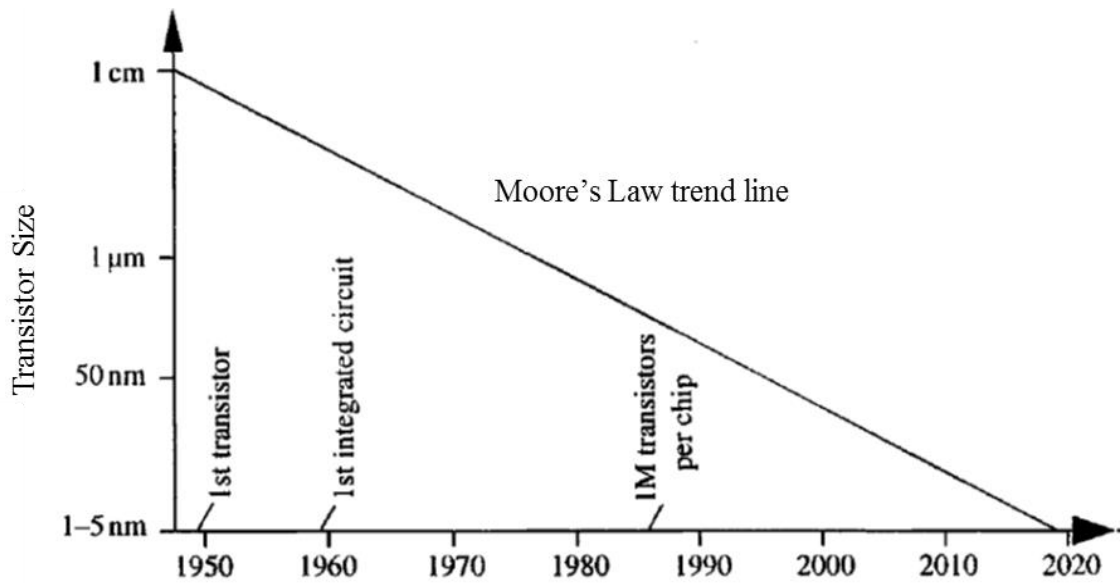


Figure 2. "Moore's Law" plot of transistor size versus year.[10]

Nanomaterials can have different physical and chemical properties in comparison with the same material in the bulk form.[12-17] Opaque materials in the bulk scale may become transparent on the nanolevel,[18] For example, Gold films (< 20 nm thick) are able to transmit large amounts of visible light while efficiently reflecting infrared light ($\lambda > 800$ nm).[19] These nanosize films are used in the fabrication of office windows, keeping heat inside in the winter and warm air outside in the summer months.

Another example of physical property that is size dependent is melting temperature (T_m). Crystals in the nanometer scale have a lower melting point with differences which can be as large as ~ 50%.[16, 20] The T_m of gold particles decreases rapidly for

diameter < 40 nm. The bulk metal has a T_m of 1337 K, which is reduced ~ 700 K at ~ 20 nm.[20] Figure 3 shows the size dependence of the melting temperature of Au particles. The melting temperature depression seen as material size is decreased, is explained by surface energy considerations. As the nanocrystal becomes smaller the number of surface atoms becomes a large fraction of the total number of atoms.[16] Here, a larger contribution of the surface energy of the system leads to a dramatic depression of the melting temperature than the case in bulk materials.

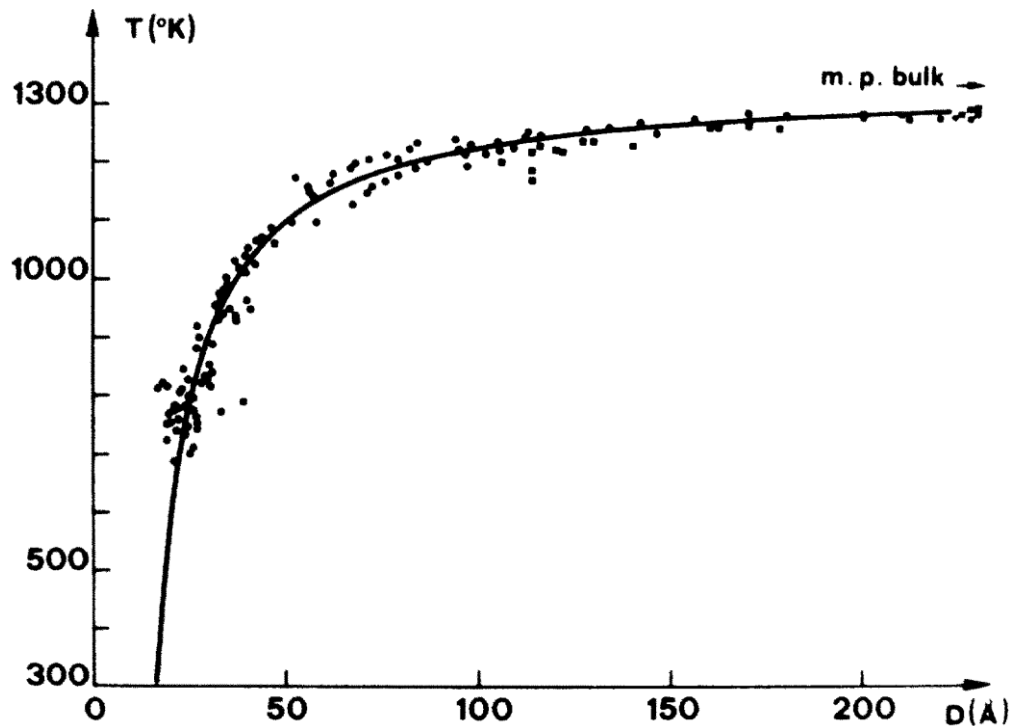


Figure 2. Melting temperature for Au particles of different sizes.[20]

The chemical reactivity of materials has also been shown to change dramatically when the size is decreased to the nano-scale. For example, stable materials like aluminium may become combustible in nanoparticle form.[18] Also gold on the bulk scale does not exhibit notable reactivity to oxygen, whereas Au nanoparticles can be used as a catalyst in some oxidation reactions.[13]

A major interest in nanomaterials is in controlling the synthesis to find new properties, and to realize novel functions.[21] For example, cadmium selenide (CdSe) is a semiconductor material which can be prepared as quantum dots (0-D nanostructures).

These semiconductor quantum dots are fluorescent, and emit colored light when exposed to ultraviolet excitation.[22] This can be seen in figure 4, where the emission of different sizes of CdSe nanoparticles changes color from blue/green to red as the particle size increases.[5] These materials are interesting because they do not photobleach and can be made in a range of sizes. And thus, in a range of colors in a single material. These types of nanomaterials are being used in displays for computers and mobile telephones, and have also been used as inks.

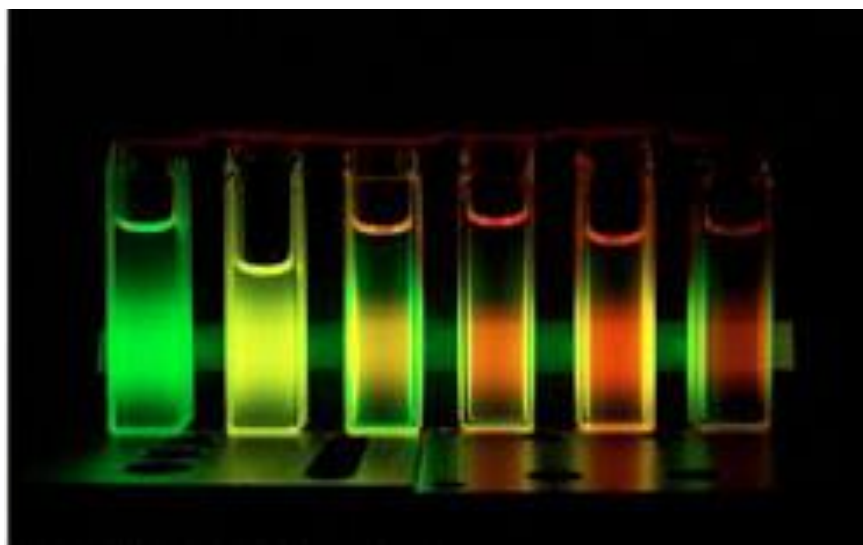


Figure 4. Photograph of the emission of different sizes of CdSe nanoparticles in solution.[5]

Nanowires and nanotubes as 1-D nanostructures are at the forefront of materials science at the nanoscale.[23] Because of their unique properties such as small dimensions, strength, remarkable physical properties and their promise for practical applications, carbon nanotubes (CNTs) are considered as a prototype for nanotubes. They are in many types, including single wall carbon nanotubes (SWNT), double wall carbon nanotubes (DWNT) and multi-wall carbon nanotubes (MWNT), figure 5. CNTs are used in several electronic, electrochemical and mechanical applications.[24] They are used in electronics for making transistors, to switch electric current. They are also used as nanoprobe for biological and chemical investigations. In addition, they are used as mechanical reinforcements in high performance composites, and are also used as templates for the fabrication of other nanostructures.

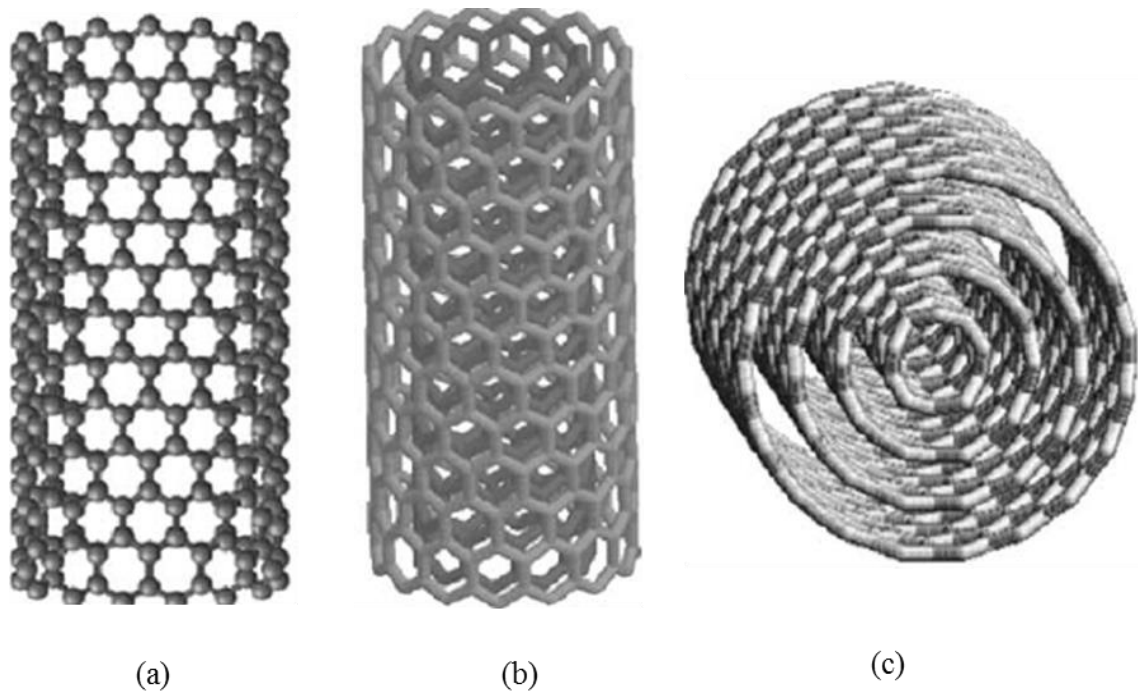


Figure 5. Schematic diagram of (a) a single wall carbon nanotube, (b) a double wall carbon nanotube, and (c) a multi-wall carbon nanotube.

Another exciting example in which to explore nanostructure fabrication and applications is at the interface between nanotechnology and biology.[25] Many biological molecules, such as proteins and nucleic acids, are comparable in size to nanoscale building blocks, and thus these structures can provide a natural bridge between biology and nano-systems.

1.2. Nanowires

One-dimensional (1D) nanostructures have been called by a variety of names including: nano-whiskers, nano-fibers, nanowires, nanotubes and nanorods. Nanowires are one-dimensional nanostructures that represent the smallest structure that can efficiently transport electrical carriers.[8, 26-28] They may be elemental, inorganic or molecular in nature.

Nanowires have potential applications in a variety of fields such as medicine, military, aerospace industry, and computing.[29-31] For example nanowires may be applicable as interconnects in nanoscale electronic devices which could provide higher speed, larger

storage capacities, and size reductions than existing devices.[32-36] Semiconducting nanowires were used as improved electrode materials in rechargeable batteries[37] leading to higher energy capacity and longer cycle life.

Nanowires (NW) are widely used as sensors, either for chemical, biological or environmental purposes.[6, 38] Due to their high surface-to-volume ratios, the electrical properties of the nanowires are extremely sensitive to species adsorbed on surface. For example, they are used as pH indicators. SiNWs were modified with 3-aminopropyltriethoxysilane (APTES) to provide a surface that can undergo protonation and deprotonation, allowing detection of changes in solution pH, figure 6.[38] The NW is contacted with two electrodes, a source (S) and drain (D), for measuring conductance. The figure shows a zoom of the APTES-modified SiNW surface illustrating changes in the surface charge state with pH. These differences in surface state perturb the charge flowing in the wire that is indicative of the pH.

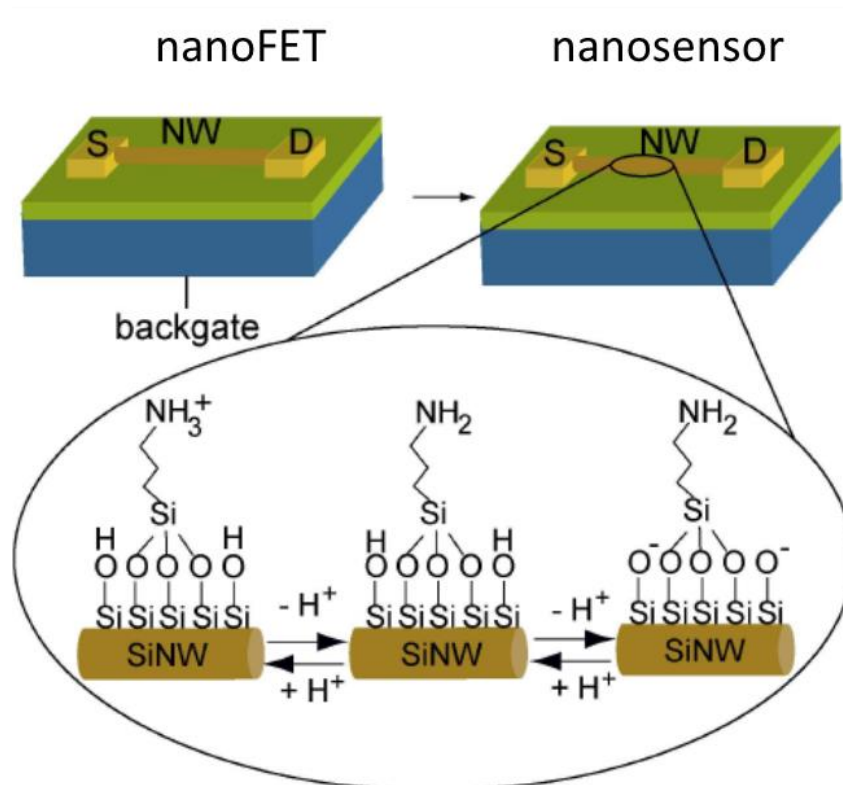


Figure 6. Schematic diagram illustrating nanowire used as nanosensor for pH detection. The conversion of a NW FET into NW nanosensors for pH sensing. The zoom shows the APTES-modified SiNW surface illustrating changes in the surface charge state with pH. (This figure has been modified from ref.[38]).

The conductance of nanowires changes upon the adsorptions of different molecules. Figure 7 shows the demonstration of this concept by Tao and co-workers,[39] for molecular detection, using arrays of Cu nanowires that contained nanoscale gaps. Upon adsorption of organic molecules onto these Cu nanowires, the conductance was reduced to a fractional value which attributed the scattering of conduction electrons by the adsorbents.

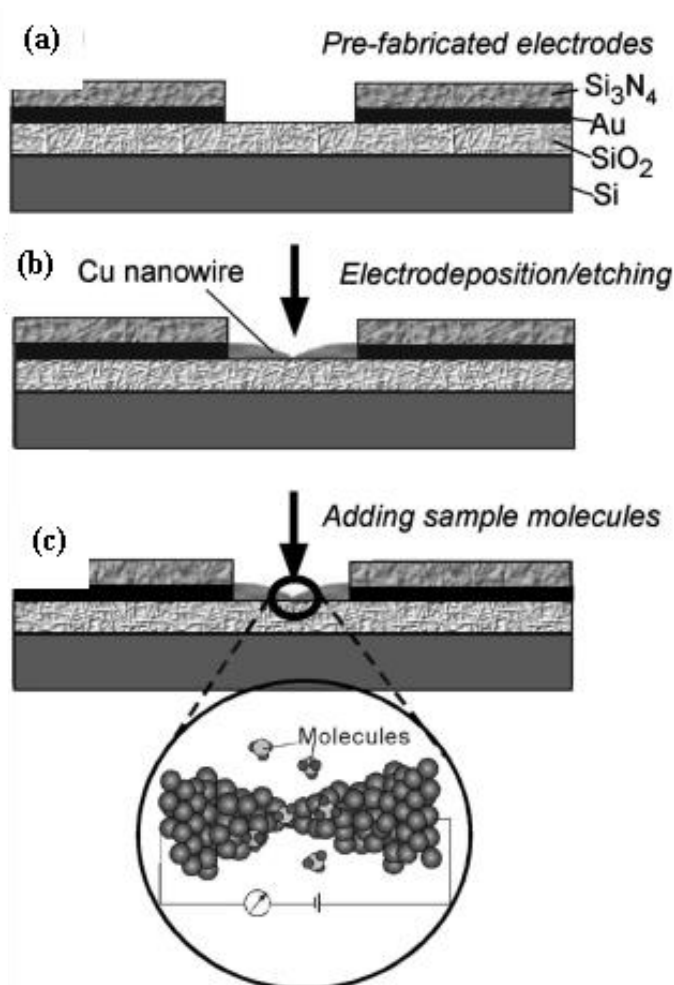


Figure 7. Schematic procedure for making stable Cu nanowires and then using it to sense molecules adsorbed onto them. A pair of Au electrodes facing each other with a gap of ~100 nm is fabricated on a Si/SiO₂ substrate (a). The gap is bridged to form a nanowire with a desirable conductance by electrochemically depositing Cu on the ends of the electrodes (b). Molecular adsorption on the nanowire is reflected by a change in the conductance (c). (This figure has been copied from ref.[39]).

Semiconducting metal-oxides nanowires such as ZnO, TiO₂, CuO, CdO and Fe₂O₃, etc., are also promising candidates for gas sensing applications.[40, 41] This kind of materials showed varying degrees of success at detecting different types of reducing and oxidizing gases such as H₂, H₂S, NH₃, CO, NO₂ and O₂, etc.

Conducting polymers (CPs) nanowires are currently attracting much attention for a variety of applications as components in electronic devices such as transistors, diodes, and as highly sensitive chemical and biological sensing elements.[28] For example, CPs nanowires have been shown to function successfully as one-dimensional organic field-effect transistors.[42] As a biological sensors, bio-functionalized PPy nanowires with cancer antigen antibodies shows excellent sensitivity as a nanobiosensor[43] for the detection and quantification of cancer antigens markers for the diagnosis and treatment of cancer patients.

The synthesis of polymeric nanowires has proceeded with remarkable development[26, 44, 45] since polymers possess certain highly desirable characteristics such as an easily tunable bandgap,[2] high mechanical flexibility,[44] and greater biocompatibility than many inorganic materials.[46] As a result there is considerable interest in developing methods for the synthesis of 1-D nanostructures involving the use of polymers by different synthetic techniques.

1.3. Nanowires fabrication methods

The synthesis of 1-D nanomaterials has been received increasing research interest in the last decades.[47-51] A number of techniques have been developed for the fabrication of nanowires. These techniques can be broadly subdivided into two approaches; either “top-down” or “bottom-up” fabrication methods.[29, 30]

Top-down techniques include methods which uses nanofabrication tools that are controlled by external parameters to create nanoscaled structures with the desired shapes and characteristics starting from larger dimensions and reducing them to the required values.[30, 48, 50] These techniques are mainly based on conventional fabrication methods such as deposition, moulding, printing and etching.[48] For

example in etching process, the required material is usually protected by a mask and the exposed material is etched chemically using acids or mechanically using ultraviolet light, X-rays, or electron beams.[30]

Bottom-up processes work in the opposite direction. The nanostructures are formed from atomic or molecular components and built up gradually until the desired nanostructure is formed.[30, 48] Several routes are now available for the bottom-up fabrication of nanowires. These include self-assembly[47] and template methods.[32] Vapour-liquid-solid (VLS) mechanism is one of the most common self-assembly methods used in the production of nanowires.[29] In this route the nanowire material in a vapour phase precursor impacts the liquid phase seed particle, producing axial growth of the nanowire.

Figure 8 shows a schematic diagram of the VLS method for the fabrication of nanowire using metal nanocluster catalyst. The mechanism is described as follows: a liquid alloy droplet (catalyst) is formed upon the substrate from which a wire is to be grown. This is followed by the introduction of the substance to be grown as a vapour (precursor gas), which absorbs on the liquid catalyst surface, and diffuses into the droplet. Finally, super saturation and nucleation at the liquid/solid interface leads to axial crystal growth of single-crystalline nanowires.[52] The liquid droplet size serves as a soft template to strictly limit the lateral growth of an individual nanowire.[53] An example of this is by Wu *et al.*[54] who reported the growth of Si nanowires by VLS mechanism using monodispersed gold nanoclusters as catalyst. However, a drawback here is that the metal catalysts contaminate the grown nanowires, which then require an extra purification process.

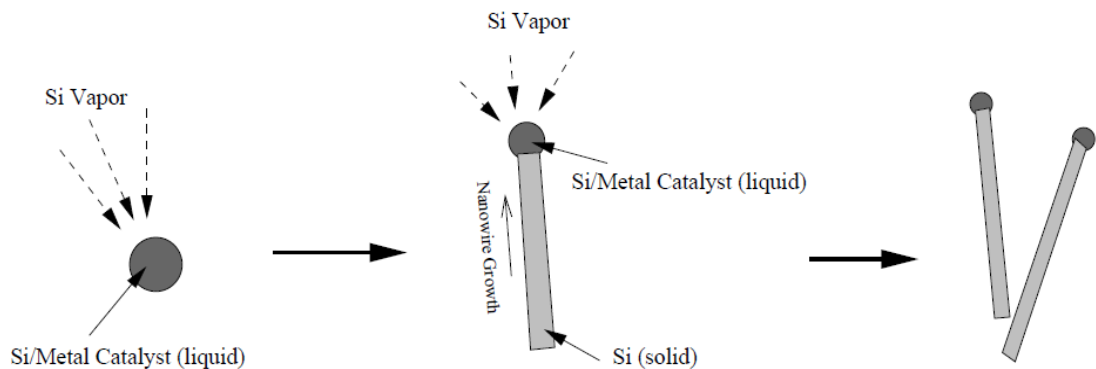


Figure 8. Schematic illustration of a typical nanowire synthesis process using a catalyst driven VLS process including the initial nucleation and the continued growth.[54]

Template-directed growth techniques are the most useful methods for forming 1D nanomaterials. The use of porous templates such as anodically etched aluminium oxide (AAO)[55, 56] have been shown to be effective for preparing 1D nanostructures with a narrow distribution of diameters. Figure 9 illustrates the AAO membrane method of templating PPy nanotubes using vapour deposition polymerization (VDP).[57] The inner surfaces of the pores were coated with FeCl_3 as an oxidant. Then the reaction chamber was evacuated at room temperature until the pressure inside reached about 10^{-1} Torr. Pyrrole monomer was vaporized into the reactor at room temperature. The vaporized monomers were polymerized into the channels of the AAO membrane and the thickness of the polymer tubules was controlled by polymerization time. Finally, the removal of the template can be achieved using strong base such as NaOH solution.

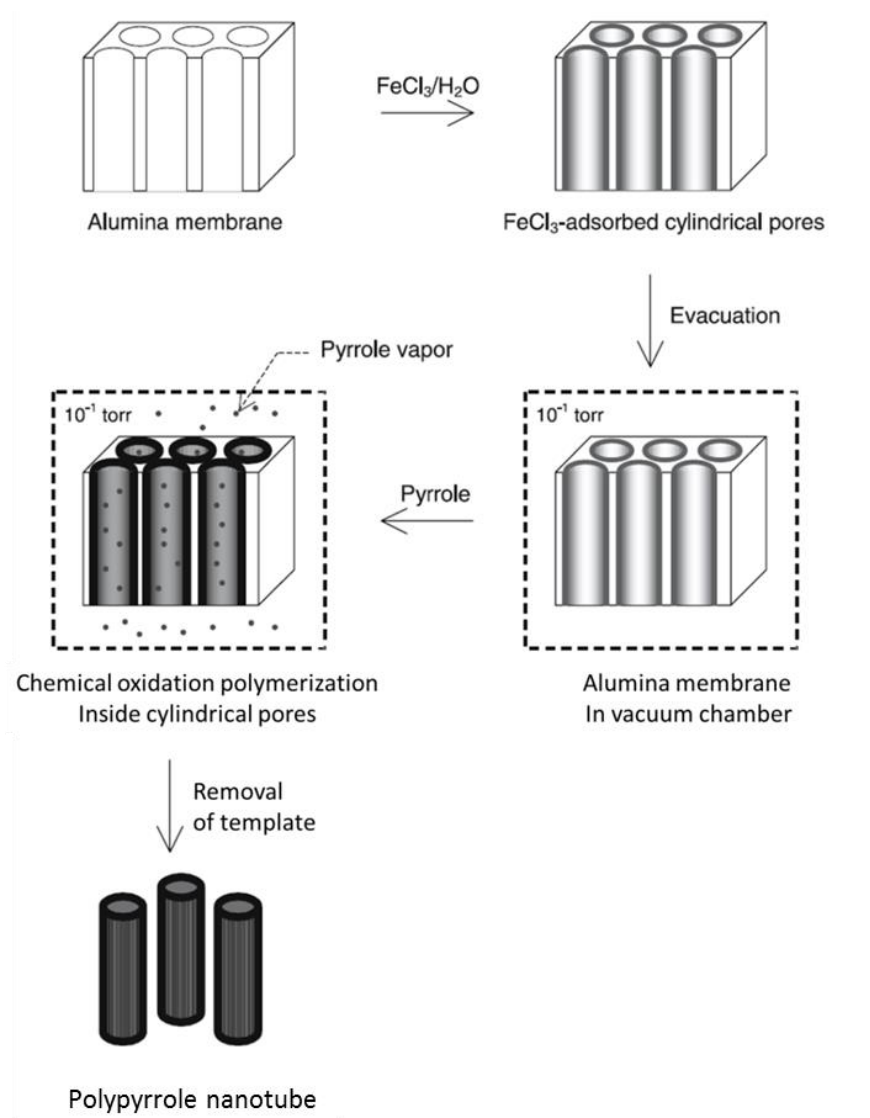


Figure 9. Schematic diagram showing the fabrication of PPy nanotubes using AAO membrane. Modified from ref.[56]

Martin et al.[58] used porous track-etched polycarbonate membranes as a template for the fabrication of conductive polymers nanostructures such as polypyrrole, poly(3-methylthiophene), and polyaniline by either chemically or electrochemically polymerisation of the corresponding monomer.

Many other methods employ different growth mechanisms to produce bottom-up growth of nanowires including the oriented attachment technique,[59] metal organic vapour phase epitaxy (MOVPE),[60] molecular beam epitaxy (MBE),[61] dislocation driven unidirectional growth,[62] and crystal habit modification[63] However, no method is perfect. Each currently used method has its disadvantages. For example, in some methods the grown nanowires were highly contaminated with metal catalysts,[32] which require an extra purification process. Moreover, porous template-directed growth techniques require post-treatment to remove the hard template before further device integration.[29] This can destroy or damage the nanostructures. Therefore, finding an efficient technique for the fabrication and control of 1-D nanostructures is desirable, and is the reason that current attempts to develop new methods have received attention.

One of the most important emerging methods in addressing the challenges of bottom-up templating is the utilisation of natural polymers such as cellulose acetate nanofibers[64] or cellulose nanocrystals[65] in the fabrication of nanostructures. Other natural biopolymers such as proteins and DNA have been used as templates for the fabrication of 1-D nanostructures.[66] For example, β -amyloid forms tubular polypeptide nanostructures which have been used for templating the synthesis of silver nanowires.[67, 68] β -amyloid nanotubes were added to an aqueous solution of silver ions. The hollow nanotubes were filled with the ionic silver solution and the silver within the tubes was reduced using citric acid. The peptide templates were then enzymatically degraded resulting in the isolation of uniform silver nanowires with diameter of ~ 20 nm, as shown in figure 10.

Viruses have also been used to fabricate nanowires.[69] For example rod-like tobacco mosaic virus (TMV) has a tubular shaped virus that is 300 nm long and 18 nm wide, with a 4 nm wide interior cavity. This virus was used as a template for the synthesis of nanotubes, including CdS, PbS, silica, and Fe_2O_3 .

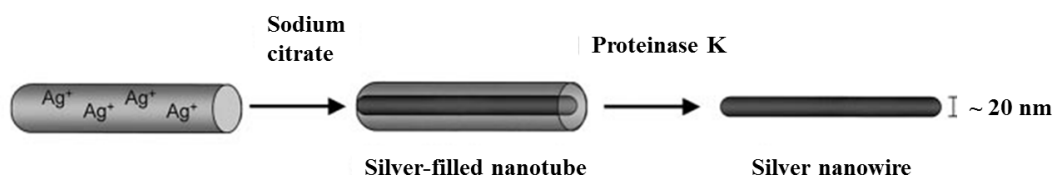


Figure 10. Casting of silver nanowires with the peptide nanotubes.[67]

However, DNA has perhaps become the most useful biopolymer for the fabrication of nanostructures and nanostructured materials. Not only has the self-assembly of DNA strands allowed the construction of a wide range of discrete and extended nanostructured materials,[70, 71] but its shape and chemical properties make it as highly affective template for the synthesis of nanowires based on metals, inorganics and polymers. This topic is the main focus of the work in this thesis and will be considered in the next section.

1.4. DNA-based nano-technology

1.4.1. DNA structure

Before describing the use of DNA as a template in the synthesis of nanowires, we need to have knowledge about its chemical structure. DNA is a linear biopolymer with a diameter of approximately 2 nm.[72-75] It is composed of four different building blocks (bases) known as adenine (A), thymine (T), cytosine (C) and guanine (G), see figure 11.

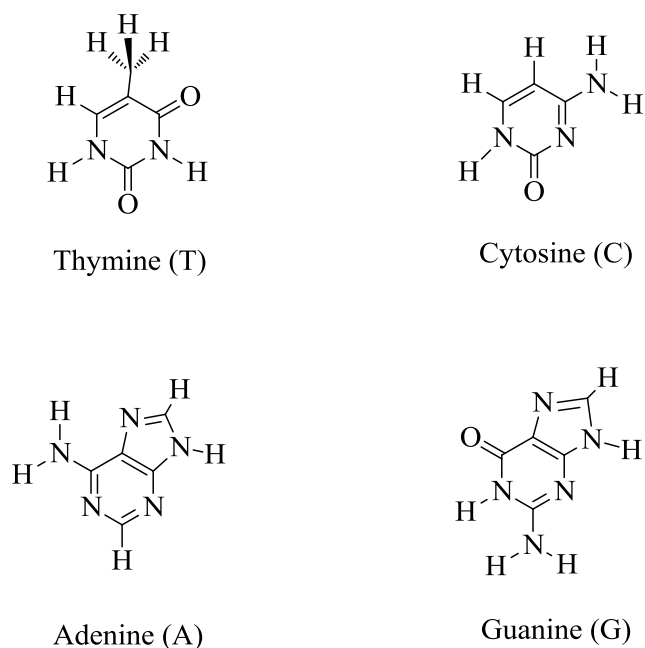


Figure 11. The four nucleobases that compose DNA.

These nucleobases are attached covalently to a sugar phosphate backbone. This macromolecule made of four different monomers, each monomer unit called a nucleotide, consists of a phosphate group, a 2'-deoxyribose (a 5-carbon sugar), and one of the four bases. Within the monomer, the 5' and 3' carbons are attached to the phosphate group on either side, figure 12, forming a linear chain. By convention the sequence of the bases is read in the 5' → 3' direction.

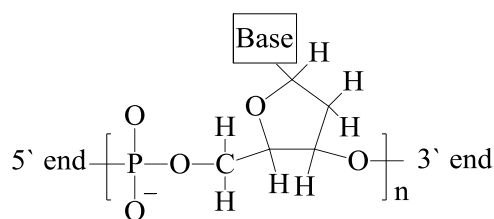


Figure 12. The polymeric scheme of DNA.

The monomers are attached through a phosphodiester link to form a DNA strand. Double-stranded DNA is formed by hydrogen bonding between complementary bases on two single strands. In regular DNA, the bases come together in what is called Watson–Crick base pairing.[76] The famous double helix structure of DNA consisting

of two strands in an antiparallel orientation bound by hydrogen bonds between the bases. The base (A) pairs with (T) via two hydrogen bonds, and the base (G) pairs with (C) via three hydrogen bonds.[74, 77, 78] The schematic structure of DNA is shown in figure 13. In an aqueous solution the phosphate backbone becomes negatively charged because each phosphate unit donates a proton into the solution.

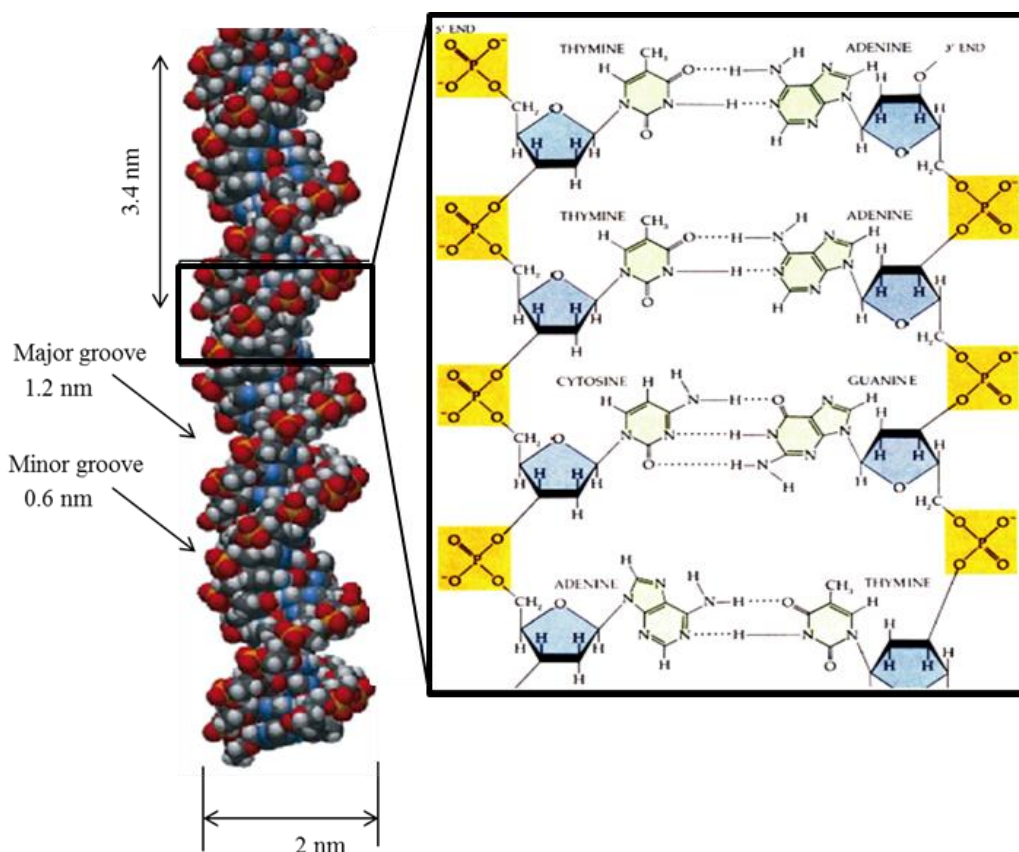


Figure 13. Schematic diagram of the structure of double-stranded DNA. Modified from reference [79].

1.4.2. DNA as a template for nanowires fabrication

DNA has become a key building block in nanoscience and nanotechnology.[80, 81] In principle, DNA has numerous properties as a nanostructured material which make it useful as a template for the synthesis of nanowires. As a material for such

bottom-up assembly of electronics components,[26, 82-84] DNA has a well-defined structure with high aspect ratio of 2 nm width and lengths that can exceed microns in precisely controlled increments.[85] Moreover, DNA has better chemical stability, mechanical rigidity,[68, 75] availability and easy synthesis compared with other biopolymers.[80, 86]

The chemical functionality of the various groups in DNA provide a wide range of binding interactions with metal ions, and small molecules, particularly those are cationic and are either highly planar or have hydrogen binding groups.[87] The negatively charged phosphate groups that are regularly arranged on its backbones, [74, 88] makes DNA as an ideal template to fabricate highly ordered nanostructures by interaction with cationic materials such as positively charged polymers or metal ions to form 1D nanostructures.[89]

Due to these facts, several approaches have been developed to use DNA as a template for the fabrication of conductive nanowires. DNA has shown to be highly effective in controlling the synthesis of metallic nanowires.[82, 90-93] Different metals can be deposited on DNA templates via the reduction of metal ions or metal complexes associated with DNA. The synthesis of silver,[90] gold[91] platinum,[93-95] copper[85, 92, 96] and palladium[97-99] metal nanowires on DNA templates has been achieved using this approach.

Fujihira *et al.*[100] reported a fabrication method using DNA molecules as a template to control and direct copper deposition. First, Pd²⁺ ions were bound to DNA molecules and these were then reduced to Pd⁰. Second, electroless deposition of copper was performed on Pd⁰ by reduction of Cu²⁺ ions using formaldehyde as reducing agent. The Pd⁰ particles act as nucleation sites for the production of copper nanowires.

Woolley *et al.*[92] developed an alternative route for forming Cu/DNA nanostructures in two steps. DNA was aligned on a silicon surface and then treated with aqueous Cu(NO₃)₂ solution. Cu²⁺ associated with the anionic DNA electrostatically, and metal-ion-coated DNA is chemically reduced with ascorbic acid to form metallic copper (Cu⁰) around the DNA forming Cu/DNA nanowires.

A similar method has been used for the fabrication of DNA templated inorganic semiconductor nanowires.[101-104] For example, Dong *et al.*[105] produced CdS nanowires by first aligning λ -DNA on mica substrates and allowed to incubate with $\text{Cd}(\text{NO}_3)_2$, followed by the treatment with Na_2S solution.

A more recent material type formed as nanowires using DNA-templating are conducting polymers.[26] Example of these include polyaniline, [83, 106] polythiophene,[107] polypyrrole,[81, 108, 109] polyindole[110] and their various derivatives.[56] For example, Nickels *et al.*[106] have synthesized and characterised DNA-templated polyaniline nanowires using three different means of oxidation for the polymerization using ammonium persulfate, enzymatic oxidation using horseradish peroxidase, and photo-oxidation using a ruthenium complex as photo-oxidant. Before discussing these in detail, however, some general information about this type of material will be given.

1.5. Conducting polymers

The key discovery in the development of conducting polymers was the finding in 1973 that the inorganic polymer polysulfur nitride (PSN) had room-temperature conductivity in the order of 10^3 S cm^{-1} .[111] This stimulated the enormous amount of work towards the synthesis of other polymeric conductors. Organic conducting polymers (CPs) have been extensively investigated since the discovery of electrically conducting polyacetylene in 1977. [112-115] Alan Heeger, Alan G. MacDiarmid and Hideki Shirakawa have awarded the Nobel Prize for chemistry in year 2000 for the discovery and development of conductive polymers.[116, 117]

Compared with the conductivity of copper, a highly conductive metal ($\sim 6 \times 10^5 \text{ S cm}^{-1}$) and polyethylene, a highly insulating polymer ($\sim 10^{-14} \text{ S cm}^{-1}$), CPs show a wide range of conductivity values from metal to insulator-like behavior.[118] Table 1 shows examples of some common conjugated conducting polymers and their electrical properties.[118, 119]

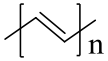
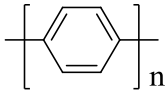
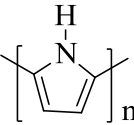
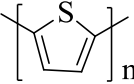
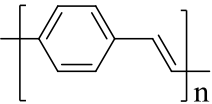
Polymer (date conductivity discovered)	Structure	π - π^* band gap (eV)	Conductivity (S cm ⁻¹)
Polyacetylene (PA)		1.5	$10^3 - 1.7 \times 10^5$
Polyparaphenylene (PPP)		3.0	$10^2 - 10^3$
Polypyrrole (PPy)		3.1	$10^2 - 7.5 \times 10^3$
Polythiophene (PT)		2.0	$10 - 10^3$
Polyparaphenylene vinylene (PPV)		2.5	$3 - 5 \times 10^3$

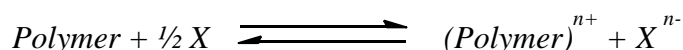
Table 1. Structure and conductivities range (in S cm⁻¹) of some of doped conducting polymers.[118, 119]

Due to their highly desirable characteristics such as high mechanical flexibility, tunability, ease of functionalization and greater biocompatibility than many inorganic materials, CPs have been received increasing attention in research for application as alternatives to metals or inorganic semiconductors.[119, 120]

It is well known that metals possess high electrical conductivity due to the free movement of electrons through their structure. For CPs they must possess not only charge carriers to be conductive but also an orbital system which allows the charge carriers to move.[121, 122] That is achieved by overlapping their π -orbitals which provide reasonable carrier mobility along the polymer backbone.

CPs in their doped form can be obtained by oxidative polymerization.[114, 123] Doping is the process that provides charge carriers[124, 125] which can be through partial oxidation (p-doping) or by partial reduction (n-doping) of the polymer chain. The doping process is more correctly called a redox process which is described by the following schemes:[123]

In the case of an oxidation process (p-doping):



And in reduction process (n-doping):



Where $X = I_2, Br_2$, etc. and $M = Na, Li$, etc.

Polypyrrole (PPy) and its derivatives have attracted interest[126] due to their easy synthesis, relatively high conductivity, and good stability in ambient conditions. They have been subjected to numerous studies for application in fields such as conducting composites,[127] conducting textiles,[128] corrosion control coatings,[129] and controlled drug release systems.[130] Moreover, they have found prospective applications in design of biosensors, food processing, environmental monitoring, veterinary medicine, etc.[127, 131-135]

PPy is also called pyrrole black or polypyrrole black.[136] It is generally synthesized by chemical or electrochemical means. Figure 14 shows the chemical structure of polypyrrole.

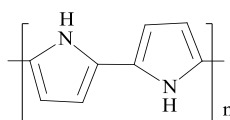


Figure 14. The chemical structure of polypyrrole.

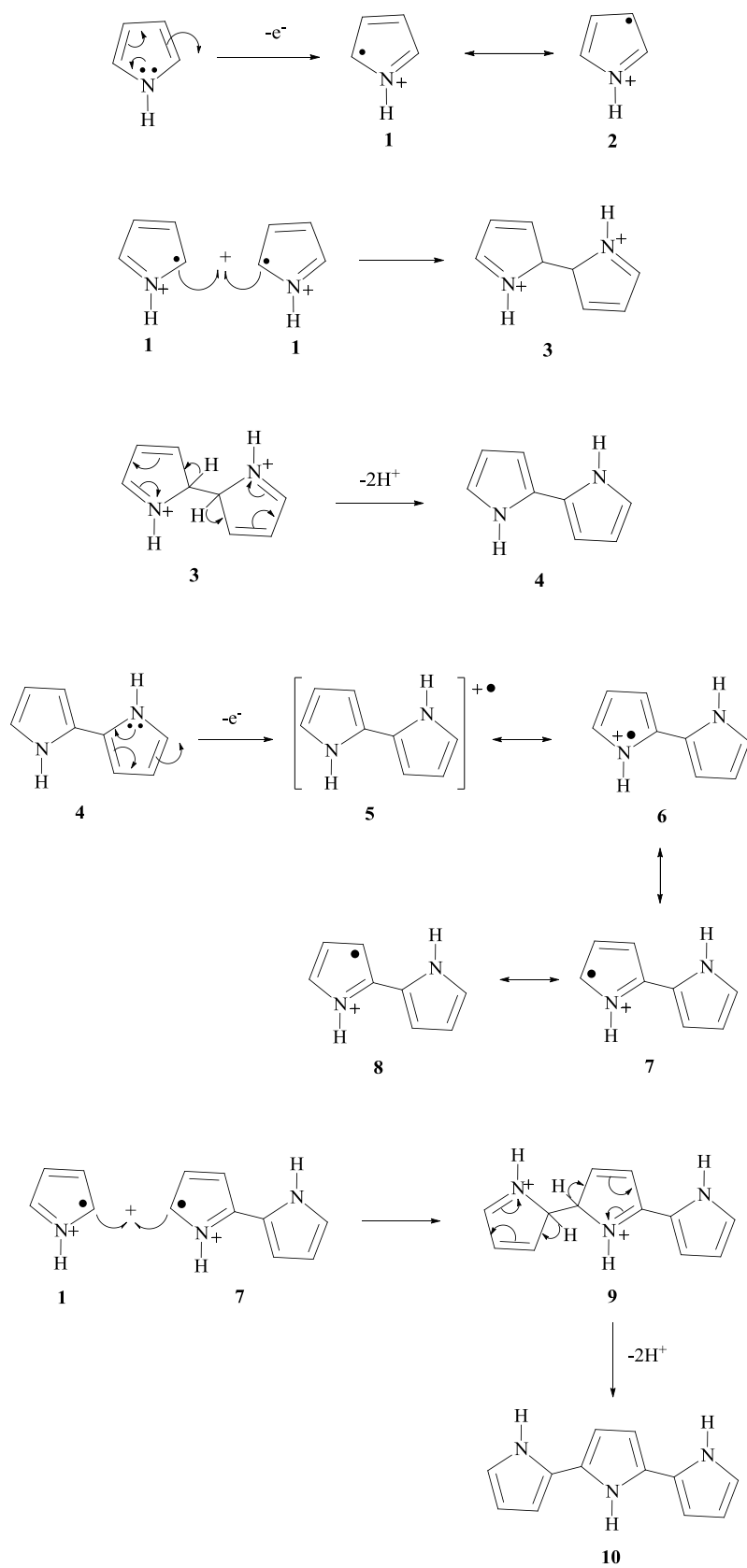
The chemical synthesis of PPy involves mixing of strong oxidizing agent, typically FeCl₃, with the monomer solution. [137] Electrochemical synthesis involves the electrodeposition of the polymer on the positively charged working electrode.

The mechanistic scheme for the formation of PPy is shown in scheme 1.[126] During polymerization of pyrrole, the monomer loses a proton at the α -position and links with another monomer of pyrrole to form the long chain of polymer (PPy). The individual pyrrole monomer maintains their structure and are linked primarily through the α -carbon sites.[138, 139] The mechanisms for chemical and electrochemical synthesis are essentially the same.

The neutral monomer is oxidized to form the radical cation. This radical cation has several resonance forms (1 and 2). The radical cations having a greater unpaired electron density in the α -position, dimerizes predominantly via the resonance form **1**. The formation of a bond between the α -positions of each two radicals results in the formation of the dication **3**.

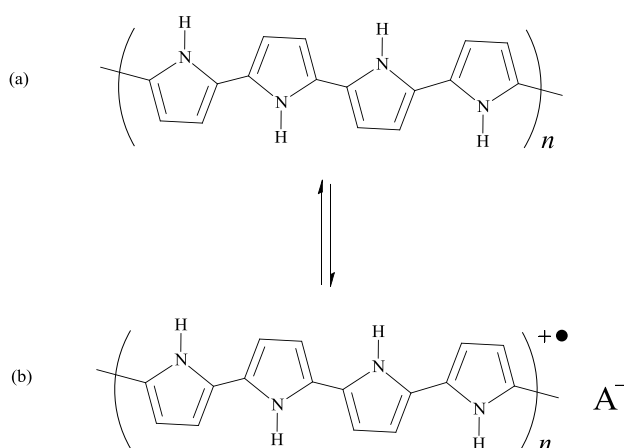
Two protons are eliminated from dication 3, forming the neutral dimer **4** (stabilization step). The neutral dimer **4** with a lower oxidation potential, oxidises to the cation radical **5**.

Since the resonance form **7** is predominant with respect to the other forms, this again reacts by the α -position with a monomer radical cation **1** to form the trimer dication **9** which deprotonates to give the neutral trimer **10**. The propagation continues via the same sequence: oxidation, coupling, deprotonation until the final polymer product is obtained.



Scheme 1. The mechanism for pyrrole oxidative polymerization.[126]

The oxidative polymerisation generally gives the oxidized conducting (doped) form of the polymer rather than the neutral non-conducting form. The final polymer chain carries a positive charge typical of one per ~3-4 pyrrole units, which is counter-balanced by an anion. The structure of the doped polymer is presented in scheme 2 where, A^- (Cl^- or SO_4^{2-} , etc.) is the counter anions incorporated along polymer backbone maintaining the charge neutrality.



Scheme 2. The reduced (a) and oxidized (b) forms of the polymer.

The redox process by an oxidizing agent (i.e. p-type doping) converts the insulating neutral polymer to a polycation. The positive charges created on the backbone of the polymer are considered as the charge carriers for the electrical transport. The electrical conduction of the conductive polymer occurs via hopping of the charges contained in the polymer.[138] The number and mobility of the charges carriers determines the electrical conductivity of the polymer. In addition, other factors influence the conductivity of the conjugated polymers, such as orientation of the polymeric chains and purity of the polymer.[140]

It is generally agreed that the mechanism of conductivity in these polymers is based on the motion of charged defects within the conjugated framework. These charge carriers, either positive (P-type) or negative (n-type), are products of oxidizing or reducing the polymer respectively. For P-type, oxidation initially generates a radical cation with spin positive charge (a polaron) comprise the cationic hole site and the structural distortion which accompanies it. The cationic hole and radicals form a bound species (polaron);

since any increase in separation would necessitate creation of additional higher energy quinoid units.

Two nearby polarons can combine to form a lower energy bipolaron, figure 15. Since the defect is simply a boundary between two moieties of equal energy – the infinite conjugated chain on either side – it can migrate in either direction without affecting the energy of the backbone, provided there, is no significant barrier to the process. This charge carriers mobility leads to the high conductivity of these polymers.

$$\text{Conductivity } (\sigma) \propto n\mu$$

Where, n = number of charge carriers, and μ = mobility.

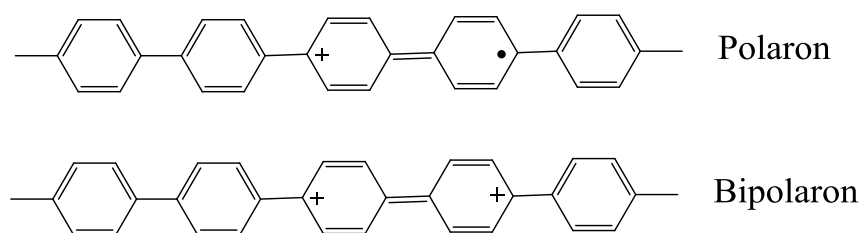


Figure 15. General structure types of polaron and bipolaron forms.

For PPy, structural changes take place in the polymer during the oxidation process.[138, 141] The removal of one electron from the π -electron system of the pyrrole ring also leads to the formation of polaron with associated quinoid-like geometry, figure 16. The polaron separation between positive hole and radical spin is up to four pyrrole rings, and this creates a new localized electronic state in the gap which is occupied by the single unpaired electron. Further oxidation can remove this single electron leading to the formation of bipolaron.

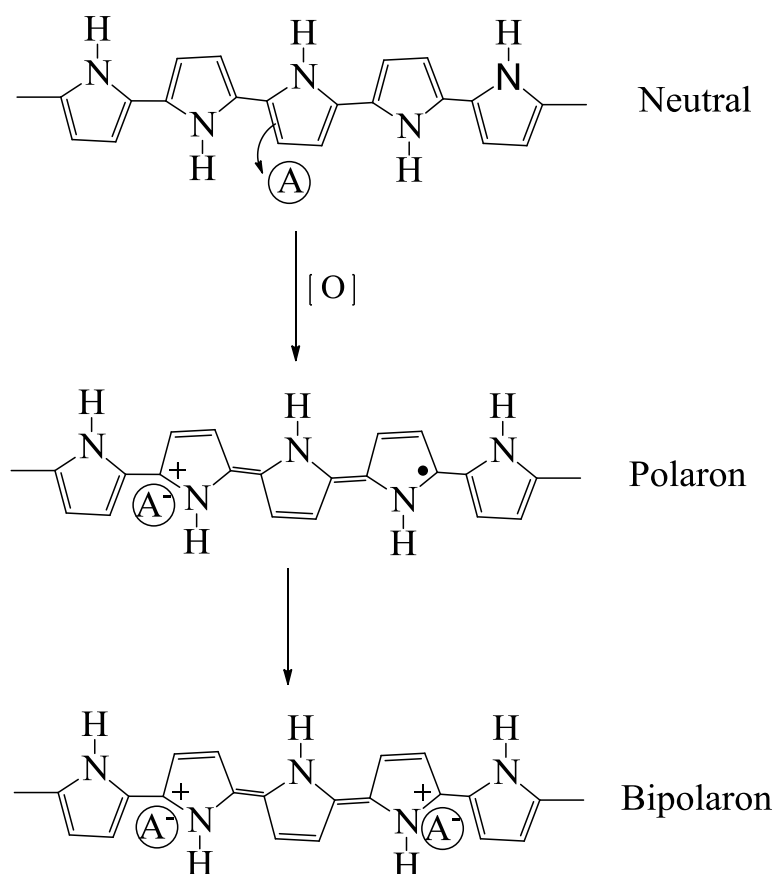


Figure 16. Ideal structure of neutral (non-conducting) polypyrrole (a) and oxidized (conducting) polypyrrole: polaron (b) and bipolaron (c) structures upon doping.

Polaron - bipolaron formation introduces two localized electronic levels in the band gap (E_g) between the valance band (VB) and the conduction band (CB), figure 17. These new electronic levels provide intermediate channels to the promotion of electrons from VB to CB, decreasing the energy required for the electronic transition.[142] The bipolaron bands then be available as charge carriers along the polymer backbone,[121, 140] which can merge in heavily doped material with VB and CB leading to partially filled bands which produces metallic-like conductivity.

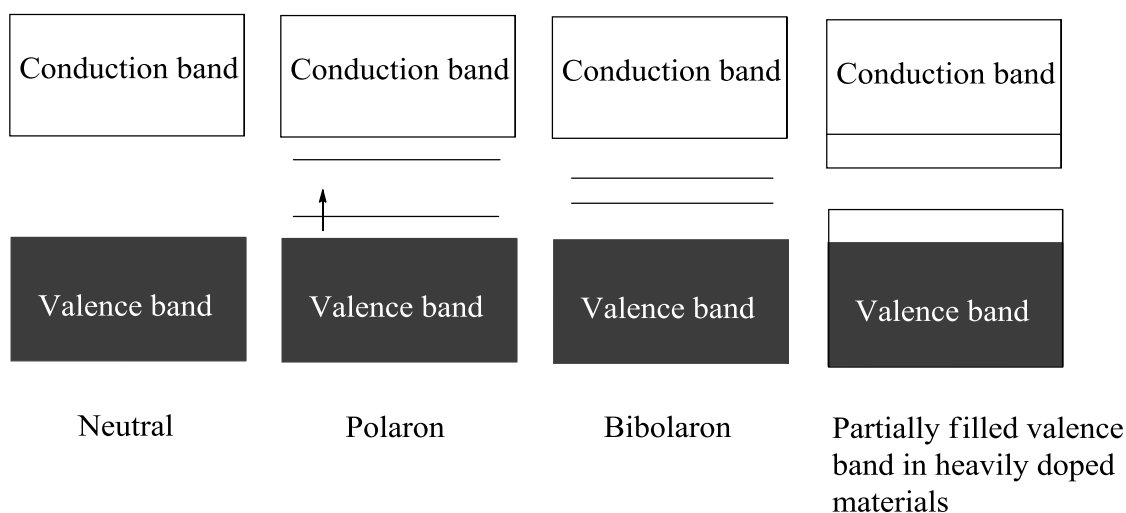


Figure 17. Electronic structure diagrams for a polymer chain containing polaron and bipolaron

1.6. Substituted polypyrrole

PPy, as with many un-functionalized conjugated polymers, are intractable because of their insolubility and some of them, such as polyacetylene, have air-instability.[140, 143] To resolve these problems, CPs can be modified conveniently by copolymerization or structural derivatization.[135, 144, 145]

As pyrrole generally polymerize by linking via the α -positions, the attachment of substituents such as alkyl or methoxy groups at β or N -position to the backbone of polypyrrole is well known to markedly enhance their solubility and consequently their processibility.[146, 147] For example, Masuda *et. al.* [148] have electrochemically polymerized β -alkylated pyrrole to produce poly(3-octylpyrrole) which is soluble in organic solvents. The conductivity of the resulted polymer was 5.0 S cm^{-1} .

A water-soluble carboxylic acid substituted polypyrrole, figure 18(a), has been obtained by electrochemical polymerization of 3-methylpyrrole-4-carboxylic acid in CH_3CN . [149] Other water-soluble substituted polypyrrole was also synthesized by the chemical (FeCl_3) oxidative polymerization of alkylsulfonic acid 3-substituted pyrrole,[146] figure 18(b). The resultant polymers exhibit electrical conductivities in the range 10^{-3} to 0.5 S cm^{-1} .

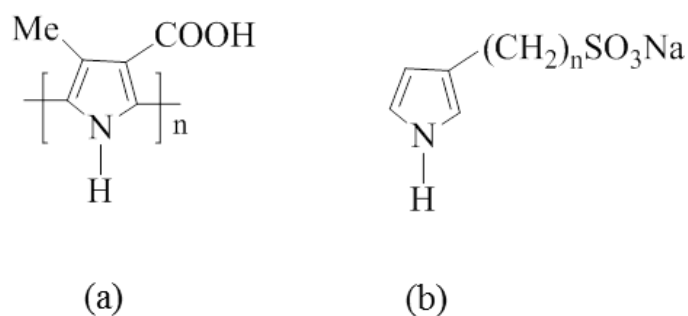
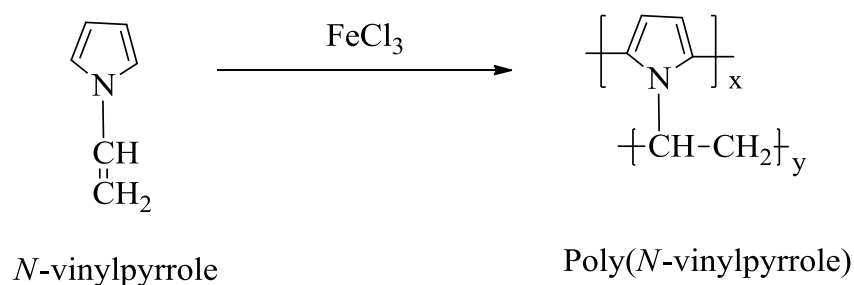


Figure 18. Chemical structure of: a) Poly(3-methylpyrrole-4-carboxylic acid), and b) alkyl sulfonic acid 3-substituted pyrrole.

A wider range of *N*-substituted polypyrrole have also been synthesized.[124] *N*-vinylpyrrole is one such monomer that has been used to form the novel polymer poly(*N*-vinylpyrrole) (PNVPy)[150] which was comprised of two chains, i.e. α -coupled polypyrrole and polyethylene, scheme 3, This was found to be soluble in common organic solvents. PNVPy, as an unfortunate consequence, has much lower electrical conductivities than those of un-substituted polypyrrole. [147, 151] This was attributed to the presence of side chain in the polymer backbone that causes loss of co-planarity of the adjacent aromatic rings due to steric hindrance, which reduces the conjugation length and conductivity of the polymer chains.[152]



Scheme 3. polymerisation of *N*-vinylpyrrole.[150]

N-substitution has also been used as a means to introduce a metal-binding functionality. Coupling transition metal complexes to π -conjugated polymers such as PPy gives hybrid materials in which the properties of the metal complex may be introduced to the conjugated backbone.[153]

The synthesis and characterization of different types of *N*-functional polypyrrole containing a variety of ligands both with and without precomplexation to metal ions have been reported.[154-157] For example, metal-containing polypyrrole-tetraphenylporphyrin complexes has been synthesized using electrochemical polymerization.[157, 158] The complexes involving the connection of pyrrole group via its nitrogen atom directly or through a flexible chain to the phenyl group, as shown in figure 19(a). All the complexes investigated lead to the corresponding polypyrrole films, but it appears that the electropolymerization of complexes in which the pyrrole is connected directly to the macrocycle has lower efficiency than that connected with a flexible chain. This was attributed to the steric hindrance which limits the efficiency of the electrochemical polymerization process. However, one of the possible flexible linker of the metal group to the polymer backbone is a chain of alkyl group.[157, 159]

Using a flexible alkyl linkers, pyrrole-macrocyclic complexes such as metalized cyclam, figure 19(b)[157] and metal-bipyridyl-pyrrole complexes[160, 161] such as 4-methyl-4'(2-pyrrol-lylethyl)-2,2'-bipyridine, figure 19(c) were successfully polymerized.

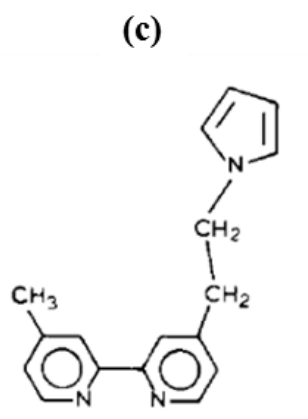
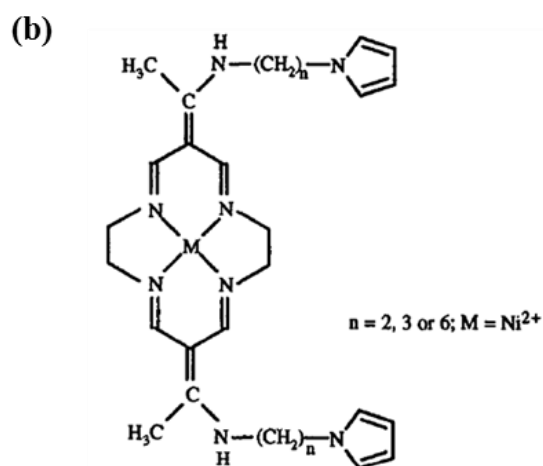
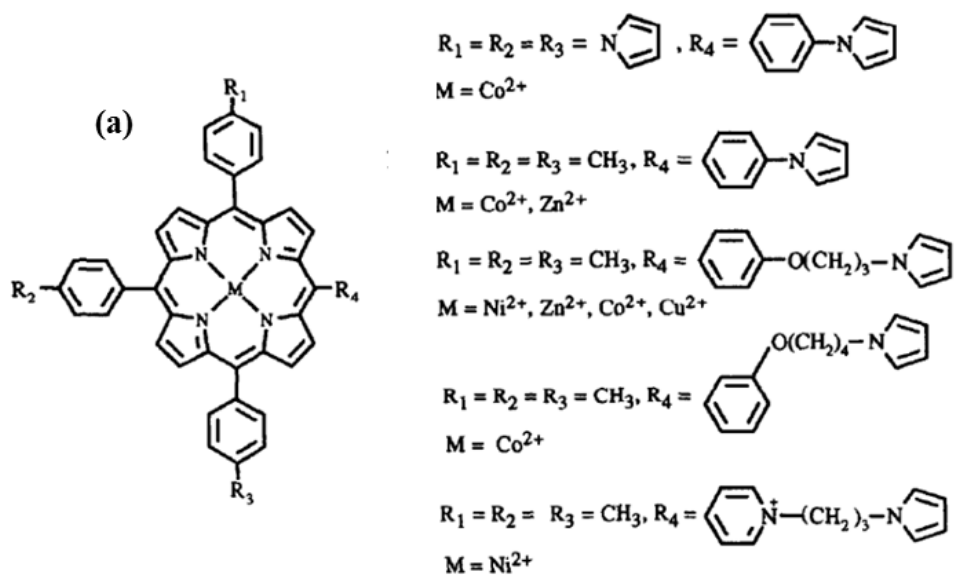


Figure 19. Chemical structure of: Pyrrole-substituted metallo porphyrins (a), metallated cyclam complexes (b), and 4-methyl-4'-(2-pyrrolylethyl)-2,2'-bipyridine (c). Structures (a) and (b) were taken from ref.[157].

1.7. Conductive polymers nanowires

Due to their unique properties arising from their nanoscale size, flexibility, chemically controlled conductivity and readily functionalization, conducting polymer nanowires are anticipated to display improved performance in nanotechnology applications compared with bulk conducting polymers.[56, 162] Moreover, CPs nanowires have been the focus of intense study for the application in the areas of nanoscience and nanotechnology. They can be tuned for a wide-range of applications such as nanoelectronics, [163] energy devices, [164] memory devices[165] gas sensors[166, 167] and actuators[168, 169], etc. As mentioned earlier, CPs nanowires can be formed using several techniques such as soft-template,[170] hard-template[171], as well as using biopolymers (e.g. DNA) as a template.[26, 81]

Templating techniques are considered an efficient route to designing and synthesizing 1-D conducting polymer nanostructures.[45] For example, Yong Lee *et al.*[172, 173] have synthesized polyaniline nanowires by chemical oxidative polymerization using nanochannel templates which were formed by e-beam lithography. The resultant nanowires have conductivity of $\sim 1.2 \text{ S cm}^{-1}$.

1-D nanostructures of poly(3,4-ethylenedioxythiophene) (PEDOT) were synthesized using chemical oxidative polymerization method by Han *et al.*[107, 174] Al_2O_3 membrane was used as a template. The diameter of PEDOT nanowires was controlled through introducing different concentrations of the FeCl_3 oxidant and modifying the polymerization temperature. The conductivity of obtained doped PEDOT nanowires was enhanced to 46 S cm^{-1} after doping process. Han *et al.* reported that this conductivity of the PEDOT nanowires was about 400 times that of the bulk PEDOT.[174]

As mentioned earlier, DNA has been shown to be highly effective in controlling the synthesis of polymeric nanowires. DNA based nanowires of conductive polymers such as polyaniline (PANI),[175] polypyrrole,[176, 177] polyindol (PIn),[110] or poly(*p*-phenylenevinylene) (PPV)[178] can potentially be synthesized along the negatively charged phosphate backbone of DNA. The resulting hybrid CP/DNA nanowires, which are considered as supramolecular polymers, [81, 110, 179] comprise anionic DNA and cationic synthetic conducting polymer.

Ma *et al.*[175] reported the synthesis of PANI/DNA nanowires using chemical oxidation method in a strong acid environment. The low pH needed to initiate the polymerization reaction of aniline, but this acidic conditions is not ideal for the structural integrity of DNA, particularly through the damage of purine bases.[180] However, strong interaction between PANI molecules and stretched DNA strands on silicon chips has been achieved. The enzyme horseradish peroxidase (HRP) has recently been successfully employed as a catalyst for the polymerization of anilines at near neutral pH conditions.[181] This enzymatic approach involving mild reaction conditions for the polymerisation of aniline in the presence of DNA.

Polypyrrole and polythiophene and their derivatives have been used in the fabrication of DNA templated nanowires at neutral pH. DNA templated PPy nanowires has been synthesised using ferric chloride as an oxidising agent.[109, 177, 180] The oxidation of pyrrole was performed at both DNA immobilised on surfaces or in solution. Figure 20 illustrates the formation of PPy/DNA nanowires in the presence of FeCl₃ as an oxidizing agent.[177] When DNA was added to the polymerisation solution, the cationic oligomers are thought to bind to the DNA template through a combination of non-covalent interactions. In particular the cationic polypyrrole is strongly attracted to the anionic phosphate backbone of DNA and these bind together through electrostatic interactions.[177, 182]

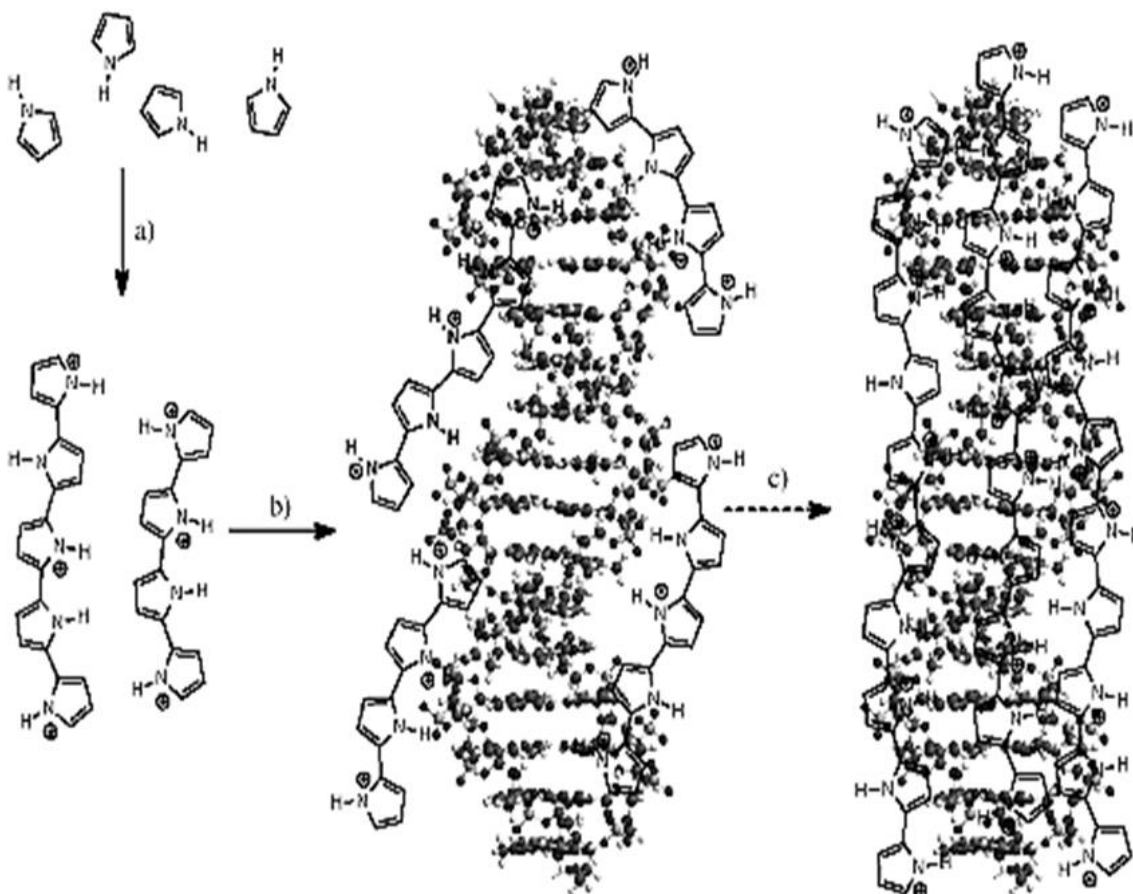
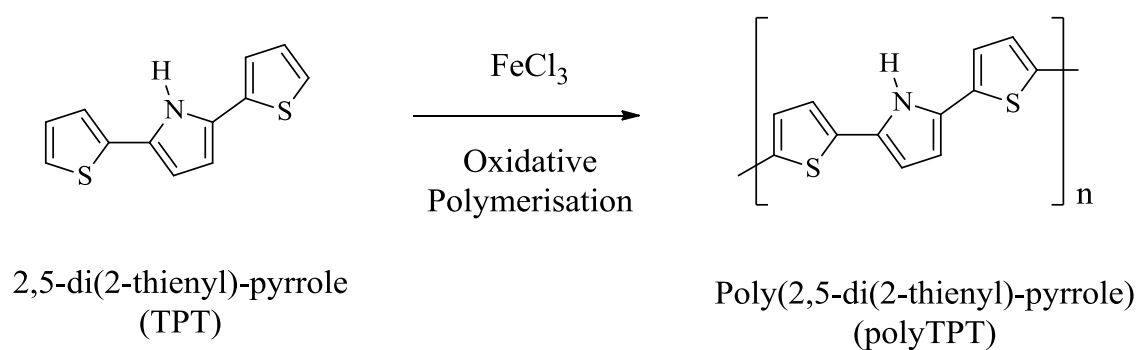


Figure 20. Proposed mechanism of self-assembly DNA/PPy nanowires (adapted from reference[177]).

The resulting PPy/DNA nanostructures were subjected to structural, morphological and electrical investigations. Nanowires from the polymerisation reactions at DNA-immobilised on surface have a beads-on-a string morphology.[177] However, reactions performed in solution produced continuous wires with rather uniform diameters.[109] The results of electrical characterization showed electrical conductivity of the resultant nanowires by use as interconnects in simple electrical devices.[180]

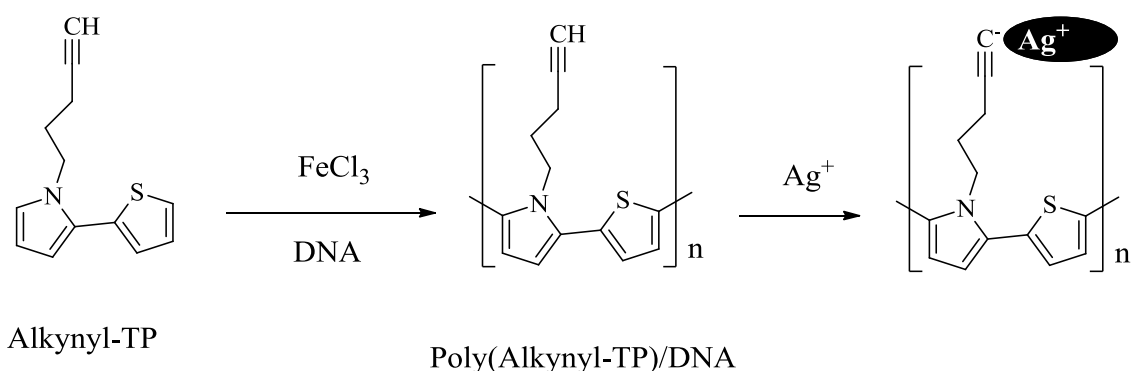
Hassanien *et al.*[110] have fabricated smooth, regular and conductive polyindole/DNA nanowires using the similar approach. The resulting nanowires had conductivity between 2.5 and 40 S cm⁻¹ at room temperature. This research group have reported that their obtained conductivity of PIn/DNA nanowires is considerably higher than that previously reported of bulk polyindole conductivity (10⁻² -10⁻¹ S cm⁻¹).[110]

Watson *et al.*[183] used the DNA-templating approach for preparing supramolecular polymer nanowires by chemical oxidation of 2,5-(bis-2-thienyl)-pyrrole (TPT) using FeCl_3 , scheme 4. In this reaction a mixed aqueous/organic solution ($\text{H}_2\text{O}/\text{MeCN}$) was used because the monomer is not water soluble. The cationic oligo TPT bind to DNA molecules through supramolecular interactions, and then further growth produces the final polyTPT/DNA nanowire. Despite the expected lower supramolecular interactions, due to the weaker potential H-bonding sites available on polyTPT compared to PPy, remarkably smooth and regular nanowires with a continuous polymer coating on DNA template were prepared. The obtained nanowires have a conductivity of $10^{-7} \text{ S cm}^{-1}$, which was several orders of magnitude lower than that of bulk polyTPT material ($10^{-2} \text{ S cm}^{-1}$).



Scheme 4. Schematic of oxidative polymerisation of 2,5-di(2-thienyl)-pyrrole (TPT).

The use of hybrid nanomaterials in the fabrication of nanowires has driven impressive research in order to improve their properties. This offers the opportunity to combine the advantageous properties of each individual constituent in a single composite material.[184] Metal-polymer/DNA nanomaterials have been fabricated in order to improve the electrical, magnetic, and structural properties of 1-D nanostructures.[81, 89, 185] One of the interesting findings related to DNA-templated conducting polymers is the recent work of Said *et al.*[185] Here it has shown that *N*-alkynyl-substituted (thienyl/ pyrrole) derived nanowires acted as highly effective templates themselves for the growth of silver nanowires, scheme 5:



Scheme 5. DNA-templated synthesis of poly(alkynyl-TP) nanowires and deposition of Ag nanocrystals.[185]

Figure 21 shows data from this work and highlights the smooth regular morphology of the metal formed on these CP/DNA templates compound to controls with bare DNA or CP/DNA structures which do not bear the alkyne group. This was ascribed to the alkyne group acting as an effective binding site for the Ag ions allowing facile nucleation of metal clusters.

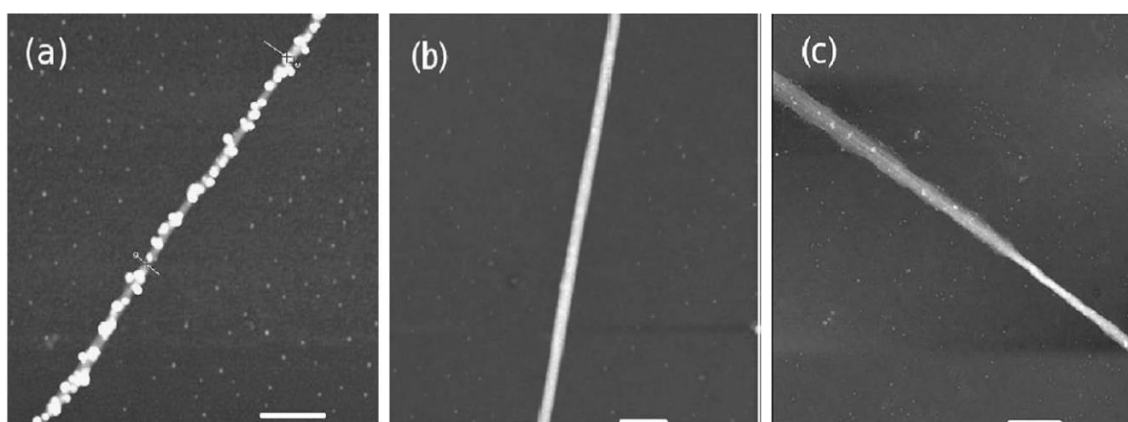


Figure 21. Tapping mode AFM images of nanowires on SiO₂/Si substrate. (a) Ag/DNA; (b) Ag/poly(alkynyl-TP)/DNA; and (c) Ag/poly(TP)/DNA. All scale bars are 1 μm. (These images have been copied from ref.[185])

1.8. Objective

The focus of this project is to develop this method further for different types of metal ion. Towards this the approach will be to synthesize functionalized conductive polymers nanowires using DNA-templating methods that may act as templates themselves for the deposition of metals. In addition to acting as templates for metal

nanowire formation the targeted nanowires may be used as sensing elements for metal ions. The approach will be to design monomers that form conducting polymers functionalized with sites for binding metal ions. Monomers will be designed in modular form to contain (i) a polymerisable group, pyrrole; (ii) a flexible alkyl, propyl-, chain linker; this was chosen to provide a balance between flexibility to allow access for metal ions, and to ensure that the metal-ion coordination was not too remote from the polymer backbone; (iii) a cationic pyridinium group to enhance binding to the anionic template; and (iv) a pyridyl group as a metal ion binding site. Figure 22 illustrates this approach schematically.

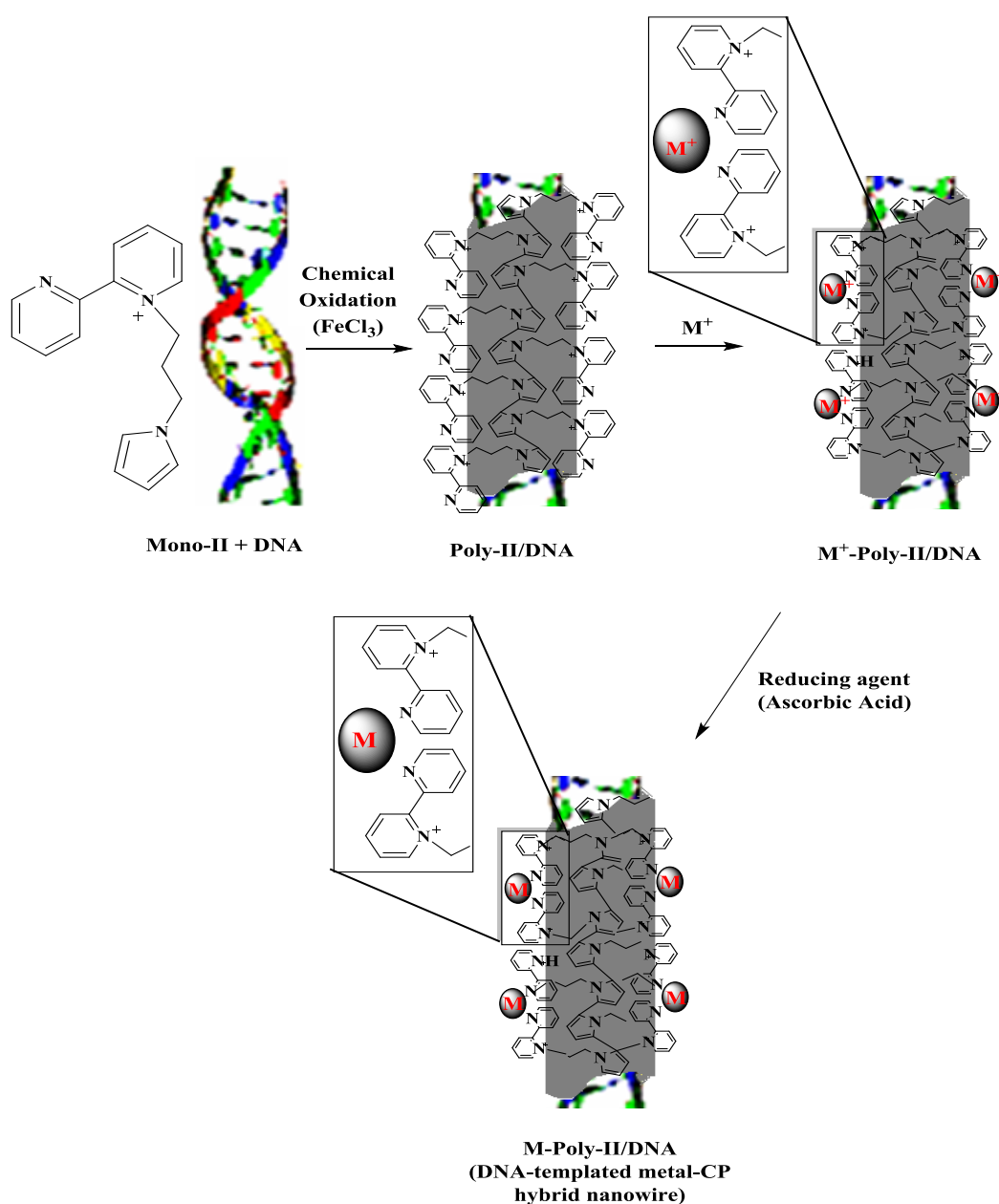


Figure 22. Synthesis of DNA-templated nanowires functionalised for enhanced deposition of metals.

Different pyrrole–pyridine derivatives will be prepared, and polymerised by using a chemical oxidising agents[186] in the presence of calf-thymus (CT) and λ -DNA leading to the formation of polymer/DNA nanowires, figure x. Afterwards, these nanowires will be metallized using different metal ions, particularly Cu and Pd. The prepared nanowires will be structurally characterized using spectroscopic techniques such as FTIR and UV-Vis spectroscopy, then morphologically and electrically characterised using atomic force microscopy (AFM) and a combination of electrostatic force microscopy (EFM), conductive atomic force microscopy (c-AFM) and two-terminal current–voltage measurements.

1.9. References

1. R. Feynman, There's Plenty of Room at the Bottom. *Microelectromechanical Systems*, 1992, **1**, 60 - 66.
2. C. N. Rao, A. Muller and A. K. Cheetham, *The chemistry of nanomaterials*, Wiley - VCH, Weinheim, 2004.
3. C. Binns, *Introduction to Nanoscience and Nanotechnology : Tiny Structure, Big Ideas and Grey Goo*, Wiley, 2010. available at <http://NCL.ebib.com/patron/FullRecord.aspx?p=537323> Accessed 30.11.2012
4. S. Fatikow and V. Eichhorn, Nanohandling automation: trends and current developments. *Proceedings of the Institution of Mechanical Engineers Part C- Journal of Mechanical Engineering Science*, 2008, **222**, 1353-1369.
5. C. Buzea, I. I. Pacheco and K. Robbie, Nanomaterials and nanoparticles: Sources and toxicity. *Biointerphases*, 2007, **2**, MR17-MR71.
6. Y. N. Xia, P. D. Yang, Y. G. Sun, Y. Y. Wu, B. Mayers, B. Gates, Y. D. Yin, F. Kim and Y. Q. Yan, One-dimensional nanostructures: Synthesis, characterization, and applications. *Advanced Materials*, 2003, **15**, 353-389.
7. Y. Imry, *Nanostructures and Mesoscopic Systems*, Academic, New York, 1992.
8. ISO/TS27687:2008, Nanotechnologies-Terminology and definitions for nano-objects-Nanoparticle, nanofibre and nanoplate. available at http://www.iso.org/iso/catalogue_detail?csnumber=44278 Accessed 2 dec. 2012
9. G. E. Moore, Cramming more components onto integrated circuits. *Electronics*, 1965, **38**, 114-117.
10. G. Cao, *Nanostructures and Nanomaterials - Synthesis, Properties and Applications*, World Scientific, 2006. available at http://knovel.com/web/portal/browse/display?_EXT_KNOVEL_DISPLAY_bookid=1334&VerticalID=0 Accessed 15/10/2012
11. J. Wu, Y.-L. Shen, K. Reinhardt and H. Szu, A NANO enhancement to Moore's Law. in *Independent Component Analyses, Compressive Sampling, Wavelets, Neural Net, Biosystems, and Nanoengineering X*, eds. H. Szu and L. Dai, Editon edn., 2012, vol. 8401.
12. C. Burda, X. B. Chen, R. Narayanan and M. A. El-Sayed, Chemistry and properties of nanocrystals of different shapes. *Chemical Reviews*, 2005, **105**, 1025-1102.

13. M. C. Daniel and D. Astruc, Gold nanoparticles: Assembly, supramolecular chemistry, quantum-size-related properties, and applications toward biology, catalysis, and nanotechnology. *Chemical Reviews*, 2004, **104**, 293-346.
14. D. H. Wells, W. N. Delgass and K. T. Thomson, Density functional theory investigation of gold cluster geometry and gas-phase reactivity with O₂. *Journal of Chemical Physics*, 2002, **117**, 10597-10603.
15. W. D. Knight, K. Clemenger, W. A. Deheer, W. A. Saunders, M. Y. Chou and M. L. Cohen, Electronic shell structure and abundances of sodium clusters *Physical Review Letters*, 1984, **52**, 2141-2143.
16. A. P. Alivisatos, Perspectives on the physical chemistry of semiconductor nanocrystals. *Journal of Physical Chemistry*, 1996, **100**, 13226-13239.
17. E. Roduner, Size matters: why nanomaterials are different. *Chemical Society Reviews*, 2006, **35**, 583-592.
18. D. Hristozov and I. Malsch, Hazards and Risks of Engineered Nanoparticles for the Environment and Human Health. *Sustainability*, 2009, **1**, 1161-1194.
19. E. C. Dreaden, A. M. Alkilany, X. Huang, C. J. Murphy and M. A. El-Sayed, The golden age: gold nanoparticles for biomedicine. *Chemical Society Reviews*, 2012, **41**, 2740-2779.
20. P. Buffat and J. P. Borel, Size effect on melting temperature of gold particles *Physical Review A*, 1976, **13**, 2287-2298.
21. G. M. Whitesides, Nanoscience, nanotechnology, and chemistry. *Small*, 2005, **1**, 172-179.
22. T. J. Bukowski and J. H. Simmons, Quantum dot research: Current state and future prospects. *Critical Reviews in Solid State and Materials Sciences*, 2002, **27**, 119-142.
23. M. S. Dresselhaus, Y. M. Lin, O. Rabin, A. Jorio, A. G. Souza, M. A. Pimenta, R. Saito, G. G. Samsonidze and G. Dresselhaus, Nanowires and nanotubes. *Materials Science & Engineering C-Biomimetic and Supramolecular Systems*, 2003, **23**, 129-140.
24. P. M. Ajayan and O. Z. Zhou, Applications of carbon nanotubes. *Carbon Nanotubes*, 2001, **80**, 391-425.
25. C. M. Lieber, Nanoscale science and technology: Building a big future from small things. *Mrs Bulletin*, 2003, **28**, 486-491.
26. A. Houlton and S. M. Watson, DNA-based nanowires. Towards bottom-up nanoscale electronics. *Annu. Rep. Prog. Chem.*, 2011, **107**, 21-42.

27. S. Banerjee, A. Dan and D. Chakravorty, Synthesis of conducting nanowires. *Journal of Materials Science*, 2002, **37**, 4261-4271.
28. G. L. Hornyak, H. F. Tibbals, J. Dutta and J. J. Moore, *Introduction to Nanoscience and Technology*, CRC Press, NY, 2009.
29. R. G. Hobbs, N. Petkov and J. D. Holmes, Semiconductor Nanowire Fabrication by Bottom-Up and Top-Down Paradigms. *Chemistry of Materials*, 2012, **24**, 1975-1991.
30. A. Biswas, I. S. Bayer, A. S. Biris, T. Wang, E. Dervishi and F. Faupel, Advances in top-down and bottom-up surface nanofabrication: Techniques, applications & future prospects. *Advances in Colloid and Interface Science*, 2012, **170**, 2-27.
31. Y. Huang and C. M. Lieber, Integrated nanoscale electronics and optoelectronics: Exploring nanoscale science and technology through semiconductor nanowires. *Pure and Applied Chemistry*, 2004, **76**, 2051-2068.
32. C. Liu, R. Wang, C. Kuo, Y. Liang and W. Chen, Recent Patents on Fabrication of Nanowires. *Recent Patents on Nanotechnology*, 2007, **1**, 11-20.
33. A. Demming, The nature of progress in nanopatterning. *Nanotechnology*, 2012, **23**, 460201-460201.
34. B. Sacca, B. Siebers, R. Meyer, M. Bayer and C. M. Niemeyer, Nanolattices of Switchable DNA-Based Motors. *Small*, 2012, **8**, 3000-3008.
35. C. M. Lieber and Z. L. Wang, Functional nanowires. *Mrs Bulletin*, 2007, **32**, 99-108.
36. C. Joachim, J. K. Gimzewski and A. Aviram, Electronics using hybrid-molecular and mono-molecular devices. *Nature*, 2000, **408**, 541-548.
37. R. Teki, M. K. Datta, R. Krishnan, T. C. Parker, T.-M. Lu, P. N. Kumta and N. Koratkar, Nanostructured Silicon Anodes for Lithium Ion Rechargeable Batteries. *Small*, 2009, **5**, 2236-2242.
38. Y. Cui, Q. Q. Wei, H. K. Park and C. M. Lieber, Nanowire nanosensors for highly sensitive and selective detection of biological and chemical species. *Science*, 2001, **293**, 1289-1292.
39. C. Z. Li, H. X. He, A. Bogozi, J. S. Bunch and N. J. Tao, Molecular detection based on conductance quantization of nanowires. *Applied Physics Letters*, 2000, **76**, 1333-1335.

40. M. M. Arafat, B. Dinan, S. A. Akbar and A. S. M. A. Haseeb, Gas Sensors Based on One Dimensional Nanostructured Metal-Oxides: A Review. *Sensors*, 2012, **12**, 7207-7258.
41. J. Cui, Zinc oxide nanowires. *Materials Characterization*, 2012, **64**, 43-52.
42. A. L. Briseno, S. C. B. Mannsfeld, S. A. Jenekhe, Z. Bao and Y. Xia, Introducing organic nanowire transistors. *Materials Today*, 2008, **11**, 38-47.
43. M. A. Bangar, D. J. Shirale, W. Chen, N. V. Myung and A. Mulchandani, Single Conducting Polymer Nanowire Chemiresistive Label-Free Immunosensor for Cancer Biomarker. *Analytical Chemistry*, 2009, **81**, 2168-2175.
44. J. Kameoka, D. Czaplewski, H. Q. Liu and H. G. Craighead, Polymeric nanowire architecture. *Journal of Materials Chemistry*, 2004, **14**, 1503-1505.
45. L. Pan, H. Qiu, C. Dou, Y. Li, L. Pu, J. Xu and Y. Shi, Conducting Polymer Nanostructures: Template Synthesis and Applications in Energy Storage. *International Journal of Molecular Sciences*, 2010, **11**, 2636-2657.
46. H. D. Tran, D. Li and R. B. Kaner, One-Dimensional Conducting Polymer Nanostructures: Bulk Synthesis and Applications. *Advanced Materials*, 2009, **21**, 1487-1499.
47. K. Ariga, J. P. Hill, M. V. Lee, A. Vinu, R. Charvet and S. Acharya, Challenges and breakthroughs in recent research on self-assembly. *Science and Technology of Advanced Materials*, 2008, **9**.
48. B. D. Gates, Q. B. Xu, M. Stewart, D. Ryan, C. G. Willson and G. M. Whitesides, New approaches to nanofabrication: Molding, printing, and other techniques. *Chemical Reviews*, 2005, **105**, 1171-1196.
49. G. M. Schmid, M. Miller, C. Brooks, N. Khusnatdinov, D. LaBrake, D. J. Resnick, S. V. Sreenivasan, G. Gauzner, K. Lee, D. Kuo, D. Weller and X. Yang, Step and flash imprint lithography for manufacturing patterned media. *Journal of Vacuum Science & Technology B*, 2009, **27**, 573-580.
50. D. Maily, Nanofabrication techniques. *European Physical Journal-Special Topics*, 2009, **172**, 333-342.
51. Y.-Z. Long, M.-M. Li, C. Gu, M. Wan, J.-L. Duvail, Z. Liu and Z. Fan, Recent advances in synthesis, physical properties and applications of conducting polymer nanotubes and nanofibers. *Progress in Polymer Science*, 2011, **36**, 1415-1442.
52. R. S. Wagner and W. C. Ellis, Vapor-liquid-solid mechanism of single crystal growth. *Appl. Phys. Lett.*, 1964, **4**, 89-91.

53. M. S. Gudixsen and C. M. Lieber, Diameter-selective synthesis of semiconductor nanowires. *Journal of the American Chemical Society*, 2000, **122**, 8801-8802.
54. Y. Y. Wu and P. D. Yang, Direct observation of vapor-liquid-solid nanowire growth. *Journal of the American Chemical Society*, 2001, **123**, 3165-3166.
55. D. Almalawi, C. Z. Liu and M. Moskovits, Nanowires formed in anodic oxide nanotemplates *Journal of Materials Research*, 1994, **9**, 1014-1018.
56. J. Jang and V. Springer, Conducting polymer nanomaterials and their applications. in *Emissive Materials: Nanomaterials*, Editon edn., 2006, vol. 199, pp. 189-259.
57. J. Jang and J. H. Oh, A facile synthesis of polypyrrole nanotubes using a template-mediated vapor deposition polymerization and the conversion to carbon nanotubes. *Chemical Communications*, 2004, 882-883.
58. C. R. Martin, Nanomaterials - A membrane-based synthetic approach *Science*, 1994, **266**, 1961-1966.
59. N. Pradhan, H. F. Xu and X. G. Peng, Colloidal CdSe quantum wires by oriented attachment. *Nano Letters*, 2006, **6**, 720-724.
60. J. Noborisaka, J. Motohisa and T. Fukui, Catalyst-free growth of GaAs nanowires by selective-area metalorganic vapor-phase epitaxy. *Applied Physics Letters*, 2005, **86**.
61. R. Calarco, M. Marso, T. Richter, A. I. Aykanat, R. Meijers, A. V. Hart, T. Stoica and H. Luth, Size-dependent photoconductivity in MBE-grown GaN-nanowires. *Nano Letters*, 2005, **5**, 981-984.
62. M. J. Bierman, Y. K. Albert Lau, A. V. Kvit, A. L. Schmitt and S. Jin, Dislocation-driven nanowire growth and Eshelby twist. *Science*, 2008, **320**, 1060-1063.
63. Y. W. Jun, J. S. Choi and J. Cheon, Shape control of semiconductor and metal oxide nanocrystals through nonhydrolytic colloidal routes. *Angewandte Chemie-International Edition*, 2006, **45**, 3414-3439.
64. W. K. Son, J. H. Youk and W. H. Park, Antimicrobial cellulose acetate nanofibers containing silver nanoparticles. *Carbohydrate Polymers*, 2006, **65**, 430-434.
65. Y. Shin, I.-T. Bae, B. W. Arey and G. J. Exarhos, Facile stabilization of gold-silver alloy nanoparticles on cellulose nanocrystal. *Journal of Physical Chemistry C*, 2008, **112**, 4844-4848.

66. S. Padalkar, J. R. Capadona, S. J. Rowan, C. Weder, Y.-H. Won, L. A. Stanciu and R. J. Moon, Natural Biopolymers: Novel Templates for the Synthesis of Nanostructures. *Langmuir*, 2010, **26**, 8497-8502.
67. M. Reches and E. Gazit, Casting metal nanowires within discrete self-assembled peptide nanotubes. *Science*, 2003, **300**, 625-627.
68. T. Scheibel, R. Parthasarathy, G. Sawicki, X. M. Lin, H. Jaeger and S. L. Lindquist, Conducting nanowires built by controlled self-assembly of amyloid fibers and selective metal deposition. *Proceedings of the National Academy of Sciences of the United States of America*, 2003, **100**, 4527-4532.
69. S.-Y. Lee, J.-S. Lim and M. T. Harris, Synthesis and application of virus-based hybrid nanomaterials. *Biotechnology and Bioengineering*, 2012, **109**, 16-30.
70. A. V. Pinheiro, D. Han, W. M. Shih and H. Yan, Challenges and opportunities for structural DNA nanotechnology. *Nature Nanotechnology*, 2011, **6**, 763-772.
71. T. Wang, D. Schiffels, S. M. Cuesta, D. K. Fygenson and N. C. Seeman, Design and Characterization of 1D Nanotubes and 2D Periodic Arrays Self-Assembled from DNA Multi-Helix Bundles. *Journal of the American Chemical Society*, 2012, **134**, 1606-1616.
72. S. Neidle, *Oxford handbook of nucleic acid structure / edited by Oxford University Press*, Oxford, 1999.
73. A. R. P. Andrew Houlton, Miguel Angel Galindo and Benjamin R. Horrocks DNA-based routes to semiconducting nanomaterials *Chem. Commun.* , 2009, 1797-1806.
74. G. Qun, C. Chuanding, G. Ravikanth, S. Shivashankar, A. Sathish, D. Kun and H. Donald., DNA nanowire fabrication *Nanotechnology*, 2006, **17**, R14-R25.
75. D. Yang, M. J. Campolongo, T. N. N. Tran, R. C. H. Ruiz, J. S. Kahn and D. Luo, Novel DNA materials and their applications. *Wiley Interdisciplinary Reviews-Nanomedicine and Nanobiotechnology*, 2010, **2**, 648-669.
76. M. D. Ventra and M. Zwolak, in *Encyclopedia of Nanoscience and Nanotechnology*, ed. H. S. Nalwa, American Scientific Publishers, Virginia, Editon edn., 2004, vol. X, pp. 1-19.
77. K. K. E. Braun, *Advances in Physics*, Taylor & Francis, 2004.available at <http://dx.doi.org/10.1080/00018730412331294688> Accessed 24 March 2009
78. M. Z. M. D. Ventra, in *Encyclopedia of Nanoscience and Nanotechnology*, ed. H. S. Nalwa, American Scientific Publishers, Virginia, Editon edn., 2004, vol. X, pp. 1-19.

79. Q. Gu, C. Cheng, R. Gonela, S. Suryanarayanan, S. Anabathula, K. Dai and D. T. Haynie, DNA nanowire fabrication *Nanotechnology*, 2006, **17**, R14–R25.
80. Q. C. Gu, Chuanding; Gonela, Ravikanth; Suryanarayanan, Shivashankar; Anabathula, Sathish; Dai, Kun; Haynie, Donald T. , DNA nanowire fabrication *Nanotechnology*, 2006, **17**, R14–R25.
81. A. Houlton, A. R. Pike, M. A. Galindo and B. R. Horrocks, DNA-based routes to semiconducting nanomaterials *Chem. Commun.* , 2009, 1797-1806.
82. E. Braun and K. Keren, From DNA to transistors. *Advances in Physics*, 2004, **53**, 441-496.
83. Y. Ma, J. Zhang, G. Zhang and H. He, Polyaniline Nanowires on Si Surfaces Fabricated with DNA Templates. *Journal of the American Chemical Society*, 2004, **126**, 7097-7101.
84. A. Kuzyk, R. Schreiber, Z. Fan, G. Pardatscher, E.-M. Roller, A. Hoegele, F. C. Simmel, A. O. Govorov and T. Liedl, DNA-based self-assembly of chiral plasmonic nanostructures with tailored optical response. *Nature*, 2012, **483**, 311-314.
85. R. M. Stoltenberg and A. T. Woolley, DNA-templated nanowire fabrication. *Biomedical Microdevices*, 2004, **6**, 105-111.
86. A. El-Sagheer and T. Brown, Synthesis and Polymerase Chain Reaction Amplification of DNA Strands Containing an Unnatural Triazole Linkage. *J. Am. Chem. Soc.*, 2009, **131**, 3958-3964.
87. Blackburn G. M., Gait M. J., Loakes D. and W. D. M., *Nucleic acids in chemistry and biology*, 3rd Ed edn., Eds. UK, Cambridge UK, 2006.
88. H. A. Becerril and A. T. Woolley, DNA-templated nanofabrication *Chem. Soc. Rev.*, 2009, **38**, 329-337
89. H. D. A. Mohamed, S. M. D. Watson, B. R. Horrocks and A. Houlton, Magnetic and conductive magnetite nanowires by DNA-templating. *Nanoscale*, 2012, **4**, 5936-5945.
90. E. Braun, Y. Eichen, U. Sivan and G. Ben-Yoseph, DNA-templated assembly and electrode attachment of a conducting silver wire. *Nature*, 1998, **391**, 775-778.
91. F. Patolsky, Y. Weizmann, O. Lioubashevski and I. Willner, Au-nanoparticle nanowires based on DNA and polylysine templates. *Angewandte Chemie-International Edition*, 2002, **41**, 2323-2327.

92. C. F. Monson and A. T. Woolley, DNA-templated construction of copper nanowires. *Nano Letters*, 2003, **3**, 359-363.
93. W. E. Ford, O. Harnack, A. Yasuda and J. M. Wessels, Platinated DNA as precursors to templated chains of metal nanoparticles. *Advanced Materials*, 2001, **13**, 1793-1797.
94. R. Seidel, M. Mertig and W. Pompe, Scanning force microscopy of DNA metallization. *Surface and Interface Analysis*, 2002, **33**, 151-154.
95. M. Mertig, L. C. Ciacchi, R. Seidel, W. Pompe and A. De Vita, DNA as a selective metallization template. *Nano Letters*, 2002, **2**, 841-844.
96. S. M. D. Watson, N. G. Wright, B. R. Horrocks and A. Houlton, Preparation, Characterization and Scanned Conductance Microscopy Studies of DNA-Templated One-Dimensional Copper Nanostructures. *Langmuir*, 2010, **26**, 2068-2075.
97. J. Richter, R. Seidel, R. Kirsch, M. Mertig, W. Pompe, J. Plaschke and H. K. Schackert, Nanoscale palladium metallization of DNA. *Advanced Materials*, 2000, **12**, 507-510.
98. J. Richter, M. Mertig, W. Pompe, I. Monch and H. K. Schackert, Construction of highly conductive nanowires on a DNA template. *Applied Physics Letters*, 2001, **78**, 536-538.
99. Z. X. Deng and C. D. Mao, DNA-templated fabrication of 1D parallel and 2D crossed metallic nanowire arrays. *Nano Letters*, 2003, **3**, 1545-1548.
100. H. Kudo and M. Fujihira, DNA-Templated copper nanowire fabrication by a two-step process involving electroless metallization. *Ieee Transactions on Nanotechnology*, 2006, **5**, 90-92.
101. T. Torimoto, M. Yamashita, S. Kuwabata, T. Sakata, H. Mori and H. Yoneyama, Fabrication of CdS nanoparticle chains along DNA double strands. *Journal of Physical Chemistry B*, 1999, **103**, 8799-8803.
102. L. Levina, W. Sukhovatkin, S. Musikhin, S. Cauchi, R. Nisman, D. P. Bazett-Jones and E. H. Sargent, Efficient infrared-emitting PbS quantum dots grown on DNA and stable in aqueous solution and blood plasma. *Advanced Materials*, 2005, **17**, 1854-1857.
103. V. Stsiapura, A. Sukhanova, A. Baranov, M. Artemyev, O. Kulakovich, V. Oleinikov, M. Pluot, J. H. M. Cohen and I. Nabiev, DNA-assisted formation of quasi-nanowires from fluorescent CdSe/ZnS nanocrystals. *Nanotechnology*, 2006, **17**, 581-587.

104. S. Hinds, B. J. Taft, L. Levina, V. Sukhovatkin, C. J. Dooley, M. D. Roy, D. D. MacNeil, E. H. Sargent and S. O. Kelley, Nucleotide-directed growth of semiconductor nanocrystals. *Journal of the American Chemical Society*, 2006, **128**, 64-65.
105. L. Dong, T. Hollis, B. A Connolly, N. G. Wright, B. R. Horrocks and A. Houlton, DNA-Templated Semiconductor Nanoparticle Chains and Wires. *Advanced Materials*, 2007, **19**, 1748-1751.
106. P. Nickels, W. U. Dittmer, S. Beyer, J. P. Kotthaus and F. C. Simmel, Polyaniline nanowire synthesis templated by DNA. *Nanotechnology*, 2004, **15**, 1524-1529.
107. M. G. Han and S. H. Foulger, 1-dimensional structures of poly(3,4-ethylenedioxythiophene) (PEDOT): a chemical route to tubes, rods, thimbles, and belts. *Chemical Communications*, 2005, 3092-3094.
108. A. H. Bae, T. Hatano, M. Numata, M. Takeuchi and S. Shinkai, Superstructural poly(pyrrole) assemblies created by a DNA templating method. *Macromolecules*, 2005, **38**, 1609-1615.
109. S. Pruneanu, S. A. F. Al-Said, L. Dong, T. A. Hollis, M. A. Galindo, N. G. Wright, A. Houlton and B. R. Horrocks, Self-assembly of DNA-templated polypyrrole nanowires: Spontaneous formation of conductive nanoropes. *Advanced Functional Materials*, 2008, **18**, 2444-2454.
110. R. Hassanien, M. Al-Hinai, S. A. F. Al-Said, R. Little, L. Siller, N. G. Wright, A. Houlton and B. R. Horrocks, Preparation and Characterization of Conductive and Photoluminescent DNA-Templated Polyindole Nanowires. *Acs Nano*, 2010, **4**, 2149-2159.
111. H. G. Kiess, *Conjugated conducting polymers* Springer-Verlag, Berlin, New York 1992.
112. T. A. Skotheim and J. Reynolds, *Handbook of Conducting Polymers*, CRC Press, New York, USA, 2007.
113. C. Weder, Synthesis, processing and properties of conjugated polymer networks. *Chemical Communications*, 2005, 5378-5389.
114. W. R. Salaneck and J. L. Bredas, Conjugated polymers *Solid State Communications*, 1994, **92**, 31-36.
115. A. J. Heeger, *Conjugated Polymers: The Interconnection of Chemical and Electronic Structure* Oxford University Press, Oxford, 1993.

116. J. S. Miller, The 2000 Nobel Prize in Chemistry - A personal accolade. *Chemphyschem*, 2000, **1**, 229-230.
117. B. G. Levi, Nobel Prize in chemistry salutes the discovery of conducting polymers. *Physics Today*, 2000, **53**, 19-22.
118. J. L. Bredas and G. B. Street, Polarons, and solitons in conducting polymers *Accounts of Chemical Research*, 1985, **18**, 309-315.
119. D. Kumar and R. C. Sharma, Advances in conductive polymers. *European Polymer Journal*, 1998, **34**, 1053-1060.
120. M. R., *Handbook of Polymers in Electronics*, Rapra Technology-Ltd UK, 2002.
121. J. L. Bredas, B. Themans, J. G. Fripiat, J. M. Andre and R. R. Chance, Highly conducting polyparaphenylene, polypyrrole, and polythiophene chains - an abinitio study of the geometry and electronic-structure modifications upon doping. *Physical Review B*, 1984, **29**, 6761-6773.
122. Kiebooms R., M. R. and L. K. H., *Handbook of Advanced Electronic and Photonic Materials and Devices*, Academic Press, San Diego, CA 2001.
123. A. K. Bakhshi and G. Bhalla, Electrically conducting polymers: Materials of the twentyfirst century. *Journal of Scientific & Industrial Research*, 2004, **63**, 715-728.
124. T. A. Skotheim, *Handbook of Conducting Polymers*, Marcel Dekker, New York, 1986.
125. J. C. W. Chien, *Polyacetylene: Chemistry, Physics and Materials Science*, Academic Press, New York, 1984.
126. S. Sadki, P. Schottland, N. Brodie and G. Sabouraud, The mechanisms of pyrrole electropolymerization. *Chemical Society Reviews*, 2000, **29**, 283-293.
127. M. M. Chehimi, M. L. Abel, C. Perruchot, M. Delamar, S. F. Lascelles and S. P. Armes, The determination of the surface energy of conducting polymers by inverse gas chromatography at infinite dilution. *Synthetic Metals*, 1999, **104**, 51-59.
128. C. L. Heisey, J. P. Wightman, E. H. Pittman and H. H. Kuhn, Surface and adhesion properties of polypyrrole-coated textiles *Textile Research Journal*, 1993, **63**, 247-256.
129. H. Ryu, N. Sheng, T. Ohtsuka, S. Fujita and H. Kajiyama, Polypyrrole film on 55% Al-Zn-coated steel for corrosion prevention. *Corrosion Science*, 2012, **56**, 67-77.

130. B. Zinger and L. L. Miller, Timed release of chemicals from polypyrrole films *Journal of the American Chemical Society*, 1984, **106**, 6861-6863.
131. M. Lin, X. Hu, Z. Ma and L. Chen, Functionalized polypyrrole nanotube arrays as electrochemical biosensor for the determination of copper ions. *Analytica Chimica Acta*, 2012, **746**, 63-69.
132. Rajesh, W. Takashima and K. Kaneto, Amperometric phenol biosensor based on covalent immobilization of tyrosinase onto an electrochemically prepared novel copolymer poly (N-3-aminopropyl pyrrole-co-pyrrole) film. *Sensors and Actuators B-Chemical*, 2004, **102**, 271-277.
133. A. Ramanavicius, A. Ramanaviciene and A. Malinauskas, Electrochemical sensors based on conducting polymer- polypyrrole. *Electrochimica Acta*, 2006, **51**, 6025-6037.
134. B. Saoudi, C. Despas, M. M. Chehimi, N. Jammul, M. Delamar, J. Bessiere and A. Walcarius, Study of DNA adsorption on polypyrrole: interest of dielectric monitoring. *Sensors and Actuators B-Chemical*, 2000, **62**, 35-42.
135. X. Li, Y. Wang, X. Yang, J. Chen, H. Fu and T. Cheng, Conducting polymers in environmental analysis. *Trac-Trends in Analytical Chemistry*, 2012, **39**, 163-179.
136. G. B. Street, Characterization of polypyrrole *Abstracts of Papers of the American Chemical Society*, 1983, **186**, 17-PMSE.
137. D. D. Ateh, H. A. Navsaria and P. Vadgama, Polypyrrole-based conducting polymers and interactions with biological tissues. *Journal of the Royal Society Interface*, 2006, **3**, 741-752.
138. R. Yang, D. F. Evans, L. Christensen and W. A. Hendrickson, Scanning tunneling microscopy evidence of semicrystalline and helical conducting polymer structures *Journal of Physical Chemistry*, 1990, **94**, 6117-6122.
139. T. C. Clarke, J. C. Scott and G. B. Street, Magic angle spinning NMR of conducting polymers *Ibm Journal of Research and Development*, 1983, **27**, 313-320.
140. L. M. Dai, Advanced syntheses and microfabrications of conjugated polymers, C-60-containing polymers and carbon nanotubes for optoelectronic applications. *Polymers for Advanced Technologies*, 1999, **10**, 357-420.
141. X. Lin, J. Li, E. Smela and S. Yip, Polaron-Induced conformation change in single polypyrrole chain: An intrinsic actuation mechanism. *International Journal of Quantum Chemistry*, 2005, **102**, 980-985.

142. J. L. Bredas, J. C. Scott, K. Yakushi and G. B. Street, Polarons and bipolarons in polypyrrole - evaluation of the band - structure and optical - spectrum upon doping *Physical Review B*, 1984, **30**, 1023-1025.
143. M. Aldissi, Review of the synthesis of polyacetylene and its stabilization to ambient atmosphere *Synthetic Metals*, 1984, **9**, 131-141.
144. Anjula, *Gas Sensor using Polymer films*, Ieee, New York, 2009.
145. S. Ahmad, S. Sen Gursoy, S. Kazim and A. Uygun, Growth of N-substituted polypyrrole layers in ionic liquids: Synthesis and its electrochromic properties. *Solar Energy Materials and Solar Cells*, 2012, **99**, 95-100.
146. G. Wallace, G. M. Spinks, L. Kane-Maguire and P. R. Teasdale, *Conductive Electroactive Polymers: Intelligent Materials Systems*, Second Edition edn., CRC PRESS, New York, USA, 2003.
147. A. F. Diaz, A. Martinez and K. K. Kanazawa, Electrochemistry of some substituted pyrroles *Journal of Electroanalytical Chemistry*, 1981, **130**, 181-187.
148. H. Masuda, S. Tanaka and K. Kaeriyama, Electrochemical polymerization of 3-octylpyrrole *Journal of Polymer Science Part a-Polymer Chemistry*, 1990, **28**, 1831-1840.
149. P. G. Pickup, Poly-(3-methylepyrrole-4-carboxylic acid)-an electronically conducting ion-exchange polymer *Journal of Electroanalytical Chemistry*, 1987, **225**, 273-280.
150. W. Wang, D. Yu and F. Tian, Synthesis and characterization of a new polypyrrole based on N-vinyl pyrrole. *Synthetic Metals*, 2008, **158**, 717-721.
151. R. J. Waltman and J. Bargon, Electrically conducting polymers- a review of the electropolymerization reaction, of the effects of chemical-structure on polymer film properties, and of applications towards technology *Canadian Journal of Chemistry-Revue Canadienne De Chimie*, 1986, **64**, 76-95.
152. M. Jaiswal and R. Menon, Polymer electronic materials: a review of charge transport. *Polymer International*, 2006, **55**, 1371-1384.
153. M. O. Wolf, Recent advances in conjugated transition metal-containing polymers and materials. *Journal of Inorganic and Organometallic Polymers and Materials*, 2006, **16**, 189-199.
154. S. J. Higgins, Conjugated polymers incorporating pendant functional groups - synthesis and characterisation. *Chemical Society Reviews*, 1997, **26**, 247-257.

155. P. N. Bartlett, L. Y. Chung and P. Moore, Conducting polymer-films-attachment of pyrrole groups to open-chain nitrogen-containing ligands and related species *Electrochimica Acta*, 1990, **35**, 1273-1278.
156. B. J. Holliday and T. M. Swager, Conducting metallopolymers: the roles of molecular architecture and redox matching. *Chemical Communications*, 2005, 23-36.
157. A. Deronzier and J. C. Moutet, Polypyrrole films containing metal complexes: Syntheses and applications. *Coordination Chemistry Reviews*, 1996, **147**, 339-371.
158. A. Bettelheim, B. A. White, S. A. Raybuck and R. W. Murray, Electrochemical polymerization of amino-substituted, pyrrole-substituted, and hydroxy-substituted tetraphenylporphyrins. *Inorganic Chemistry*, 1987, **26**, 1009-1017.
159. M. O. Wolf, Transition-metal-polythiophene hybrid materials. *Advanced Materials*, 2001, **13**, 545-553.
160. F. Daire, F. Bedioui, J. Devynck and C. Biedcharreton, Electropolymerization and redox properties of bipyridine polypyrrole and Cu(II) bipyridyl polypyrrole film electrodes *Journal of Electroanalytical Chemistry*, 1986, **205**, 309-318.
161. A. Deronzier, J. C. Moutet and E. Saintaman, Electrocatalytic hydrogenation of organic-compounds on carbon electrodes modified by poly(pyrrole-bis 2,2'-bipyridyl palladium(II) complex) films *Journal of Electroanalytical Chemistry*, 1992, **327**, 147-158.
162. S.-H. Yeom, B.-H. Kang, K.-J. Kim and S.-W. Kang, Nanostructures in biosensor-a review. *Frontiers in Bioscience-Landmark*, 2011, **16**, 997-1023.
163. C. G. Wu and T. Bein, Conducting polyaniline filaments in a mesoporous channel host *Science*, 1994, **264**, 1757-1759.
164. G. Nystrom, M. Stromme, M. Sjodin and L. Nyholm, Rapid potential step charging of paper-based polypyrrole energy storage devices. *Electrochimica Acta*, 2012, **70**, 91-97.
165. A. Kathalingam and J.-K. Rhee, Fabrication of Bistable Switching Memory Devices Utilizing Polymer-ZnO Nanocomposites. *Journal of Electronic Materials*, 2012, **41**, 2162-2168.
166. S. Virji, J. X. Huang, R. B. Kaner and B. H. Weiller, Polyaniline nanofiber gas sensors: Examination of response mechanisms. *Nano Letters*, 2004, **4**, 491-496.
167. J. Huang, S. Virji, B. H. Weiller and R. B. Kaner, Nanostructured polyaniline sensors. *Chemistry-a European Journal*, 2004, **10**, 1314-1319.

168. T. F. Otero, J. J. Sanchez and J. G. Martinez, Biomimetic Dual Sensing-Actuators Based on Conducting Polymers. Galvanostatic Theoretical Model for Actuators Sensing Temperature. *Journal of Physical Chemistry B*, 2012, **116**, 5279-5290.
169. Y. Berdichevsky and Y. H. Lo, Polypyrrole nanowire actuators. *Advanced Materials*, 2006, **18**, 122-125.
170. M. Wan, A template-free method towards conducting polymer nanostructures. *Advanced Materials*, 2008, **20**, 2926-2932.
171. L. Pan, L. Pu, Y. Shi, S. Song, Z. Xu, R. Zhang and Y. Zheng, Synthesis of polyaniline nanotubes with a reactive template of manganese oxide. *Advanced Materials*, 2007, **19**, 461-464.
172. S.-Y. Lee, H. Lim, G.-R. Choi, J.-D. Kim, E.-K. Suh and S.-K. Lee, Metal-to-Insulating Transition of Single Polyaniline (PANI) Nanowire: A Dedoping Effect. *Journal of Physical Chemistry C*, 2010, **114**, 11936-11939.
173. S.-Y. Lee, G.-R. Choi, H. Lim, K.-M. Lee and S.-K. Lee, Electronic transport characteristics of electrolyte-gated conducting polyaniline nanowire field-effect transistors. *Applied Physics Letters*, 2009, **95**.
174. M. G. Han and S. H. Foulger, Facile synthesis of poly(3,4-ethylenedioxythiophene) nanofibers from an aqueous surfactant solution. *Small*, 2006, **2**, 1164-1169.
175. Y. F. Ma, J. M. Zhang, G. J. Zhang and H. X. He, Polyaniline nanowires on Si surfaces fabricated with DNA templates. *Journal of the American Chemical Society*, 2004, **126**, 7097-7101.
176. S. Pruneanu, S. Al-Said, L. Dong, T. A. Hollis, M. A. Galindo, N. G. Wright, A. Houlton and B. R. Horrocks, Self-Assembly of DNA-Templated Polypyrrole Nanowires: Spontaneous Formation of Conductive Nanoropes. *Advanced Functional Materials*, 2008, **18**, 2444-2454.
177. L. Dong, T. Hollis, S. Fishwick, B. A. Connolly, N. G. Wright, B. R. Horrocks and A. Houlton, Synthesis, Manipulation and Conductivity of Supramolecular Polymer Nanowires. *Chem. Eur. J.*, 2007, **13**, 822 - 828.
178. Y. Eichen, E. Braun, U. Sivan and G. Ben-Yoseph, Self-assembly of nanoelectronic components and circuits using biological templates. *Acta Polymerica*, 1998, **49**, 663-670.
179. B. Saoudi, N. Jammul, M. L. Abel, M. M. Chehimi and G. Dodin, DNA adsorption onto conducting polypyrrole. *Synthetic Metals*, 1997, **87**, 97-103.

180. S. Pruneanu, L. Dong, T. A. Hollis, N. G. Wright, M. A. Galindo, A. R. Pike, B. A. Connolly, B. R. Horrocks and A. Houlton, DNA-based Inorganic and Polymer Nanowires: Synthesis, Characterization and Electrical Properties of Nanoelectronic Components. in *DNA-Based Nanodevices*, eds. W. Fritzsche and F. Bier, Editon edn., 2008, vol. 1062, pp. 33-42.
181. R. Nagarajan, W. Liu, J. Kumar, S. K. Tripathy, F. F. Bruno and L. A. Samuelson, Manipulating DNA conformation using intertwined conducting polymer chains. *Macromolecules*, 2001, **34**, 3921-3927.
182. P. Das, *LONG-range charge transfer in plasmide DNA condensates and DNA-directed assembly of conducting polymers*. Georgia Institute of Technology, 2007.
183. S. M. D. Watson, J. H. Hedley, M. A. Galindo, S. A. F. Al-Said, N. G. Wright, B. A. Connolly, B. R. Horrocks and A. Houlton, Synthesis, Characterisation and Electrical Properties of Supramolecular DNA-Templated Polymer Nanowires of 2,5-(Bis-2-thienyl)-pyrrole. *Chemistry-a European Journal*, 2012, **18**, 12008-12019.
184. E. Lahiff, C. Lynam, N. Gilmartin, R. O'Kennedy and D. Diamond, The increasing importance of carbon nanotubes and nanostructured conducting polymers in biosensors. *Analytical and Bioanalytical Chemistry*, 2010, **398**, 1575-1589.
185. S. A. F. Al-Said, R. Hassanien, J. Hannant, M. A. Galindo, S. Pruneanu, A. R. Pike, A. Houlton and B. R. Horrocks, Templating Ag on DNA/polymer hybrid nanowires: Control of the metal growth morphology using functional monomers. *Electrochemistry Communications*, 2009, **11**, 550-553.
186. C. R. Martin, Template Synthesis of Electronically Conductive Polymer Nanostructures. *Accounts of Chemical Research* 1995, **28**, 61-68.

2. Experimental techniques used in nanowires characterisation

2.1. Alignment of DNA-templated Nanowires

One of the main challenges in the assembly of DNA-based nanoscale devices is in ordering the nanowires in parallel or crossed patterns. For example, the main challenge in two terminal I-V techniques is the alignment of nanowires between Au microelectrodes. Several methods to stretch and align DNA molecules have been reported.[1-4] Braun *et al.*[5] interconnected the DNA-templated silver nanowires with two gold electrodes exploiting the hybridisation process, figure 23. The sticky ends at the 3'- and 5'-termini of the duplex λ -DNA were captured by complementary synthetic oligonucleotides attached to each of the gold electrodes.

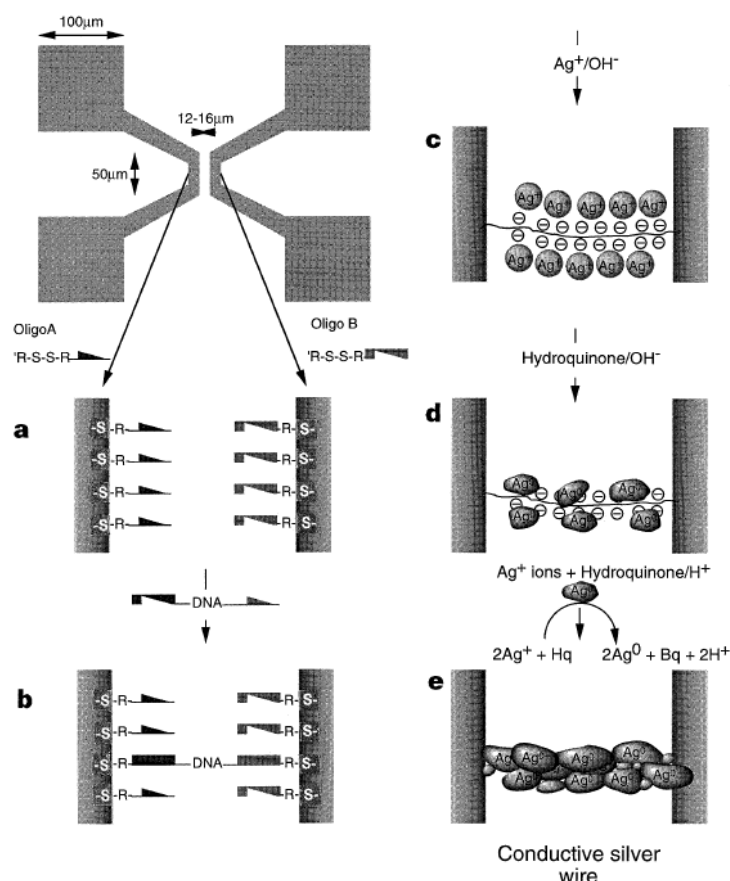


Figure 23. Construction of a silver wire connecting two gold electrodes:[5] **a**, Oligonucleotides with two different sequences attached to the electrodes. **b**, interconnecting of DNA bridge between the two electrodes. **c**, loading of Silver ions on DNA. **d**, Metallic silver aggregates bound to the DNA. **e**, Fully developed silver wire.

Another convenient means of fabricating two-terminal devices is the use of a ‘molecular combing’ procedure.[6-8] This method was mainly used in the work discussed in this thesis for the alignment of DNA-templated nanowires and for the fabrication of two-terminal I-V devices. The molecular combing was first developed by Bensimon et al.[8] It was used as an effective approach to align the nanowires on surfaces without any special equipment by moving DNA template nanowires solution upon the substrate surface. This method relies on using directed air stream to move a small droplet of the nanowires solution. The surface tension forces induced by the motion of solution droplet was utilised to elongate and align the nanowires on the solid surface in the direction of the flow. Figure 24 illustrates this method for parallel alignment of stretched DNA.[9]

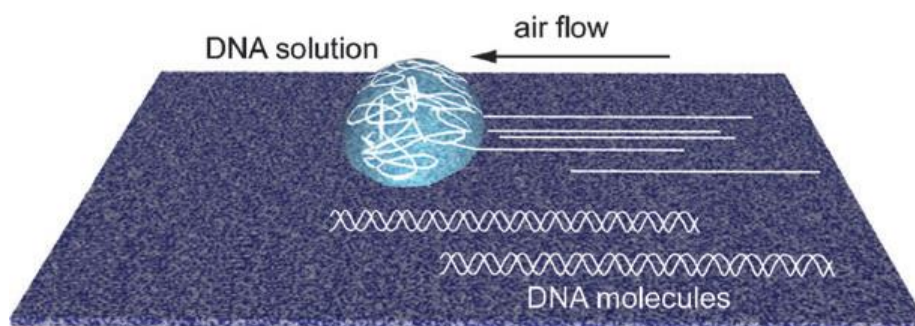


Figure 24. Schematic mechanism of the DNA combing method. Based on ref.[9]

Woolley *et al.*[10] and Becerril *et al.*[11] used the same approach to stretch DNA molecules by wicking off the solution droplet using an absorbent tissue. The surface tension force of the droplet which is induced while it was whicked off the substrate stretched and aligned the DNA in a single orientation on the surface. Nakao *et al.*[12] have used molecular combing for aligning DNA nanowires by sucking up a droplet of DNA solution by a pipette on a solid surface. The surface tension of air/water interface motion provided sufficient force to align the DNA molecules in the direction of the droplet centre, as shown in figure 25.

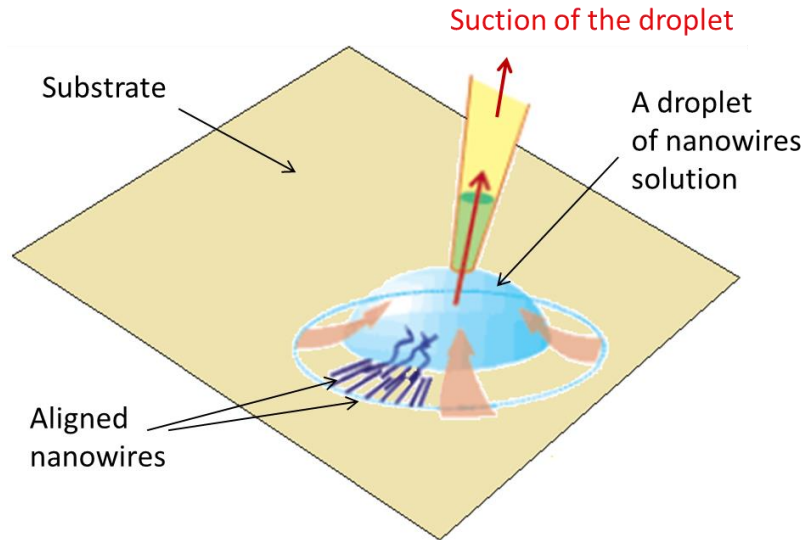


Figure 25. Schematic showing the pipette method for nanowires combing by droplet suction.

Houlton *et al.*[13] fabricated two-terminal nanowire device to measure the conductivity of DNA-templated PPy nanowires by stretching the nanowires across the gap between two gold electrodes using molecular combing. Watson *et al.*[14] used the same technique for constructing two terminal I-V device by aligning DNA/polyTPT nanowire between two Au electrodes, figure 26. The Au electrodes were typically embedded in an insulating SiO₂ layer on a silicon substrate separated by a gap of 2-8 μm.

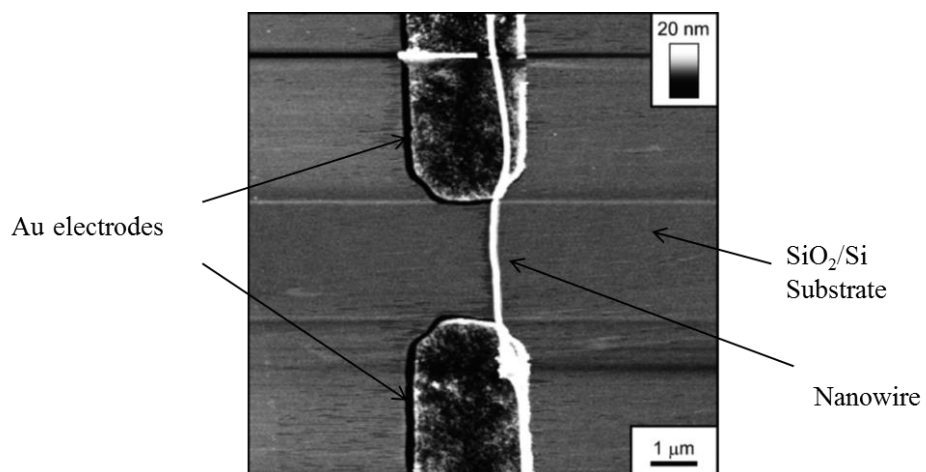


Figure 26. Tapping Mode AFM image of DNA/polyTPT nanowire aligned across a 2.5 μm gap between two Au microelectrodes. The Au electrodes are embedded in a 200 nm thick insulating SiO₂ layer on a Si substrate.[14]

2.2. Spectroscopic techniques used for the characterisation of nanowires

Different spectroscopic techniques were used for the chemical and structural characterisation of nanowires including Fourier Transformer Infrared (FTIR) spectroscopy, Ultraviolet-Visible (UV-Vis) absorption spectroscopy and X-ray photoelectron spectroscopy (XPS) as in the following:

2.2.1. *Fourier transformer Infrared (FTIR) spectroscopy*[15]

Fourier transform infrared (FTIR) spectroscopy is a useful vibrational method for the analysis of chemical reactions and final products characterization. It is a rapid and non-destructive test which requires a relatively small amount of sample. FTIR spectroscopy is extremely used for identifying types of chemical bonds and functional groups. It is sensitive to structural changes as absorption peaks correspond to the frequencies of vibrations of bonds. Chemical bonds vibrate at characteristic frequencies representative of their structure, and when exposed to infrared radiation, they absorb the radiation at specific wavelengths that match their vibration modes. The absorptions of the sample as a function of frequency can then be identified and assigned to individual chemical bond or groups. FTIR can be used for some quantitative analyses using the absorption strength which is proportional to the material concentration.

An IR spectrum is usually presented with wavenumber (cm^{-1}) as the x-axis and absorption intensity (A) or percent transmittance (T %) as the y-axis. Transmittance (T) is the ratio of radiant power transmitted by the sample (I) to the radiant power incident on the sample (I_0). Absorbance (A) is the \log_{10} of the reciprocal of the transmittance (T), (Lambert-Beer law):

$$T = I/I_0$$
$$A = \log_{10}(1/T) = -\log_{10}T = -\log_{10}I/I_0 = \epsilon cd$$

As T: transmittance, A: absorbance, ϵ : molar absorption coefficient, c: concentration and d: path length

Figure 27 shows a schematic diagram of the FTIR instrument and illustrating the normal instrument components.

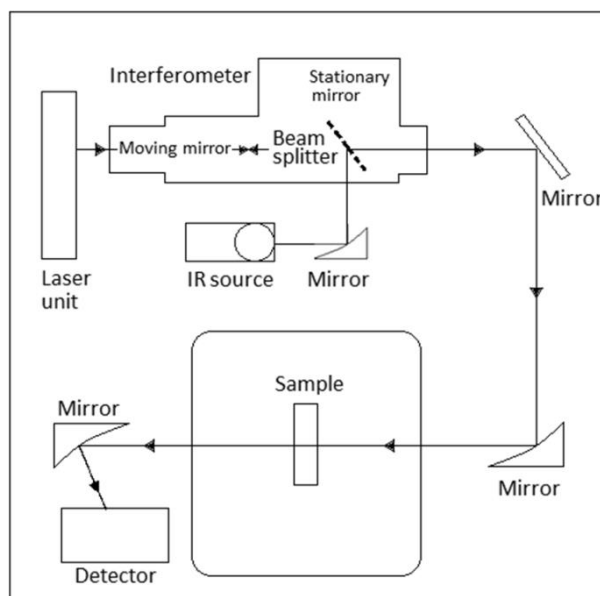


Figure 27. a schematic diagram of the FTIR instrument.

In this work, FTIR was used with other techniques to study synthesised *N*-alkylated pyrrole and pyrrole-pyridine derivatives and to assess their chemical polymerisation on the bulk scale. It was also used in the characterisation of CPs/DNA nanowires and their subsequent metallization process.

FTIR have been widely used to assess the synthesis and chemical structure of conductive nanowires using DNA as a template. As an example, FTIR spectra was demonstrated by Houlton *et al.* [13] in the preparation of ppy/DNA nanowires, where the FTIR spectra provided evidence of the formation of a supramolecular hybrid polymer containing DNA and polypyrrole. Figure 28 shows the FTIR spectra of ppy/DNA sample compared with polypyrrole and pure DNA samples. Significant feature indicating the interaction between conducting polypyrrole and DNA is the appearance of a broad absorption band above 2000 cm^{-1} , which is well known to be due to charge carriers. A similar broad absorption band was present in the FTIR spectrum of pure polypyrrole, but is not observed in DNA itself.

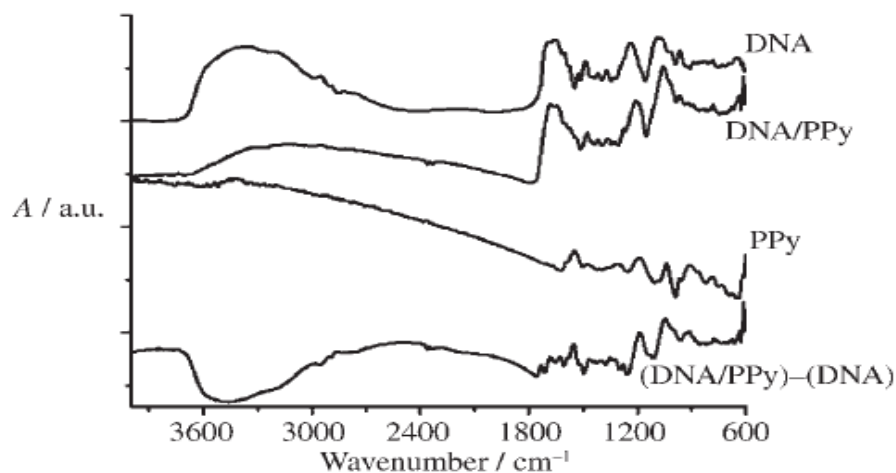


Figure 28. FTIR spectra of DNA, DNA/PPy, PPy and the difference spectrum (DNA/PPy)-(DNA).[13]

The process of metal/DNA nanowires formation has also been studied by FT-IR spectroscopy. For example, figure 29 shows the FT-IR spectra of Cu^{2+} /DNA prior to reduction with ascorbic acid prepared by Watson *et al.* [16] compared with DNA. The FTIR spectra provided support for that Cu^{2+} interacted with both the phosphate backbone and nucleobases in the DNA structure as indicated by shifts in the positions of the relevant bands.

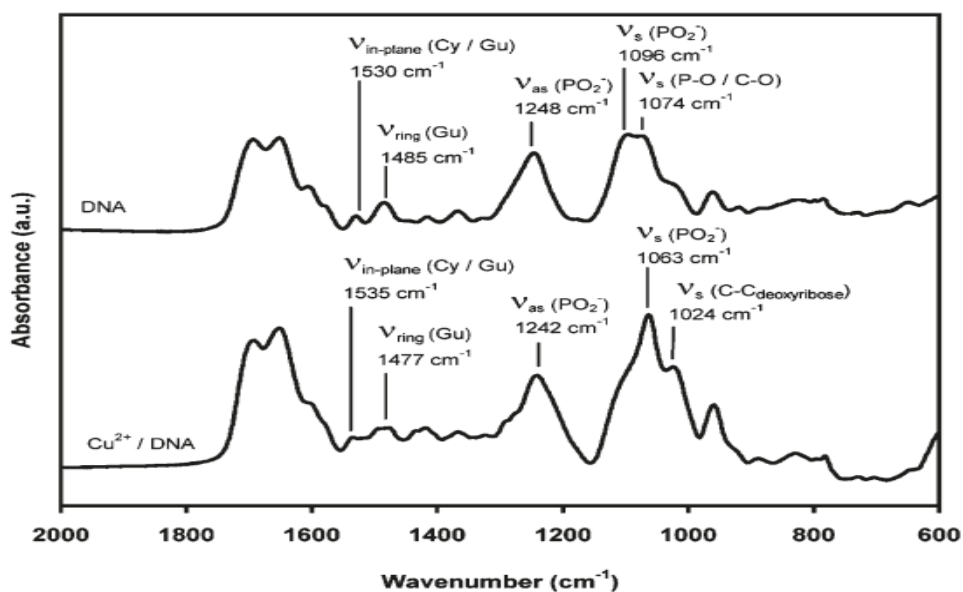


Figure 29. FTIR spectra of DNA vs the Cu^{2+} /DNA complex in the 600 - 2000 cm^{-1} region.[16]

The FTIR spectrometer which used in the work of this project was “Varian FTS 3000 FTIR”. FTIR Spectra range ($600\text{-}4000\text{ cm}^{-1}$) with 4 cm^{-1} spectral resolution.

2.2.2. Ultraviolet-Visible (UV-Vis) absorption spectroscopy[15]

When an atom or molecule absorbs energy, this excites the system from its ground states to higher excited state configurations. The absorption of UV-Vis radiation (UV = 200 - 400 nm, Vis. = 400 - 800 nm) leads to electronic transitions.

The UV-Vis spectrum typically shows a number of absorption bands corresponding to the transitions within the molecule. When an organic molecule absorbs UV-Vis radiation, different electron transitions may occur. Possible electron transitions involve the transition of π , σ , and n electrons from the ground state to higher energy state e.g. (σ^* or π^*). These higher energy states are described by molecular orbitals that are vacant in the ground state and are commonly called anti-bonding orbitals. The anti-bonding orbitals associated with σ bond is called the σ^* orbital and that associated with π bond is called the π^* orbital, (figure 30).

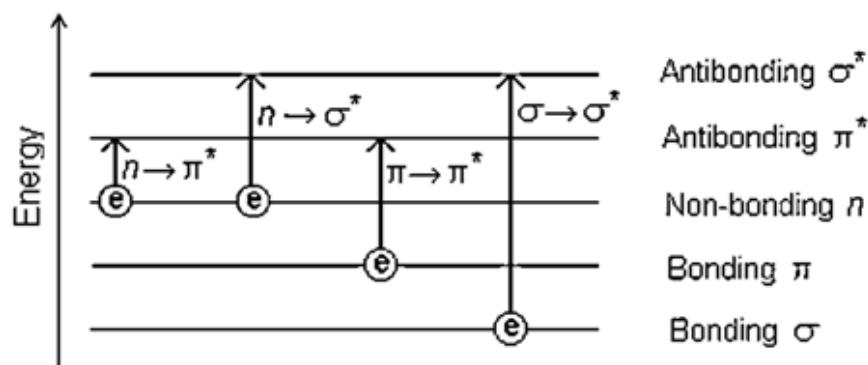


Figure 30. Possible electronic transitions of π , σ , and n electrons.

UV-Vis absorption spectroscopy is the measurement of the attenuation of a beam of light after it passes through the sample. For concentration determinations Beer-Lambert law is used. Beer's Law states that the absorbance (A) is directly proportional to the path length (l) and the concentration (c) of the absorbing species.

$$A = \epsilon lc$$

Where ϵ is the molar absorptivity constant for a particular substance at a specific wavelength.

In addition, UV-Vis spectroscopy (electronic spectroscopy) is an excellent tool for determining the band energy, which is an important parameter used in investigating the conduction mechanism in the organic conductors. In addition, it is a powerful probe for characterization of the electronic transitions between fundamental levels and polaronic or bipolaronic levels that occur in the polymer.[17-19]

The instrument used to measure these electronic transitions is generally double beam UV-visible absorption spectrometer consists of two beam paths, as shown in figure 31, one beam passes through the sample cell, and the other beam pass through the reference cell. The sample and reference cells are small rectangular glass or quartz containers. They are usually designed so that the light beam travels a distance of 1 cm through the contents.

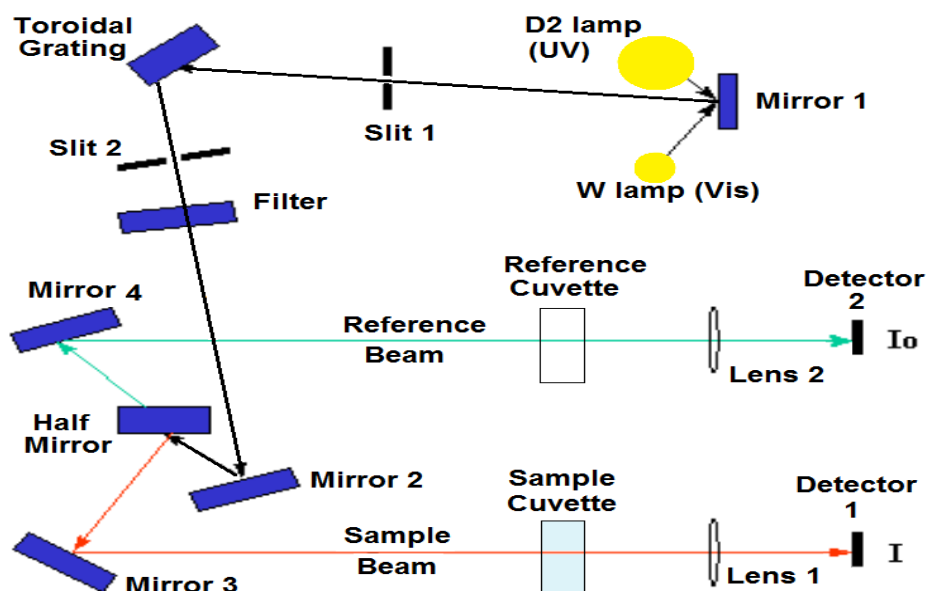


Figure 31. Schematic diagram of double beam UV-visible absorption spectrometer.

UV-Vis spectroscopy is widely used in the preparation and characterisation of conductive polymers. The electronic absorption bands due to polymer moiety are clearly observed in UV-Vis spectra. Absorption bands of ppy solutions apparent in the 400 – 500 nm ranges are attributed to transitions from the valence band to uppermost bipolaron band, and which dominated by the $\pi - \pi^*$ transitions.[19-21]

UV-Vis spectroscopy has also been used for the investigation of nanowires synthesis using DNA as a template. For example, Hassanien *et al.*[22] compared the UV-Vis spectrum of $\text{Cu}_2\text{O}/\text{Ct-DNA}$ nanowires solution with the spectra of a bare Ct-DNA solution and Benedict's solution, figure 32. The broad absorption in the range 600 – 900 nm in the spectrum of Benedict's solution, which is characteristic of aqueous Cu^{2+} , disappeared after the addition of ascorbic acid indicating the chemical reduction of Cu^{2+} .

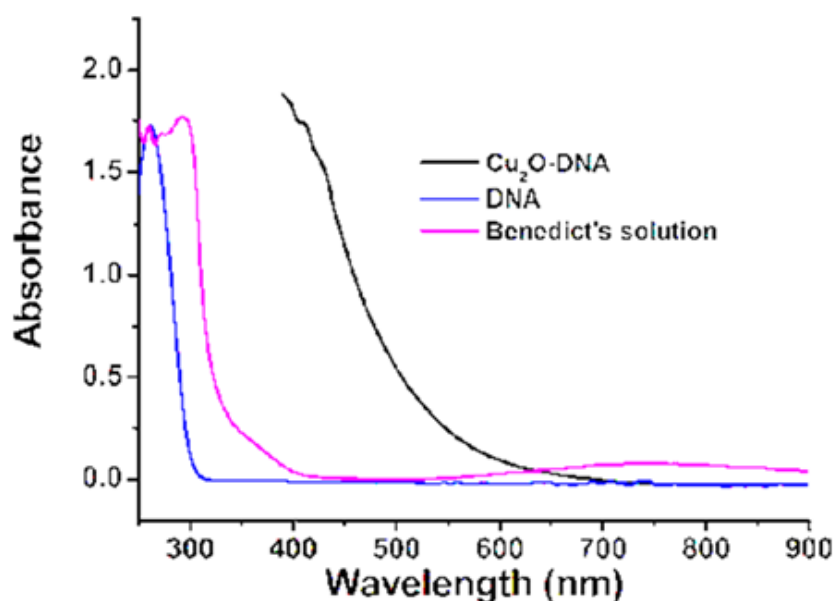


Figure 32. UV-Vis spectra of $\text{Cu}_2\text{O}/\text{Ct-DNA}$ nanowires (black), Ct-DNA solution (blue) and Benedict's solution (Purple), by Hassanien *et al.*[22]

In the work of this project, the UV-vis absorption spectra (wavelength range from 250 to 900 nm) were recorded on a VARIAN-CARY 100 Bio spectrophotometer at room temperature.

2.2.3. X-ray photoelectron spectroscopy (XPS)[23]

X-ray photoelectron spectroscopy (XPS) is a surface sensitive analytic technique used to study the composition and chemical state of the elements that are present within a material. It is also sometimes called by the alternative acronym, ESCA (Electron Spectroscopy for Chemical Analysis) due to its ability to clearly identify element types that are present. XPS involves irradiation under vacuum of the sample surface (usually to < 10 nm depth of the material being analysed) by a beam of X-rays with known energy. X-ray is produced by bombarding a metallic target (usually Al: 1486 eV, or Mg: 1254 eV) with high-energy electrons. When the incoming photons hit the sample it causes photo-ejection ionization of the electrons from the inner shell orbitals, figure 33. These core level electrons are attracted to the nucleus protons with certain binding energy (BE). When the electron is pulled away from the nucleus, the attraction between the electron and the nucleus decreases and the BE decreases. Finally, there will be a point when the electron will be free of the nucleus. This is the point with zero energy of attraction between the electron and the nucleus. At this point the electron is free from the atom and enters the ionization continuum.

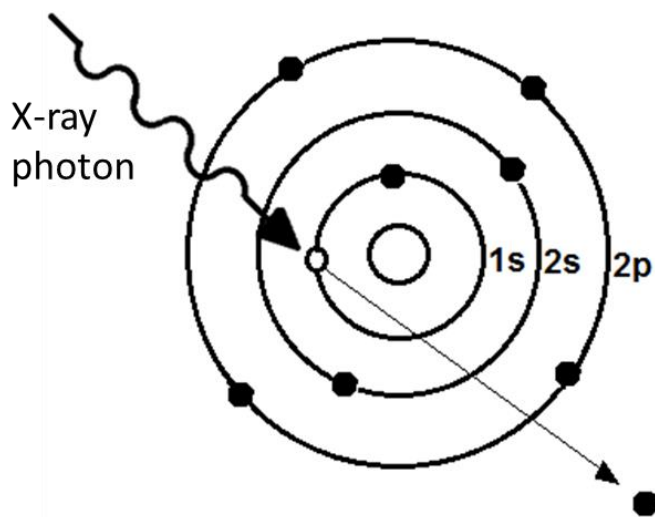


Figure 33. Schematic of principle of X-ray photoelectron spectroscopy.

When the incoming photons hit the sample, as shown in figure 34, they excite the electrons into higher energy levels – (photo) excitation, or eject them into the continuum leaving an ion and a free electron - (photo) ionisation.

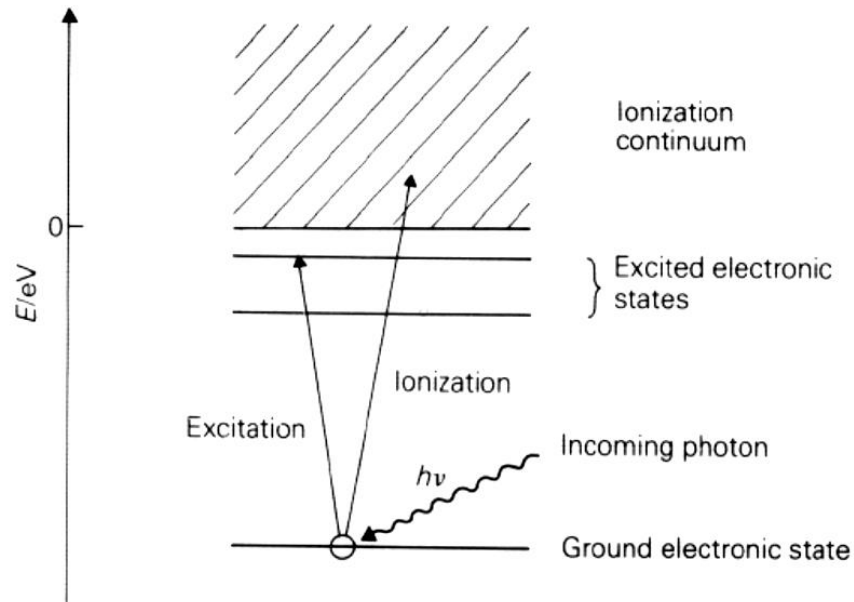


Figure 34. Schematic overview of the photo-excitation processes in atoms.[24]

The binding energy (BE) of the photoelectrons is determined from the energy of the X-ray radiation ($h\nu$), required to remove the electron from its initial level to the vacuum level, and the Kinetic energy (KE) of the photoelectron as given by:

$$KE = h\nu - BE - \phi$$

Where ϕ is known as the spectrometer work function (a characteristic of the instrument used).

The binding energy of core electrons in each element is very specific, so the atoms involved in the material can be identified from the characteristic binding energies of the photoelectron. This will give information on the elemental composition of the sample since the characteristic peaks correspond to the configuration of the electrons within the atoms. For example, figure 35 shows a survey XPS scan of fluorinated double-walled carbon nanotubes (F-DWNTs),[25] which shows all of the detectable elements present

in the sample. The peak's intensity is directly related to the atomic concentration in the sample. The peaks in XPS spectrum are labelled according to the shell from which the electron is removed.

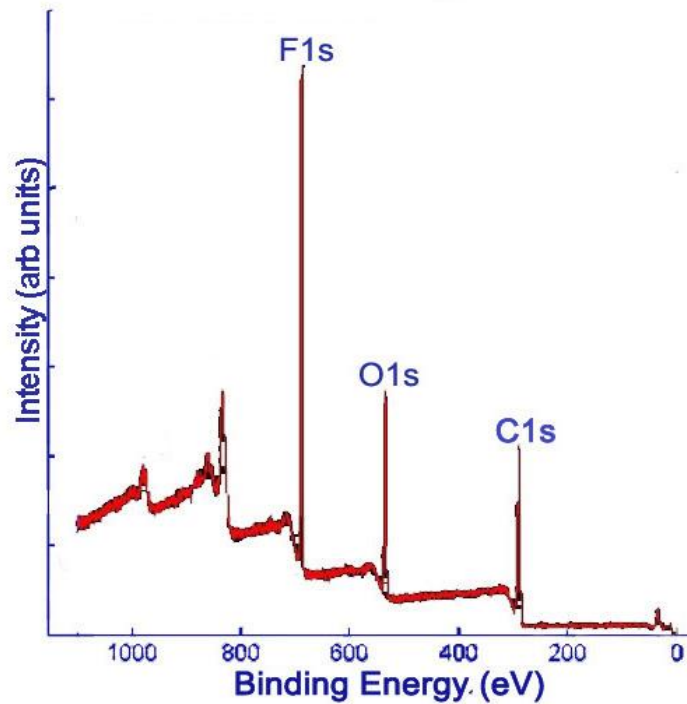


Figure 35. Survey XPS spectrum of F-DWNTs.[25]

One of the most important features of XPS is that the core level energy depends on the chemical state of the atom. When the element is in different chemical state, e.g. oxidation state, its corresponding energy level will be different, thus giving out photoelectrons at slightly different energies. The energy shift is the so-called “chemical shift”. The chemical shift in binding energy correlates with the overall charge on the atom and with the presence of any chemical bonding. This can be interpreted by XPS data to give information of a chemical nature of the sample such as the oxidation state of the atom, number and type of surrounding atoms, and the electronegativity of atoms. For example, as shown in figure 36 and in table 2, elemental Si (oxidation state = 0) has a Si 2p_{3/2} peak at the binding energy of ~99eV, while Si in SiO₂ has the corresponding peak at higher energy ~104eV. There is a difference of about 5 eV. As a result, the chemical shift of Si 2p allows us to identify the chemical states of Si.[26]

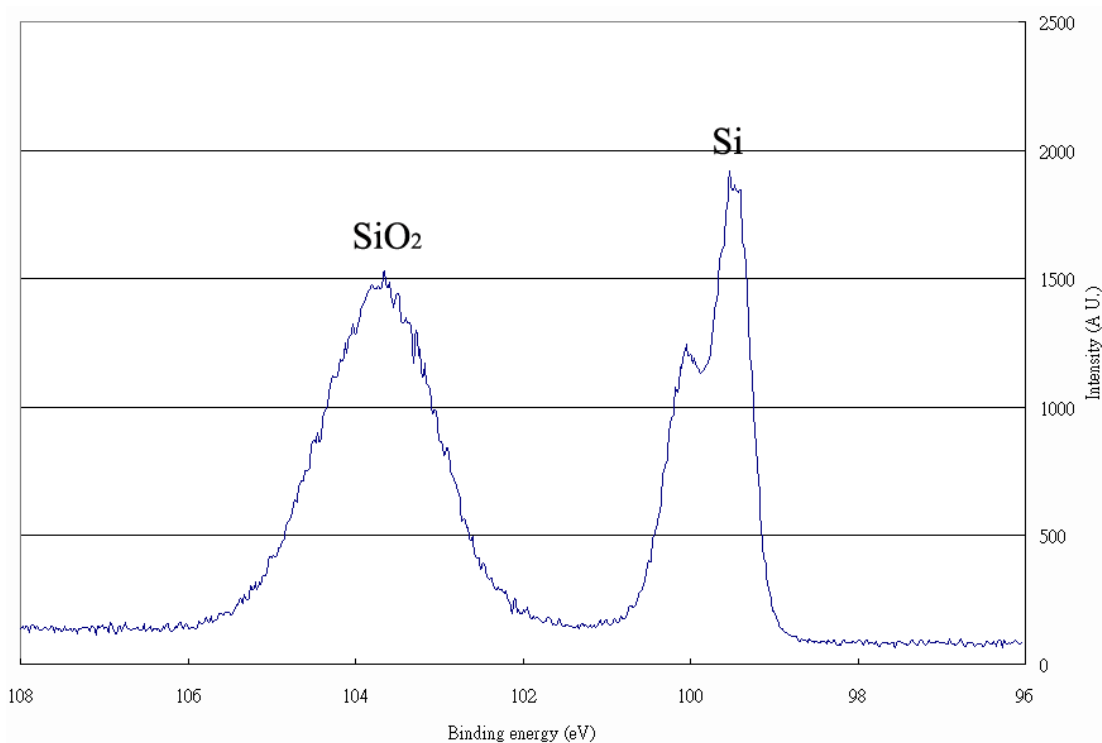


Figure 36. The XPS Si 2p spectrum of silicon dioxide overlayer on silicon substrate.[26]

	B.E. (eV)	Oxidation State
Si	99	Si ⁰
SiO ₂	104	Si ⁺⁴

Table 2. Chemical shifts in different oxidation states of Si.

X-Ray Photoelectron Spectroscopy is a surface sensitive technique. Electrons exhibit low ability to penetrate easily through the sample. Electrons with energy of 1 KeV will only penetrate 10 nm into sample surface. When X-ray photons enter below the sample surface, photoelectrons are produced. Some of the electrons travel out from the surface without losing any energy and some of them lose energy owing to inelastic collisions, as shown in figure 37.

The surface sensitivity can be explained in terms of the Inelastic Mean Free Path of electrons (IMFP), λ . [27] The IMFP is defined as the average distance that an electron with certain energy travels between successive inelastic collisions. The higher the kinetic energy of the electron the longer the inelastic mean free path.

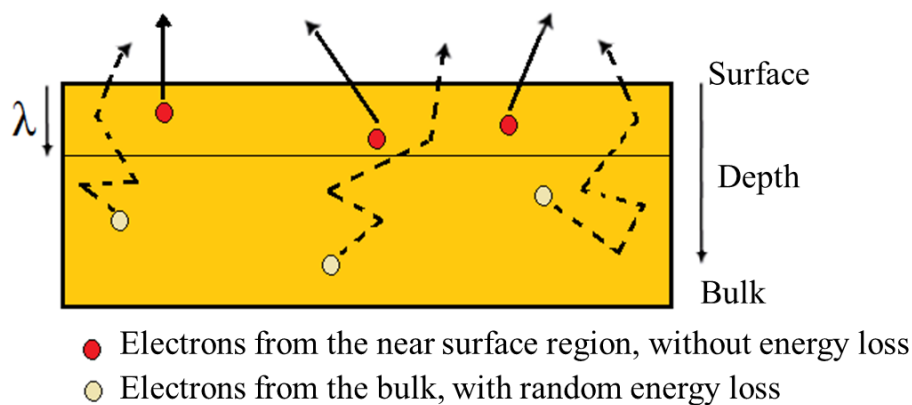


Figure 37. Schematic of electrons from the near surface region and from the bulk.

XPS instruments consist mainly of an X-ray source, an energy analyser for the photoelectrons, and an electron detector. The analysis and detection of photoelectrons requires that the sample be placed in an ultra-high vacuum (UHV) chamber. The X-ray source illuminates the specimen with monochromatic X-rays. Since the photoelectron energy depends on X-ray energy, the excitation source must be monochromatic. Photoelectrons ejected from the irradiated specimen are collected by a lens system which focuses them into an energy analyser. The energy of the photoelectrons is analysed by the electrostatic analyser, and recorded by an electron detector. A schematic diagram for a typical XPS instrument is shown in figure 38.

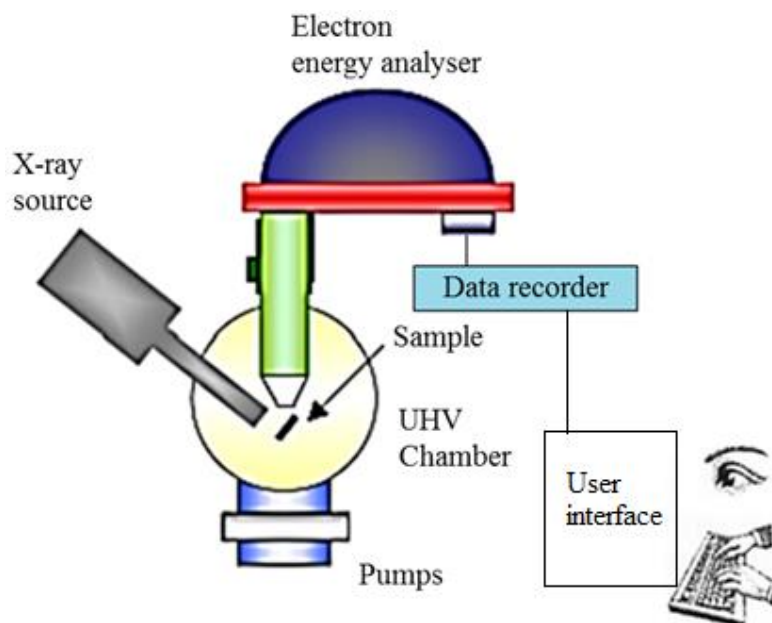


Figure 38. Schematic diagram of the essential components of an XPS instrument.

2.3. Scanning probe microscopic techniques used for the characterisation of nanowires

A large portion of experimental results presented in this research was concerned with the morphology and electrical characterization of nanowires. This was obtained using Scanning Probe Microscopy techniques (SPM) such as atomic force microscope (AFM), electrostatic force microscopy (EFM) and conductive atomic force microscopy (c-AFM). This section provides an introduction to the principles of these techniques.

2.3.1. The atomic force microscopy (AFM)[28]

The AFM is one of the Scanning Probe Microscopic techniques which was invented by Binnig, Gerber and Quate in 1986.[29] It is an indispensable tool for monitoring surface topography on the nanoscale because its high resolution which is applicable to conducting and non-conducting samples.[30] AFM is an ideal tool for assessing the topography of nanoscale structures and can now also their electrical, mechanical and magnetic properties.[31, 32] The topography of nanostructures can be imaged using tapping mode AFM. The basic principle of the operation of tapping mode AFM is to measure the forces at the atomic level between the sharp probing tip and the sample surface. [30, 33] This is measured by multiplying the changes in tip height (Z) with the spring-constant (k) of the cantilever (Hooke's law):

$$F = kz$$

The electrical measurements can be performed by contact mode AFM (Conductive AFM) using conductive tips which directly contact with the sample. The contact AFM topographical image is generated using the feedback signal. When the tip is brought close to the sample surface, an attractive force exists between the tip and the surface. Since the tip is attached to a flexible cantilever spring, so it is attracted to making a contact with the surface. As the piezo retracts, the tip snaps free of the attractive force and repelled from the sample surface. The repulsive force (F) is calculated via Hooke's

law ($F = kz$). This repulsive force is usually used as a feedback parameter to obtain the sample morphology and to generate a map of surface topography.

Tips have to be as sharp as possible, commonly available tips have a radius ranging from 10 to 100 nm.[30] Figure 39 illustrates the principle of operation of AFM.

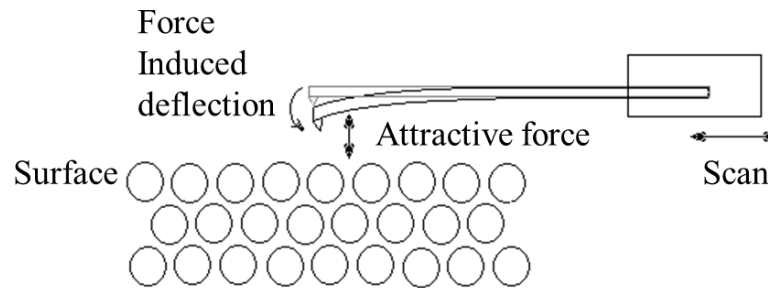


Figure 39. Schematic showing principle of atomic force microscopy.

The cantilever oscillates freely at its resonant frequency when it is away from the surface. The resonant frequency (ν) is given by the equation:

$$\nu = \frac{1}{2\pi} \sqrt{\frac{k}{m}}$$

Where k is the cantilever force constant and m its mass.[34] A high resonance frequency can be obtained by reducing the cantilever mass.

The piezo crystal attached to the cantilever is used to excite the tip vertically causing the cantilever itself to oscillate. The tip is mounted at the free end of the cantilever upon which a laser beam is focused. The sample is mounted under a piezoelectric scanner allowing extremely precise movement in the x , y , and z directions. As the cantilever oscillates, the photodiode detector detects the laser beam reflected from the back of the cantilever causing an electrical signal. This detects the deflection of the laser beam arising from the cantilever moving as the sample is mapped. In principle, the deflection of the cantilever is associated with the force exerted on the tip. The reflected laser beam reveals topographical information about the sample surface under scanning.

The height of the sample is measured by continuously scanning the sample and recording the deflection of the cantilever. The z -feedback loop controls the z -sample

position, and the nanoscope controller and computer are used to control the system and display and analyse the data.

Images are taken by scanning the sample relative to the probing tip and measuring the deflection of the cantilever as a function of lateral position. A schematic diagram[35] of an atomic force microscope is shown in figure 40.

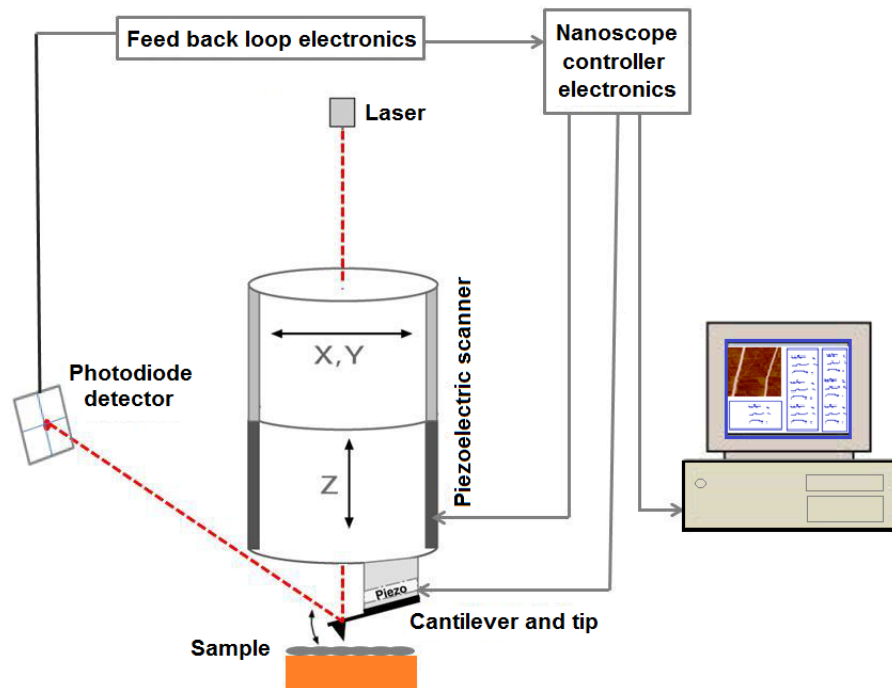


Figure 40. Schematic diagram of the main components of the AFM, adopted from [35].

2.3.2. *Electrostatic force microscopy (EFM)*[31]

The EFM technique, has also been called scanned conductance microscopy (SCM).[36] It is useful in the qualitative assessment of the polarizability and conductivity of nanostructure materials as well as determining their surface charges distribution. It provides a useful method to investigate the conduction pathways in nanostructures immobilized on a dielectric substrate. For example, it has been used to detect charges in semiconductor[4, 37] and silicon nanocrystals[38] on SiO₂ dielectric films. The EFM technique has been also used to probe the conductivity of DNA, carbon nanotubes[39, 40] and poly(ethylene oxide) nanofibers.[41] In addition, it was used to assess the

electrical conductivity of DNA-templated metal nanowires.[4] In this method a direct current (dc) bias is applied between a conductive AFM probe and the sample. This can be considered as two plates in a small capacitor. The force gradient above the sample is mapped with the application of a DC potential bias between the sample and the tip and observing the phase angle between the driving force applied to the cantilever and the tip response.

Data collection involves the use of a ‘two-pass’ technique. The first scan across a line over the sample records the topography of the sample in tapping mode AFM. The second pass obtains information relating to the changes in the phase shift ($\Delta\Phi$), figure 41. The AFM probe oscillates over the sample and detects any changes in the electrostatic field gradient. The measured phase difference can be interpreted to confirm electrical conductivity.

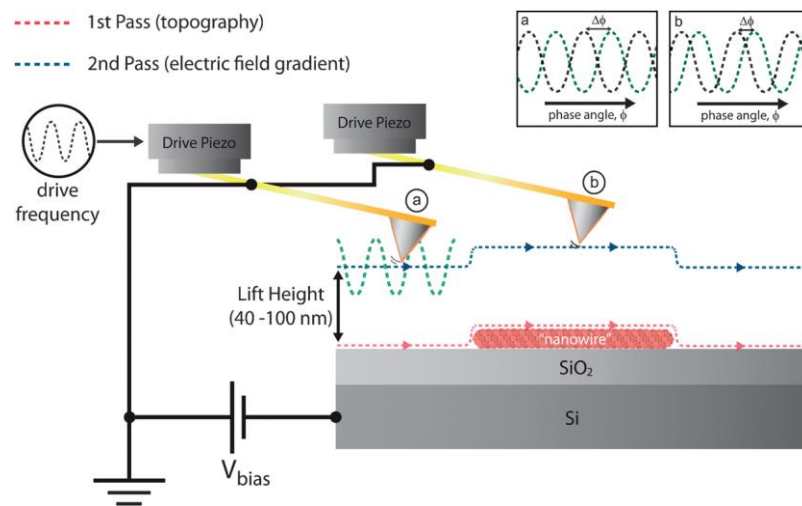


Figure 41. Principles of scanned conductance microscopy operation and its use to detect conductive objects (e.g. nanowires) on a dielectric film (e.g. SiO₂). (quoted with permission from reference [4])

Briefly, the phase shift is proportional to the second derivative of the tip/surface capacitance with respect to the lift height. The capacitance is the series combination of the tip/nanowire and nanowire/surface capacitors. The phase shift can be estimated by the following equation: [16, 22, 42]

$$\tan(\Delta\phi) \approx \Delta\phi = \frac{Q}{2K} V_{\text{tip}}^2 \left[\frac{2\pi R_{\text{tip}}^2 \epsilon_0}{(h+t/\epsilon_{\text{ox}})^3} - \frac{2\pi R_{\text{tip}}^2 \epsilon_0}{(h+t/\epsilon_{\text{ox}} + d/\epsilon)^3} \right] \quad \text{Eq. 1}$$

Where Q is the quality factor, k = cantilever spring constant, V is the applied voltage, t = oxide thickness, and d = nanowire diameter, ϵ_0 and ϵ are the relative permittivity of the oxide and the nanowire. The first term in (Eq. 1) derives from the tip-substrate capacitance ($C_{\text{substrate}}$) and the second term derives from the tip-nanowire (C_{NW}) capacitance. Therefore $C_{\text{substrate}}$ and C_{NW} are calculated as:[41]

$$C_{\text{substrate}} = \frac{2\pi R_{\text{tip}}^2 \epsilon_0}{(h+t/\epsilon_{\text{ox}})^3} \quad \text{Eq. 2}$$

$$C_{\text{NW}} = \frac{2\pi R_{\text{tip}}^2 \epsilon_0}{(h+t/\epsilon_{\text{ox}} + d/\epsilon)^3} \quad \text{Eq. 3}$$

When the nanowire is conductive, the charge stored on the nanowire/Si capacitor can be spread along the whole length of the nanowire. The relevant length related to the nanowire length not the tip radius. This increases the effect of the nanowire capacitance (C_{NW}) (eq. 3), so the second term in Eq. 1 becomes significantly larger ($C_{\text{NW}} > C_{\text{substrate}}$) which can result in a negative phase shift ($-\Delta\Phi$). Therefore, a negative phase shift in EFM measurement is an indication that the nanowire is conductive. Some references provide more details about EFM principles and the theoretical concepts of phase shift.[40, 41, 43]

Equation (1) also exhibits a parabolic dependence of the tangent of the phase shift on the applied dc voltage. This contrasts with the linear dependence of the phase shift on potential that arises from the electrostatic force caused by trapped charges. It also possible that the hydrophobic nanostructure enclose a thin layer of surface-adsorbed water molecules which can trap charges.[43]

It was shown in previous works,[40, 41, 44] negative phase shifts, with respect to the background, are only observed when imaging one-dimensional structures that are conductive. For example, figure 42 shows AFM image (a) and EFM image (b) of polyindole/DNA nanowires prepared by hassanien *et. al.*[44]. The nanowires appear as dark lines in the EFM image. This is attributed to the negative phase shift which demonstrates the existence of charge conduction in the nanowire. Figure 42 (c) shows the parabolic dependence of phase shift potential over the range from -10 to +10 V, and no presence of any linear dependence which confirms that trapped charge makes no significant contribution to this data.

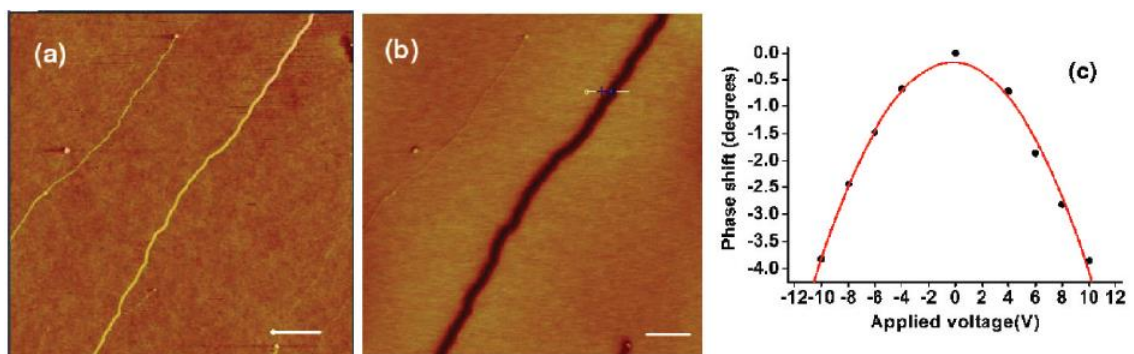


Figure 42. (a) AFM image of PIn/DNA nanowire with a diameter of 5 nm, EFM phase image of the same nanowire at a tip/sample bias of -6 V, and (c) Phase shift as a function of applied voltage of PIn/DNA nanowire with a diameter of 28 nm on a SiO₂/Si surface.[44]

2.3.3. Conductive atomic force microscopy (C-AFM)[28]

Conductive atomic force microscopy (C-AFM) is a contact-mode AFM method that characterizes the surface topography of the individual nanowire as well as the conductivity variations across the sample surface in order to measure the conductance and allow an estimate of the conductivity of the nanowires.[45]

In c-AFM experiments a constant bias is applied between a metal coated tip and the sample. The conductive probe tip is usually attached to a very soft cantilever with a spring constant of (0.1- 1.0 N/m). The applied bias between the tip and the sample is used to generate a current map and therefore to measure the conductance and estimate the conductivity of the nanowires. The set-point for minimum contact force can be

adjusted to increase or decrease the cantilever deflection and the contact force of the tip on the sample. It is important to reduce the set point, in order to lower the force of the mechanical contact between the tip and the sample surface, to prevent the delicate nanostructures from deforming, as the force on the sample can result in cutting thin nanowires. Therefore, conducting measurements on thick nanowires (or a bundle of nanowires) is often preferred when using this technique.

In C-AFM experiments, a 3 μL of solution of the prepared nanowires is drop-cast onto a hydrophilic Si/SiO₂ substrate. This drop of nanowire solution is allowed to dry. The receding surface of the liquid can cause a few nanowires to be stretched out from the dense network of nanowires along the substrate. Single nanowires can then be selected at the edge of the dense mass for analysis as shown in figure 43.

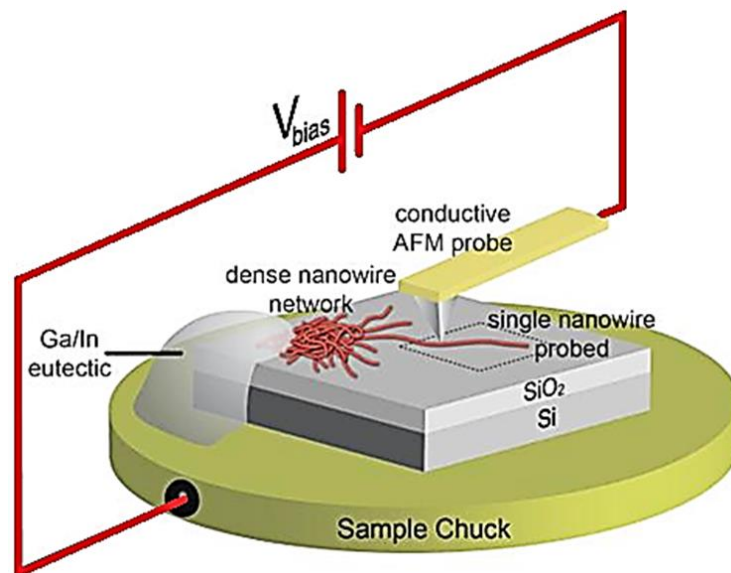


Figure 43. Schematic diagram of C-AFM technique for electrical characterisation. Measurements are recorded upon individual nanowires located at the periphery of a dense network of the nanowires deposited upon the substrate support.[14]

The dense mass of nanowires serve as one contact to the wire, with the dense mass itself connected to the metallic chuck on the microscope using In/Ga eutectic. The other electrical contact to the external circuit is the conductive AFM tip. The imaged area is at least 1 mm away from the In/Ga contact to avoid shortage.

The data is interpreted in terms of a simple series circuit comprising three resistances; R_{tip} , R_{ext} and R_{wire} . Where R_{tip} is the tip/nanowire contact resistance, R_{ext} is the resistance between the nanowire and the external circuit and R_{wire} is the resistance of the portion of the nanowire between the tip and the main drop deposit. The measured circuit resistance is clearly the sum of these, and it is assumed that all the distance dependence lies in R_{wire} .

The dependence of conductivity on distance (d) along the nanowire can also be measured by C-AFM.[44] In order to measure the changes of resistance with distance (length), the I-V curves should be recorded at different points along the nanowire, figure 44 (a). The circuit resistance increases in a linear manner with d because R_{wire} is the largest resistance in the circuit and by increasing the distance the current must flow through a longer portion of the nanowire. Figure 44(b) shows a plot of the resistance as a function of the relative distance, d , of the tip along DNA-PIm-Pd nanowire with different contact forces by increasing the set point voltage from 0 to 2V.[46] It clearly shows that resistance increases with increasing distance of the contact position. The inset shows the current map of DNA-PIm-Pd nanowire with different positions which are indicated by red crosses.

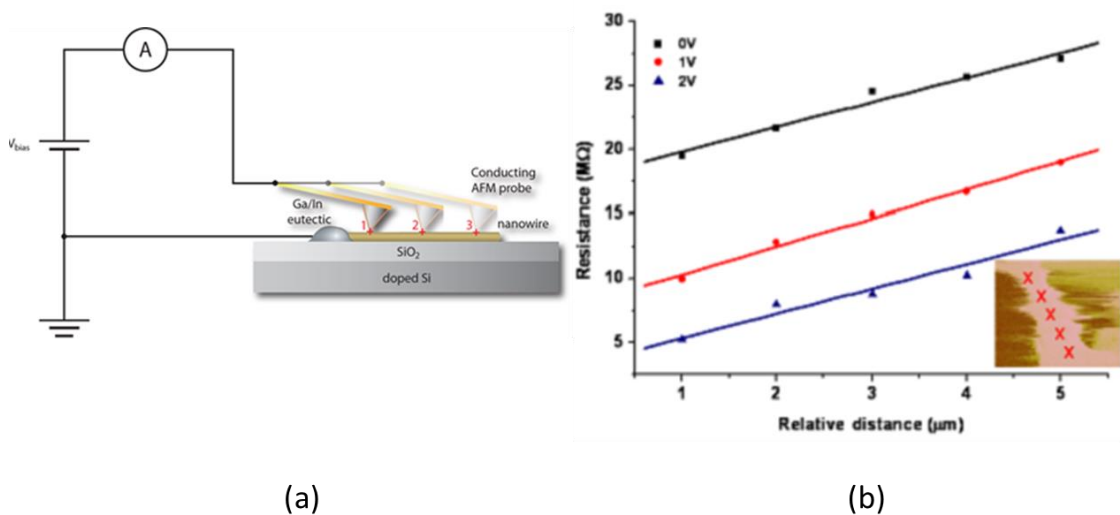


Figure 44. (a) schematic diagram shows the measurement of changes in resistance with distance (length) Using C-AFM, the I-V curves should be recorded at different points along the nanowire. (b) DNA-PIm-Pd nanowires resistance as a function of tip-contact relative distance for different applied forces in c-AFM I-V measurements. The inset shows the current map of the nanowires, and several I-V measurement positions are indicated by red crosses.[46]

2.3.4. *The two terminal I-V measurements*[47]

Two probe I-V characterization is a typical method for the measurement of the electronic transport properties of semiconductors. The I-V studies over a range of temperatures are performed in order to provide useful qualitative and quantitative information regarding I-V behaviour and to elucidate details of conduction mechanism. This method relies on the alignment of the nanowires by molecular combing across two microfabricated Au electrodes on a thermally oxidized Si chip.

Figure 45 shows photographs of the probe station used in the electrical measurements of materials prepared in this thesis (a), the Au electrodes inside the probe station which inserted inside the chamber (b) and AFM image of PPy-DNA nanowire aligned across Au electrodes prepared for I-V measurements (c).[48]

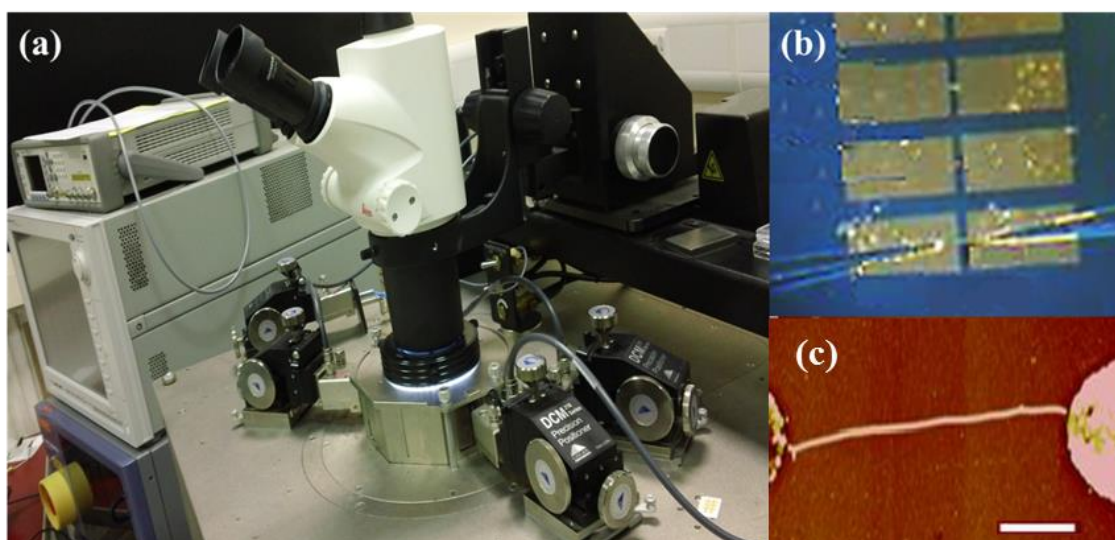


Figure 45. a) Probe station used in the electrical measurements. b) Au electrodes inside the probe station. c) AFM image of PPy-DNA nanowire aligned across Au electrodes and inserted inside the chamber, scale bar 1 μm . The image (c) was taken from ref.[48]

The conductivity σ (S cm^{-1}) of a nanowire at room temperature can be calculated from the resistance R of a material with given cross sectional area A and length l using the relationship:[49]

$$\sigma = l/RA$$

The length, diameter and cross-sectional area are estimated from AFM images of the nanowire. The resistance is calculated from the ohmic part at the origin of the I-V curve and the conductance in Siemens (S) is the reciprocal value of the resistance.

The nature of the measured material (metal, semiconductor etc.) could be identified depending on the changes of its conductivity with temperature.[50, 51] For example, the conductivity of semiconductors increases with increasing the temperature, because more valence electrons are excited into the conduction band, but in the case of metals the electrical conductivity decreases with increasing temperature because of electron-phonon scattering. Most conducting polymers show an increase in conductivity with temperature typical of hopping conductors;[50, 52] however, the precise nature of the temperature dependence might be affected by many factors such as the polymer structure, degree of crystallinity, and dimensionality.[53]

The conjugated polymers conductivity is usually described by hopping models;[54-56] the electrical transport occurs by charge carriers hopping between sites. Electrons can hop from one localized site to another when receiving energy. Generally, several hops may be possible from a given site, which differ with respect to the energy barrier or hopping distance. The relation between conductance G and temperature T is given by Variable Range Hopping (VRH), where the thermal average over the different hops leads to a temperature-dependent hopping range.[52, 55, 57] The temperature dependence of the conductivity can be described by an exponential law, which is typical of VRH conductivity.

$$G = G_0 \exp \left[- \left(\frac{T_0}{T} \right)^\beta \right]$$

Where the exponent β is related to the electronic dimensionality of the sample, $\beta = 1/(d + 1)$, where d is the dimensionality of the system. Thus, it is may expected that $\beta = 1/4$, $1/3$, and $1/2$ for 3D, 2D, and 1D respectively.[49, 57] Experimental data on conjugated polymers shows the behaviour consistent with $\beta = 1$ in 1-dimensional objects such as nanowires,[54] $\beta = 1/4$ for bulk samples,[58] and for thin films,[59] $\beta = 1/2$ at low temperatures and $\beta = 1$ at higher temperatures. G_0 and T_0 are related to the electronic density of the states at the Fermi level.

2.4. References

1. Q. Gu, C. D. Cheng, R. Gonela, S. Suryanarayanan, S. Anabathula, K. Dai and D. T. Haynie, DNA nanowire fabrication. *Nanotechnology*, 2006, **17**, R14-R25.
2. H. J. Kim, Y. Roh and B. Hong, Selective Formation of a Latticed Nanostructure with the Precise Alignment of DNA-Templated Gold Nanowires. *Langmuir*, 2010, **26**, 18315-18319.
3. Z. X. Deng and C. D. Mao, DNA-templated fabrication of 1D parallel and 2D crossed metallic nanowire arrays. *Nano Letters*, 2003, **3**, 1545-1548.
4. Andrew Houlton and S. M. D. Watson, DNA-based nanowires. Towards bottom-up nanoscale electronics. *Annu. Rep. Prog. Chem*, 2011, **107**, 21-42.
5. E. Braun, Y. Eichen, U. Sivan and G. Ben-Yoseph, DNA-templated assembly and electrode attachment of a conducting silver wire. *Nature*, 1998, **391**, 775-778.
6. J. W. Li, C. L. Bai, C. Wang, C. F. Zhu, Z. Lin, Q. Li and E. H. Cao, A convenient method of aligning large DNA molecules on bare mica surfaces for atomic force microscopy. *Nucleic Acids Research*, 1998, **26**, 4785-4786.
7. A. Bensimon, A. Simon, A. Chiffaudel, V. Croquette, F. Heslot and D. Bensimon, Alignment and sensitive detection of DNA by a moving interface. *Science*, 1994, **265**, 2096-2098.
8. D. Bensimon, A. J. Simon, V. Croquette and A. Bensimon, Stretching DNA with a receding meniscus - experiments and models. *Physical Review Letters*, 1995, **74**, 4754-4757.
9. X. Liu, H. Diao and N. Nishi, Applied chemistry of natural DNA. *Chemical Society Reviews*, 2008, **37**, 2745-2757.
10. A. T. Woolley and R. T. Kelly, Deposition and characterization of extended single-stranded DNA molecules on surfaces. *Nano Letters*, 2001, **1**, 345-348.
11. H. A. Becerril and A. T. Woolley, DNA-templated nanofabrication. *Chemical Society Reviews*, 2009, **38**, 329-337.
12. H. Nakao, H. Hayashi, T. Yoshino, S. Sugiyama, K. Otobe and T. Ohtani, Development of novel polymer-coated substrates for straightening and fixing DNA. *Nano Letters*, 2002, **2**, 475-479.

13. L. Dong, T. Hollis, S. Fishwick, B. A. Connolly, N. G. Wright, B. R. Horrocks and A. Houlton, Synthesis, manipulation and conductivity of supramolecular polymer nanowires. *Chemistry-a European Journal*, 2007, **13**, 822-828.
14. S. M. D. Watson, J. H. Hedley, M. A. Galindo, S. A. F. Al-Said, N. G. Wright, B. A. Connolly, B. R. Horrocks and A. Houlton, Synthesis, Characterisation and Electrical Properties of Supramolecular DNA-Templated Polymer Nanowires of 2,5-(Bis-2-thienyl)-pyrrole. *Chemistry (Weinheim an der Bergstrasse, Germany)*, 2012, **18**, 12008-12019.
15. D. H. Williams and I. Fleming, *Spectroscopic methods in organic chemistry*, McGraw-Hill Book Company, Maidenhead, England, 1980.
16. S. M. D. Watson, N. G. Wright, B. R. Horrocks and A. Houlton, Preparation, Characterization and Scanned Conductance Microscopy Studies of DNA-Templated One-Dimensional Copper Nanostructures. *Langmuir*, 2010, **26**, 2068-2075.
17. T. F. Otero and M. Bengoechea, UV-visible spectroelectrochemistry of conducting polymers. Energy linked to conformational changes. *Langmuir*, 1999, **15**, 1323-1327.
18. A. O. Patil, A. J. Heeger and F. Wudl, Optical Properties of Conducting Polymers *Chemical Reviews*, 1988, **88**, 183-200.
19. J. L. Bredas, J. C. Scott, K. Yakushi and G. B. Street, Polarons and Bipolarons in polypyrrole - Evolution of The Band-Structure and Optical-Spectrum Upon Doping. *Physical Review B*, 1984, **30**, 1023-1025.
20. K. M. Cheung, D. Bloor and G. C. Stevens, The Influence of Unusual Conterions on the Electrochemistry and Physical- Properties of Polypyrrole. *Journal of Materials Science*, 1990, **25**, 3814-3837.
21. G. B. Street, T. C. Clarke, M. Krounbi, K. Kanazawa, V. Lee, P. Pfluger, J. C. Scott and G. Weiser, Preparation and Characterisation of Neutral and Oxidized polypyrrole Films. *Molecular Crystals and Liquid Crystals*, 1982, **83**, 1285-1296.
22. R. Hassanien, S. A. F. Al-Said, L. Siller, R. Little, N. G. Wright, A. Houlton and B. R. Horrocks, Smooth and conductive DNA-templated Cu₂O nanowires: growth morphology, spectroscopic and electrical characterization. *Nanotechnology*, 2012, **23**.

23. C. D. Wagner, W. M. Riggs, L. E. Davis, J. F. Moulder and G. E. Mulenberg, *Handbook of X-Ray photoelectron spectroscopy*, Physical Electronic Inc, Eden Prairie, 1979.
24. E. A. Ebsworth, D. W. Rankin and S. Cradock, *Structural Methodes in Inorganic Chemistry*, Second edition edn., Blackwell Scientific Publications, Osney Mead, Oxford, 1991.
25. E. P. Dillon, C. A. Crouse and A. R. Barron, Synthesis, characterization, and carbon dioxide adsorption of covalently attached polyethyleneimine-functionalized single-wall carbon nanotubes. *Acs Nano*, 2008, **2**, 156-164.
26. J. C. Vickerman, *Surface analysis - the principal techniques*, , John Wiley & Sons 1997.
27. C. J. Powell, A. Jablonski, S. Tanuma and D. R. Penn, Effects of elastic and inelastic electron-scattering on quantitative surface-analyses by aes and xps. *Journal of Electron Spectroscopy and Related Phenomena*, 1994, **68**, 605-616.
28. Nan Yao and Z. L. Wang, *Handbook of Microscopy for Nanotechnology*, Springer Science, New York, USA, 2005.
29. G. Binnig, C. F. Quate and C. Gerber, Atomic Force Microscope *Physical Review Letters*, 1986, **56**, 930-933.
30. B. Bhushan, Nanoscale tribophysics and tribomechanics. *Wear*, 1999, **225**, 465-492.
31. D. Sarid, *Scanning Force Microscopy : With Applications to Electric, Magnetic, and Atomic Forces*, Oxford U.P., New York, 1991.
32. D. Rugar and P. Hansma, Atomic force microscopy. *Physics Today*, 1990, **43**, 23-30.
33. G. Binnig, C. Gerber, E. Stoll, T. R. Albrecht and C. F. Quate, Atomic Resolution with Atomic Force microscpe *Europhysics Letters*, 1987, **3**, 1281-1286.
34. G. Attard and C. Barnes, *Surfaces*, Oxford Science publications, 1998.
35. L. Chen., "Atomic force microscope (Veeco-3100) user instruction". available at <http://cnst.nist.gov/nanofab/pdf/AFM-DI-3100.pdf> Accessed 10/02/2012
36. N. Tessler, Y. Preezant, N. Rappaport and Y. Roichman, Charge Transport in Disordered Organic Materials and Its Relevance to Thin-Film Devices: A Tutorial Review. *Advanced Materials*, 2009, **21**, 2741-2761.

37. T. D. Krauss, S. O'Brien and L. E. Brus, Charge and photoionization properties of single semiconductor nanocrystals. *Journal of Physical Chemistry B*, 2001, **105**, 1725-1733.
38. C. Y. Ng, T. P. Chen, H. W. Lau, Y. Liu, M. S. Tse, O. K. Tan and V. S. W. Lim, Visualizing charge transport in silicon nanocrystals embedded in SiO₂ films with electrostatic force microscopy. *Applied Physics Letters*, 2004, **85**, 2941-2943.
39. A. Gil, P. J. de Pablo, J. Colchero, J. Gomez-Herrero and A. M. Baro, Electrostatic scanning force microscopy images of long molecules: single-walled carbon nanotubes and DNA. *Nanotechnology*, 2002, **13**, 309-313.
40. M. Bockrath, N. Markovic, A. Shepard, M. Tinkham, L. Gurevich, L. P. Kouwenhoven, M. S. W. Wu and L. L. Sohn, Scanned conductance microscopy of carbon nanotubes and lambda-DNA. *Nano Letters*, 2002, **2**, 187-190.
41. C. Staii, A. T. Johnson and N. J. Pinto, Quantitative analysis of scanning conductance microscopy. *Nano Letters*, 2004, **4**, 859-862.
42. S. Pruneanu, S. A. F. Al-Said, L. Dong, T. A. Hollis, M. A. Galindo, N. G. Wright, A. Houlton and B. R. Horrocks, Self-assembly of DNA-templated polypyrrole nanowires: Spontaneous formation of conductive nanoropes. *Advanced Functional Materials*, 2008, **18**, 2444-2454.
43. T. S. Jespersen and J. Nygard, Charge trapping in carbon nanotube loops demonstrated by electrostatic force microscopy. *Nano Letters*, 2005, **5**, 1838-1841.
44. R. Hassanien, M. Al-Hinai, S. A. F. Al-Said, R. Little, L. Siller, N. G. Wright, A. Houlton and B. R. Horrocks, Preparation and Characterization of Conductive and Photoluminescent DNA-Templated Polyindole Nanowires. *Acs Nano*, 2010, **4**, 2149-2159.
45. J. Alvarez, I. Ngo, M.-E. Gueunier-Farret, J.-P. Kleider, L. Yu, P. R. Cabarrocas, S. Perraud, E. Rouviere, C. Celle, C. Mouchet and J.-P. Simonato, Conductive-probe atomic force microscopy characterization of silicon nanowire. *Nanoscale Research Letters*, 2011, **6**.
46. M. A. Hinai, *Self-assembly of conductive nanowires using DNA as a template* Newcastle University, 2012.
47. D. K. Schroder, *Semiconductor Material and Device Characterization*, 2nd Edn edn., Wiley, New York, USA, 1998.

48. S. Al-Ghamdi, *Synthesis and characterization of conductive nanowires using DNA as a template*. Newcastle University, 2010.
49. G. Givaja, P. Amo-Ochoa, C. J. Gomez-Garcia and F. Zamora, Electrical conductive coordination polymers. *Chemical Society Reviews*, 2012, **41**, 115-147.
50. A. B. Kaiser, Systematic conductivity behavior in conducting polymers: Effects of heterogeneous disorder. *Advanced Materials*, 2001, **13**, 927-941.
51. M. Jaiswal and R. Menon, Polymer electronic materials: a review of charge transport. *Polymer International*, 2006, **55**, 1371-1384.
52. A. B. Kaiser, Electronic transport properties of conducting polymers and carbon nanotubes. *Reports on Progress in Physics*, 2001, **64**, 1-49.
53. M. S. Tyagi, *Introduction to Semiconductor Materials and Devices*, Wiley and Sons, New York, USA, 1991.
54. M. M. Fogler, S. Teber and B. I. Shklovskii, Variable-range hopping in quasi-one-dimensional electron crystals. *Physical Review B*, 2004, **69**.
55. A. L. Efros and B. I. Shklovskii, Coulomb gap and low-temperature conductivity of disordered systems. *Journal of Physics C-Solid State Physics*, 1975, **8**, L49-L51.
56. P. Pipinys and A. Kiveris, Variable range hopping and/or phonon-assisted tunneling mechanism of electronic transport in polymers and carbon nanotubes. *Central European Journal of Physics*, 2012, **10**, 271-281.
57. A. N. Aleshin, Quasi-one-dimensional transport in conducting polymer nanowires. *Physics of the Solid State*, 2007, **49**, 2015-2033.
58. J. Joo, J. K. Lee, S. Y. Lee, K. S. Jang, E. J. Oh and A. J. Epstein, Physical characterization of electrochemically and chemically synthesized polypyrroles. *Macromolecules*, 2000, **33**, 5131-5136.
59. C. C. B. Bufon and T. Heinzel, Transport properties of chemically synthesized polypyrrole thin films. *Physical Review B*, 2007, **76**.

3. Preparation and chemical polymerisation of substituted pyrrole derivatives

3.1. Introduction

Pyrrole is one of the most common and important simple heterocycles and is found in substituted form in a wide range of natural products and drug molecules[1] It is a key component in the biological macrocycles, heme and chlorophyll, as well as in bioactive small molecules such as the bacterial antibiotic pioluteorine and nakamuric acid from marine sources (figure 46). Substituted pyrroles are increasingly important in material science too, as with highly fluorescent 4,4-difluoro-4-boradipyrriin (BODIPY) compounds and organic semiconductors molecules such as hexa(N-pirrolyl)benzene.

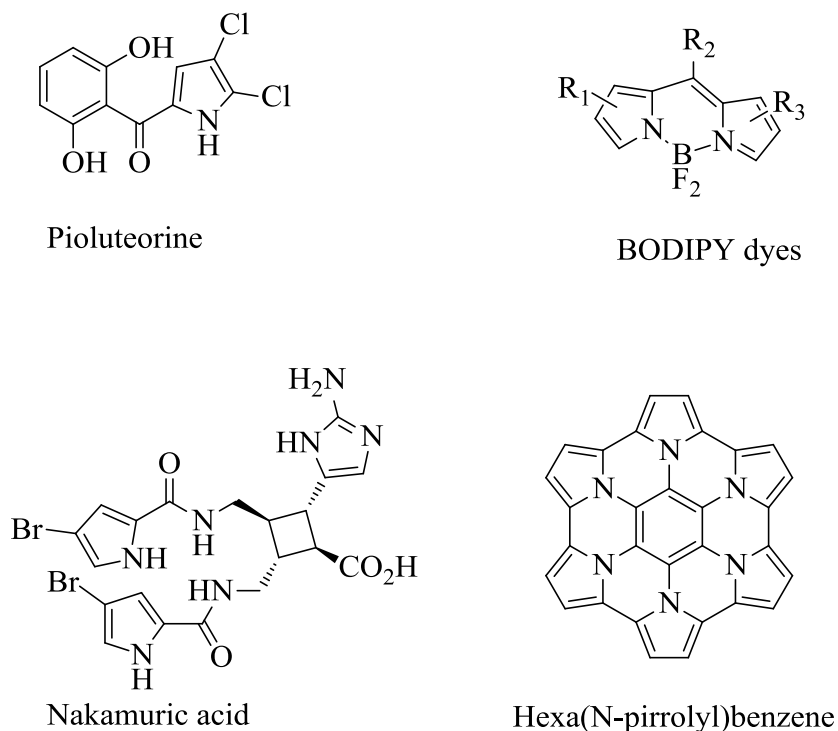
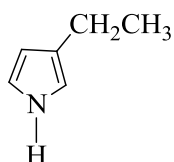


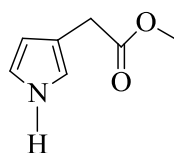
Figure 46. Examples of pyrrole-containing natural products and materials.

Substituted pyrroles can undergo polymerisation, predominantly through the 2,5-positions,[2] to form the corresponding conducting polypyrrole when the ring is substituted at either the *N*-atom, the 3 or 3,4 positions.[3-5] Figure 74 illustrates some examples of substituted pyrrole derivatives that have been prepared as polymers.

N-(3-Pyrrol-1-yl-propyl)pyridinium-tetrafluoroborate was synthesized in good yield by Cosnier and co-workers[6] by refluxing overnight (*N*-bromo-3-propyl)pyrrole with pyridine, in ethanol.



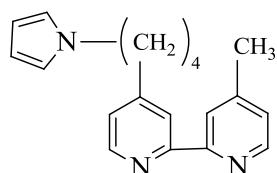
1-(3-pyrrolyl)ethane



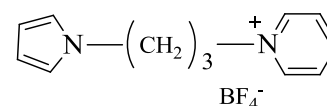
(3-pyrrolyl)ethanoic acid methyl ester



N-methylpyrrole



N-(4-pyrrol-1-yl-butyl)4'-methyl-2,2'-bipyridine

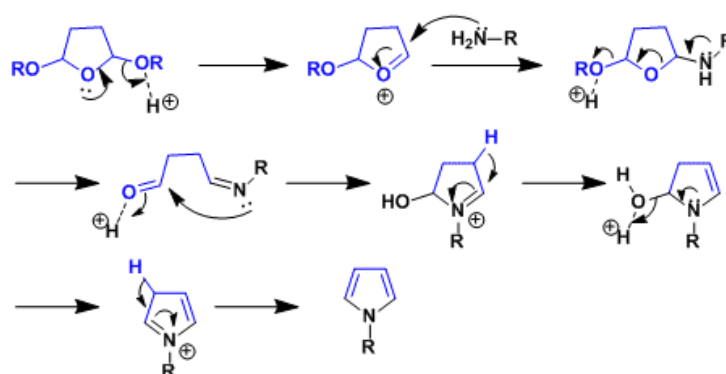


N-(3-Pyrrol-1-yl-propyl)pyridinium tetrafluoroborate

Figure 47. Substituted pyrrole derivatives that have been prepared as conducting polymers.

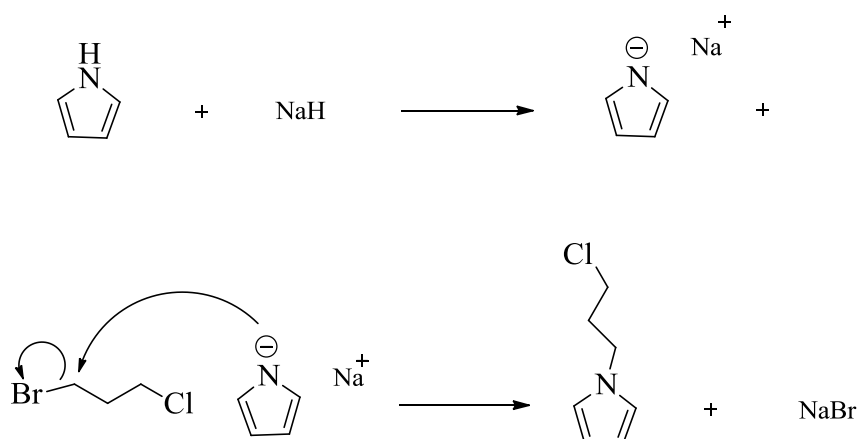
N-substituted pyrroles are particularly useful for preparing substituted polypyrroles due to the relatively straightforward means of introducing new functionality that avoids the stereochemical ambiguity that can arise with the asymmetric 3-derived compounds. The Clauson-Kaas reaction[7-9] involving the condensation between a primary aliphatic or

aromatic amine and 2,5-dimethoxy-tetrahydrofuran in the presence of an acid catalyst, is one common route to the synthesis of *N*-substituted pyrrole derivatives, scheme 6.



Scheme 6. Reaction mechanism for the Clauson-Kaas synthesis of *N*-substituted pyrrole derivatives.

An alternative approach involves the direct alkylation of pyrrole using an appropriate alkylating agent. This is generally achieved in polar solvents such as THF, DMF, and DMSO[10] using a stoichiometric amount of a strong base,[11] such as potassium alkoxide,[12] sodium hydride[13] or sodium hydroxide, to deprotonate the nitrogen atom.[14] Deprotonation increases the nucleophilicity of the nitrogen atom to attack by the incoming electrophilic carbon atom of the alkyl chain, where the bromine as a leaving group has been expelled as a Br^- ion. The general scheme for this stepwise reaction for *N*-alkylation of pyrrole is shown in scheme 7.



Scheme 7. The mechanism for the *N*-alkylation of pyrrole by nucleophilic substitution reaction.

The influence of *N*-substitution on the electropolymerization characteristics of substituted pyrrole was examined by Waltman et al.[15] The polymer yield and the rate of oxidation were found to decrease as the size of the alkyl group increases. The effect of *N*-substitution tends to slow the level of oxidation in the polymer films which are decreased with increasing the size of substituent.[16] Moreover, the reactivity of the chain is dependent on the electrode potential. Hence, the growing chains of which possess lower oxidation potential will be lower, resulting in lower rate of polymerisation than the highly oxidized non-substituted polymer. [6, 15, 17]

The *N*-substituted derivatives of polypyrrole have a lower conductivity than the non-substituted polymer, and their conductivity considerably decreases with increasing the size of the substituent.[6, 15] This is attributed to the reduced co-planarity of the polypyrrole chains as a result of the substituents' steric bulk, resulting in disruption of the delocalised π electron backbone.

Moreover, numerous investigations also have been carried out on the polymerization of *N*-substituted pyrrole, which are known to give rise to an increase in the polymer's solubility and fusibility.[18, 19]

This type of substitution pattern has been used quite extensively as a means to introduce metal ion binding capacity into the corresponding polymers.[20, 21] This is particularly the case for pyridine-type units, and a range of different mono- di- and even tridentate derivatives have been reported, see figure 48. As a result, a wide range of metal ions have been incorporated into polypyrrole films as pyridyl complexes, including Cu(I),[22, 23] Cu(II)[24] and Pd(II).[25]

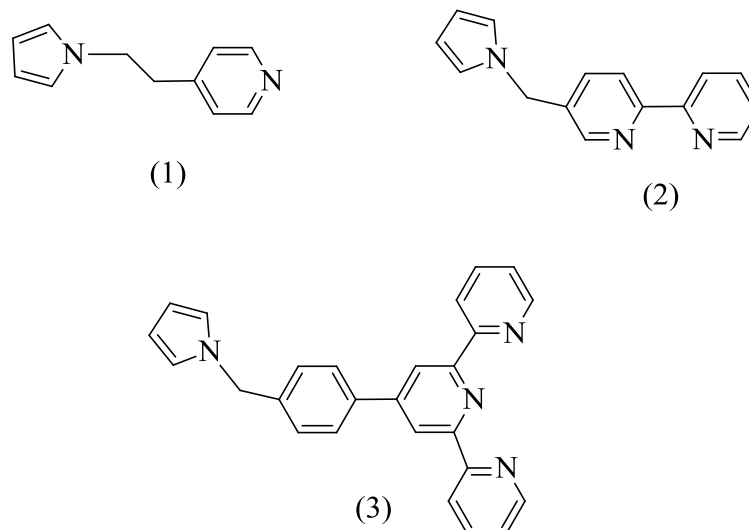


Figure 48. N-substituted pyrrole-pyridine derivatives that have: (1) monodentate, (2) bidentate and (3) tridentate.

A number of pyridinium-containing polypyrrole derivatives have also been reported in the literature. For instance, Cosnier et al (1989) [6] reported the electrochemical synthesis of a new class of electrically conducting polymers based on pyridine-containing pyrrole, including *N*-(3-Pyrrol-1-yl-propyl)pyridinium, which allowed effective binding and extraction of metal complexes from organic and aqueous media (ion exchange).

Moutet and coworkers[26] prepared viologen-containing polypyrrole films (*N,N'*-disubstituted-4,4'-bipyridinium dications) which are attractive materials because of their chemical stability and possible applications for electrochromic devices.[27, 28] Also more recently polypyrrole films have been prepared from *N*-(3-pyrrol-1-yl-propyl)-4,4'-bipyridinium which contain both a cationic pyridinium moiety as well as a pyridyl group with a free nitrogen. These have been developed for use in immobilising redox-active enzymes at electrodes using polymer matrices.[29, 30]

As mentioned in section 1.8, this project focuses on the synthesis and characterisation of nanowires based on pyridine-containing pyrrole-derived polymers using the DNA-templating.[31-33] Here, a range of monomers has been designed in modular form with the polymerisable group, pyrrole with an *N*-substituted flexible linker (alkyl group) which itself is attached to a pyridine derivatives. By introducing the

pyridine is part of a bipyridine group it is hoped desirable features will be introduced. First, it will provide a pyridyl group for with enhanced the metal ion binding capability for subsequent metal deposition. Second, the pyridinium moiety will enhance the cationic charge of the polymer and ensure less non-specific polymer formation during the templating reactions. Since the DNA template is highly anionic, the electrostatic interactions between the polypyrrole and the template are thought to play an important role in the formation of nanowires. However, polymer is also found to form as isolated particles indicating that not all the material formed interacts with the template. By introducing a cationic charge onto the monomer unit this extent of this non-specific polymerisation may be reduced.

The specific pyrrole-pyridine derivatives used in this work are *N*-(3-Pyrrol-1-yl-propyl)-pyridine hexafluorophosphate (**mono-I**), *N*-(3-Pyrrol-1-yl-propyl)-2,2'-bipyridinium hexafluorophosphate (**mono-II**) and *N*-(3-Pyrrol-1-yl-propyl)-4,4'-bipyridinium hexafluorophosphate (**mono-III**), shown in figure 49.

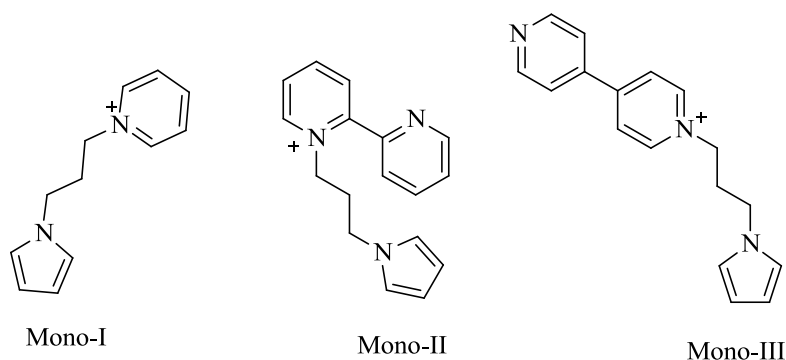
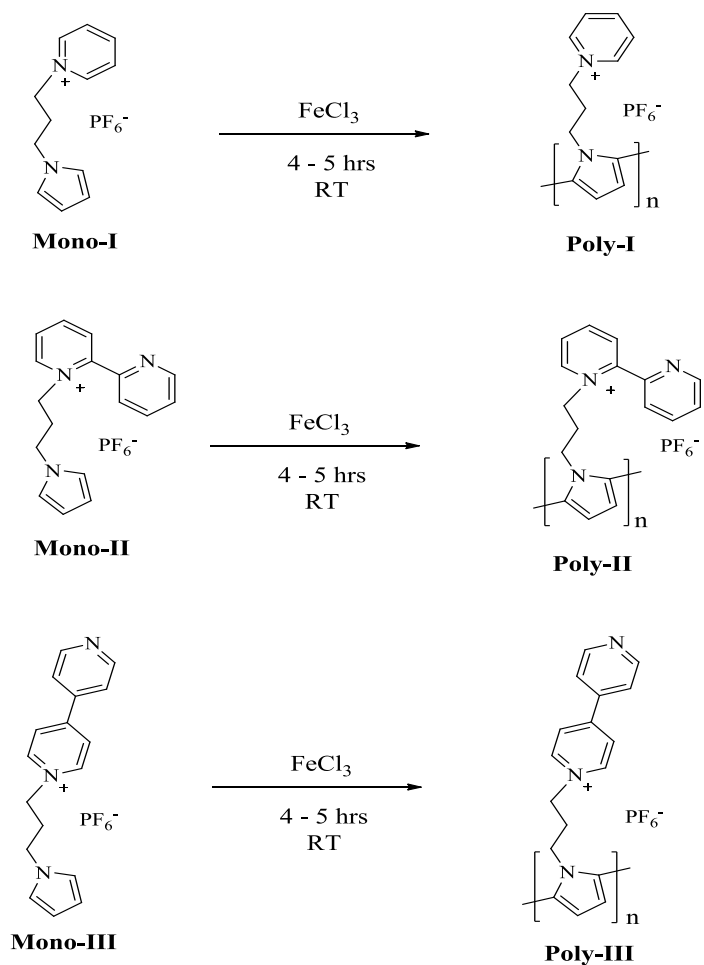


Figure 49. Suggested monomers for the conductive templated nanowires.

Reports for **mono-I** [6, 12, 20] and **mono-II**[29, 30] indicated that these compounds form the corresponding polymer whereas **mono-III** offers slightly different stereochemical properties compared to **mono-II**. [34] **Mono-I** was prepared to so as to allow control experiments to assess the effect of the free pyridyl group. This chapter describes the preparation and characterisation of these compounds. In addition, the pyrrole-pyridine derivatives monomer units are chemically polymerised using FeCl_3 as an oxidant and spectroscopic data and electrical conductivity of the resulting polymers

are presented and discussed. The Proposed products of the chemical polymerisation of mono-I, mono-II and mono-III are shown in scheme 8.



Scheme 8. Proposed products of the chemical polymerisation of mono-I, mono-II and mono-III.

3.2. Experimental

3.2.1. Materials and instruments

For the monomers synthesis and characterization, all reagents are of Analar grade or equivalent. Pyrrole, Pyridine, 2,2'-bipyridine, 4,4'-bipyridine, 1-Chloro,3-Bromopropane and Sodium hydride (NaH 60% dispersion in mineral oil) were purchased from Sigma-Aldrich. Pyrrole (99%, Alfa) was distilled under N₂ prior to use. Anhydrous dimethylformamide (DMF) was of analytical reagent grade. Ethanol was dried over molecular sieves. Water was purified with a deionization system (NANOpure Dlamond, Barnstead international) and had a resistivity of 18.2 MOhm/cm.

All monomers preparation reactions were performed under N₂ using standard Schlenk techniques. ¹H NMR spectra were recorded in CDCl₃ or D₂O on a BRUKER 300 instrument at 300 MHz and Chemical shifts (δ) were referred to TMS. The high resolution mass spectra were obtained with a LCT Premier Mass spectrometer. The FTIR spectra (range 600-4000 cm⁻¹ with 4 cm⁻¹ spectral resolution) were obtained using a Varian FTS 3000 FTIR spectrometer. For FTIR the samples solutions were adsorbed on silicon chips and dried at 40 °C in vacuum for 2 hours. Elemental analysis was performed on a Carlo Erba 1108 Elemental Analyser controlled with CE Eager 200 software, run in accordance with the manufacturer's instructions and weighed using a certified Mettler MX5 Microbalance.

All X-Ray structure data were measured on an Oxford Diffraction Gemini A Ultra diffractometer at 150 K, with Mo K α ($\lambda = 0.71073\text{\AA}$) (x-y) or Cu K α ($\lambda = 1.54178\text{\AA}$) (z) radiation. Semi empirical absorption corrections were applied based on symmetry-equivalent and repeated reflections. Structures were solved by direct methods and refined on all unique F₂ values, with anisotropic non-H atoms and constrained riding isotropic H atoms. Programs were CrysAlisPro for data collection, integration, and absorption corrections, SHELXTL for structure solution, refinement, and Olex2 for graphics.

For the chemical and electrochemical polymerization and characterization, Pyrrole and Iron (III) chloride (FeCl_3) were purchased from Sigma–Aldrich. Pyrrole was distilled under N_2 prior to use. Water was purified with a deionization system (NANOpure Dlamond, Barnstead international) and had a resistivity of 18.2 MOhm/cm. The FTIR spectra (in the range $600\text{-}4000\text{ cm}^{-1}$) of the chemically prepared polymers samples were recorded in absorbance mode with a 4 cm^{-1} spectral resolution on a Varian FTS 3000 FTIR spectrometer. The UV-vis absorption spectra (wavelength range from 250 to 900 nm) were recorded on a Varian Cary-100 Bio-spectrophotometer at room temperature. Elemental analysis was performed on a Carlo Erba 1108 Elemental Analyser controlled with CE Eager 200 software, run in accordance with the manufacturer’s instructions and weighed using a certified Mettler MX5 Microbalance.

Electrochemical polymerisation process was carried out at room temperature in a conventional single compartment cell, by the use of the Analyser/ Workstation CH1760B, Model 700B Series by CH Instruments, Inc., USA with sensitivity of up to picoamperes. The instrument is controlled by an external laptop under Windows environment. The resulting voltammogram was processed by the PC (under Windows environment) attached to the electrochemical workstation which measures the current as a function of applied voltage.

3.2.2. Synthesis of 1-(3-chloropropyl)pyrrole

In 250 ml two necked round bottom flask, pyrrole (6.9 mL, 100 mmol) was added to DMF (250 mL) under N_2 at room temperature while stirring. NaH (60% in oil) (4.0 g, 100 mmol) was then added to the solution under N_2 and stirred for 30 min at room temperature. 1-Chloro,3-bromopropane (50 ml, 500 mmol) was then added and the mixture was allowed to stir overnight. The reaction mixture was filtered using a Buchner funnel through filter agent (CELITE 521) and then the solvent was removed in vacuo. The product was extracted with ethyl acetate (three times), dried over anhydrous magnesium sulphate, and the solvent removed in vacuo. The product was purified by silica column chromatography using hexane:ethyl acetate (95:5) as the eluting solvent to give compound **1** as a yellow oil (Yield 5.0 g, 22.05 %). ^1H NMR (300 MHz, CDCl_3 ,

25 °C) δ = 2.18 ppm (2H, m, CH_2), 3.51 ppm (2H, t, $Cl-CH_2$), 4.12 ppm (2H, t, $N-CH_2$), 6.21 ppm (2H, d, β CH -pyrrole), 6.71 ppm (2H, d, α CH -pyrrole). FTIR: 3101 cm^{-1} (C-H, pyrrole), 2933, 2880 cm^{-1} (C-H aliphatic stretching), 1090 cm^{-1} (C-N), 1497, 1361 and 1282 cm^{-1} (pyrrole ring stretching vibration), 726 cm^{-1} (C-H, pyrrole).

3.2.3. Synthesis of *N*-(3-Pyrrol-1-yl-propyl)pyridine hexafluorophosphate (Mono-I)

In a two necked round bottom flask pyridine (0.3 mL, 3.85 mmol) was added to dry ethanol (2.0 mL) under nitrogen and 1-(3-chloropropyl)pyrrole (0.5 g, 3.5 mmol) was added to the solution while stirring. The solution was refluxed overnight under nitrogen. After 24 hours, the reaction solution was allowed to cool to the room temperature. The ethanol was removed on a rotary evaporator. To the resulting residue chloroform was added and this was extracted with water (3 x 20 ml). The aqueous solution was concentrated and mono-I was precipitated as the $(PF_6)^-$ salt by addition of a concentrated solution of KPF_6 . Filtration gave a yellow solid (0.47 g, 59 %). Mt. 88.0 °C. Elemental analysis: $C_{12}H_{15}N_2 PF_6^-$ theoretical: C, 43.38%, H, 4.55, %, N, 8.43%; found: C, 43.53%, H, 4.49%, N, 8.43%. 1H NMR (300 MHz, D_2O , 25 °C) δ = 2.44 ppm (2H, m, CH_2), 4.03 ppm (2H, t, CH_2), 4.48 ppm (2H, t, CH_2), 6.09 ppm (2H, d, CH -pyrrole), 6.67 ppm (2H, d, CH -pyrrole), 7.92 ppm (2H, t, CH -pyridine), 8.39 ppm (H, t, CH -pyridine), 8.62 ppm (2H, d, CH -pyridine). FTIR: 3131 cm^{-1} (C-H aromatic stretching), 2938, 2869 cm^{-1} (C-H aliphatic stretching), 1637 cm^{-1} (C=C aromatic ring stretching), 1487 cm^{-1} (C-C aromatic ring stretching), 1181 cm^{-1} (H_2C-N^+) and 839 cm^{-1} (PF_6^- stretching vibration). HRMS (ESI, m/z): calculated for $C_{12}H_{15}N_2^+$: 187.1230, found: 187.1216.

3.2.4. Synthesis of *N*-(3-Pyrrol-1-yl-propyl)-2,2'-bipyridinium hexafluorophosphate (mono-II)

1-(3-chloropropyl)pyrrole (0.5 g, 2.7 mmol) was added to 2,2-Dipyridyl (0.60 g, 3.85 mmol) which was dissolved in dry ethanol (2.0 ml). The same procedure as

described for the synthesis of mono-I was applied to obtain the product which was isolated from aqueous solution by addition of a saturated solution of KPF_6 . The brownish yellow precipitate was dried (1.0 g 51.5 %), mt. 104.0 °C. Elemental analysis: $\text{C}_{17}\text{H}_{18}\text{N}_3 \text{PF}_6^-$ theoretical: C, 49.88%, H, 4.40, %, N, 10.27%; found: C, 49.41%, H, 4.08%, N, 10.06%. ^1H NMR (300 MHz, D_2O , 25 °C) δ = 2.26 ppm (2H, m, CH_2), 3.88 ppm (2H, t, CH_2), 4.50 ppm (2H, t, CH_2), 6.13 ppm (2H, d, β CH - pyrrole), 6.58 ppm (2H, d, α CH - pyrrole), 7.68 ppm (H, m, CH -dipyridyl), 7.766 ppm (H, m, CH -dipyridyl), 8.06 ppm (H, m, CH -dipyridyl), 8.28 ppm (H, m, CH -dipyridyl), 8.58 ppm (H, m, CH -dipyridyl), 8.62 ppm (H, d, CH -dipyridyl), 8.76 ppm (H, m, CH -dipyridyl), 8.85 ppm (H, d, CH -dipyridyl). FTIR: 3202, 3113 cm^{-1} (C–H aromatic stretching), 2930, 2881 cm^{-1} (C–H aliphatic stretching), 1632 cm^{-1} (C=C aromatic ring stretching), 1476 cm^{-1} (C–C aromatic ring stretching), 1179 cm^{-1} ($\text{H}_2\text{C}-\text{N}^+$) and 838 cm^{-1} (PF_6^- stretching vibration). HRMS (ESI, m/z): calculated for $\text{C}_{17}\text{H}_{18}\text{N}_3^+$: 264.1495, found: 264.1491.

3.2.5. Synthesis of *N*-(3-Pyrrol-1-yl-propyl)-4,4'-bipyridinium hexafluorophosphate (mono-III)

1-(3-chloropropyl)pyrrole (0.5 g, 2.7 mmol) was added to 4,4-bipyridyl (0.60 g, 3.85 mmol) which was dissolved in dry Ethanol (2 ml). The same procedure as described in the synthesis of previous monomers (I and II) was applied to give the product which was obtained from the aqueous solution by addition of a saturated solution of potassium hexafluorophosphate. The yellow precipitate was dried (1.5 g, 55.6 %), mt. 174.0 °C. Elemental analysis: $\text{C}_{17}\text{H}_{18}\text{N}_3 \text{PF}_6^-$ theoretical: C, 49.88%, H, 4.40, %, N, 10.27%; found: C, 48.18%, H, 4.13%, N, 9.65%. ^1H NMR (300 MHz, D_2O , 25 °C) δ = 2.55 ppm (2H, m, CH_2), 4.09 ppm (2H, t, CH_2), 4.61 ppm (2H, t, CH_2), 6.04 ppm (2H, t, β CH - pyrrole), 6.68 ppm (2H, t, α CH - pyrrole), 7.82 ppm (H, m, CH -dipyridyl), 8.23 ppm (H, m, CH -dipyridyl), 8.71 ppm (H, m, CH -dipyridyl). FTIR: 3129, 3051 (C–H aromatic stretching), 2924, 2872 (C–H aliphatic stretching), 1641 (C=C aromatic ring stretching), 1458 (C–C aromatic ring stretching), and 1166 cm^{-1} ($\text{H}_2\text{C}-\text{N}^+$) and 812 cm^{-1} (PF_6^- stretching vibration). HRMS (ESI, m/z): calculated for $\text{C}_{17}\text{H}_{18}\text{N}_3^+$: 264.1495, found: 264.1508.

3.2.6. Chemical polymerisation

Pyrrole and mono-I, mono-II and mono-III were chemically polymerised in aqueous solution using iron(III) chloride (FeCl_3) as oxidant (1.0 ml, 1.0 mmol) added dropwise to an aqueous solution of the appropriate monomer (1.0 ml, 3 mmol) at room temperature while stirring in 10 ml tube glass vial. After 4-5 hours of reaction, a black precipitate in the case of ppy or dark brown precipitate in case of poly-I, poly-II and poly-III were formed as small thin flakes. The polymers were isolated from the reaction mixture by filtration and washed with excess amount of DI water to remove the iron containing species. The polymer was dried under vacuum at 40 °C for 5 hours. Ppy was not soluble in organic solvents, while the other resulting polymers (poly-I, poly-II and poly-III) were soluble in some organic solvents such as THF and ethanol. The as-prepared polymers were characterised using FTIR, Uv-Vis spectroscopy, elemental analysis and two terminal I-V measurements.

For UV-vis measurements, polymers solutions were made using 0.5 mL of FeCl_3 (3.0 mM) which was added dropwise to 0.5 mL of 1.0 mM freshly prepared monomer solution. The mixture was stirred and allowed to react at room temperature and the reaction was monitored by the Uv-Vis spectroscopy over 6 hours. Monomers solutions were prepared and used as a control.

Poly-I: FTIR: 3128 (C–H aromatic stretching), 2945 and 2875 cm^{-1} (C–H aliphatic stretching), 1630 cm^{-1} (C=C aromatic ring stretching), 1482 (C–C aromatic ring stretching), and 1188 cm^{-1} ($\text{H}_2\text{C–N}^+$) and 818 cm^{-1} (PF_6^- stretching vibration). Elemental analysis: $\text{C}_{12}\text{H}_{13}\text{N}_2\text{PF}_6^-$ theoretical: C, 43.65%, H, 3.97, %, N, 8.48%; found: C, 43.34%, H, 4.34%, N, 8.48%.

Poly-II: FTIR: 3237, 3124 cm^{-1} (C–H aromatic stretching), 3086, 2928 cm^{-1} (C–H aliphatic stretching), 1635 cm^{-1} (C=C aromatic ring stretching), 1463 cm^{-1} (C–C aromatic ring stretching), 1157 cm^{-1} ($\text{H}_2\text{C–N}^+$) and 826 cm^{-1} (PF_6^- stretching vibration). Elemental analysis: $\text{C}_{17}\text{H}_{16}\text{N}_3\text{PF}_6^-$ theoretical: C, 50.12%, H, 3.93, %, N, 10.32%; found: C, 49.40%, H, 4.10%, N, 10.32%.

Poly-III: FTIR: 3130, 3069 (C–H aromatic stretching), 2932, 2847 (C–H aliphatic stretching), 1636 (C=C aromatic ring stretching), 1499 (C–C aromatic ring stretching),

and 1159 cm^{-1} ($\text{H}_2\text{C}-\text{N}^+$) and 831 cm^{-1} (PF_6^- stretching vibration). Elemental analysis: $\text{C}_{17}\text{H}_{16}\text{N}_3\text{PF}_6^-$ theoretical: C, 50.12%, H, 3.93, %, N, 10.32%; found: C, 49.40%, H, 4.00%, N, 10.14%.

3.2.7. *Electrochemical polymerisation*

The electrochemical polymerisation of monomers I, II and III was carried out in a three electrode electrochemical cell which is comprised of a working electrode, auxiliary electrode, and reference electrode. The potential was cycled between -2.5 V to $+2.5\text{ V}$ in acetonitrile containing LiClO_4 as an electrolyte. All experiments were carried out with the working electrode was platinum electrode with surface area of 0.008 cm^2 . A Tungsten wire and a Ag/AgCl electrode were used as an auxiliary electrode and reference electrode respectively. The solutions were degassed by dry nitrogen bubbling prior to the experiments. Electro-oxidative polymerisations were carried out in acetonitrile containing 0.05 M of monomer and 0.05 M of LiClO_4 at a scan rate of 100 mV s^{-1} .

3.2.8. *Two-terminal current – voltage measurements*

The conductivity of chemically prepared PPy bulk film and the polymers of *N*-alkylated pyrrole-pyridine derivatives (poly-I, poly-II, and poly-III) and the temperature dependence of I-V curves of these polymers samples was measured. SiO_2/Si chips containing the adsorbed polymer sample were placed on the CMS cascade Microtech Summit 11000 series probe station for variable temperature measurements.

A series of applied voltages (V) and current (I) passing through the film sample were recorded. The temperature was then raised and allowed to stabilise before the same measurements were recorded again. This process was repeated over a range of temperatures (from 293K to 373K) . All measurements were taken in the dark and under N_2 . The conductivity σ of thin polymer films with an average cross-sectional area A at

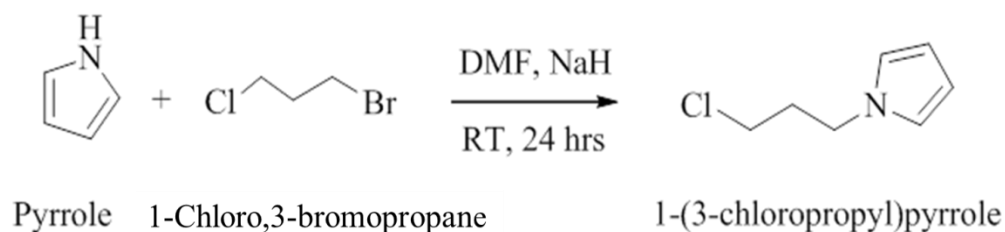
room temperature was calculated from its resistance R , in Ohm (Ω), and length l using the relationship as shown in section 2.3.4.

The resistance R was calculated from the ohmic part at the origin of the I-V curve and accordingly, the conductance in Siemens (S), could be obtained from the reciprocal value of the resistance. The temperature dependence of I-V data was recorded in the range between -1.0V and 1.0V, and over a range of temperatures range from 293 to 373 K.

The conductivity of the as-prepared polymers (PPy, poly-I, poly-II, and poly-III) was measured on bulk film on SiO₂/si chips onto which the polymer film was deposited. The wet polymer films were deposited onto the chips and dried at 40 °C for 5 hours under vacuum and kept under nitrogen before and during measurements to avoid oxidation. The samples were then placed on a vibration isolation table inside the chamber of a CMS cascade Microtech Summit 11000 probe station under nitrogen gas. A high performance DC probe holder with probe tips of 19 μm radius was used to connect the polymer film to the external microcircuits. A Leica S8 stereo zoom microscope was used to observe the probe tips, to ensure that the tips were not damaged by applying excessive force. Temperature variation was achieved using a thermal chuck system (Model ETC-200 L, ESPEC, Japan) equipped with refrigerator unit. The current-voltage sweep measurements were carried out on polymer film using a Hewlett Packard semiconductor device analyser (HP/Agilent B1500A) controlled by Aligent Easy EXPERT software.

3.3. Results and discussion

3.3.1. Synthesis of 1-(3-chloropropyl)pyrrole



Scheme 9. Synthesis of 1-(3-chloropropyl) pyrrole

The reaction of pyrrole with 1-chloro,3-bromopropane using NaH as a base in DMF solution under conditions that discussed above afforded the expected N-alkylated product, 1-(3-chloropropyl)pyrrole, in a reasonable yield. Based on comparison with $^1\text{H-NMR}$ data of pyrrole and 1-chloro-3-bromopropane, the $^1\text{H-NMR}$ (300 MHz, CDCl_3 , 25 °C) spectrum, figure 50, confirmed TLC results which indicated the formation of a new compound. The signal at 3.74 ppm corresponding to the $\text{CH}_2\text{-Br}$ of 1-chloro-3-bromopropane was absent, and instead, a new signal appeared at 4.12 ppm (2H, t, CH_2). This downfield shift is expected for substitution of $\text{CH}_2\text{-Br}$ with $\text{CH}_2\text{-N}$. [18] Further, the peak at 7.25 ppm (assigned to NH of pyrrole) [35] had also disappeared. The two doublets at 6.71 and 6.21 ppm are assigned to α and β positions of pyrrole ring. The two triplets at 4.12 and 3.51 ppm and one multiplet at 2.18 ppm, assigned to the positions c, e and d of the propyl group respectively.

FT-IR spectra are shown in figure 51. The introduction of the propyl chain can be judged from the bands at $\sim 2900\text{ cm}^{-1}$ corresponding to aliphatic C-H stretches. The C-H aromatic ring stretching in pyrrole ring has been characterized at 3101 cm^{-1} . The strong characteristic bands at 1497, 1361 and 1282 cm^{-1} was assigned to pyrrole ring stretching vibration. [18] Further, the N-H characteristic bands at 3400 cm^{-1} had disappeared, implying that N-substituted pyrrole had been synthesized. These FTIR results and $^1\text{H-NMR}$ results are of diagnostic value for the formation of N-alkylated pyrrole.

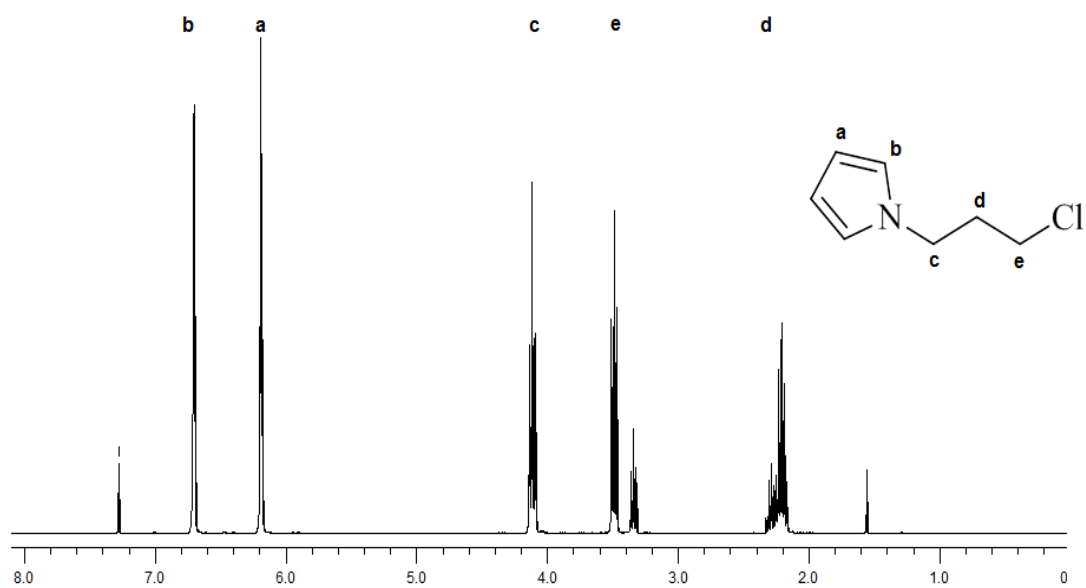


Figure 50. ^1H NMR spectrum of 1-(3-chloropropyl)pyrrole.

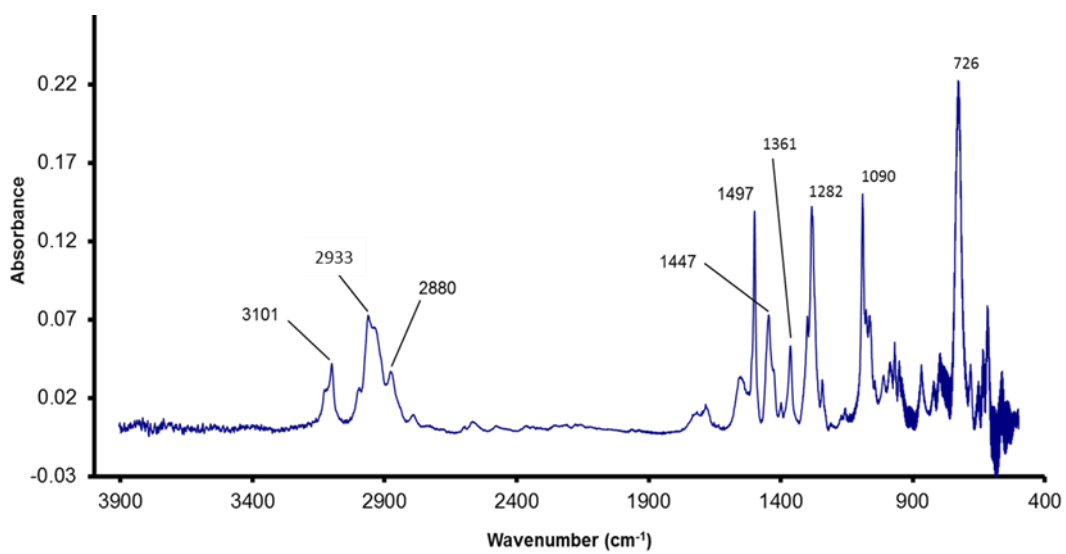
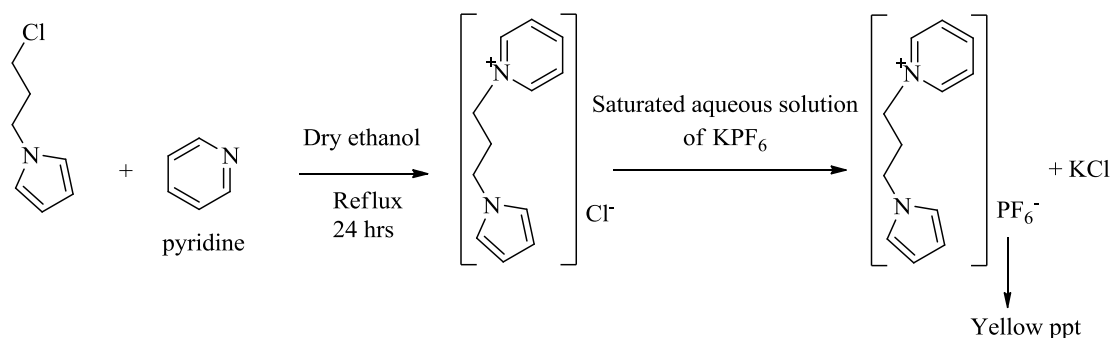


Figure 51. FTIR spectrum of 1-(3-chloropropyl)pyrrole.

3.3.2. Synthesis of Mono-I



Scheme 10. Synthesis of mono-I.

This compound was prepared to act as a control to later experiments. The synthesis of Mono-I, N-(3-Pyrrol-1-yl-propyl)pyridinium hexafluorophosphate, is illustrated in scheme 10. It involves the alkylation of pyridine using 1-(3-chloropropyl)pyrrole. The reaction of the chloro-alkyl pyrrole and pyridine was indicated by TLC which indicated the formation of a new compound. The product was then isolated by addition of a saturated aqueous solution of potassium hexafluorophosphate. The cationically charged pyrrole-pyridinium salt was precipitated as yellow powder in moderate yield with good purity. ¹H NMR spectrum was consistent with the formation of pure N-(3-Pyrrol-1-yl-propyl)pyridinium salt, appendix A1. The downfield shifting of the triplet 3.35 ppm (CH₂- Cl) signal 4.48 ppm (CH₂- N, pyridine) due to the effect of the pyridine ring was indicated. It also shows the appearance of the expected aromatic pyridine signals between 7.0 and 9.0 ppm. The two triplets at 7.92 and 8.39 ppm and one doublet at 8.62 ppm, assigned to positions f, g and h on pyridine ring respectively.

The FTIR spectrum shows the C-H aromatic stretching at 3131 cm⁻¹. The bands that appeared around 2938 and 2869 cm⁻¹ were attributed to aliphatic C-H stretches of the saturated alkyl group (propyle linker),[18] thus indicating the N-alkylated pyrrole pyridinium salt was prepared. The C=C aromatic ring stretching at 1637 cm⁻¹ in heterocyclic aromatic have been characterized. The strong band at 839 cm⁻¹ belongs to the stretching vibration of hexafluorophosphate anion (PF₆⁻). Furthermore, HRMS confirmed the formation of N-(3-Pyrrol-1-yl-propyl)pyridinium hexafluoro-phosphate, appendix A3, with a peak at 187.1216 corresponding to C₁₂H₁₅N₂ PF₆.

Single crystals suitable for study by X-ray diffraction were grown by slow evaporation from water and were used to confirm as the molecular structure of the compound, N-(3-Pyrrol-1-yl-propyl)pyridinium hexafluorophosphate, was obtained. Figure 52 shows that all bond lengths and angle lie in the expected range of mono-I. The full crystal structure data are shown in appendix G.

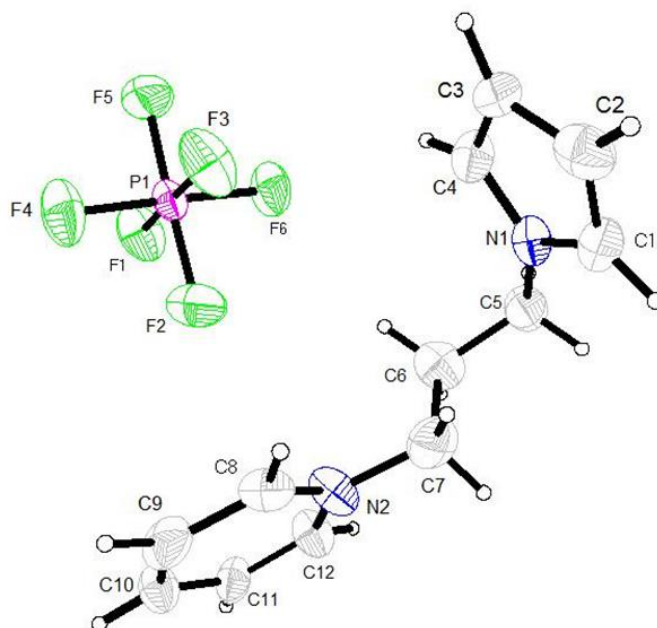
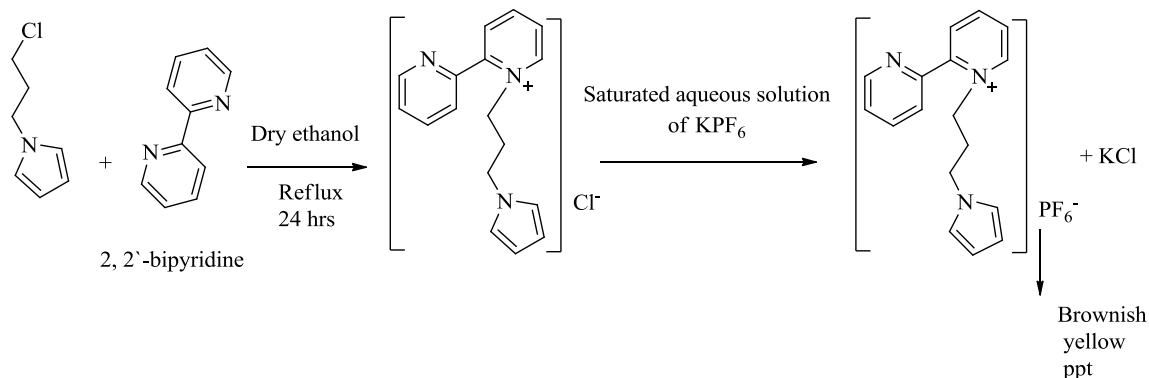


Figure 52. Molecular structure of one independent molecule of N-(3-Pyrrol-1-yl-propyl)pyridinium hexafluoro-phosphate.

3.3.3. Synthesis of Mono-II



Scheme 11. Synthesis of mono-II.

Mono-II was prepared by the reaction of 1-(3-chloropropyl)pyrrole with 2,2-dipyridyl under the same conditions which are mentioned in the preparation of Mono-I. The product was indicated by TLC and then was isolated from the aqueous solution by adding a saturated solution of potassium hexafluorophosphate. The cationic charged pyridinium salt was precipitated as a brownish yellow powder in reasonably good yield. ¹H NMR spectrum was consistent with the formation of product; Appendix B1 shows the expected increase in the number of aromatic signals between 7.0 and 9.0 ppm, due to the new asymmetry of the 2,2'-bipyridyle moiety and downfield shifting of the 3.35 ppm signal of CH₂-Cl to 4.50 ppm of the CH₂-N (dipyridyl) due to the effect of N-substitution. The two doublets at 6.58 and 6.13 ppm are assigned to α and β positions of pyrrole ring and the two triplets at 4.50 and 3.88 ppm and one multiplet at 2.26 ppm, assigned to the positions c, e and d of the propyl linker respectively. Evidence of the alkylation at one of the bipyridyle N atoms can be judged from the ¹H NMR spectrum. One of the resonances for the proton (f) adjacent to the N in the bipyridyle rings is shifted to the downfield from 8.6 ppm to 8.9 ppm (f^{''}), while the other remains relatively unperturbed at 8.6 ppm.

The FTIR spectrum of mono-II shows the C-H aromatic stretching at 3202 cm⁻¹ and 3113 cm⁻¹. The C=C aromatic ring stretching cm⁻¹ in heterocyclic aromatic has been characterized at 1632 cm⁻¹. The bands that appeared around 2930 and 2881 cm⁻¹ were attributed to the C-H aliphatic stretching of the propyl linker. These are not so intense as in mono-I, perhaps reflecting the increase of aromatic groupings in mono-II. The

strong band of PF_6^- stretching vibration was observed at 838 cm^{-1} . Mass spectroscopy confirms the presence of mono-II with a molecular ion peak at 264.1491 amu corresponding to $\text{C}_{17}\text{H}_{18}\text{N}_3\text{PF}_6$. From these results the synthesis of N-alkylated pyrrole-bipyridinium salt (mono-II) was indicated. Confirmatory evidence of this was obtained from a single crystal X-ray diffraction study. Figure 53 shows the molecular structure of mono-II. The full crystal structure data are shown in appendix H. All the bond lengths and angles are in the expected ranges.

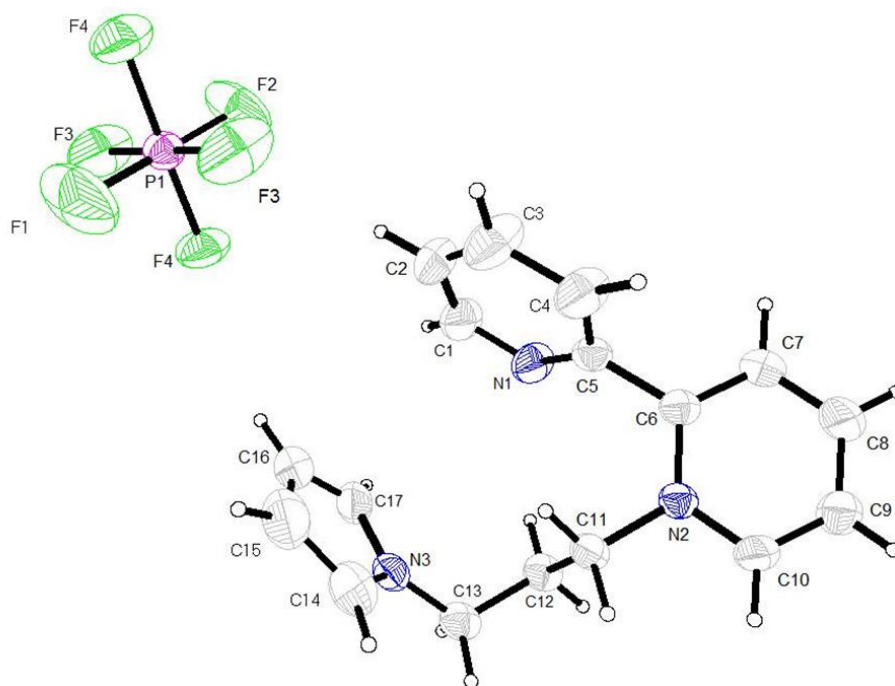
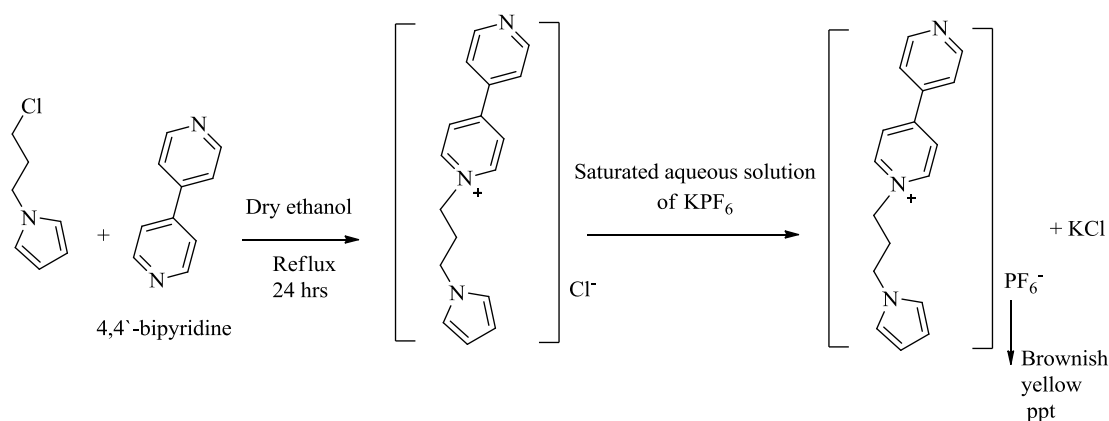


Figure 53. Molecular structure of one independent molecule of mono-II.

3.3.4. Synthesis of mono-III



Scheme 12. Synthesis of Mono-III.

Mono-III was prepared using the same procedure that was used for the previous monomers. The PF₆⁻ salt was precipitated as a brownish yellow powder in a reasonably good yield. Mono-III was identified by ¹H NMR, FTIR, elemental analysis and High resolution mass spectra. ¹H NMR spectrum shows the expected aromatic signals between 7.0 and 9.0 ppm, and downfield shifting of the 3.35 ppm signal of the CH₂-N (dipyridyl) to 4.65 ppm due to the effect of 4,4'-dipyridyl rings. The two doublets at 6.69 and 6.05 ppm are assigned to α and β positions of pyrrole ring. FTIR spectrum shows the C-H aromatic stretching at 3129 cm⁻¹ and 3051 cm⁻¹. The C=C aromatic ring stretching in heterocyclic aromatic was located at 1641 cm⁻¹. The bands that appeared around 2924 and 2872 cm⁻¹ were attributed to the C-H aliphatic stretching of the propyl linker, which are not so intense as in mono-I, reflecting the increase of aromatic groupings in mono-III. The strong band of PF₆⁻ stretching vibration was observed at 812 cm⁻¹. Mass spectroscopy confirms the presence of mono-III with a molecular ion peak at 264.1508 amu corresponding to C₁₇H₁₈N₃PF₆, appendix C3.

3.3.5. Chemical Polymerisation of monomers and characterisation

Electrically conducting polymers (CPs) can generally be prepared by electrochemical [36, 37] or chemical oxidative-polymerization methods.[6, 38, 39] Chemical oxidative polymerisation is a simple and fast process with no need for special instruments. *N*-

substituted pyrrole derivatives can undergo chemical polymerization to produce corresponding polymers, since the 2 and 5 (α -) positions remain available for coupling.[3]

Here, **py** and monomers: **mono-I**, **mono-II** and **mono-III** were polymerised in bulk as control samples for comparison with the polymer/DNA nanostructures whose preparation will be explained in the following chapters. These monomers were polymerized using FeCl_3 as oxidant, and scheme 8 shows the suggested reaction scheme for the oxidant. The typical synthetic method used was as follows; 0.5 mL of 18 mM FeCl_3 aqueous solution was added into 0.5 ml, 6.0 mM of pyrrole or substituted derivatives (3:1, FeCl_3 :monomer ratio). The colourless solution, which is initially little turbid spontaneously darkens, turning to black in case of polypyrrole and brownish yellow in case of the other compounds. The formation of polymer is also indicated by the appearance of solid material, as flakes, precipitating from the reaction solutions as a result of the oxidation by iron (III) chloride.

Each prepared sample was filtered and washed using copious amounts of DI water (3x100mL) to remove the residual monomers and any Fe-containing species. The collected polymer was dried under vacuum at 40 °C for 5 hours. The final polymer samples were stored in glass vials for further characterization steps. Unlike ppy, the N-substituted polymers (poly-I, poly-II and poly-III) had some solubility in organic solvents such as THF and ethanol. This is consistent with observations made by Roussel et al (2007) reported that the functionalization of pyrrole via its N-alkylation followed by its subsequent polymerization, led to enhanced solubility of the resulting N-alkylated polypyrrole.[40]

The UV-Vis spectra of the chemically prepared polymers (poly-I, poly-II and poly-III) are shown in figure 54, appendix D2 and appendix E2 respectively. These spectra indicate the appearance of new electronic absorption bands due to the polymer formation. The absorption band apparent at 350 nm can be attributed to the π - π^* transition of the polymer. The broad absorption bands which are apparent in the 450-550 nm region is assigned to the bipolaron state (radical cation) formed during the polymerisation process.[40, 41] By contrast, the corresponding monomers show little absorption in the visible region.

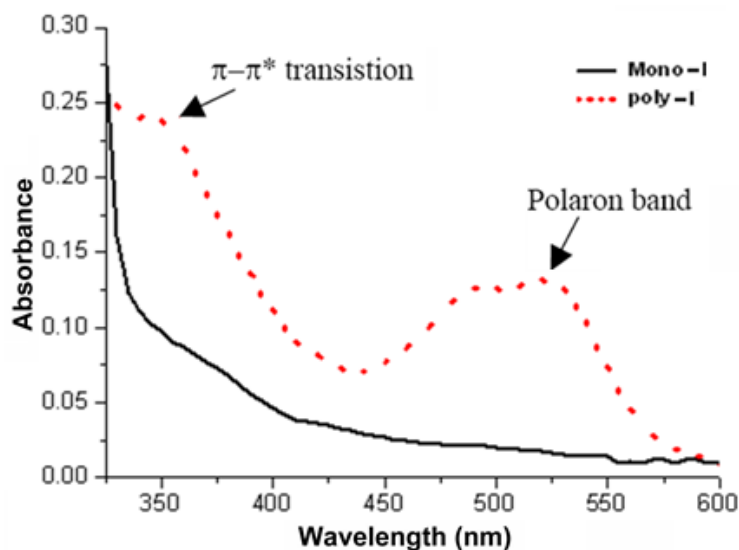


Figure 54. UV-Vis spectra of poly-I prepared by chemical polymerisation using FeCl_3 as oxidising agent.

FTIR spectra comparing mono-I and poly-I are shown in figure 55. The most important difference that is indicative of polymerisation is the appearance of the broad absorption above 2000 cm^{-1} , as shown in figure 55(a). This is well known to be due to intrachain (free carrier) excitations responsible for the conduction in these types of material.[42] The sample of pure polypyrrole prepared using the same procedure exhibits a similar broad absorption band in this region, see figure 55(b). Other than this, the spectrum of the poly-I exhibits rather similar absorption bands to those of mono-I. However, further evidence of polymerisation can be judged through enhancement and/or shifting of various bands. Figure 55(c) shows the changes observed in the $1400\text{--}1800\text{ cm}^{-1}$ region of the spectra.[43, 44] The C=C aromatic ring and C-C aromatic ring stretching bands are found at 1630 cm^{-1} and 1482 cm^{-1} respectively, after polymerisation compared to 1637 and 1487 in Mono-I respectively. Figure 55(d) shows the higher frequency region of the spectra and highlights the shifting of absorption band arising from aromatic C-H stretching vibration at 3131 cm^{-1} in mono-I to 3128 cm^{-1} in poly-I spectrum.[45] The asymmetric CH_2 in mono-I is observed at 2938 cm^{-1} and 2869 cm^{-1} [18] are shifted to 2945 cm^{-1} and 2875 cm^{-1} after polymerisation. Both compounds also show strong bands at 839 cm^{-1} and 818 cm^{-1} which belong to the hexafluorophosphate anion (PF_6^-).

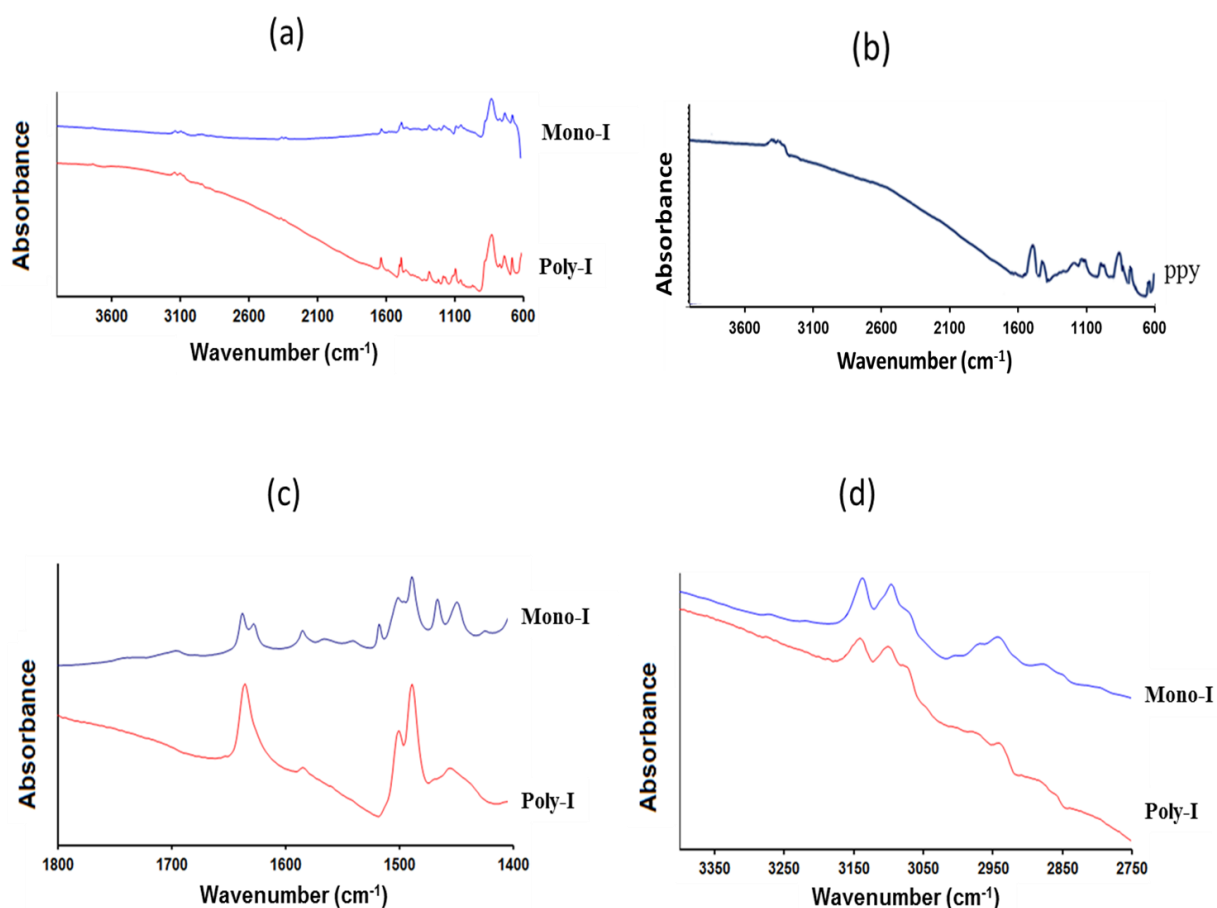


Figure 55. FTIR spectra of: (a) mono-I and chemically prepared poly-I in the range (600 cm^{-1} - 4000 cm^{-1}), (b) Chemically prepared PPy using FeCl_3 as oxidizing agent in the range (600 cm^{-1} - 4000 cm^{-1}), (c) mono-I and poly-I in the range ($1400\text{ cm}^{-1} - 1800\text{ cm}^{-1}$) and (d) mono-I and poly-I in the range ($2750\text{ cm}^{-1} - 3400\text{ cm}^{-1}$).

FTIR spectra for poly-II and poly-III in the range ($600\text{ cm}^{-1} - 4000\text{ cm}^{-1}$) compared with their relative monomers are shown in appendix D1 and appendix E1. Again, as for **poly-I**, it is expected that the spectra of the polymers will exhibit similar absorption bands as those of the corresponding monomers with slight shifting of some bands. The spectra of these polymers (II and III) samples showed little absorption due free carrier excitation can be observed above 2000 cm^{-1} . However, the enhancement of the C=C and C-C aromatic ring stretching vibration bands at 1635 and 1463 cm^{-1} respectively for poly-II (figure 56) and 1636 and 1499 cm^{-1} respectively for poly-III (figure 57) is generally consistent with the predicted enhancement of chain conjugation intensity and consequent higher concentration of bipolarons as charge carriers which indicates that the polymerisation has occurred.[46, 47] The strong absorption bands at 838 and 825 cm^{-1} for mono-II and mono-III respectively are attributed to the stretching vibration of PF_6^- which were unchanged after polymerisation.

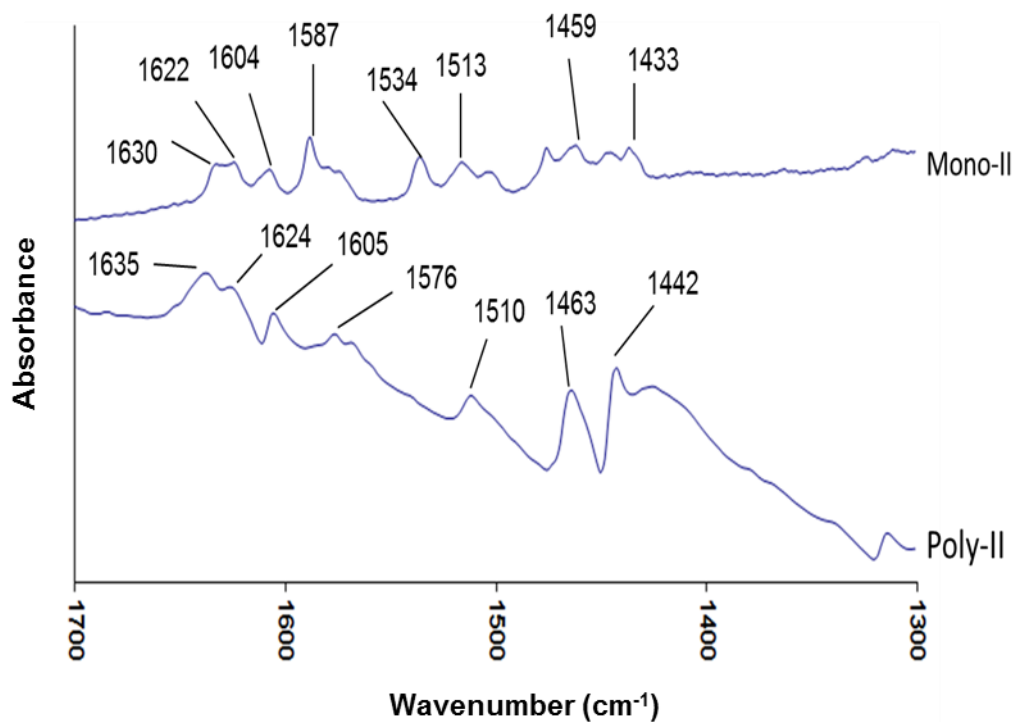


Figure 56. FTIR spectra of mono-II and chemically prepared poly-II in the range (1300 cm^{-1} - 1700 cm^{-1}).

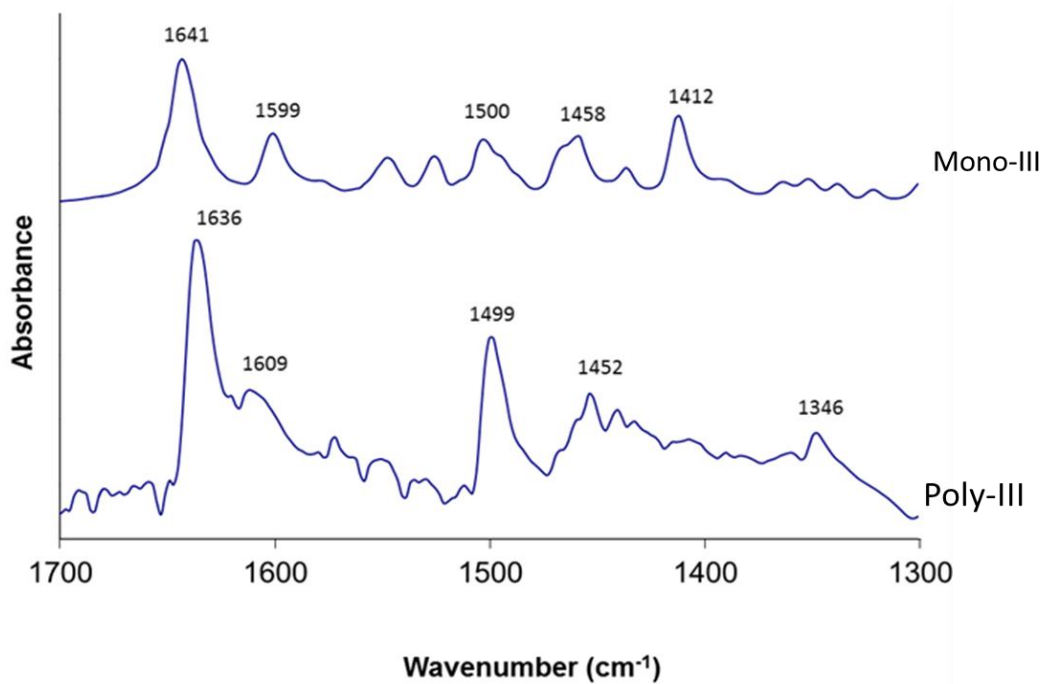


Figure 57. FTIR spectra of mono-III and chemically prepared poly-III in the range (1300 cm^{-1} - 1700 cm^{-1}).

3.3.6. Electrochemical Polymerisation of mono-I, mono-II and mono-III

Mono-I, mono-II and mono-III were electrochemically polymerised on platinum electrode, in acetonitrile containing 50 mM of LiClO₄ electrolyte. The potential was scanning between -1.8 and +1.8 V versus Ag/AgCl. Figure 58 shows typical CVs for poly-I, poly-II and poly-III.

Irreversible oxidation peaks attributed to the pyrrole-localized process in all monomers (mono-I, mono-II and mono-III) appear at ca. +1.4 V as shown in figures 58(a), 58(b) and 85(c) respectively. The amplitude of these peaks decrease upon consecutive scanning due to the monomers consumption and the formation of poly-I, poly-II and poly-III, respectively.[34] The redox waves of the polymers were observed, where the current of this peak remained constant upon continuous scanning. This is likely because a fraction of the monomers was oxidized into oligomers and were dissolved or dispersed into the solution. This is mainly due to that the *N*-substituted group, (in this case alkylated-pyridinium, alkylated-2,2'- or alkylated-4,4'-bipyridinium groups) in poly-I, poly-II and poly-III respectively, which increased the solubility of the polymer in the reduced state.[48, 49] This was experimentally observed as the amount of polymer on the electrode was not increased, and the colour of the solution near to the working electrode surface changed from turbid colourless to brown. Cathodic waves owing to the reduction of the oxidized polymers, which increased upon consecutive scanning, were also observed.

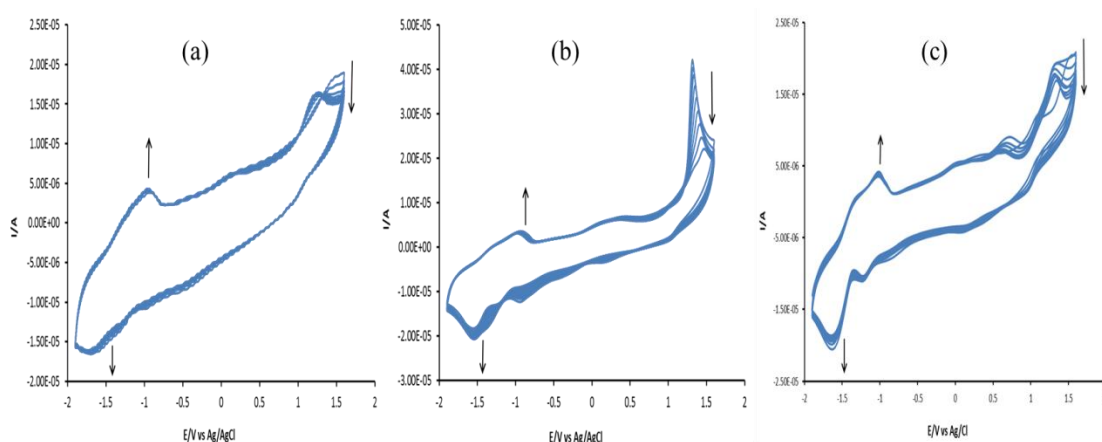


Figure 58. Consecutive cyclic voltammograms for a platinum electrode in contact with a 50 mM of LiClO₄ /AN solution containing 0.05 M of (a) mono-I (b) mono-II and (c) mono-III at a scan rate of 100 mV s⁻¹.

3.3.7. Electrical characterisation using two terminal I/V measurements

The conductivity of chemically prepared PPy bulk film and the polymers of *N*-alkylated pyrrole-pyridine derivatives (poly-I, poly-II, and poly-III) and the temperature dependence of I-V curves of these polymers samples has been investigated. SiO₂/Si chips containing the adsorbed sample were placed on the probe station, where the temperature was controlled and monitored. The temperature dependence of I-V data was recorded in the range between -1.0V and 1.0V, and over the temperatures range, 293 to 373 K.

As the conductivity values of conducting polymers are sensitive to the preparation conditions, a sample of polypyrrole was also prepared and measured on the same instrument to allow ready comparison. I-V curves of PPy sample prepared chemically using FeCl₃ as an oxidant is depicted in figure 59. These I-V curves show that the current passing through the PPy film increases with increasing temperature. Most conducting polymers show an increase in conductivity with temperature because more valence electrons are excited by temperature into the conduction band.[50-53] However, the temperature dependence can also be affected by factors, such as the polymer structure, degree of crystallinity and dimensionality.[50, 54-57]

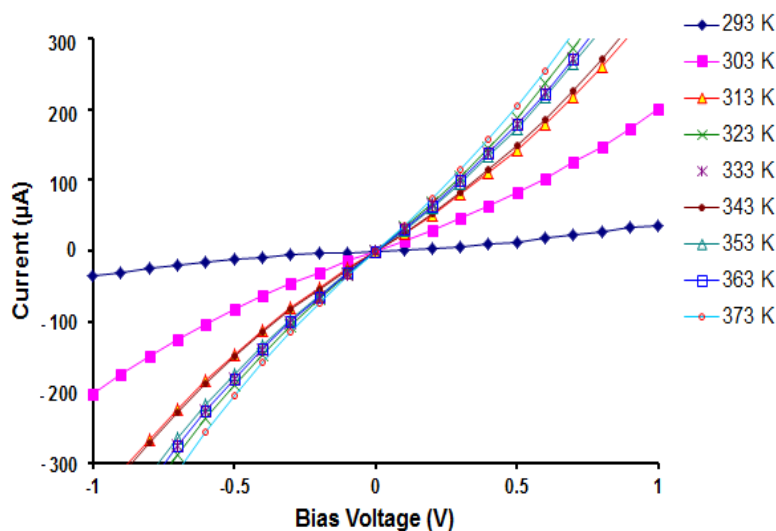


Figure 59. Temperature dependence of I-V curves of chemically prepared PPy film.

The room temperature conductivity value, $\bar{\sigma}$, of the chemically prepared PPy thin film ($l=1.0$ mm and contact area $A= 1134 \mu\text{m}^2$) determined from the slope of the I-V curve at 0 V was calculated as $\bar{\sigma} = 86.2 \text{ S cm}^{-1}$. The room temperature conductivity of thin film of PPy doped with hexafluorophosphate was $\sim 300 \text{ S cm}^{-1}$, [58] where its conductivity when doped by sulphated polyhydroxyether was $\sim 10 \text{ S cm}^{-1}$. [58, 59]

However the structure and preparation technique of polypyrrole film have strong influences on the electrical conductivity. For example, a doped PPy film, synthesised by J. Kim *et. al.* [41] using the in situ vapour-phase polymerisation method, has a conductivity about 10^2 S cm^{-1} . PPy films which fabricated by G. Qi *et. al.* [60] using in-situ freezing interfacial polymerization method have a conductivity up to $2.0 \times 10^3 \text{ S cm}^{-1}$. In previous study by Diaz *et. al.* [61] on a series of *N*-substituted pyrrole polymers, the conductivity of electrochemically prepared PPy film was 100 S cm^{-1} , where the poly-1-methylpyrrole film was five orders of magnitude less ($10^{-3} \text{ S cm}^{-1}$) and conductivity of poly-1-isobutylpyrrole film was $10^{-5} \text{ S cm}^{-1}$.

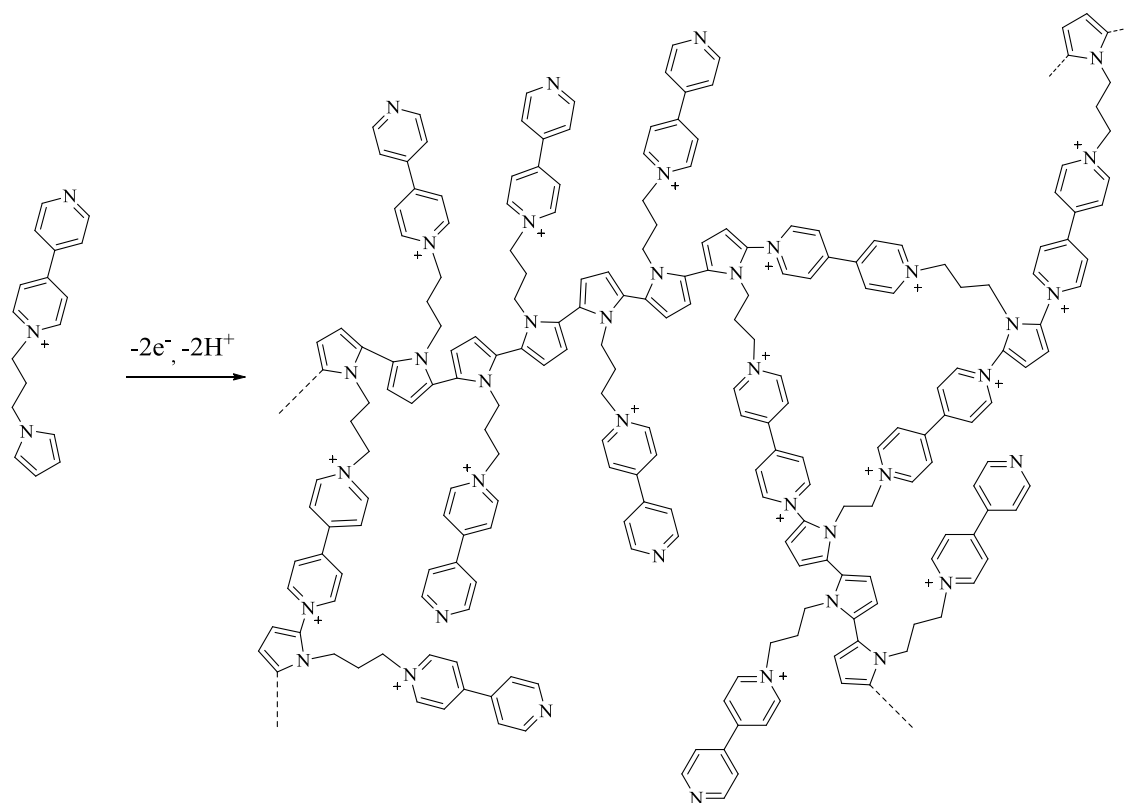
The same technique was applied for the I-V measurements of chemically prepared poly-I ($l=1.5$ mm and contact area $A= 1134 \mu\text{m}^2$), poly-II ($l=1.5$ mm and contact area $A= 1134 \mu\text{m}^2$) and poly-III ($l=1.5$ mm and contact area $A= 1134 \mu\text{m}^2$) films using FeCl_3 as an oxidizing agent. Their I-V curves are shown in appendixes F1, F2 and F3 respectively. At room temperature, the conductivity of the films of poly-I, poly-II and poly-III (using the two-terminal I-V technique) are in the range 10^{-8} to $10^{-12} \text{ S cm}^{-1}$, see table 3. These are significantly lower than the determined conductivity of PPy film prepared by the same method (86.2 S cm^{-1}).

These results obviously reflect the effect of *N*-substitution on the conductivity. The large effect on *N*-alkylation of decreasing the conductivity of the polymer has been explained as being due to the steric hindrance of the alkyl side chain in the polymer backbone which resulting in twisting from co-planarity of adjacent pyrrolyl groups. [40, 62-64] This reduces significantly the conjugation throughout the polymer chains leading to a reduction in conductivity, especially with increasing size of the substituent. The presence of the particular substituent groups used here, *N*-propyl-pyridinium, *N*-propyl-2,2'-bipyridinium or *N*-propyl-4,4'-bipyridinium in poly-I, poly-II and poly-III respectively, could be anticipated as similarly reducing the conductivity.

Polymer	σ (S cm⁻¹) @ RT
PPy	86.2
Poly-I	4.5×10^{-8}
Poly-II	2.0×10^{-12}
Poly-III	1.0×10^{-12}

Table 3. Electrical conductivity of chemically prepared polymers.

The very significantly lower conductivity of poly-II and poly-III compared to poly-I, and other *N*-substituted polypyrrole derivatives, was surprising given the similar nature of the monomers. In fact, the approximately four-orders of magnitude reduction strongly suggested the possibility of a rather different type of structure for the resulting polymers in the two different cases. Reviewing the relevant literature, work by Abruña[34] on further studies of the electropolymerisation of *N*-(3-Pyrrol-1-yl)-4,4'-bipyridinium (mono-III) indicating this to be the case. These workers suggested that the polymerisation mechanism of mono-III was more complex than previously reported.[29, 30] Based on cyclic voltammetric studies an alternative structure for the polymer was proposed (scheme 13).[34] This formed by including the possibility for nucleophilic attack at the C2- and C5-positions of the pyrrolyl moiety by the non-quaternised nitrogen of the bipyridyl unit. This additional chain extension route leads to the formation of direct pyrrolyl-bipyridinium bonds, with the introduction of saturated alkyl linkages into the polymer backbone. This obviously reduces the extended conjugation and will be expected to reduce dramatically the electrical conductivity. The electrical data is consistent with this, and also suggests that this occurs less readily in the case of mono-II compared to mono-III.



Scheme 13. Proposed mechanism for the polymerization reaction of N-(3-Pyrrol-1-yl)-4,4'-bipyridinium (mono-III).

To test this, the three polymers, poly-I, poly-II and poly-III, were studied electrochemically. Most importantly, and in support of the proposed mechanism, figure 60 shows the oxidation/reduction peaks during the electrochemical polymerisation of Mono-I, Mono-II and Mono-III. The localized redox processes of bipyridinium (quaternized) and bipyridine (nonquaternized) nitrogen in these complexes are pointed and discussed. The peaks **2** correspond to the localized redox processes of the quaternized nitrogens (**N2**) of pyridinium connected to the alkyl chain in all polymers. Two additional oxidation peaks (**1** and **3**) were enhanced upon consecutive scanning of poly-II and poly-III rather than poly-I. These two peaks have potential values of ~ 0.1 and -1.35 V respectively in both cases. Peaks **1** are attributed to the localized redox processes of nonquaternized nitrogens of bipyridine that has become quaternized by reaction with pyrrole (**N1**). This peak increased upon consecutive scanning in poly-III more than poly-II. The other peaks, **3**, correspond to the localized redox processes of nonquaternized pyridine units (bearing **N3**) of bipyridine in poly-II and poly-III.[34]

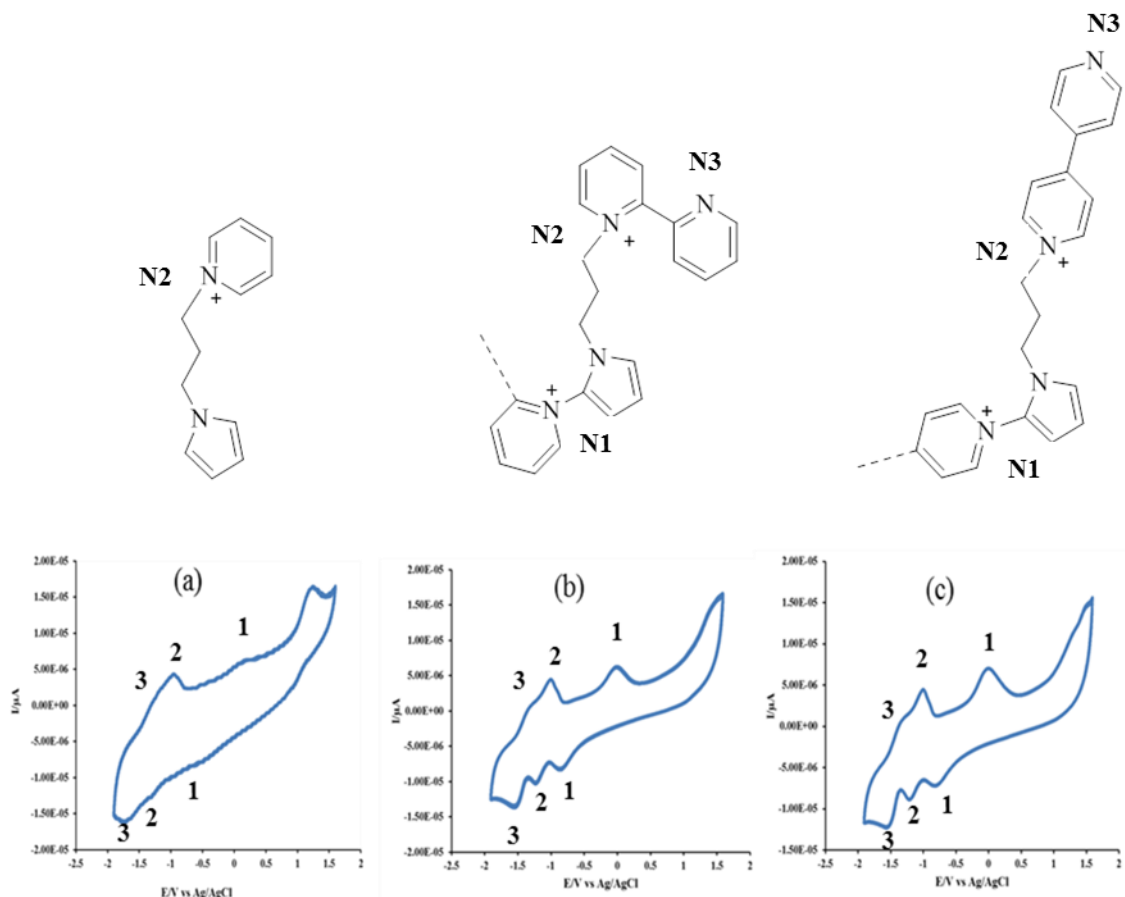


Figure 60. Cyclicvoltammograms for a platinum electrode in contact with a 50 mM of LiClO_4 /AN solution containing 0.05 M of (a) mono-I (b) mono-II and (c) mono-III at a scan rate of 100 mV s^{-1} . This figure points the oxidation/reduction peaks in each CV. The number **1** indicates the oxidation/reduction peaks of nonquaternized nitrogens of bipyridine that has become quaternised by reaction with pyrrole. Number **2** indicates the oxidation/reduction peaks of quaternized nitrogens of bipyridinium connected to N of pyrrole in the monomer. Number **3** indicates the oxidation/reduction peaks of nonquaternized nitrogens of bipyridine.

Consequently, the percentage fraction of free (nonquaternized) nitrogen of bipyridine in each case was calculated by integration of the CV peaks. This was calculated using the formula:

$$\% \text{fraction} = 100 \times \frac{Q_3}{Q_1 + Q_3}$$

Where Q_1 and Q_3 are the peak intensities of the **N1** and **N3** oxidation peaks respectively.

The % fraction of nonquaternized nitrogens of bipyridine (**N3**) in poly-II found to be 51%, where the % fraction of nonquaternized nitrogens of bipyridine (**N3**) in poly-III found to be 42%.

These results, support the proposed mechanism[34] for the polymerization reaction of mono-II and mono-III being similar and also indicate that the involvement of pyridine in the polymerization is reduced in case of mono-II compared to mono-III.

Other supporting results are provided by the XPS of N1s spectrum for poly-II and poly-III, which are shown in figure 61. Previous reports of the N1s XPS spectrum were used to assign the nitrogen configurations,[65-67] and binding energy (BE) regions of: pyridinic nitrogen (398.1-399.3 eV), pyrrolic nitrogen (399.8-401.2 eV), and quaternised nitrogen (401.1-402.7 eV) can be assigned.

In our samples, N1s spectra were calibrated versus the C1s peak which is generally set to be at 284.6 eV. Figure 61(a) shows the N1s spectrum of poly-II, which can be resolved into three main components at 399.3, 400.1, and 401.9 eV. The first peak at the lowest binding energy (at about 399.3eV) was assigned to the pyridinic (non-quaternised) nitrogen in poly-II. The second peak (at about 400.1eV) was assigned to pyrrolyl nitrogen atom. The third peak (at 401.9 eV) corresponds to the quaternised nitrogen of the bipyridinium group. Figure 61(b) shows the N1s spectrum of poly-III. This spectrum also contains three components (399.3, 399.9, and 401.4 eV) which can be assigned to the pyridinic (non-quaternised), pyrrolic, and quaternised nitrogen sites respectively. These components are similar to that observed in the case of poly-II, but in different intensities.

From these N1s XPS spectra of poly-II and poly-III, a ratio of the different types of nitrogen atoms, that is, pyridinic:pyrrolic:quaternised nitrogens, can be estimated from the ratio of the peak areas. It was found that the ratio is about 1:1:1 for poly-II and 1:3:1.5 for poly-III. These data clearly support the electrochemical data and indicate considerable fraction of the pyridinic nitrogen in poly-III is converted into quaternised nitrogen, while less is formed in the case of poly-II.

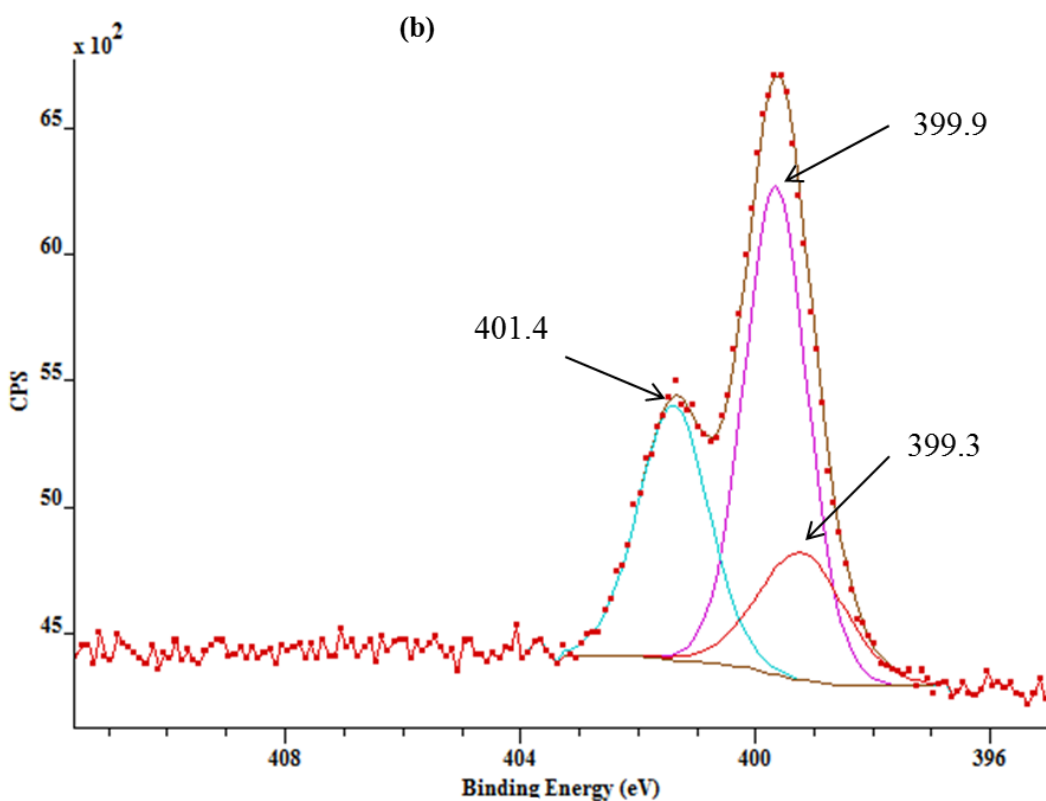
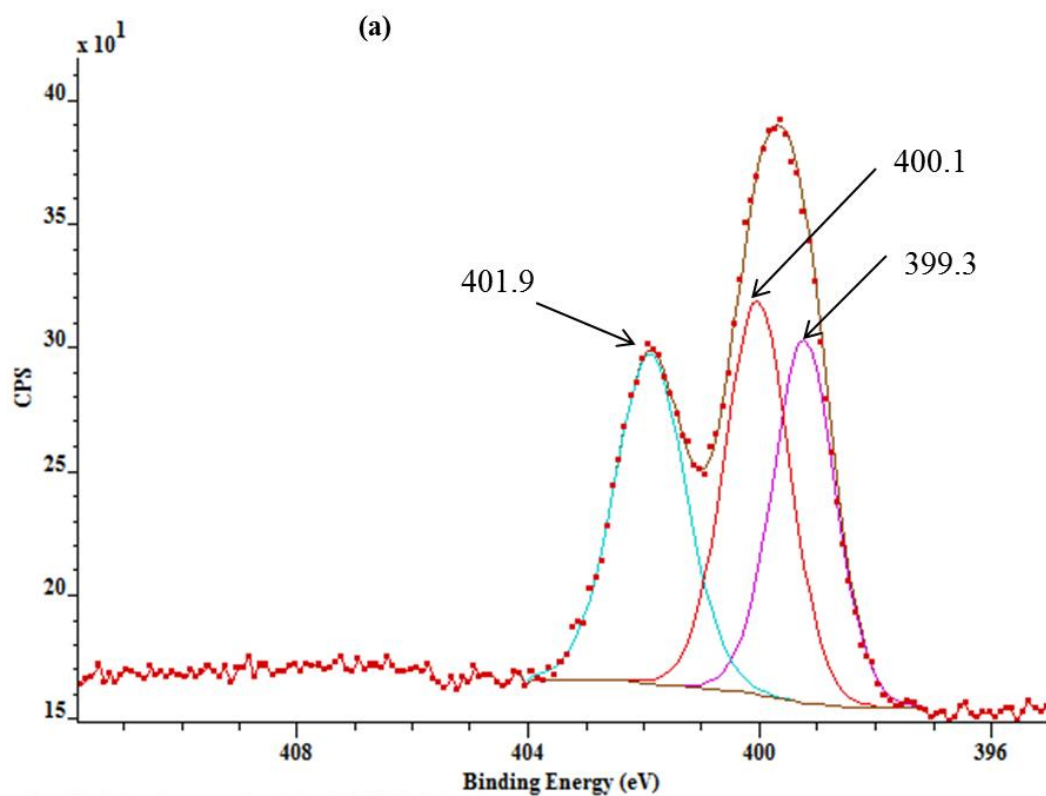


Figure 61. XPS N1s spectrum of poly-II (A) and poly-III (B) with contributions of pyridinic nitrogen, pyrrolic nitrogen, and quaternary nitrogen.

These conclusions are consistent with the proposal of direct pyrrolyl-pyridinium bond formation in poly-II and poly-III, which reduces the conjugation length of the polymer backbone. These data also help to understand the electrical data which indicated that the conductivity decreases as pyridinium-pyrrole bond formation increases. The conductivity results show poly-II has a conductivity of $2.0 \times 10^{-12} \text{ S cm}^{-1}$, which is slightly higher than the conductivity of poly-III ($1.0 \times 10^{-12} \text{ S cm}^{-1}$).

The constraints of time meant that these materials were used in the subsequent stages of the project though, particularly for the mono-III, they are not ideal as the number of non-quaternised nitrogen groups is reduced.

3.4. Summary

In this chapter, three different pyrrole-pyridine derivatives (mono-I, mono-II and mono-III) were synthesised in reasonable yields in a two-step process. First, NaH was used as a base to deprotonate pyrrole prior to alkylation using 1-chloro-3-bromopropane. Quaternisation of the pyridyl group of pyridine, 2,2'-bipyridine or 4,4'-bipyridine with 1-(3-chloropropyl)pyrrole gave the corresponding pyridinium derivatives. These were characterised by means of elemental analysis, ¹H NMR, FTIR, MS and single crystal X-ray crystallography in the cases of mono-I and mono-II. Further, these monomers were successfully polymerised using FeCl₃ as an oxidant to form three bulk polymer films of N-alkylated Pyrrole-Pyridine derivatives (poly-I, poly-II and poly-III). The polymerisation reactions of these three polymers were characterised using Uv-Vis, FTIR spectroscopy and elemental analysis. The electrical conductivity of the polymers was measured using the two-terminal technique and compared with that of PPy film prepared by same method. The results show a significant decrease in conductivity resulting for all the materials compared to PPy, but especially for the bipyridinium derivatives. The enhanced reduction in these cases is suggested as being due to the competing involvement of the non-quaternised pyridyl nitrogen in the nucleophilic attack on pyrrolyl groups in the polymerisation reaction. The extent of this is rather less in the case of the 2,2'- compared to the 4,4'-isomer.

3.5. References

1. V. Estevez, M. Villacampa and J. Carlos Menendez, Multicomponent reactions for the synthesis of pyrroles. *Chemical Society Reviews*, 2010, **39**, 4402-4421.
2. D. D. Ateh, H. A. Navsaria and P. Vadgama, Polypyrrole-based conducting polymers and interactions with biological tissues. *Journal of the Royal Society Interface*, 2006, **3**, 741-752.
3. G. P. Evans, *Advances in Electrochemical Science and Engineering*, Cambridge Life Science, Cambridge, 1990.
4. K. Kaeriyama and H. Masuda, Synthesis and properties of 3-substituted polypyrroles. *Synth. Met.*, 1991, **41**, 389-392.
5. B. Costello, P. Evans, N. Guernion, N. M. Ratcliffe, P. S. Sivanand and G. C. Teare, The synthesis of a number of 3-alkyl and 3-carboxy substituted pyrroles; their chemical polymerisation onto poly(vinylidene fluoride) membranes, and their use as gas sensitive resistors. *Synth. Met.*, 2000, **114**, 181-188.
6. S. Cosnier, A. Deronzier, J. C. Moutet and J. F. Roland, Alkylammonium and Pyridinium Group - Containing Polypyrroles, A New Class of Electronically Conducting Anion-Exchange Polymers *Journal of Electroanalytical Chemistry*, 1989, **271**, 69-81.
7. N. Clauson-Kaas and Z. Tyle, *Acta Chem. Scand.*, 1952, **6**, 667.
8. N. Elming and N. Clauson- Kaas, *Acta Chem. Scand.* , 1952, **6**, 867.
9. A. D. Josey and E. L. Jenner, *J. Org. Chem.*, 1962 **27**, 2466.
10. Z. Le, T. Zhong, Z. Xie, X. Lue and X. Cao, Green and Efficient Protocol for N-Alkylation of Benzotriazole Using Basic Ionic Liquid Bmim OH as Catalyst Under Solvent-Free Conditions. *Synthetic Communications*, 2010, **40**, 2525-2530.
11. Y. R. Jorapur, J. M. Jeong and D. Y. Chi, Potassium carbonate as a base for the N-alkylation of indole and pyrrole in ionic liquids. *Tetrahedron Letters*, 2006, **47**, 2435-2438.
12. H. Heaney and S. V. Ley, N-Alkylation of Indole and pyrrole in dimethyl sulfoxide *Journal of the Chemical Society-Perkin Transactions 1*, 1973, 499-500.
13. P. Hamel and M. Girard, Base-promoted in situ generation of methyl acrylate from dimethyl 3,3'-dithiodipropionate. Application to N-alkylation of heterocycles. *Journal of Organic Chemistry*, 2000, **65**, 3123-3125.

14. P. R. Giles, M. Rogers-Evans, M. Soukup and J. Knight, An improved process for the N-alkylation of indoles using chiral N-protected 2-methylaziridines. *Organic Process Research & Development*, 2003, **7**, 22-24.
15. R. J. Waltman and J. Bargon, Electrically conducting polymers - a review of the electropolymerization reaction, of the effects of chemical-structure on polymer film properties, and of applications towards technology. *Canadian Journal of Chemistry- Revue Canadienne De Chimie*, 1986, **64**, 76-95.
16. N. Gospodinova and L. Terlemezyan, Conducting polymers prepared by oxidative polymerization: Polyaniline. *Progress in Polymer Science*, 1998, **23**, 1443-1484.
17. J. Heinze, Electrochemistry of conducting polymers. *Synth. Met.*, 1991, **41-43**, 2805-2823.
18. W. Wang, D. Yu and F. Tian, Synthesis and characterization of a new polypyrrole based on N-vinyl pyrrole. *Synth. Met.*, 2008, **158**, 717-721.
19. G. Zotti, S. Zecchin, G. Schiavon, B. Vercelli, A. Berlin and S. Grimoldi, Poly(N-hexyl-cyclopenta c pyrrole) - A novel 1,3,4-alkyl-substituted polypyrrole soluble in organic solvents and redox conducting. *Macromolecular Chemistry and Physics*, 2004, **205**, 2026-2031.
20. B. Keita, D. Bouaziz, L. Nadjo and A. Deronzier, Surface functionalization with oxometallates entrapped in polymeric matrices .2. substituted pyrrole-based ion-exchange polymers *Journal of Electroanalytical Chemistry*, 1990, **279**, 187-203.
21. A. Deronzier and J. C. Moutet, Polypyrrole films containing metal complexes: Syntheses and applications. *Coordination Chemistry Reviews*, 1996, **147**, 339-371.
22. G. Bidan, B. Divisiablohorn, M. Lapkowski, J. M. Kern and J. P. Sauvage, Electroactive films of polypyrroles containing complexing cavities preformed by entwining ligands on metallic centers. *Journal of the American Chemical Society*, 1992, **114**, 5986-5994.
23. G. Bidan, B. Divisiablohorn, J. M. Kern and J. P. Sauvage, Electroactive films of cu(2,9-diphenyl-1,10-phenanthroline)₂ + covalently attached to polypyrrole. *Journal of the Chemical Society-Chemical Communications*, 1988, 723-724.
24. F. Daire, F. Bedioui, J. Devynck and C. Biedcharreton, Electropolymerization and redox properties of bipyridyl polypyrrole and cu(II) bipyridyl polypyrrole film electrodes. *Journal of Electroanalytical Chemistry*, 1986, **205**, 309-318.
25. A. Deronzier, J. C. Moutet and E. Saintaman, Electrocatalytic hydrogenation of organic-compounds on carbon electrodes modified by poly(pyrrole-bis 2,2'-bipyridyl

- palladium(II) complex) films. *Journal of Electroanalytical Chemistry*, 1992, **327**, 147-158.
26. L. Coche, A. Deronzier and J. C. Moutet, An Attempt at The Preparative Alkyl Dibromide Reduction using Electrodes Coated by Polypyrrole Film Containing the Viologen (4,4'-Bipyridinium) System *Journal of Electroanalytical Chemistry*, 1986, **198**, 187-193.
 27. T. Komura, K. Kijima, T. Yamaguchi and K. Takahashi, Electrostatic binding and release: incorporation of IrCl₆³⁻ into polypyrrole containing viologen groups. *Journal of Electroanalytical Chemistry*, 2000, **486**, 166-174.
 28. R. J. Mortimer, Organic electrochromic materials. *Electrochimica Acta*, 1999, **44**, 2971-2981.
 29. Q. Wu, G. D. Storrer, F. Pariente, Y. Wang, J. P. Shapleigh and H. D. Abruna, A nitrite biosensor based on a maltose binding protein nitrite reductase fusion immobilized on an electropolymerized film of a pyrrole derived bipyridinium. *Analytical Chemistry*, 1997, **69**, 4856-4863.
 30. Z. Naal, J. H. Park, S. Bernhard, J. P. Shapleigh, C. A. Batt and H. D. Abruna, Amperometric TNT biosensor based on the oriented immobilization of a nitroreductase maltose binding protein fusion. *Analytical Chemistry*, 2002, **74**, 140-148.
 31. X. Liu, H. Diao and N. Nishi, Applied chemistry of natural DNA. *Chemical Society Reviews*, 2008, **37**, 2745-2757.
 32. R. M. Stoltenberg and A. T. Woolley, DNA-templated nanowire fabrication. *Biomedical Microdevices*, 2004, **6**, 105-111.
 33. A. Houlton and S. M. Watson, DNA-based nanowires. Towards bottom-up nanoscale electronics. *Annu. Rep. Prog. Chem., Sect. A*, 2011, **107**, 21-42.
 34. K. Takada, Z. Naal and H. D. Abruna, Detailed Study of N-(3-Pyrrol-1-yl-propyl)-4,4-bipyridinium (PPB) Electropolymerization. *Langmuir*, 2003, **19**, 5402-5406.
 35. G. R. Fulmer, A. M. Miller, N. H. Sherden, H. E. Gottlieb, A. Nudelman, B. M. Stoltz, J. E. Bercaw and K. I. Goldberg, NMR Chemical Shifts of Trace Impurities: Common Laboratory Solvents, Organics, and Gases in Deuterated Solvents Relevant to the Organometallic Chemist. *Organometallics*, 2010, **29**, 2176-2179.
 36. O. Niwa, M. Kakuchi and T. Tamamura, Polypyrrole-based conducting polymer alloy-film - physical properties and film morphology *Macromolecules*, 1987, **20**, 749-753.

37. J. K. Xu, G. Q. Shi, L. T. Qu and J. X. Zhang, Electrosyntheses of high quality polypyrrole films in isopropyl alcohol solution of boron trifluoride diethyl etherate. *Synth. Met.*, 2003, **135**, 221-222.
38. A. Diaz and J. Bargon, *Handbook of Conducting Polymers*, T. A. Skotheim Ed., 1986.
39. S. Rapi, V. Bocchi and G. P. Gardini, Conducting polypyrrole by chemical synthesis in water *Synth. Met.*, 1988, **24**, 217-221.
40. R. C. King, M. Boussoualem and F. Roussel, Spectroscopic and electrical properties of 3-alkyl pyrrole-pyrrole copolymers. *Polymer*, 2007, **48**, 4047-4054.
41. J. Kim, D. Sohn, Y. Sung and E. Kim, Fabrication and characterization of conductive polypyrrole thin film prepared by in situ vapor-phase polymerization. *Synth. Met.*, 2003, **132**, 309-313.
42. L. Dong, T. Hollis, S. Fishwick, B. A. Connolly, N. G. Wright, B. R. Horrocks and A. Houlton., Synthesis, Manipulation and Conductivity of Supramolecular Polymer Nanowires. *Chem. Eur. J.* , 2007 **13**, 822-828.
43. P. LARKIN, *Infrared and Raman Spectroscopy: Principles and Spectral Interpretation*, Elsevier, USA, 2011.
44. A. R. Katritzky, C. A. Ramsden, J. A. Joule and V. V. Zhdankin, *Handbook of Heterocyclic Chemistry*, 3rd edition edn., Elsevier, Netherlands, 2010.
45. H. Kato, O. Nishikawa, T. Matsui, S. Honma and H. Kokado, Fourier-transform infrared-spectroscopy study of conducting polymer polypyrrole - higher-order structure of electrochemically synthesized film. *Journal of Physical Chemistry*, 1991, **95**, 6014-6016.
46. R. G. Davidson and T. G. Turner, An IR Spectroscopic Study of The Electrochemical Reduction of Polypyrrole Doped With Dodecyl-Sulfate Anion *Synth. Met.*, 1995, **72**, 121-128.
47. B. Tian and G. Zerbi, Lattice-Dynamics and vibrational - spectra of polypyrrole *Journal of Chemical Physics*, 1990, **92**, 3886-3891.
48. G. Han, Electrochemical growth of aligned N-chiral alkyl substituted polypyrrole micro-ribbons. *Journal of Materials Science*, 2004, **39**, 4451-4457.
49. R. J. Waltman and J. Bargon, Electrically conducting polymers: a review of the electropolymerization reaction, of the effects of chemical structure on polymer film properties, and of applications towards technology. *Can. J. Chem.*, 1986, **64**, 76-95.

50. J. P. Spatz, et al., Observation of crossover from three- to two-dimensional variable-range hopping in template-synthesized polypyrrole and polyaniline. *Physical Review B (Condensed Matter)*, 1994, **50**, 14888-14892.
51. D. Moses, A. Denenstien, A. Pron, A. J. Heeger and A. G. Macdiarmid, Specific-heat of pure and doped polyacetylene. *Solid State Communications*, 1980, **36**, 219-224.
52. A. B. Kaiser, Systematic conductivity behavior in conducting polymers: Effects of heterogeneous disorder. *Advanced Materials*, 2001, **13**, 927-932.
53. A. B. Kaiser, Electronic transport properties of conducting polymers and carbon nanotubes. *Reports on Progress in Physics*, 2001, **64**, 1-49.
54. R.S. Kohlman, T. Ishiguro, H. Kaneko and A.J. Epstein, Metallic state of polypyrrole: Effects of disorder. . *Synthetic Metals, Proceedings of the International Conference on Science and Technology of Synthetic Metals*,, 1995, **69**, 325-328.
55. H. Narayan, M. L. Hernández, J. A. Hernández, C. P. González and C. A. Ortiz, Synthesis, characterization and ac-conductivity measurements of polyaniline based composites with fly-ash and clinker. *J. Mater. Environ. Sci.*, 2012, **3**, 137-148.
56. G. Givaja, C. J. Gomez-Garcı and F. Zamora., Electrical conductive coordination polymers. *Chem. Soc. Rev.*, 2012, **41**, 115-147.
57. D. Talukdar, K. K. Bardhan, C. C. Bof Bufon, T. Heinzl, A. De and C. D. Mukherjee., Nonlinearity exponents in lightly doped conducting polymers. *Physical Review.*, 2011, **84**, 054205-054201 - 054205-054218.
58. T. A. Skotheim, *Handbook of conducting polymers* 2nd edn., M. Dekker, New York, USA, 1998.
59. T. A. Skotheim, *Handbook of Conducting Polymers : 2 Volume Set*, CRC, 2007.available at <http://NCL.ebib.com/patron/FullRecord.aspx?p=359967> Accessed 28/11/2012
60. G. Qi, L. Huang and H. Wang, Highly conductive free standing polypyrrole films prepared by freezing interfacial polymerization. *Chem. Commun.*, 2012, **48**, 8246-8248.
61. A. F. Diaz, J. Castillo, K. K. Kanazawa and J. A. Logan, Conducting Poly-N-Alkylpyrrole polymer Films. *J. Electroanal. Chem.*, 1982, **133**, 233 - 239.
62. R. D. McCullough, R. D. Lowe, M. Jayaraman and D. L. Anderson, Design, synthesis and control of conducting polymer architectures - structurally homogeneous poly (3-alkyl thiophenes) *Journal of Organic Chemistry*, 1993, **58**, 904-912.

63. D. Delabouglise, J. Roncali, M. Lemaire and F. Garnier, Control of The Lipophilicity Of Polypyrrole By 3-Alkyl Substitution *Journal of the Chemical Society-Chemical Communications*, 1989, 475-477.
64. G. B. Street, Characterization of polypyrrole. *Abstracts of Papers of the American Chemical Society*, 1983, **186**, 17-25.
65. H. Wang, T. Maiyalagan and X. Wang, Review on Recent Progress in Nitrogen-Doped Graphene: Synthesis, Characterization, and Its Potential Applications. *Acs Catalysis*, 2012, **2**, 781-794.
66. J.-P. Boudou, A. Schimmelmann, M. Ader, M. Mastalerz, M. Sebito and L. Gengembre, Organic nitrogen chemistry during low-grade metamorphism. *Geochimica Et Cosmochimica Acta*, 2008, **72**, 1199-1221.
67. K. C. Heo, K. S. Nahm, S.-H. Lee and P. Kim, Heat-treated 2,2'-bipyridine iron complex supported on polypyrrole-coated carbon for oxygen reduction reaction. *Journal of Industrial and Engineering Chemistry*, 2011, **17**, 304-309.

4. Polymer nanowire synthesis and characterisation

4.1. Introduction

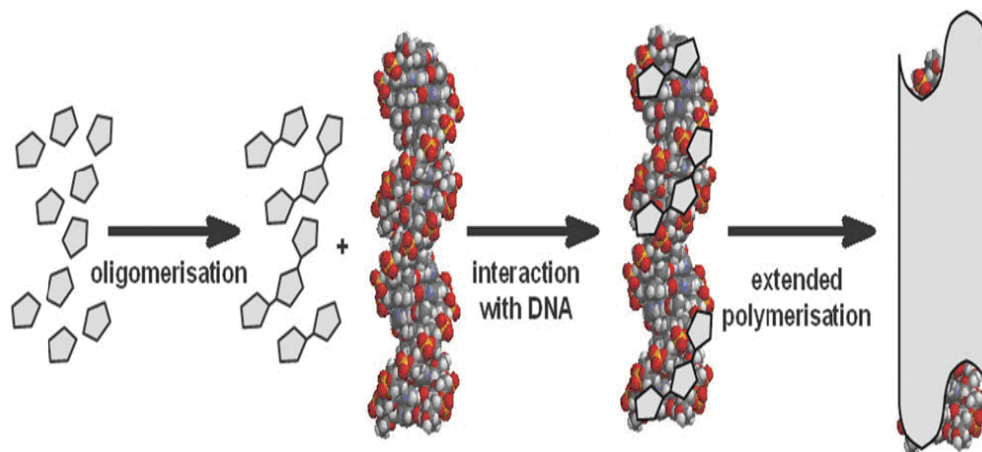
In recent years, conducting polymer nanostructures have received increasing attention in terms of both synthesis and applications.[1, 2] Due to the unique properties, arising from their nanoscale size, such as large surface area and the sensitivity of electrical conduction to perturbation,[2, 3] these materials are expected to be highly useful in different areas include nanoscale electronics, energy storage,[2] photodetectors,[4, 5] waveguides[6, 7] as well as for chemical and biological sensors.[8, 9] Another important factor here is the ability to tune the conductivity of those CPs by molecular design. The molecular nature of such materials provides a straightforward means by which to tune the electrical properties, as well as enabling functionalization through derivatisation.[3]

As with other material types there are several different methods that have been used to prepare conducting polymer nanowires. The most frequently used approach is the use of porous membrane like anodically etched aluminium oxide (AAO).[10, 11] In this method, the pores were used as templates for the synthesis of the nanostructures of the desired material.

More recently, the synthesis of polymer nanowires using DNA-templating has been shown to be effective.[3, 8, 12-16] Specific examples of DNA-templated polymer nanowires include polyaniline (PA),[17] polypyrrole (PPy)[13] and polyindole (PIn).[14] The resulting hybrid materials are considered as supramolecular polymers because they comprise both anionic DNA strands and cationic synthetic polymer.

The general concept of templating conducting polymer on DNA is outlined in the scheme14. This approach relies on non-covalent interactions oligomeric CP fragments with DNA. By adding the monomer to DNA containing solutions, the electrostatic interaction between the cationic oligomers formed upon monomer oxidation and the anionic phosphate groups in the DNA backbone organizes the growing CP along the

DNA duplex. [13]. Subsequent continued polymerisation leads to the formation of the desired polymer grown along the DNA strands. However, the reaction conditions are important to control the morphology and dimensions of the resulting material.[13]



Scheme 14. Generalised reaction sequence for the growth of nanoscale conducting polymers at a DNA template. Reproduced with permission from ref. [13].

One of the first CP to be prepared as DNA-templated nanowires was polypyrrole.[13, 18] This is a well-known conducting polymer that has attracted a great deal of interest because of its good electrical conductivity, environmental stability and easy synthesis.[3, 19, 20] It can be prepared by either chemical or electrochemical oxidation of the monomer, pyrrole, at neutral pH. For the preparation of DNA/ppy nanowires, different approaches have been explored. [13, 21] One method templating the nanowires by first depositing duplex DNA molecules onto a solid substrate support, followed by incubation with reaction mixture contains pyrrole and FeCl_3 as the oxidant. After a suitable incubation time the reaction mixture is removed. The resulting hybrid DNA/PPy nanostructures formed in this case have a beads-on-a-string morphology as measured by AFM, figure 62, a. Alternatively,[22] the reaction is most commonly performed in solution. This method provides DNA/ppy nanowires which exhibit a continuous, regular and smooth coverage, although some height variation along individual nanowires can be observed. See figure 62, b.

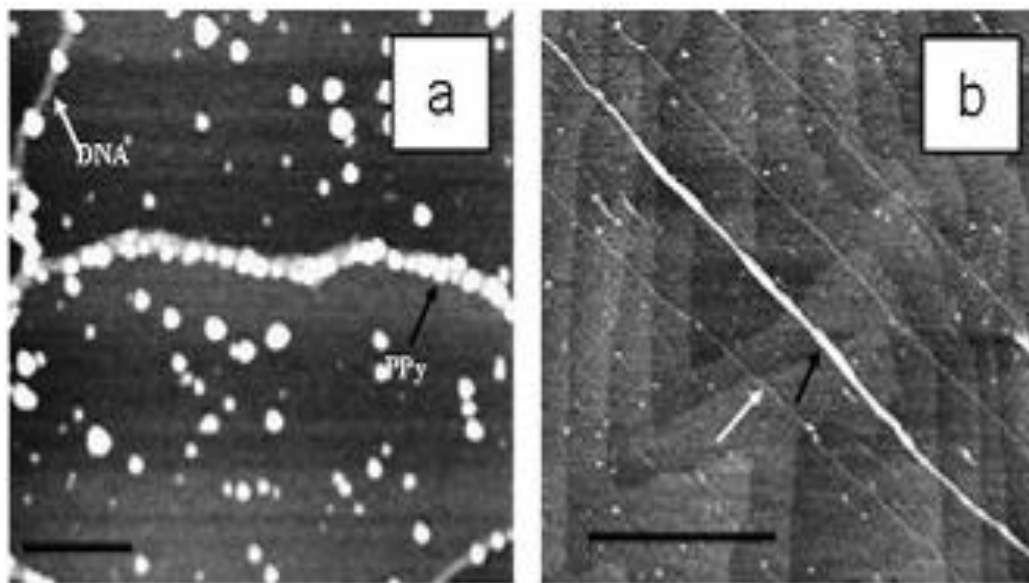


Figure 62. (a) AFM image of DNA immobilised on mica after polymerisation of pyrrole. Bar, 200 nm, height scale is 4 nm. (b) AFM image showing that material isolated from the reaction contains both bare DNA molecules (white arrow) and thicker DNA/PPy nanowire (black arrow). The nanowires are notably smooth. Bar, 1 μ m, height scale is 4 nm. Reproduced with permission from ref. [22].

Currently, there is much interest in using functionalised monomers to generate conducting polymers as novel materials for different applications such as biosensors.[20] However, for selective binding of other materials for sensing or materials assembly it is not sufficient to produce conducting structures of CP-DNA hybrid nanowires; these must also be functionalised with appropriate binding sites so as to prime them for the desired target. As stated earlier the target in this work is metal ions. In this chapter the preparation and characterisation of functionalised DNA/PPy-based nanowires is described. These are derived from the monomer units discussed the earlier chapters and are based on N-(3-Pyrrol-1-yl-propyl)-bipyridinium salts. The resulting materials, poly-I, poly-II and poly-III, have been characterized by means of Fourier transform infrared (FTIR) UV-Vis and X-ray photoelectron (XPS) spectroscopies, scanning probe microscopy (AFM, EFM, c-AFM) and two-terminal I-V measurement.

4.2. Experimental

4.2.1. Materials

All monomers, except pyrrole, were prepared as described in chapter 3. Pyrrole was purchased from Alfa Aesar and purified prior to use by distillation. The other chemicals were of Analar, or equivalent, grade and purchased from Sigma-Aldrich and used as received without further purification. Lambda DNA (λ -DNA; 500 ng μL^{-1}) was purchased from New England Biolabs, cat no. N30011S (New England Biolabs (UK) Ltd. Hitchin, HertsU.K.). All water used was passed through a deionization system (NANOpure Dlamond, Barnstead international) and had a resistivity of 18.2 MOhm cm.

4.2.2. Preparation of polymer/DNA nanowires

The method is essentially the same for all materials (poly-I, poly-II and poly-III) so a general method of preparation is given here. An aqueous solution of the monomer (5 μL , 3mM) was added to λ -DNA (20 μL , 500 ng μL^{-1}) in the presence of MgCl_2 solution (5 μL , 0.5mM). Then FeCl_3 (5 μL , 1mM) was added dropwisely into the reaction solution. The ratio of monomer/DNA was approximately 1 monomer per base pair (~46583 monomer per DNA molecule). The solution was thoroughly mixed and allowed to react at room temperature.

4.2.3. Preparation of substrates for AFM studies

For AFM analysis, n-doped Si <111> wafers were used where Si/SiO₂ wafers were used for EFM and C-AFM measurements. The wafers were cut into small pieces (1.0 cm x 1.0 cm) with a diamond tip pen, then sequentially cleaned using a cotton bud soaked in acetone, propanol and finally water, and treated with “piranha” solution (4:1 H₂SO₄/H₂O₂) for 45 minutes (Caution! Piranha solution should be handled with extreme care; it is a strong oxidant and reacts violently with many organic materials. It also presents an explosion danger).[23] This provides a highly hydrophilic surfaces rich in

OH-termini which was rinsing in DI water and dried in an oven for 15 minutes at 50 °C. In order to obtain a hydrophobic surface the Si substrate was treated with a vapour of trimethylsilane (TMS) by placing the surface (polished side facing up) on the top of a specimen bottle containing 100 µL of chlorotrimethylsilane (Me₃SiCl) for 2 min. Static contact angle measurements of the substrate before and after TMS-modification were carried out using a CAM100 system (KSV Instruments Ltd., Helsinki, Finland). The contact angle before TMS treatment was < 5° and measurements after treatment with TMS for 2 minutes typically gave contact angles between 60° and 70°.

Wetting measurements were performed using Cam-100 contact angle meter (KSV Instruments Ltd. Helsinki, Finland) using deionized water as a solvent. Mean contact angle was determined by the included software (using a Young-Laplace method) via the mounted high resolution camera.

4.2.4. Deposition of DNA-templated nanowires on substrates

The CPs/DNA nanowires were aligned on the silanized Si/SiO₂ substrates described above by “molecular combing”. [24, 25] In this process a 5 µL drop of the polymer/DNA reaction mixture was pipetted onto the surface and left for 10 seconds. The droplet was then combed on the surface using a pipette to pull the solution across the surface in one direction. Then the droplet was removed with a micropipette or by wicking with filter paper. The sample was dried at room temperature in a laminar flow hood (Model VLF 4B, Envair, Haslingden, Lancs, U.K.) to minimize contamination before being analysed.

4.2.5. FTIR spectroscopy

FTIR spectra (in the range 600-4000 cm⁻¹) were recorded in absorbance mode using a Bio-Rad Excalibur FTS-40 spectrometer (Varian Inc., Palo Alto, CA) equipped with a liquid nitrogen cooled deuterated triglycine sulfate (DTGS) detector. Data was collected at 128 scans with 4 cm⁻¹ resolution. All samples were prepared by the

deposition of approximately 10 μL of the sample solution upon a clean Si-(100) substrate and left to dry for 1 h prior to measurements. Data acquisition and analysis were carried out using Digilab Merlin version 3.1 software (Varian Inc.). A clean Si-(100) chip served as the background.

4.2.6. Atomic Force Microscopy (AFM)

Tapping Mode AFM imaging was performed in air on either a Multimode Nanoscope IIIa or a Dimension Nanoscope V (Veeco Instruments Inc., Metrology Group, Santa Barbara, CA) using TESP7 probes (n-doped Si cantilevers, Veeco Instruments Inc., Metrology Group), with a resonant frequency of 234-287 kHz, and a spring constant of 20-80 Nm^{-1} . Data acquisition was carried out using Nanoscope version 5.12b36 (Multimode IIIA) and Nanoscope version 7.00b19 (Dimension Nanoscope V) software (Veeco Instruments Inc., Digital Instruments). For both AFM systems, vibrational noise was reduced with an isolation table/acoustic enclosure (Veeco Inc., Metrology Group).

4.2.7. Electrostatic Force Microscopy (EFM)

EFM measurements were carried out in air on a Dimension Nanoscope V system using MESP probes (n-doped Si cantilevers, with a metallic Co/Cr coating, Veeco Instruments Inc., Metrology Group), with a resonant frequency of ca. 70 kHz, a quality factor of 200-260, and a spring constant of 1-5 Nm^{-1} . Data acquisition was carried out using the Nanoscope software (version 7.00b19). In EFM experiments, an electrostatic field was created between the tip and sample by applying an independently controlled bias to the sample, while the tip was grounded. More details about AFM and EFM were described in the chapter of experimental techniques (Chapter 2).

4.2.8. Conductive AFM (c-AFM)

For c-AFM measurements, in order to facilitate the alignment of nanowires, Si/SiO₂ substrates were silanized as described above (section 4.2.3). 2-3 μ L droplet of nanowire solution was placed on the silanized surface; as the droplet dries and the meniscus recedes, the nanowires at the periphery are aligned by a process similar to molecular combing.[14] A macroscopic contact can be made to the large mass of nanowires and the AFM tip can make contact to a single nanowire extending from the dried mass. Electrical contact was made by applying a drop of In/Ga eutectic to one corner of the chip and to the metallic chuck. Constant bias was applied between the tip and the sample (the tip was grounded). The c-AFM imaging was performed in contact mode, with an applied bias of 7.0 V. The resistance was estimated from the reciprocal of the slope of the I-V curve.

4.2.9. Two-Terminal Current-Voltage (I-V) measurements

Two-terminal conductivity measurements were performed using gold electrodes deposited on clean silanized Si/SiO₂ chips. The gap between each pair of Au electrodes ranged from 1 - 8 micrometers. A 2 μ L drop of an aqueous solution of Polymer/DNA nanowires was placed on these electrodes and aligned across the gap between the Au fingers by molecular combing. A Cascade Microtech Summit 11000 series probe station with Hewlett Packard semiconductor device analyzer (HP/Agilent B1500A) controlled by Agilent EasyEXPERT software were used for the I-V measurements. The nanowires device was placed inside the chamber of the probe station, which was sited on a vibration isolation table. The chamber was put under nitrogen to exclude moisture. All of the electrical measurements were carried out under nitrogen without illumination. I-V curves at various temperatures were performed on the probe station using a thermal chuck system (Model ETC- 200 L, ESPEC, Japan). For each of the electrical tests, the current was measured for applied voltages from -4 to 4 V in steps of 0.5 V.

4.3. Results and discussion

4.3.1. Nanowires synthesis

As described in chapter 3 the monomers: Py, mono-I, mono-II and mono-III can be transformed to the corresponding polymers PPy, poly-I, poly-II and poly-III by chemical oxidation using FeCl_3 . Here the results of attempts to prepare these materials as nanowires using λ -DNA-templating are presented and discussed.

The nanowires were synthesized by chemical polymerization of the monomers in the presence of DNA in a one-pot reaction [18, 26]. This process involves the addition of FeCl_3 as an oxidant to effect the polymerisation in the presence of λ -DNA as a template. This involved the use of double stranded λ -DNA to template the growth of the conducting polymers (poly-I, poly-II and poly-III) from their corresponding monomers (mono-I, mono-II and mono-III) respectively, figure 63. The scheme 15 illustrates this DNA-templating process for forming polymer nanowires. Primarily, the electrostatic interactions between the cationic CP polymer chains and the anionic phosphate groups of the DNA are considered to be important in directing the growth of the nanowires, as well as other supramolecular interactions, such as hydrogen bonding.

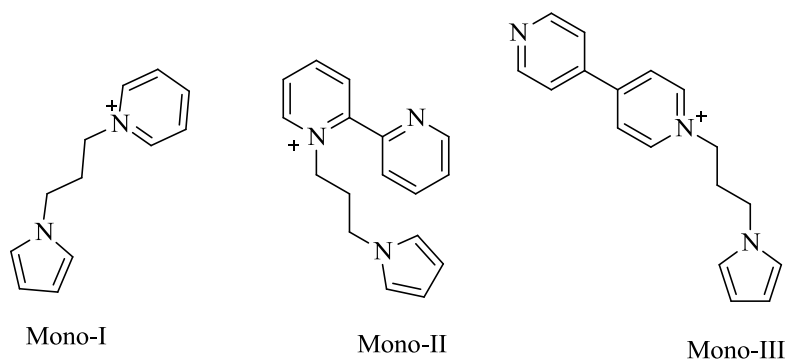
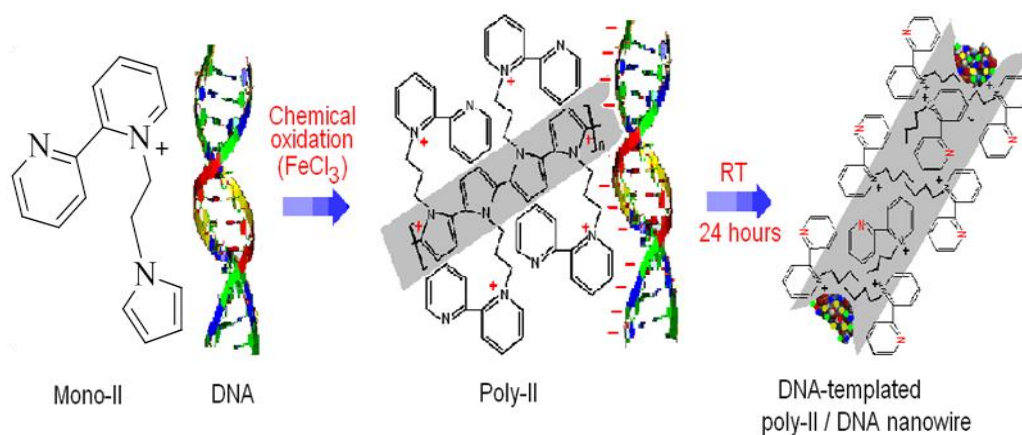


Figure 63. Monomers for the conductive templated nanowires.



Scheme 15. Formation of Polymer/DNA nanowires by self-assembly.

The synthesis of DNA/poly-I, II or III nanowires involved the addition of an aqueous solution of the appropriate monomers to an aqueous solution of DNA. The monomer-to-DNA ratio was approximately 1 monomer per base pair. The same conditions were used in each case for the four types of monomers prepared. Solution of FeCl₃ was immediately added to start the polymerisation. The solution was mixed and incubated for between 2 hours to 24 hours at room temperature. The resulting material was analysed by FTIR, AFM, EFM and I-V measurements after standing for these different reaction times.

4.3.2. *Fourier transform infrared spectroscopy investigation*

The materials isolated from the reactions solution after 2 hours of reaction time were analysed using FTIR spectroscopy. This was used in order to establish if the CP/DNA complex is formed and to assess whether it is a simple mixture or not.

- ***FTIR spectroscopy of poly-I/DNA***

Figure 64 shows the FTIR spectra in the region 4000–600 cm⁻¹ for the prepared material of poly-I/DNA as well as for the parent polymer and DNA. Table 4 presents assignments for the absorption bands for DNA and the poly-I/DNA. The broad band in Poly-I/DNA spectrum at 3300-3500 cm⁻¹ is due to bound water in DNA. The negative

feature in the difference spectrum at 3300 cm^{-1} shows that bound water has been displaced upon interaction of poly-I with DNA.[8, 14, 27] This gives a good evidence for the material involves strong interaction between the two types of polymers rather than the sample being a simple mixture.

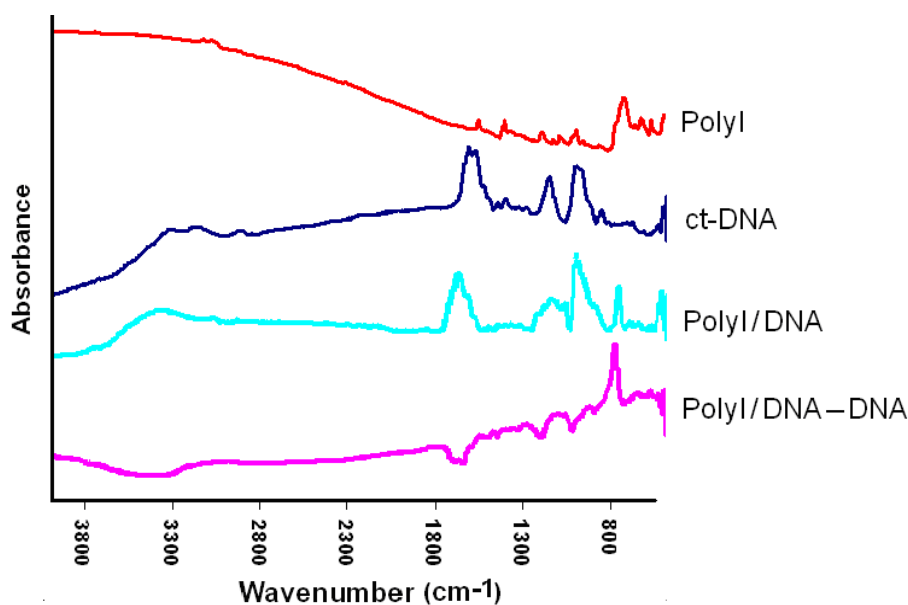


Figure 64. FTIR spectra of poly-I / DNA complex vs. controls. Infrared spectra of polyI, ct- DNA, poly-I / DNA complex and the difference spectrum (poly-I / DNA-DNA).

An expanded region of the FTIR spectra around $1800\text{--}600\text{ cm}^{-1}$ is shown in figure 65 and provided further evidence of the formation of a supramolecular hybrid polymer containing DNA and poly-I.

The fingerprint region of the spectrum of DNA itself shows two strong absorption bands at 1248 and 1096 cm^{-1} which are assigned mainly to the asymmetric and symmetric stretching vibrations of the PO_2^- groups, respectively. A shoulder on the symmetric band is also observed around 1024 cm^{-1} due to C-C stretches of the deoxyribose rings in the DNA structure.[28-31] In the poly-I/DNA complex, a significant reduction in the intensity of the asymmetric PO_2^- absorption band is observed and there is also a shift of this vibration to a lower frequency $\sim 1219\text{ cm}^{-1}$. A shift to lower frequency is also noted for the symmetric PO_2^- stretch from 1096 cm^{-1} to 1065 cm^{-1} . These spectral changes were attributed to the interaction between the PO_2^- groups of DNA and poly-I.

Significant changes in band shape and intensities reduced in the region of 1500-1700 cm^{-1} corresponding to nucleobase vibrations are also observed. These may be attributed to the interaction of polymers chains with the nucleobases, however more specific assignments of bands is difficult due to the large number of contributing vibrational modes which are difficult to assay with more certainty.

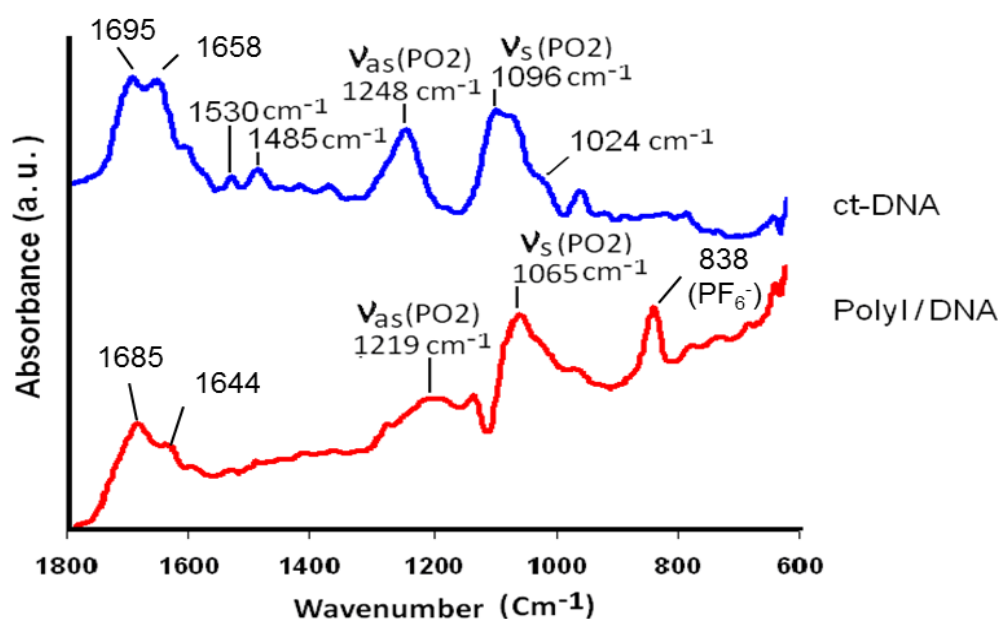


Figure 65. FTIR spectra of DNA and poly-I/DNA complex in the 600 - 1800 cm^{-1} region.

Wavenumber (cm^{-1}) in DNA	Wavenumber (cm^{-1}) in poly-I/DNA	Assignment*
1658, 1695	1644, 1685	C=O stretch of pyrimidine bases
1248	1219	PO_2^- asymmetric stretch
1096	1065	PO_2^- symmetric stretch
1024	1021	C-C stretches of deoxyribose rings.
-	838	stretching vibration of hexafluorophosphate anion (PF_6^-)

*Assignments of DNA vibration bands reference to [30, 32-34].

Table 4. Selected bands in positions and assignments in the FTIR spectrum of DNA and poly-I/DNA spectra and their assignments.

- **FTIR spectroscopy of poly-II/DNA**

The region of the FTIR spectra between 1800–600 cm^{-1} for poly-II/DNA nanowires is shown in figure 66. Significant changes in shape and intensities of the absorption bands are observed. In particular, a shift to lower frequencies and intensity changes of the asymmetric and symmetric PO_2^- stretch vibration bands is observed. These changes were attributed to interactions between the PO_2^- groups of DNA and the cationic polymer (poly-II). Also evident is the presence of the PF_6^- anion as indicated by the strong P-F stretching vibration at 835 cm^{-1} . Table 5 presents assignments for the absorption bands for DNA and the poly-II/DNA.

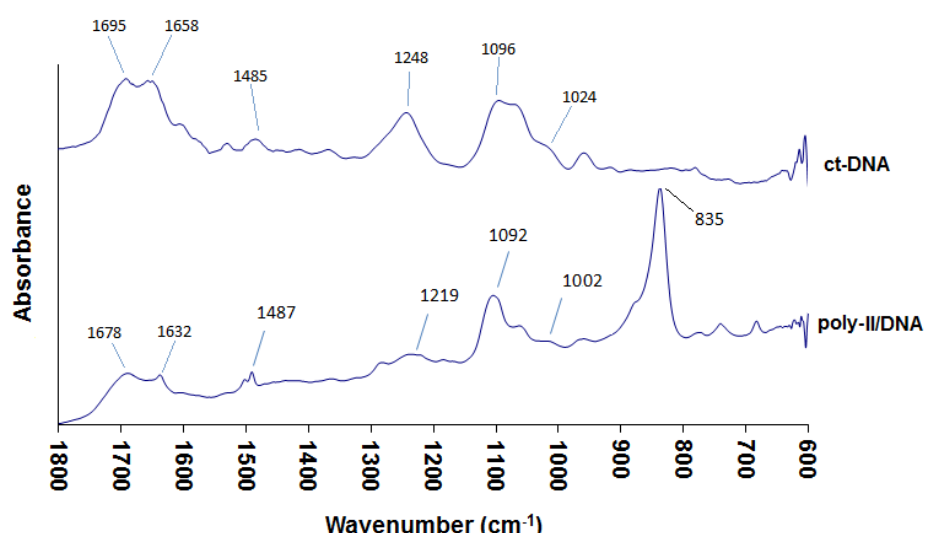


Figure 66. FTIR spectra of DNA vs the poly-II/DNA complex in the 600 - 1800 cm^{-1} region.

Wavenumber (cm^{-1}) in DNA	Wavenumber (cm^{-1}) in poly-II/DNA	Assignment
1658, 1695	1632, 1678	C=O stretch of pyrimidine bases
1248	1219	PO_2^- asymmetric stretch
1096	1092	PO_2^- symmetric stretch
1024	1002	C-C stretches of deoxyribose rings.
-	835	stretching vibration of hexafluorophosphate anion (PF_6^-)

Table 5. Selected bands in DNA and poly-II/DNA spectra and their assignments.

- **FTIR spectroscopy of poly-III/DNA**

The FTIR spectra for poly-III/DNA nanowires in the region around 1800–600 cm^{-1} is shown in figure 67. As with the other cases of poly-I and poly-II changes in the poly-III/DNA material spectrum compared to DNA itself indicate the material is not simple mixture but involves interaction between the two types of polymers. Changes in shape, intensity and position are noted particularly for the PO_2^- stretches of the backbone of DNA and the carbonyl groups of the nucleobases. Table 6 presents assignments for the absorption bands for DNA and the poly-III/DNA.

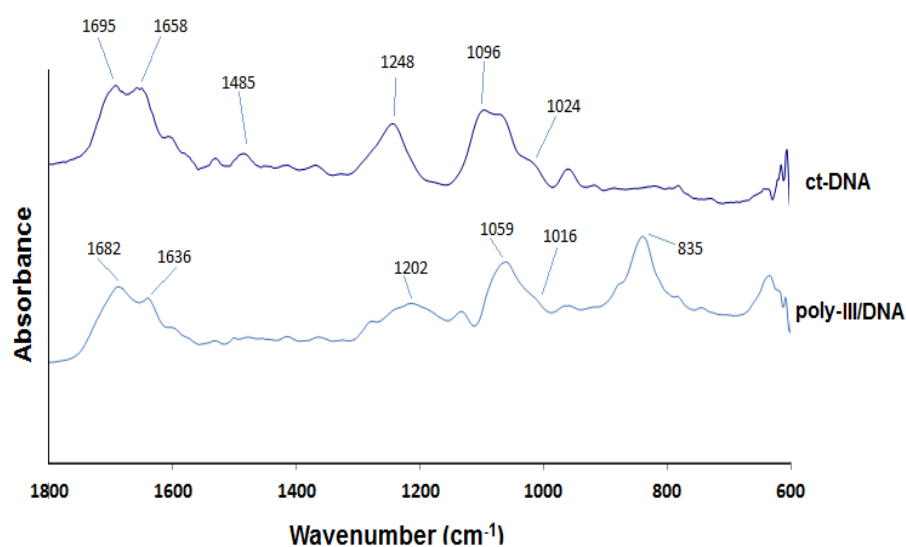


Figure 67. FTIR spectra of DNA vs the poly-III/DNA complex in the 600 - 1800 cm^{-1} region.

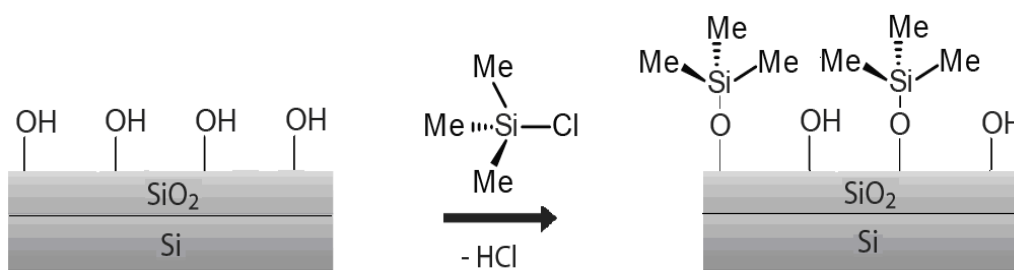
Wavenumber (cm^{-1}) in DNA	Wavenumber (cm^{-1}) in poly-III/DNA	Assignment
1658, 1695	1636, 1682	C=O stretch of pyrimidine bases
1248	1202	PO_2^- asymmetric stretch
1096	1059	PO_2^- symmetric stretch
1024	1016	C-C stretches of deoxyribose rings.
-	835	stretching vibration of hexafluorophosphate anion (PF_6^-)

Table 6. Selected bands in DNA and poly-III/DNA spectra and their assignments.

4.3.3. AFM characterisation of poly-I/DNA nanowires:

For AFM characterisation, the Si/SiO₂ substrate surface used as supports for depositing the materials was treated with chlorotrimethylsilane, Me₃SiCl, (TMS) vapour for 2 -10 minutes to assist with alignment of the nanowires. A hydrophobic methyl-terminated monolayer is formed due to the reaction between hydroxyl-terminated SiO₂ and Me₃SiCl, scheme 16. This increases the water contact angle and reduces the surface wettability. The resulting hydrophobic surface inhibits the adsorption of the Polymer/DNA nanowires and this allows imaging of individual structures more easily. Previous studies[23, 26] have shown that the density of nanowires deposited on the substrate was controlled by adjusting the hydrophobicity of the substrate by increasing the extent of silanization; hydrophobic surfaces favour the adherence of fewer wires, and hydrophilic surfaces adsorbed a higher density.

The contact angle measurements[18] were carried out on a droplet of DI water on Si/SiO₂ surface which was treated with Piranha solution, then modified with TMS as described in section 3.2.4. The increase of contact angle indicated successful modification of the oxide surface.



Scheme 16. TMS modification of silicon substrates

AFM images provide a convenient method to observe the DNA templating of the polymer nanowires. This technique can detect the thickening of the strands as the polymerization process proceeds. The apparent height of bare DNA molecules is typically ≤ 2 nm, whereas the templated polymer nanowires are substantially thicker (>2 nm). As controls, bare DNA, were studied initially by AFM. A drop (3 μ L) of ct-DNA solution (1 mg/ml) was deposited on silanized Si/SiO₂ substrates. After 10 seconds the

drop was dragged across the surface using a pipette to align the DNA across the surface. The surface tension at the moving air/water interface is sufficient to stretch the molecules in the direction of movement.[8] A typical AFM image shown in figure 68, is dominated by DNA strands with height in the range 1.0 - 2.0 nm (blue and green crosses respectively). There are some larger structure heights, up to 8.0 nm (red cross) but these have a much lower frequency. It is suggested that these large structures arise from bundling of the DNA molecules when deposited on the substrate from solution.[18, 23]

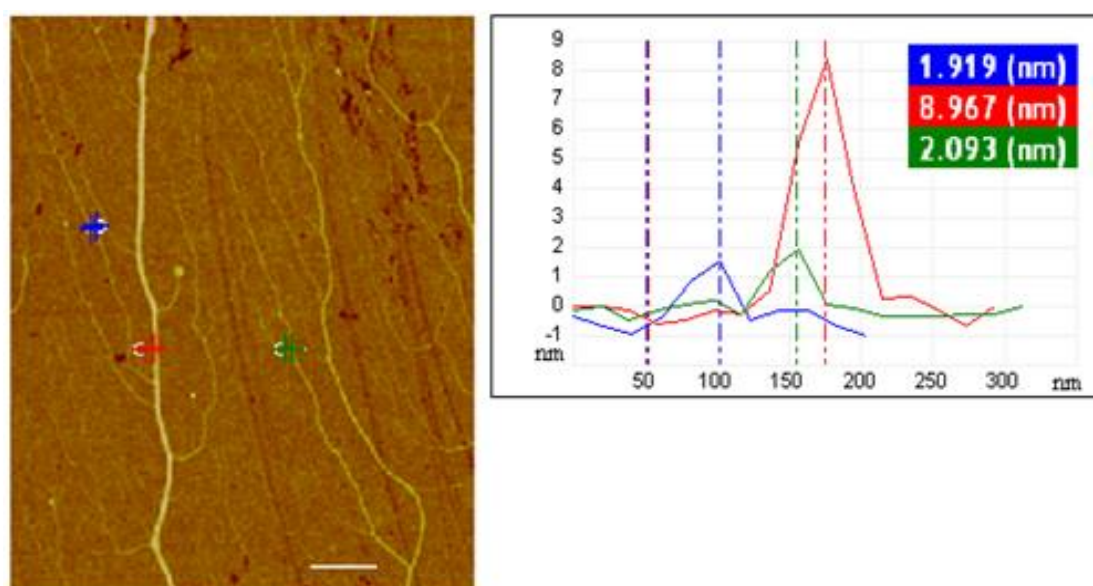


Figure 68. AFM image of ct-DNA deposited onto TMS-modified Si/SiO₂ surface. Blue and green crosses highlight DNA strands with heights of 1.0 nm and 2.0 nm respectively. Red cross highlights an example of some larger structure heights, up to 8.0 nm. Scale bar = 500 nm, height scale = 20 nm. The inset shows a typical height cross section at various points in the image.

Samples of poly-I/DNA nanowires were isolated and aligned on Si/SiO₂ substrates 2 and 24 hours after the addition of oxidant to start the nanowires synthesis. Generally the AFM images show the formation of continuous, regular and smooth poly-I/DNA nanowires after 2 hours of incubation. In the image shown in figure 69 a number of poly-I/DNA nanowires can be observed, along with smaller structures that are assigned as bare DNA molecules. The latter are recognized as they have an average diameter of about 1-2 nm, green circled, and indicates that not all the DNA template is used in the reaction. The red circled wire has a larger diameter (average ~ 7 nm), while the blue

circled wires show much larger average diameter (~ 17 nm) contain some lumps along their length. These are attributed to poly-I/DNA nanowires.

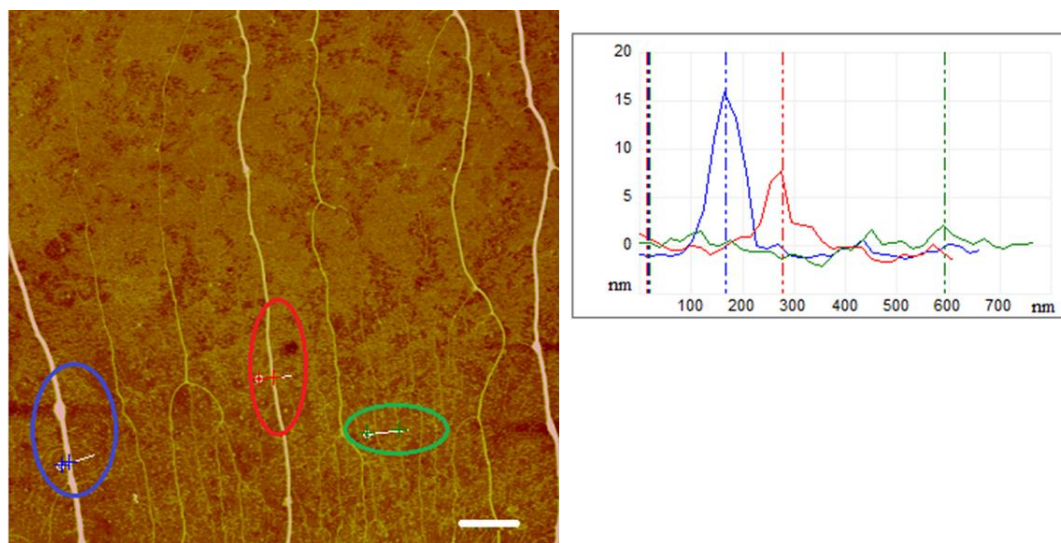


Figure 69. Tapping Mode AFM height image of a section of poly-I/DNA nanowires aligned on Si/SiO₂ substrate modified with TMS, observed 2 hrs after preparation, Scale bar = 1 μ m, height scale = 20 nm, and inset shows a typical height cross section of the nanowires.

A statistical analysis of heights of ~ 100 λ -DNA structures before and after poly-I templating is shown in figure 70. The peak height of bare DNA is observed to be 1.0 – 2.0 nm. Some larger heights of about 3.0 nm and even larger are observed in much lower frequency and these are again attributed to bundling of DNA molecules, leading to a small number of DNA ropes aligned upon the substrate.

The distribution of poly-I/DNA nanowire heights measured 2 hours after initiation of the reaction shows that the poly-I deposition results in a spread of structure sizes within the range 2.0-18.0 nm, with an average diameter of ~ 9.0 nm. The common sized structures with a modal diameter of 9.0-11.0 nm. A small number of larger height structures, up to 31 nm, is observed but at much lower frequency.

It is also apparent from the histogram that some peak values observed at 2.0-3.0 nm, which represent some bare DNA strands. This indicates that not all the DNA in the reaction is involved in templating.

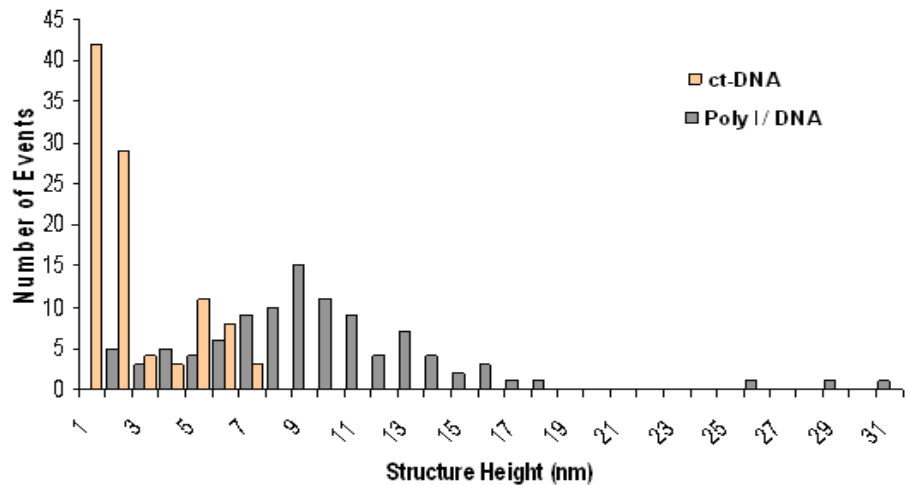


Figure 70. Height distribution of 100 λ -DNA molecules before and after treatment with poly-I, measured after 2 hours of reaction time. The heights were determined from Tapping Mode AFM images.

AFM images taken 24 hours after initiating the reaction show thicker nanowires with a measured heights (corresponding to the nanowire diameter) typically in the 15 – 25 nm range. Again some larger structure heights, up to 35 nm (blue circle) were also observed but these are with lower frequency, figure 71.

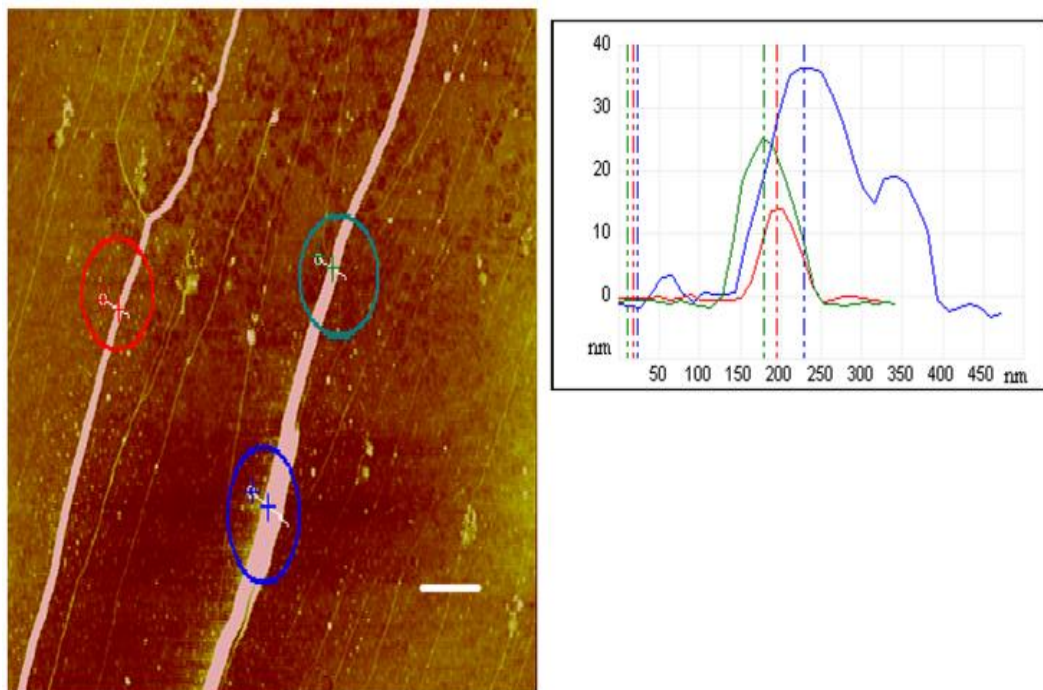


Figure 71. Tapping Mode AFM height image of a section of poly-I/DNA nanowires aligned on TMS-modified Si/SiO₂ substrate modified with TMS, observed 24 hrs after initiation of reaction, Scale bar = 1 μ m, height scale = 20 nm, and inset shows a typical height cross section of the nanowires.

Longer incubation time (up to 15 days) resulted in thicker structures where individual nanowires with diameters of 5 – 10 nm, were found to combine together to form ropes with an average diameter up to 50 nm, figure 72. As evidenced by AFM studies, this behaviour has been observed previously for DNA-templated polypyrrole nanowires[14] and it is suggested that this is, at least in part, due to hydrophobic interactions of the conducting polymer allied with the charge on the DNA being compensated by the cationic conductive polymer.

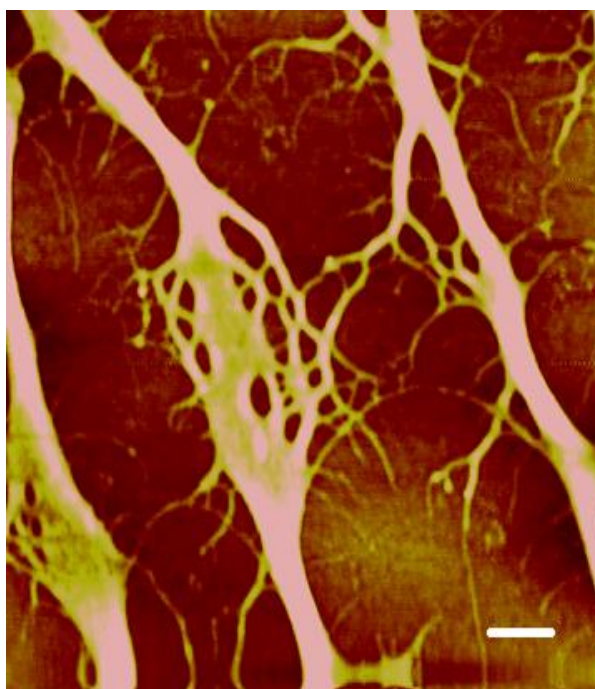


Figure 72. Tapping Mode AFM height image of a section of a poly-I/DNA nanowires aligned on Si/SiO₂ substrate modified with TMS, observed 15 days after initiation of the reaction, Scale bar =200 nm, height scale = 20 nm.

An interesting comparison of poly-I/DNA with PPy-DNA system is that the DNA templates covered by poly-I are smoother and more uniform along the length than the DNA templates covered by ppy. Figure 73 shows AFM images of poly-I/DNA (73. a) and ppy/DNA (73. b) nanowires aligned on Si/SiO₂ substrate modified with TMS, observed 24 hours after initiation of the reaction. The uniform diameters and defect-free surfaces of poly-I/DNA nanowires are clearly visible in the surface plot shown on Figure (73. c), while (73. d) shows greater variation in diameters of the ppy/DNA nanowires. The height variation of the line trace along around 5 μ m on poly-I/DNA nanowire (73. e) shows a minimum height of ~ 18 nm and maximum height of ~ 25 nm.

This gives a variation in height of about 7 nm. But the height variation along around 5 μm on PPy/DNA nanowire (73. f) shows a minimum height of ~ 15 nm and maximum height of ~ 45 nm, with a variation of about 30 nm. So, the line trace of particular single poly-I/DNA nanowire provides comprehensive profile of more uniformity of poly-I/DNA nanowire than PPy/DNA nanowire.

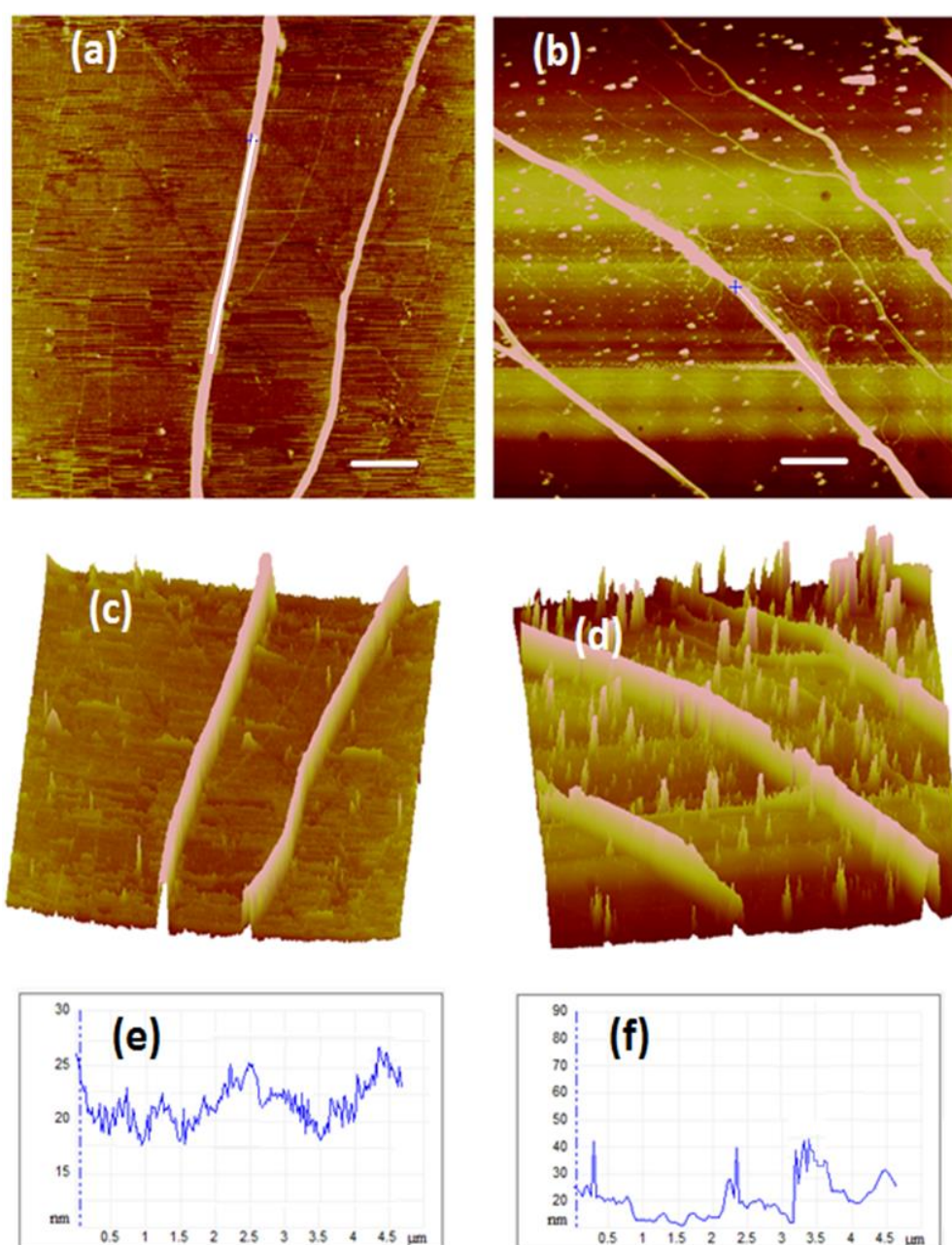


Figure 73. Tapping Mode AFM height images of (a) poly-I/DNA and (b) PPy/DNA nanowires immobilized upon a Si/SiO₂ substrate, modified with a TMS. Scale bar= 1 μm , height scale=20 nm. (c) and (d) showing the corresponding surface plot of (a) and (b) respectively. (e) and (f) are the corresponding line trace of particular nanowires in (a) and (b) respectively.

Another estimation of the uniformity of a single nanowire diameter can be made by the formula[35]:

$$Du = \Delta D/l$$

Where: Du is diameter uniformity of the nanowire, ΔD is the maximum diameter deviation from the diameter at the centre of the nanowire (D_c) and l is the length of the nanowire.

For a single poly-I/DNA nanowire (the largest nanowire shown in figure 73(a)):

With $l = 5.0 \mu\text{m}$, $D_c = 25.0 \text{ nm}$ and $\Delta D = 30.0 - 25.0 = 5.0 \text{ nm}$.

$$Du = 5/5000 = 1 \times 10^{-3}$$

For a single ppy/DNA nanowire (the largest nanowire shown in figure 73(b)):

With $l = 5.0 \mu\text{m}$, $D_c = 23.0 \text{ nm}$ and $\Delta D = 38.0 - 23.0 = 15.0 \text{ nm}$.

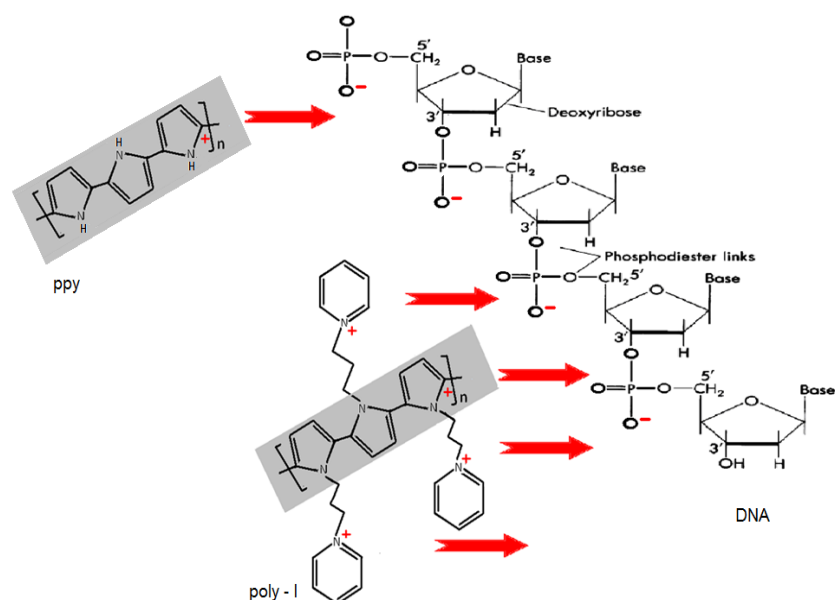
$$Du = 15/5000 = 3 \times 10^{-3}$$

The previous calculations indicate that both nanowires show high uniformity, while poly-I/DNA nanowire is the more uniform.

Another notable difference between poly-I and PPy is the lower level of particles on the substrate surface in the former case compared to the latter. Figure 73 shows a relatively high level of nonspecific deposition of PPy particulates which are observed across the substrate surface(73.b) (mean estimated to be ca. 10 particles/ μm^2). Nonspecific poly-I particulates are also present upon the substrate (73.a), but at a significantly lower density (ca. 2 particles/ μm^2).

Studies [36, 37] suggest that electrostatic interaction between the negatively charged DNA and the positively charged CPs surfaces depends on the positive charge density on the polymer backbone. This is in addition to many other aspects such as the effect of pH, ionic strength, the nature of buffer solution and the nature of the counterion incorporated during the chemical synthesis. Since all the latter aspects are similar in both preparations (PPy/DNA and poly-I/DNA), so the higher charge density of poly-I compared with ppy leads to stronger electrostatic interaction between the cationic poly-I and anionic phosphate groups of DNA, consequent for a cleaner substrate surface. Scheme 17 shows that each pyrrolyl-ring in the main chain of poly-I bears a cationic pyridinium ring. So, a total of four positive charges per three pyrrole units in the

backbone of poly-I can be expected based on typical oxidation levels. But in an equivalent level of oxidation for ppy, only one positive charge per three pyrrole units is present along the polymeric chain. This difference in charge density leads to an effective stronger interaction in poly-I/DNA hybrid which leads to lower level of non-specific particles on the substrate surface.



Scheme 17. Diagram shows the higher cationic charge of poly-I compared to equivalently oxidized PPy. These stronger interactions produce less non-specific polymer formation as judged by AFM.

4.3.4. *Electrostatic force microscopy (EFM) investigation of polyI/DNA nanowires:*

EFM is used as a qualitative method to demonstrate the conductive nature of nanostructures such as CP/DNA nanowires.[18, 38] It has also been referred to as “scanned conductance microscopy” (SCM) when used to detect conductive objects on a dielectric film through their effect on the capacitance between the tip and the substrate. (Chapter 2 provides details of this technique). One of the advantages of using this technique is that it is a non-contact form of scanning probe microscopy and so does not damage the sample under investigation nor require contact to be made to the object, which can be difficult.[39] EFM measurements for the as-prepared nanowires were

carried out in air on a Dimension Nanoscope V system where an electrostatic field was created between the tip and sample by applying a controlled bias to the sample, while the tip was grounded.

Topographic AFM and EFM images of Poly-I/DNA nanowires are acquired simultaneously. Figure 74(a) shows AFM image which reveals a mixture of bare DNA molecules (height from 1 to 3 nm) and poly-I/DNA nanowires (heights from 4 to 17 nm). The electrical conductivity of poly-I/DNA nanowires was demonstrated by monitoring the phase shift in EFM experiment. The corresponding EFM image at +6 V is presented in figure 74(b). The nanowires appear as dark lines in the scanned conductance images; this corresponds to a negative phase shift as the tip crosses the nanowire and demonstrates the existence of charge conduction in the wire. As shown by previous workers,[18] negative phase shifts (with respect to the background) are only observed when imaging one-dimensional structures that are conductive.[40] Figure 74(b) shows some nanowires, e.g. wire “A”, which are continuous with no breaks in the conduction.

The presence of non-fully formed wires is also indicated, red circled parts, which indicates that some parts of the structure are partially covered by the polymer. Some DNA molecules also shown in this image, e.g. “B” and “C”; which are non-conductive as judged by their positive phase shift. The positive phase shift also suggests the presence of static charges as a result of the combing process[18]. The negative phase shift of the nanowires, e.g. “A”, is wider than the nanowire itself compared to the ordinary AFM image because of the long range electric interaction.[41, 42]

The profile of the phase shift along a cross section of the nanowire has a W-shape, figure 74(c). This has been observed for other semiconducting and polymers materials. [14, 41-43]

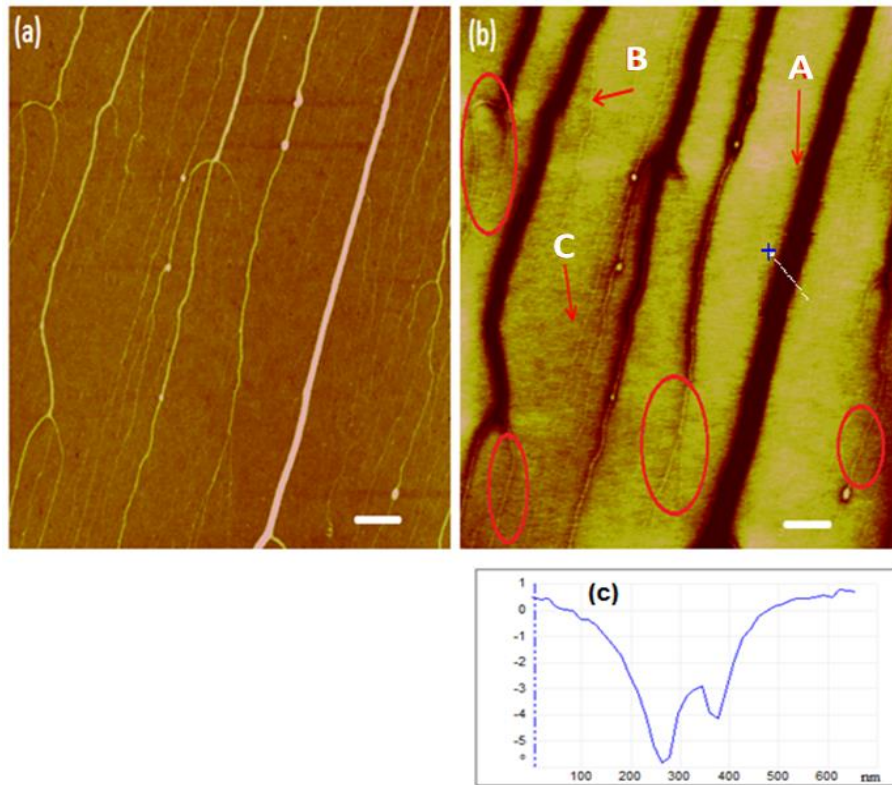


Figure 74. (a) AFM image of poly-I/DNA nanowires on SiO₂/Si surface, observed 24 hrs after preparation, scale bar is 500 nm, height scale=20 nm. (b) EFM phase image of the same nanowires at a tip/sample bias of +6 V and lift height of 60 nm. (c) The corresponding profile of the phase shift along a cross section of the nanowire at a diameter of 17 nm.

Since EFM is also sensitive to trapped charges, the quadratic variation of phase shift with bias voltage is a useful test that the data observed are due to conductance effects rather than trapped charge or topography.[14] The expected parabolic dependence of phase shift on bias for voltages between -10 and +10 V was observed, (figure 75). This confirms the phase shift is due to the scanned conductance effect rather than the trapped charge effect, which produces phase shifts that depend linearly on bias voltage.[44] It also been seen from figure 75 that the magnitude of the phase shift is dependent on the size of the nanowire. This reflects the change in capacitance of the tip/nanowire/substrate system as the wire diameter increases. Quantitative calculations of the phase shift as a function of nanostructure diameter are described in references[45].

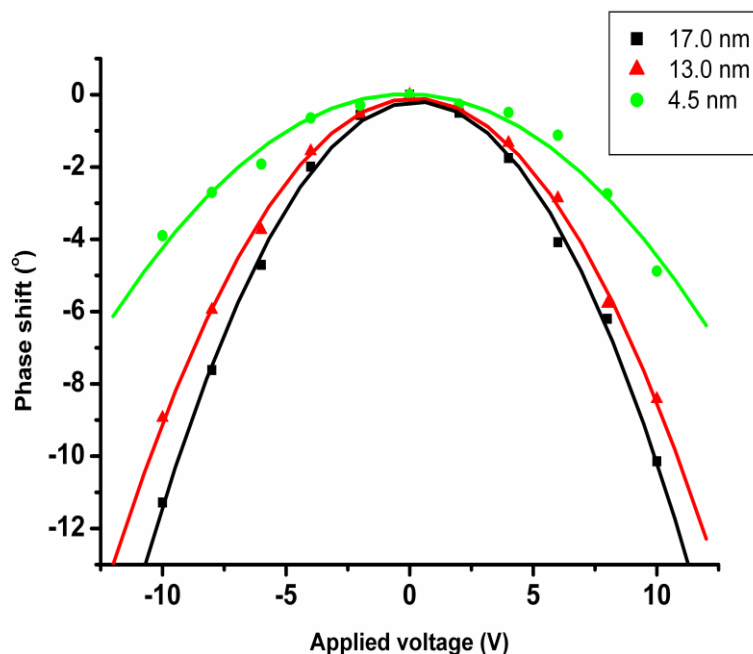


Figure 75. Phase shift versus tip sample bias of poly-I/DNA nanowires with different diameters 17, 13, and 4.5 nm.

4.3.5. Conductive atomic force microscopy (c-AFM) of polyI/DNA nanowires:

Conductive atomic force microscopy (c-AFM) can provide direct quantitative electrical characterization as well as surface topography of individual nanowires by using a metallized tip to contact the nanowire.[46, 47] c-AFM measurements of poly-I/DNA were performed on individual nanowire located on hydrophobic Si/SiO₂ substrate with 200 nm thickness of SiO₂ layer. The dense mass of nanowires served as one electrical contact. The other contact was the tip of the metal-coated cantilever, figure 76.

In order to measure the conductance and estimate the conductivity of the nanowires, a drop (2 - 3 μ L) of solution was drop-cast onto Si/SiO₂ substrates. By dragging the drop to one edge of the substrate and leaving to dry, a few nanowires stretch out along the substrate surface. From the several such nanowires at the edge of the dense network, the

tip was placed on a single nanowire. The network was connected to the metallic chuck using a drop of In-Ga eutectic.

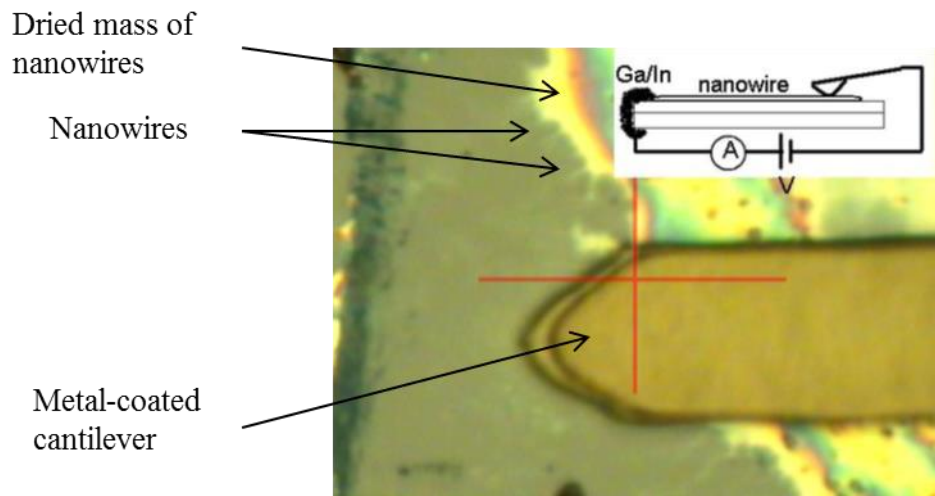


Figure 76. Optical image of AFM cantilever and nanowires. Inset; Schematic illustration of the experimental c-AFM set-up.

PPy/DNA nanowires were used as a reference for the measurement of c-AFM for poly-I nanowires. The c-AFM images of a PPy/DNA nanowire with a diameter of 20 nm were recorded with a bias of 7.0 V applied between the cantilever and the metallic chuck. Figure 77 shows C-AFM measurements of PPy/DNA nanowires aligned on a SiO₂/Si substrate. The usual contact mode height image (figure 77(a)) shows the presence of several nanowire. The mean diameter of the measured nanowire was 20 nm. Figure 77(b) provides slightly clearer image of the deflection error, which is the difference between the measured deflection and the setpoint. The current image, figure 77(c), shows the associated current on the nanowires with a bias of 7.0 V applied between the cantilever and the metallic chuck. The bright contrast indicates an electrical current in the order of Nano-amps passing through the nanowire, thus confirming its electrical conductivity.

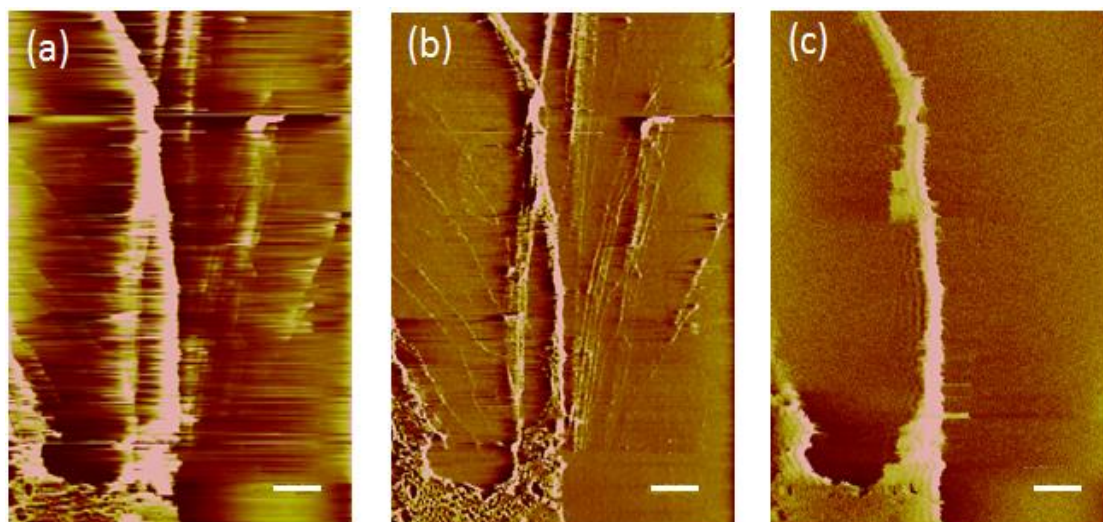


Figure 77. C-AFM of ppy/DNA nanowire aligned on a Si/SiO₂ (200nm) substrate (a) Contact mode image, the datascale corresponds to a height of 60 nm; (b) Deflection error image (the data scale corresponds to a height of 20 nm) and (c) c-AFM current image (the datascale corresponds to a current of 100 nA). The tip-sample bias was 7.0V; the images (a)-(c) were acquired simultaneously. Scale bar 500 nm (a-c).

Essentially, zero current was observed when the tip was on a clean area of Si/SiO₂ surface, but currents were observed when the tip was in contact with the nanowire. After collecting an image, the closed loop positioning system of the Nanoscope V was used to touch the nanowire at defined points along its length and an I-V curve was recorded at each point over the range of -4 to 4 V at deflection set point 0.5V. The slope of this I-V curve was used to estimate the conductance of the nanowire circuit. Figure 78 shows a plot of the resistance as a function of the relative distance, *d*, of the tip along the nanowire in the direction away from the mass deposit of PPy/DNA at set point voltage of 0.5 V. The circuit resistance increases in a linear manner with the distance.

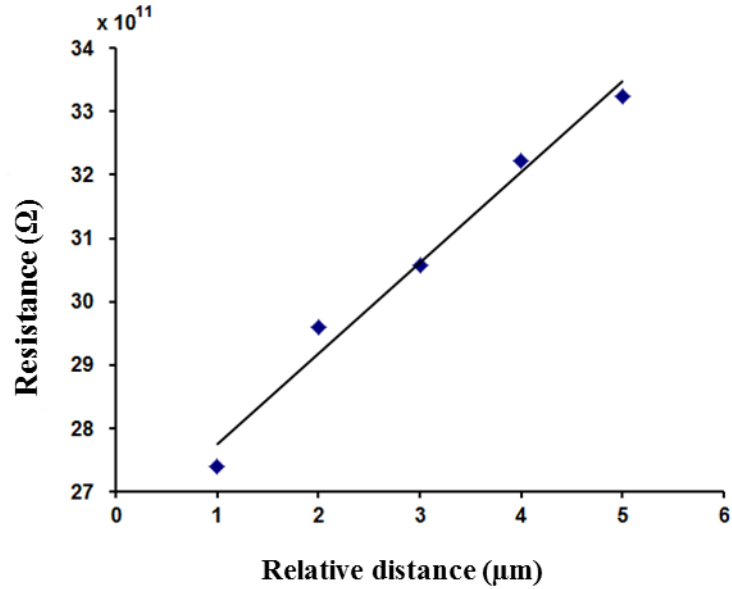


Figure 78. PPy/DNA nanowire resistance as a function of tip-contact relative distance in c-AFM measurements. Sample bias = 7.0 V at 0.5 deflection set point.

The slope of this linear fit gives the resistance per unit length of the PPy/DNA nanowire = $1.0 \times 10^{11} \text{ } \Omega \text{ cm}^{-1}$. Moreover, by using the diameter (20 nm) and the width (150 nm) of the nanowire to calculate the cross-section area, the nanowire conductivity was calculated to be approximately $2.1 \times 10^{-1} \text{ S cm}^{-1}$. This is more conductive than for ppy/DNA nanowires ($2 \times 10^{-3} \text{ S cm}^{-1}$) reported previously[18] using the same preparation and characterisation methods. But it is significantly less conductive than (86 S cm^{-1}) determined by two terminal I-V measurements at room temperature, for bulk ppy film prepared chemically using FeCl_3 as oxidant (chapter 3).

Using the same method as described above, sample of poly-I/DNA nanowire aligned on a Si/SiO₂ substrate (SiO₂ thickness = 200 nm) were analysed. Figure 79 shows simultaneously acquired images of Contact mode, deflection error, and c-AFM current image.

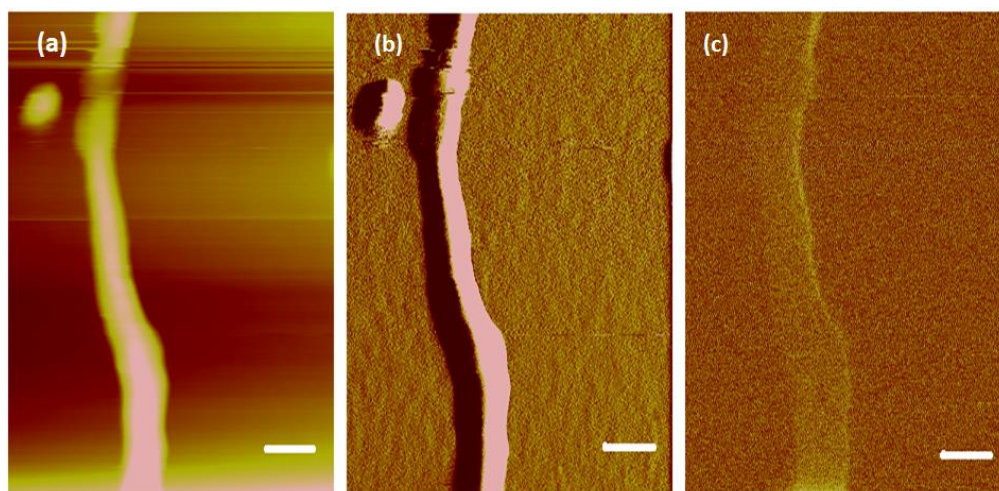


Figure 79. C-AFM of poly-I/DNA nanowire aligned on a Si/SiO₂ (200nm) substrate (a) Contact mode image, the datascale corresponds to a height of 60 nm; (b) Deflection error image (the data scale corresponds to a height of 20 nm) and (c) c-AFM current image (the data scale corresponds to a current of 100 nA). The tip-sample bias was 7.0V; the images (a)-(c) were acquired simultaneously. Scale bar 500 nm (a-c).

The mean diameter of the nanowire was measured by the AFM to be 25 nm. I-V curve was recorded over the range of -4 to 4 V at deflection set point 0.5V. Figure 80 shows that the circuit resistance increases in a roughly linear manner with distance. The slope of the line gives the resistance per unit length of poly-I/DNA nanowire as $1.0 \times 10^{12} \Omega \text{ cm}^{-1}$. Based on the measured diameter (25 nm) and width (170 nm) of the nanowire, the conductivity was estimated to be $2.0 \times 10^{-2} \text{ S cm}^{-1}$. This is less conductive compared with ($2 \times 10^{-1} \text{ S cm}^{-1}$) for PPy/DNA nanowire reported above.

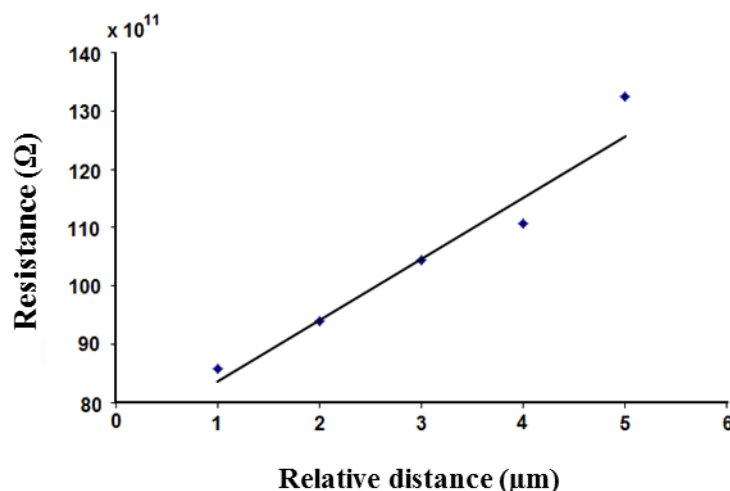


Figure 80. Poly-I/DNA nanowire resistance as a function of tip-contact relative distance in c-AFM measurements. Sample bias = 7.0 V at 0.5 deflection set point.

4.3.6. Two terminal I-V measurements of PPy/DNA and polyI/DNA nanowires:

Further characterisation of the electrical properties of CPs/DNA nanowires involved two terminal I-V technique. This technique is extremely useful as the temperature dependence of the conductivity can be readily determined. Most CPs show an increase in conductivity with temperature [48-50]. However, the temperature dependence might be affected by many factors such as the polymer structure, degree of crystallinity, and dimensionality.[51, 52]

For direct two-terminal I-V characterization of the as-prepared nanowires, Au electrodes on Si/SiO₂ chips have been used. Figure 81 schematically shows the arrangement which features two small gold fingers which provide the direct contacts to the nanowires, and the two large gold pads serve as contacts for macroscopic probes for measurement of the system.

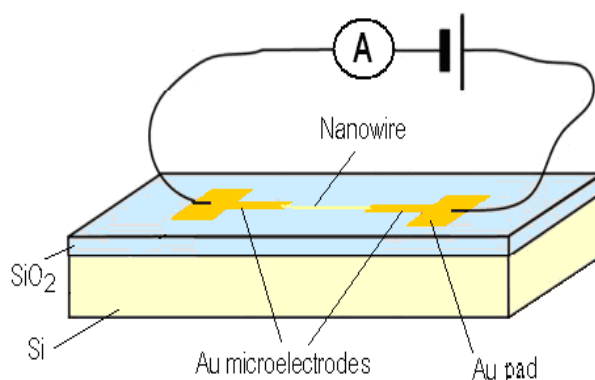


Figure 81. Schematic diagram of two-terminal conductivity measurements apparatus.

This device can be fabricated by using molecular combing to align a single or small number of nanowires between the Au electrodes.[14] The surrounding SiO₂ surface was treated with TMS for 2 minutes to produce an appropriate hydrophobic surface prior to stretching and aligning the nanowires. Figure 82 shows a tapping mode AFM image of a PPy/DNA nanowire with a diameter of 30 nm and width of 600 nm aligned between two Au electrodes with an ~8 μm gap.

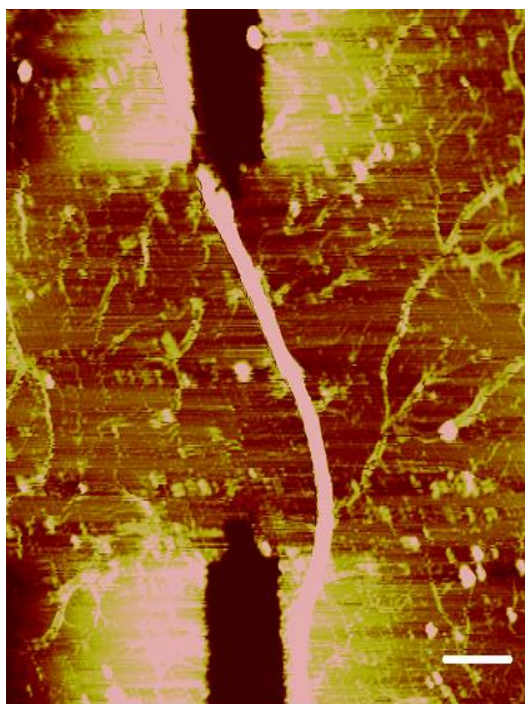


Figure 82. Tapping mode AFM image of a PPy/DNA nanowire aligned across Au microelectrodes. The mean nanowire diameter is 25 nm, and the interelectrode gap is 8.0 μm . The scale bar is 2.0 μm .

I-V curves for this PPy/DNA nanowire device were recorded under nitrogen at a series of temperatures over the range of 293 K to 373 K. The resulting I-V curves are presented in figure 83. As can be seen the current-voltage curves show nonlinearity at large bias voltages. The nature of the charge transport in conductive polymers is different compared to crystalline semiconductors.[53, 54] This type of I-V characteristic is expected for redox hopping polymers. All the I-V curves display increases with temperature. This is consistent with results of similar measurements on PIn/DNA and PPy/DNA nanowires in other studies. [14, 18, 55, 56] In addition, this figure shows a current offset at zero bias. This suggests that this behaviour is a result of the presence of static charges on the substrate owing to the dry nitrogen atmosphere used to avoid parasitic currents due to humidity.[15]

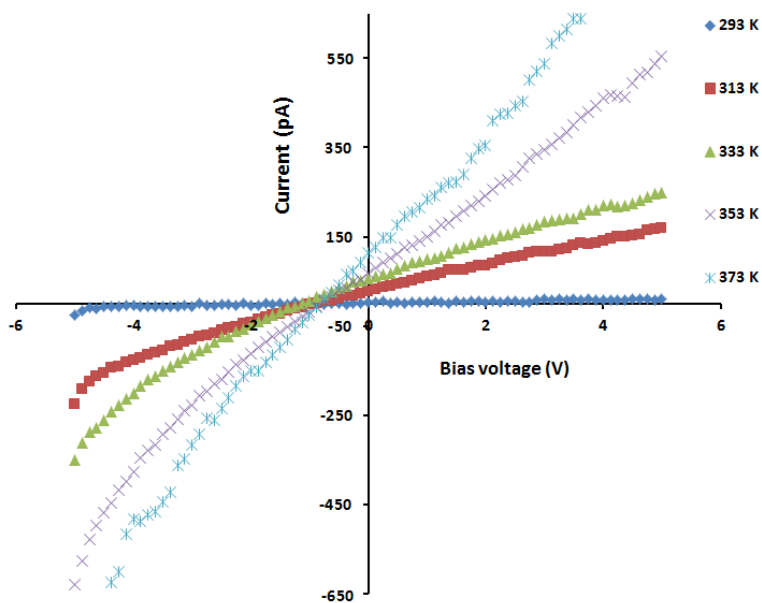


Figure 83. Current-voltage curves for the PPy/DNA nanowire of figure 82. Each curve was recorded at a fixed temperature covers the range of 293 - 373 K.

The conductivity of the PPy/DNA nanowire at room temperature was calculated using the height and width from the AFM image and was $\sim 1.1 \times 10^{-2} \text{ S cm}^{-1}$. This is lower than ($2.1 \times 10^{-1} \text{ S cm}^{-1}$) reported above for ppy/DNA nanowires which prepared by the same method and measured by c-AFM, (section 4.3.5). However, both values for ppy/DNA nanowires are significantly lower than (86 S cm^{-1}) determined by I-V Two-terminal conductivity measurement apparatus for the chemically prepared bulk PPy film, (chapter 3).

Figure 84 shows that the conductance increases with temperature and the change is reversed upon cooling. The repeatability of the conductance measurements was observed using two cycles of heating and cooling. No significant changes were observed in the conductance (G) versus temperature (T) plots during this treatment. This indicates the thermal stability of the PPy/DNA nanowires.

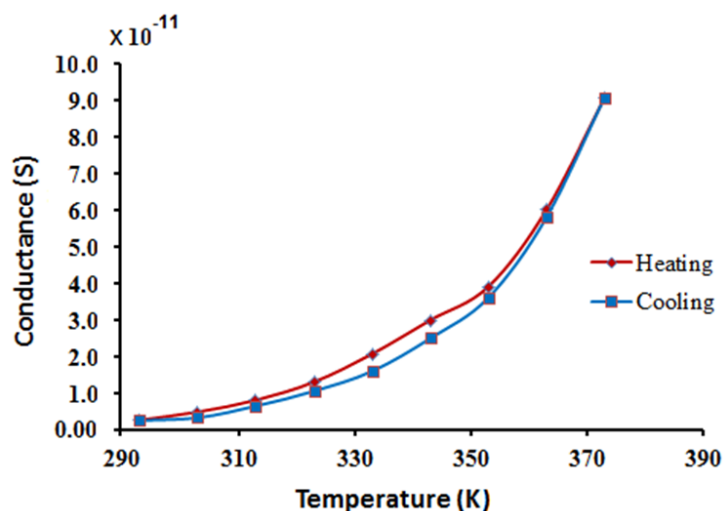


Figure 84. Conductance vs temperature for a single PPy/DNA nanowire over two cycles of heating and cooling.

Figure 85 shows the corresponding Arrhenius plot for conductance of the device fabricated here. These temperature-dependence measurements showed a simple Arrhenius behaviour characteristic. The plot of $\ln G$ versus T^{-1} shows a straight line over a range of temperatures. Such Arrhenius behaviour can be interpreted in terms of a simple nearest – neighbour hopping model ($\beta = 1$). This can be expressed in the form $\ln G = \ln G_0 - (T_0/T)^\beta$ with $\beta = 1$. This Arrhenius equation describes the conductance data over the full range of temperatures, and the fitted parameters are $\ln G_0 = 16.5$ and $T_0 = 4730$ K.

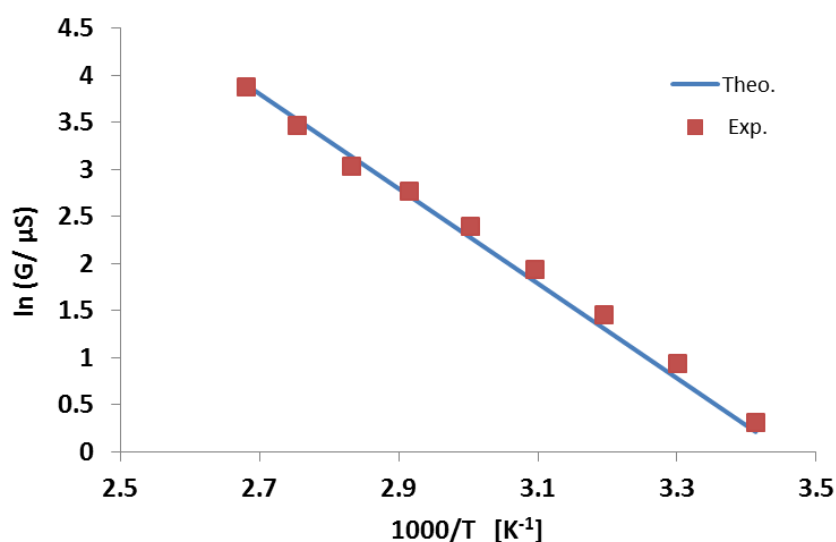


Figure 85. Arrhenius plot for the zero-bias conductance of single PPy/DNA nanowire.

A similar device was fabricated for poly-I/DNA nanowires and an AFM image of this device is shown in figure 86. The nanowire here has a diameter of 25 nm, width of 250 nm and length of 6.5 μm aligned across two Au electrodes.



Figure 86. AFM tapping Mode image of single poly-I/DNA nanowire aligned across two Au electrodes. Length of the nanowire (L)=6.5 μm and average diameter (D)=30 nm. Scale bar 1.0 μm and height scale 20 nm.

The current–voltage curves for this nanowire device were recorded under nitrogen at a series of temperatures over the range of 293 K to 373 K. Figure 87 shows the resulting data, and as can be seen these are nonlinear, and quite different to the PPy/DNA device. Here, the asymmetry of the curves in these results indicates that one of the Au/polymer/Au contacts was poor and the device ought to behave like a diode, resulting in asymmetrical I–V characteristic. [15]

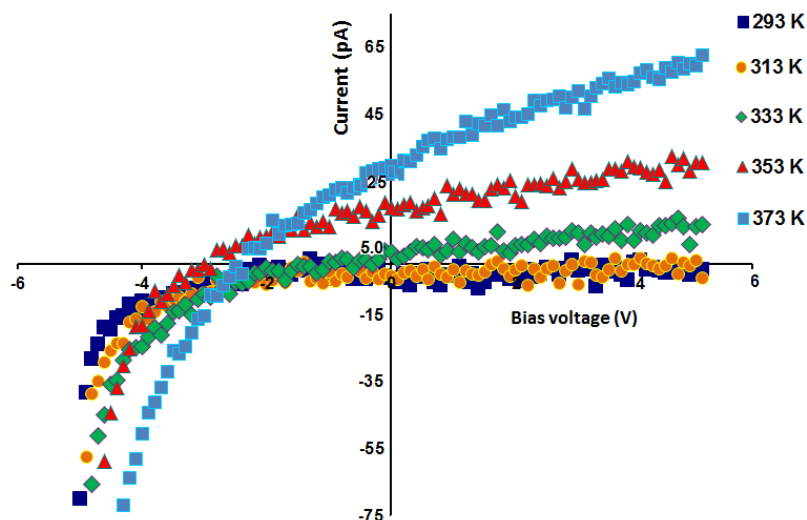


Figure 87. Current-voltage curves for the poly-I/DNA nanowire of figure 86. Each curve was recorded at a fixed temperature covers the range of 293 - 373 K.

The repeatability of the conductance measurements with temperature was again checked. A small degree of hysteresis is observed during the heating and cooling during the experiment. This was attributed to the loss of residual water bound to the polymer during the heating of the sample. No significant changes were observed indicating the good thermal stability of the poly-I/DNA nanowires.

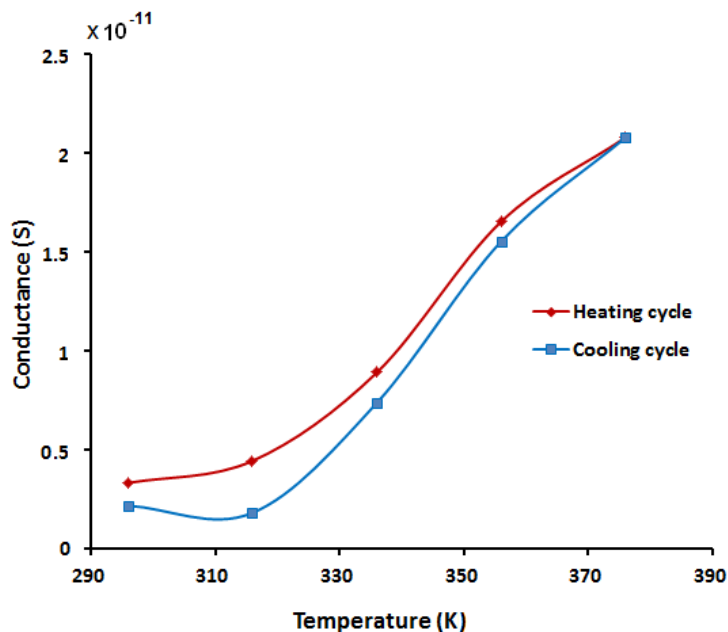


Figure 88. Conductance vs temperature for a single poly-I/DNA nanowire aligned across two Au electrodes.

This nanowire shows again a simple Arrhenius behaviour over a temperature range 293-373 K, figure 89, similar to the PPy/DNA nanowires.

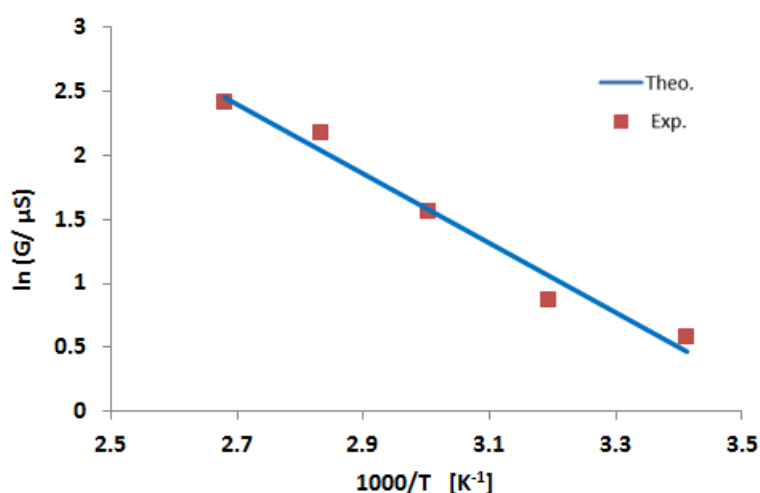


Figure 89. Arrhenius plot for the zero-bias conductance of single Poly-I/DNA nanowire.

The conductivity of poly-I/DNA device was found to be $3.3 \times 10^{-5} \text{ S cm}^{-1}$. This conductivity is significantly lower than the value determined for ppy/DNA nanowire ($1.1 \times 10^{-2} \text{ S cm}^{-1}$) using two-terminal I-V measurements. It is also lower than both values for PPy/DNA ($2.1 \times 10^{-1} \text{ S cm}^{-1}$) and poly-I/DNA ($2.0 \times 10^{-2} \text{ S cm}^{-1}$) nanowires determined by C-AFM. This variation in conductivity may reflect the effect of structure and planarity difference between ppy and poly-I structures as described in chapter 3. However, two terminal I-V measurements are less straightforward to implement than c-AFM, due to the difficulties of locating and aligning the nanowires across the Au microelectrode gap.

4.3.7. AFM characterisation of poly-II/DNA and poly-III/DNA nanowires

In order to align poly-II/DNA and poly-III/DNA nanowires on Si/SiO₂ substrate, it is desirable to have a low density of nanowires on the surface. A suitable contact angle of the surface to produce single nanowires has been found to be in the range of 65°-75°.[23] Nanowires were combed by dragging a droplet (3μL) of polymer/DNA

solution across the surface: the fluid flow causes alignment of nanowires in the direction of movement.

For these nanowires prepared at short reaction times, 2 hours, AFM images shown in figure 90 reveal a mixture of bare DNA molecules (red arrows) with poly-II/DNA (blue arrows), figure 90(a), and poly-III/DNA (blue arrows), figure 90(b). The measured thickness (AFM height) of the bare DNA strands was found in the range 0.5 to 2.0 nm. Poly-II/DNA nanowires are straight, continuous and with several micrometers long, ranging from 4 to 15 nm. Individual nanowire typically smooth and regular in diameter. The nanowire strands of poly-III/DNA nanowires are also continuous and have the same range of diameters (4 to 15 nm) with similar regularity and uniformity along the length. Figure 90(b) shows nanowires appear to have uniform polymer coverage and the substrate surface was mainly clear of polymer deposits from not templated material. These observations support that poly-II and poly-III polymer chains formed during the chemical oxidation are strongly templated on the DNA molecules.

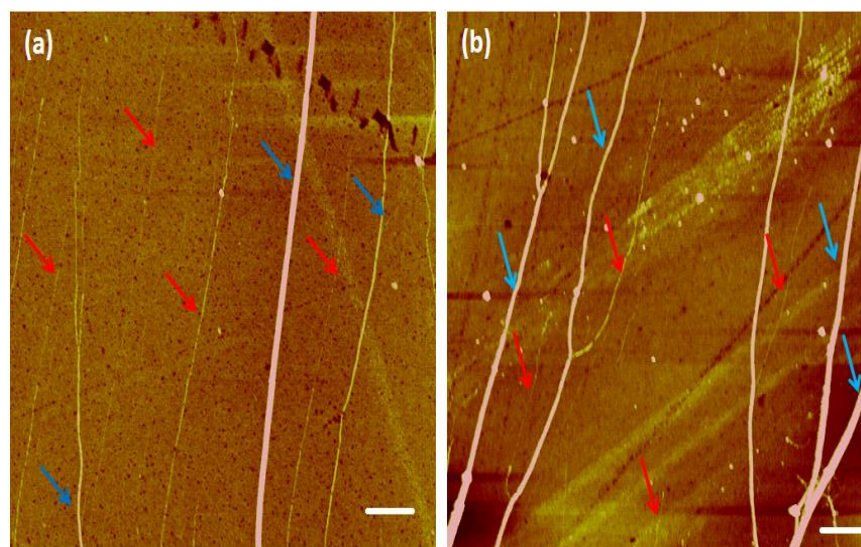


Figure 90. AFM images of poly-II/DNA (a) and poly-III/DNA nanowires (b), observed 2 h after preparation on a SiO_2/Si surface. The red arrows indicate the bare DNA molecules, where the blue arrows indicate the poly-II/DNA nanowires. These images were taken in tapping mode. Data scales correspond to height range of 10 nm. The scale bar of all images is 1.0 μm .

Statistical treatment carried out on ~100 ct-DNA strands before and after templating for 2 hours of poly-II and poly-III provide more comprehensive profile of the reaction producing nanowires. Figure 91 shows the mean diameters of free DNA with a modal diameter 1.0 - 2.0 nm. Some heights larger than 3.0 nm observed in much lower frequency.

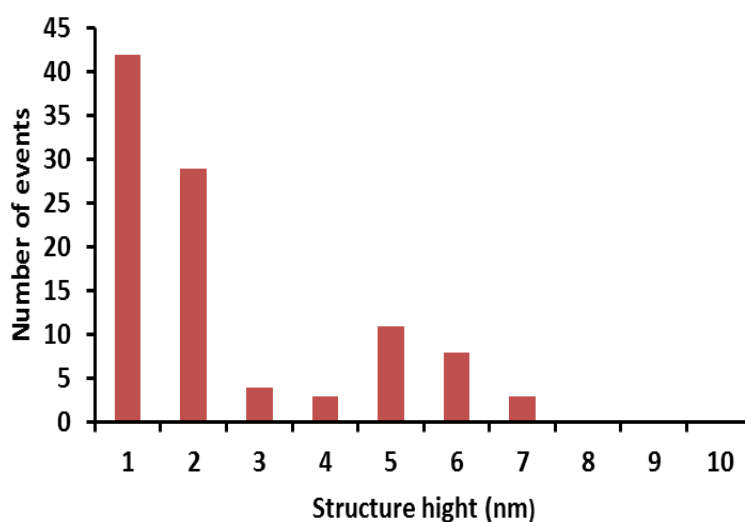


Figure 91. Height distribution of ~100 ct-DNA molecules before treatment with polymers. The heights were determined from Tapping Mode AFM images.

The distribution of heights of poly-II/DNA, figure 92(a) shows a spread of structure heights within the range 3.0 - 8.0 nm, with an average diameter of ~5.0 nm. The structure heights observed at 1.0-2.0 nm considered for bare DNA strands. This indicates that not all the DNA in the reaction is involved in templating. The common sized structures of poly-II/DNA are 3.0-4.0 nm, where some larger structure were also observed in much lower frequency with diameters up to 18 nm.

poly-III/DNA structures aligned 2 hours after templating show distribution heights with a modal value in the range 3.0-12 nm, figure 92(b), with an average diameter of ~7.0 nm. Larger heights up to 18 nm also observed in much lower frequencies. The structure heights attributed to bare DNA strands are observed at 2.0 nm only, indicating more DNA was involved in templating this polymer than that in poly-II.

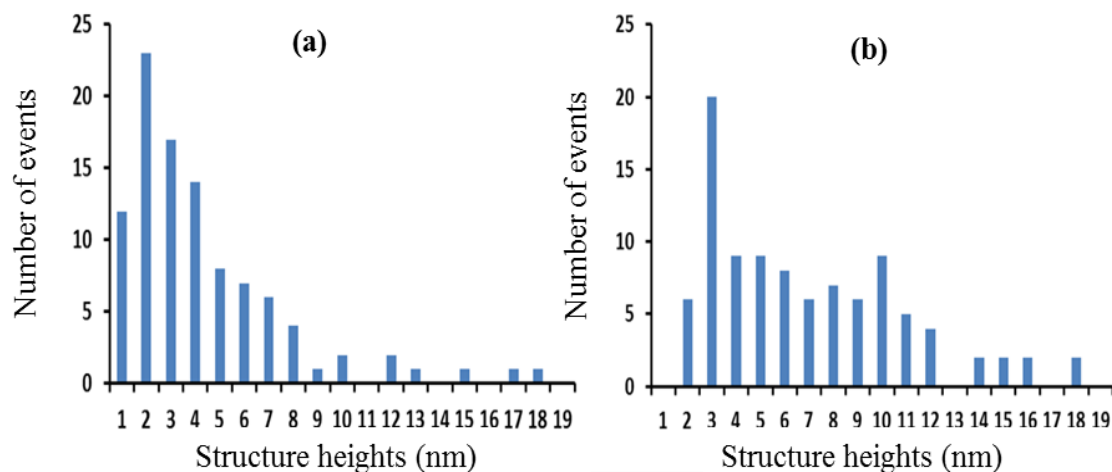


Figure 92. Height distribution of ~ 100 λ -DNA molecules after treatment with poly-II (a) and poly-III (b). The heights were determined from Tapping Mode AFM images 2 hours after preparation.

At longer reaction times, The AFM images show evidence that the thicker structures comprise ropes of individual nanowires. Figure 93 (a) shows tapping mode image of poly-II/DNA nanorope formed 24 hours after preparation with a diameter of 30 nm. As can be seen, the rope looks like two nanowires with diameters of 10 and 20 nm contacting together forming one thicker nanorope with a diameter of 30 nm, figure 93(b). It was suggested that the rope-like structures is quite general for DNA template polymer nanowires in which the charge on the DNA is compensated by the cationic conductive polymer.[14] The uniform diameter of poly-II/DNA nanowires is clearly visible in the line trace shown on figure 93(c).

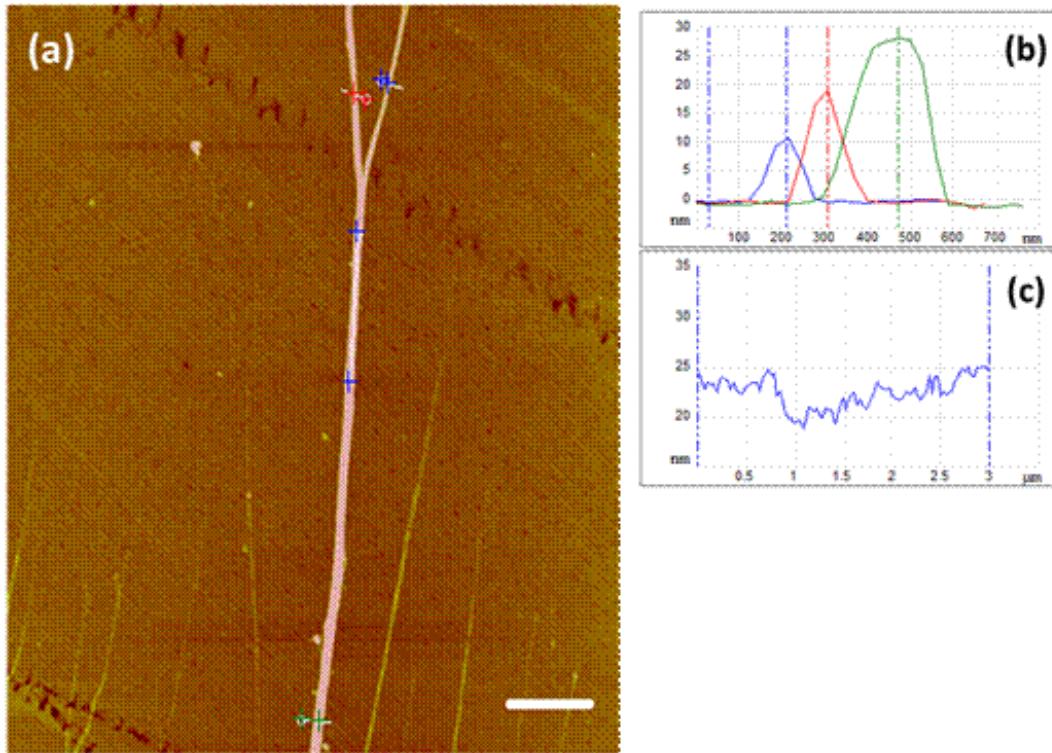


Figure 93. (a):Tapping mode AFM image of poly-II/DNA nanorope observed 24 h after preparation aligned on a Si/SiO₂ substrate. The data scale is 20 nm, and the scale bar is 2.0 μm. (b): The corresponding surface plots. (c): showing the corresponding line trace of (a).

For this particular nanowire shown in figure 93, the mean diameter estimated from the AFM height, is 25 nm. The variation in the cross-section of the rope over the length shown is relatively small:

The nanowire diameter uniformity can be estimated as described in (section 4.3.3), using the formula:

$$Du = \Delta D / l$$

For this single poly-II/DNA nanowire (shown in figure 93): With $l = 5.0 \mu\text{m}$, $D_c = 32.0 \text{ nm}$ and $\Delta D = 32.0 - 22.0 = 10.0 \text{ nm}$,

$$Du = 10/5000 = 2.0 \times 10^{-3}$$

This means that the variation of the nanowire diameter is slightly larger than poly-I/DNA nanowire (1.0×10^{-3}), but lower than ppy/DNA nanowire (3.0×10^{-3}), as shown earlier (section 4.3.3).

Larger structures were also observed for poly-III/DNA nanowires observed 24 hours after preparation. The nanowires based structures range from 20 to 40 nm and even larger in few instances. These structures are attributed to nanorope formed through bundling of individual nanowire structures into larger assemblies as previously described for poly-I/DNA and poly-II/DNA.

For poly-III/DNA structure observed 24 hours after preparation (shown in figure 49):

With $l = 5.0 \mu\text{m}$, $D_c = 43.0 \text{ nm}$ and $\Delta D = 45.0 - 43.0 = 2.0 \text{ nm}$.

$$D_u = 2/5000 = 0.4 \times 10^{-3}$$

This relatively small value indicates that poly-III/DNA nanowires have the most uniform diameters along their lengths compared with PPy, poly-I and poly-II/DNA nanowires.

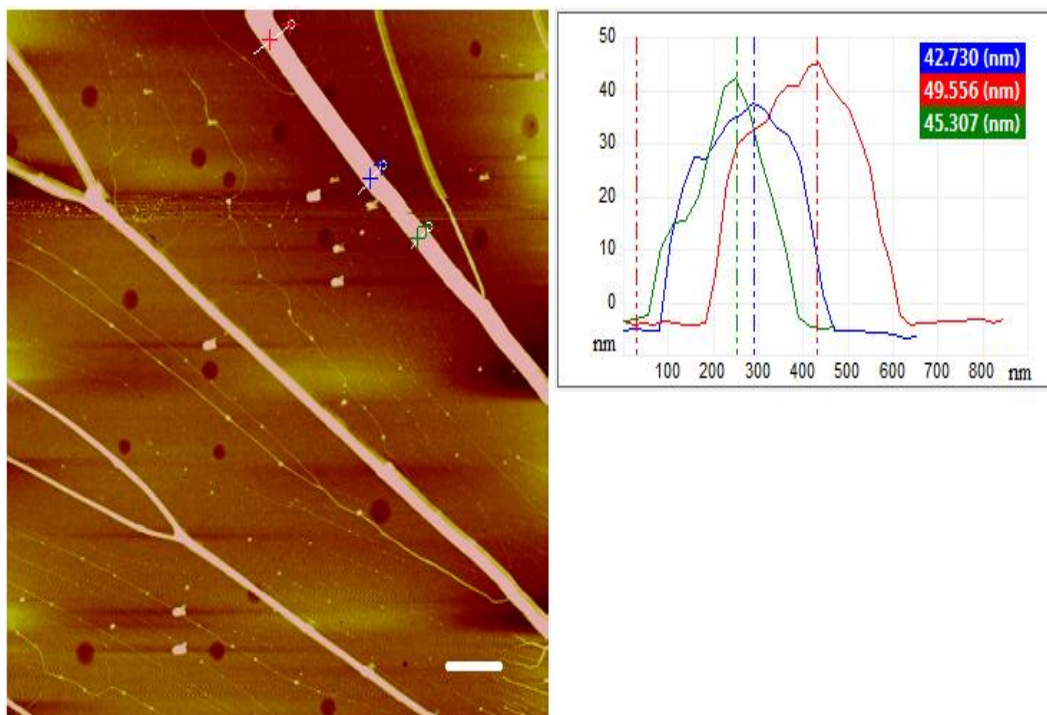


Figure 94. Tapping mode AFM image of poly-III/DNA nanorope observed 24 h after preparation aligned on a Si/SiO₂ substrate. The data scale is 20 nm, and the scale bar is 1.0 μm.

4.3.8. Electrical characterisation of poly-II/DNA and poly-III/DNA nanowires using EFM

EFM was used for characterising the electrical properties of poly-II/DNA and poly-III/DNA nanowires. Samples were prepared for EFM experiments by depositing the material upon silicon substrates with a 200 nm thick SiO₂ layer on top, and aligned by molecular combing as described previously. EFM phase images were recorded with the tip typically lifted 60 nm above the sample surface, with a dc voltage was applied to the samples.

Figure 95(a) shows EFM phase image of a typical poly-II/DNA nanowires recorded at bias voltage= +6 V. As the tip crossed the nanowires, a negative-positive-negative (W-shape) phase variation was observed, figure 95(b), which was reported previously for conductive polymer nanowires.[14, 41] Some DNA molecules are also seen in this image, (red arrow), which are non-conductive as judged by their positive phase shift.

The phase shift was measured along a cross section of the nanowire at a diameter of 10 nm upon the variation of applied bias for voltages between -10V and +10V, figure 95(c). The expected symmetrical parabolic dependence of phase shift was observed which confirms that it is due to the scanned conductance effect rather than the trapped charge effect [42].

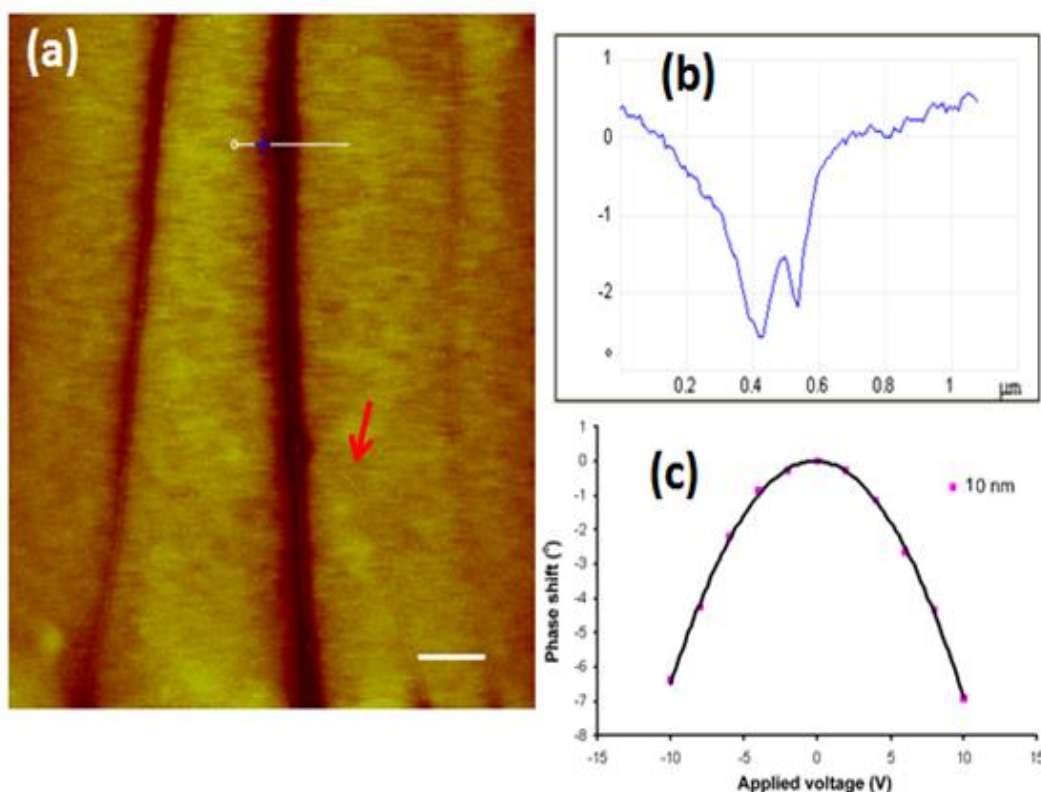


Figure 95. (a) EFM phase image of poly-II/DNA nanowires at a tip/sample bias of +6 V and lift height of 60 nm. The red arrow indicates a DNA molecule with positive phase shift. Scale bare = 500 nm. (b) The corresponding profile of the phase shift along a cross section of the nanowire at a diameter of 10 nm. (c) The phase shift of poly-II/DNA nanowires as a function of applied voltage between -10 and +10 V at diameter of 10 nm.

The EFM image of poly-III/DNA nanowires (applied bias $V = +6V$ and lift height 60 nm) is shown in figure 96. This figure shows that these nanowires also exhibit dark lines (negative phase shift) compared to the background of the insulator SiO_2 surface, indicating a conductive nature. The imaging of conduction pathways by EFM demonstrates the continuous conduction along the DNA-templated poly-III strands, visible as continuous dark lines in figure 96(a). Parts of one nanowire shown in the image (red arrows) appear incomplete, which is indicated by the lighter colour of negative phase shift. The profile of the phase shift along the cross-sections of the nanowires, figure 96(b), exhibits a double negative phase shift (negative-positive-negative) pattern, which corresponds to semiconducting and polymers materials.[41, 45].

The phase shift of the nanowires were then determined as a function of applied voltage (from -10 V to +10 V) for different nanowires with different diameters (7.0, 10 and 20 nm), figure 96(c). It depicts a parabolic variation with voltage, but with a slightly asymmetric shape. This later feature may be attributed to trapped charges on the nanowires. It can be seen that the nanowire of larger diameter ($D= 20$ nm) exhibits a larger phase-shift than the nanowire of smaller diameter ($D= 7.0$ nm). This reflects the change in capacitance of the tip/nanowire/substrate system as the nanowire diameter increases.

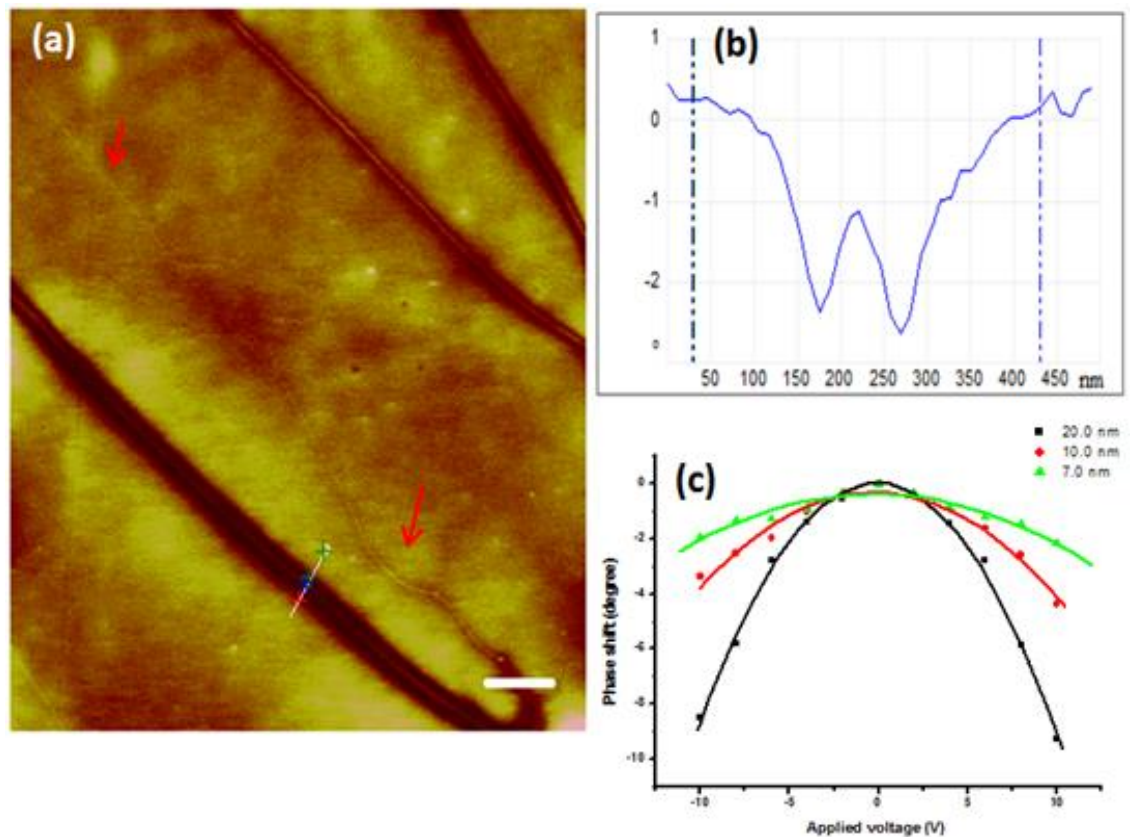


Figure 96. (a) EFM phase image of poly-III/DNA nanowires at a tip/sample bias of +6 V and lift height of 60 nm. The red arrows indicate non-covered parts of nanowires with positive phase shift. Scale bar = 500 nm. (b) The corresponding profile of the phase shift along a cross section of the nanowire at a diameter of 20 nm. (c) The phase shift of poly-III/DNA nanowires as a function of applied voltage between -10 and +10 V for different nanowires with different diameters.

4.3.9. Conductive atomic force microscopy (c-AFM) for poly-II/DNA and poly-III/DNA nanowires

In order to measure the conductance and estimate the conductivity of poly-II and poly-III/DNA, the nanowires network was connected to the metallic chuck using a drop of In-Ga eutectic as discussed previously (section 4.3.5).

Figure 97 shows C-AFM images of poly-II/DNA nanowire aligned on a Si/SiO₂ substrate; these images were acquired simultaneously. Image (a) is contact mode image with data scale corresponds to a height of 60 nm. This image shows a large feature, about 40 nm in diameter, aligned down from the left hand edge of the image, and large non-specific features over the substrate surface. The image (b) is deflection error image with data scale of 20 nm, provides slightly clearer image of the deflection error, which is the difference between the measured deflection and the setpoint. Image (c) is the current image by datascale corresponds to a current of 100 nA. This image shows the associated current on the nanowires with a bias of 7.0 V applied between the cantilever and the metallic chuck. The bright contrast in this image indicates an electrical current passing through the nanostructure, which confirms its electrical conductivity.

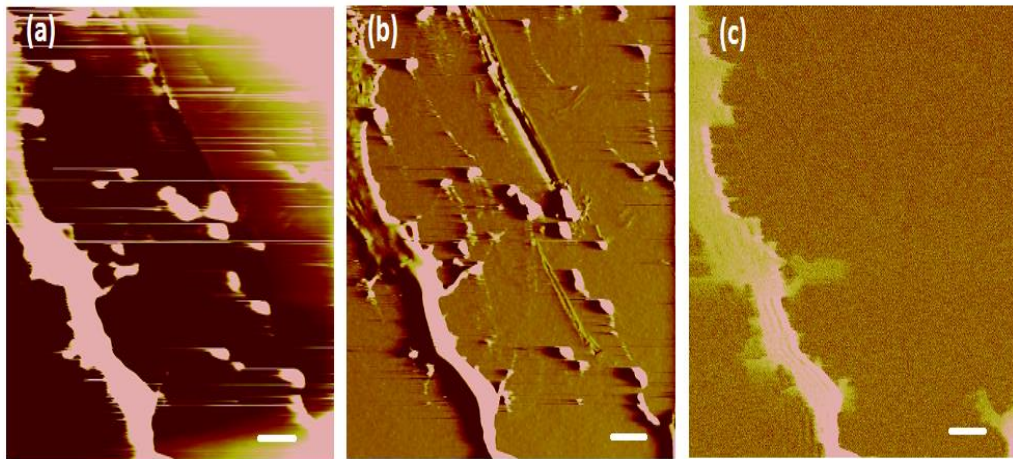


Figure 97. C-AFM of poly-II/DNA nanowire aligned on a Si/SiO₂ (200nm) substrate (a) Contact mode image, the datascale corresponds to a height of 60 nm; (b) Deflection error image (the data scale corresponds to a height of 20 nm) and (c) c-AFM current image (the data scale corresponds to a current of 100 nA). The tip-sample bias was 7.0V; the images (a)-(c) were acquired simultaneously. Scale bar 500 nm (a-c).

Figure 98 shows the resistance change of a single nanostructure with distance along the wire from the bulk contact. The circuit resistance increases in a linear manner with distance, d . The slope of this line gives the resistance per unit length of poly-II/DNA nanowire $1.0 \times 10^{12} \Omega \text{ cm}^{-1}$.

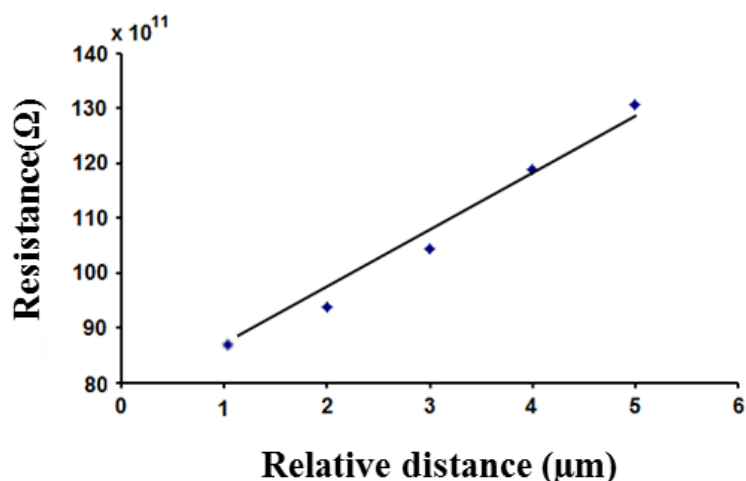


Figure 98. Poly-II/DNA nanowire resistance as a function of tip-contact relative distance in c-AFM measurements. Sample bias = 7.0 V at 0.5 deflection set point.

Based on the measured diameter (40 nm) and width (420 nm) of this poly-II/DNA nanowire, its conductivity was estimated to be $5.0 \times 10^{-3} \text{ S cm}^{-1}$. This is less conductive compared with poly-I/DNA nanowires ($2 \times 10^{-2} \text{ S cm}^{-1}$) and ppy/DNA nanowires ($2 \times 10^{-1} \text{ S cm}^{-1}$) reported above.

Poly-III/DNA samples were also prepared and characterised using the same technique. Figure 99 shows again that the circuit resistance increases linearly with distance along the nanowire. Based on the measured diameter (32 nm) and width (430 nm) of poly-III/DNA nanowire, its conductivity was estimated to be $9.0 \times 10^{-3} \text{ S cm}^{-1}$. This is less conductive compared with poly-I/DNA nanowires ($2 \times 10^{-2} \text{ S cm}^{-1}$) and PPy/DNA nanowires ($2 \times 10^{-1} \text{ S cm}^{-1}$) reported above, while it is slightly higher than the conductivity of poly-II/DNA nanowires ($5.0 \times 10^{-3} \text{ S cm}^{-1}$).

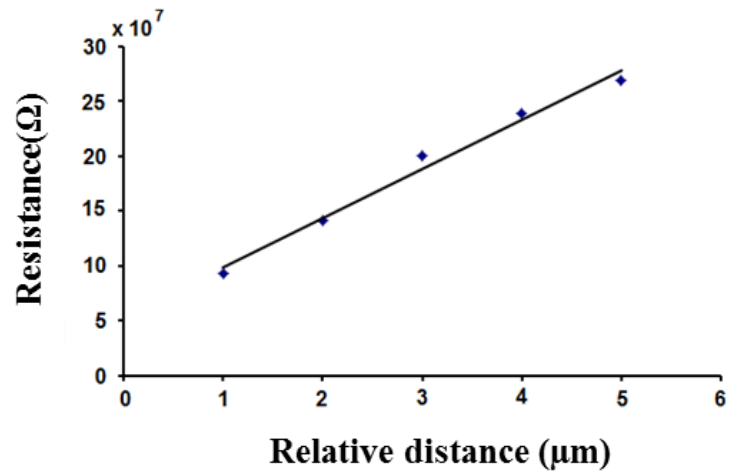


Figure 99. Poly-III/DNA nanowire resistance as a function of tip-contact relative distance in c-AFM measurements. Sample bias = 7.0 V at 0.5 deflection set point.

4.4. Summary

Nanowires of poly-I, poly-II and poly-III have been prepared using DNA-templating, and characterized using a variety of techniques. These nanowires were chemically synthesized using FeCl_3 as an oxidant in aqueous solution in the presence of duplex DNA. The expected interaction between the anionic phosphate group of DNA and cationic polymers was indicated by FTIR which reveals changes in the vibrational frequencies and intensity of some characteristic bands. The nanowires' morphology was demonstrated using tapping mode AFM. Nanowires obtained with this approach have a uniform diameter and surface smoothness. These individual nanowires can further assemble into large rope-like structures as induced in particular by frayed ends of thicker structures. The conductivity of uniform nanostructures was demonstrated by EFM, C-AFM and two-terminal I-V techniques. The results of conductivity reveals that the conductivities of poly-I, poly-II and poly-III/DNA nanowires are generally lower than PPy/DNA nanowires showing the large effect on N-alkylation in decreasing the conductivity of the polymer, but these are higher than the conductivity of their corresponding bulk films. This enhancement in conductivity could be attributed to the ordering of the polymer chains on DNA during the templating process.

4.5. References

1. H. D. Tran, D. Li and R. B. Kaner, One-Dimensional Conducting Polymer Nanostructures: Bulk Synthesis and Applications. *Adv. Mater.*, 2009, **21**, 1487-1499.
2. L. Pan, H. Qiu, C. Dou, Y. Li, L. Pu, J. Xu and Y. Shi, Conducting Polymer Nanostructures: Template Synthesis and Applications in Energy Storage. *Int. J. Mol. Sci.*, 2010, **11**, 2636-2657.
3. A. Houlton and S. Watson, DNA-based nanowires. Towards bottom-up nanoscale electronics. *Annu. Rep. Prog. Chem., Sect. A*, 2011, **107**, 21-42.
4. M. S. Hu, H. L. Chen, C. H. Shen, L. S. Hong, B. R. Huang, K. H. Chen and L. C. Chen., Photosensitive gold-nanoparticle-embedded dielectric nanowires. *Nat. Mater.*, 2006, **5**, 102-106.
5. C. H. Hsieh, L. J. Chou, Y. B. G. R. Lin and D. Golberg, Nanophotonic Switch: Gold-in-Ga₂O₃ Nanowires. *Nano Lett.*, 2008, **8**, 3081-3085.
6. Y. S. Zhao, A. Peng, H. Fu, Y. Ma and J. Yao, Nanowire Waveguides and Ultraviolet Lasers Based on Small Organic Molecules. *Adv. Mater.*, 2008, **20**, 1661-1665.
7. D. O'Carroll, I. Lieberwirth and G. Redmond, Microcavity effects and optically pumped lasing in single conjugated polymer nanowires. *Nat. Nanotech.*, 2007, **2**, 180-184.
8. L. Dong, T. Hollis, S. Fishwick, B. A. Connolly, N. G. Wright, B. R. Horrocks and A. Houlton, Synthesis, Manipulation and Conductivity of Supramolecular Polymer Nanowires. *Chem. Eur. J.*, 2007, **13**, 822-828.
9. Z. L. Wang, Nanobelts, Nanowires and Nanodeskittes of semiconducting oxides - From Materials to Nanodevices. *Adv. Mater.*, 2003, **15**, 432-436.
10. J. C. Hulteen and C. R. Martin, A general template-based method for the preparation of nanomaterials. *J. Mater. Chem.*, 1997, **7**, 1075-1087.
11. Y. Berdichevsky and Y. H. Lo, Polypyrrole nanowire actuators. *Adv. Mat.*, 2006, **18**, 122-125.
12. Q. Gu, C. Cheng, R. Gonela, S. Suryanarayanan, S. Anabathula, K. Dai and D. T. Haynie, DNA nanowire fabrication. *Nanotech.*, 2006, **17**, R14-R25.
13. A. Houlton, A. R. Pike, M. Galindo and B. R. Horrocks., DNA-based routes to semiconducting nanomaterials. *Chem. Commun.*, 2009, 1797-1806.

14. R. Hassanien, M. Al-Hinai, S. Al-Said, R. Little, L. Siller, N. Wright, A. Houlton and B. Horrocks, Preparation and Characterization of Conductive and Photoluminescent DNA Templated Polyindole Nanowires. *Am. Chem. Soc.* , 2010, **4**, 2149-2159.
15. S. M. D. Watson, J. H. Hedley, M. A. Galindo, S. A. F. Al-Said, N. G. Wright, B. A. Connolly, B. R. Horrocks and A. Houlton, Synthesis, Characterisation and Electrical Properties of Supramolecular DNA-Templated Polymer Nanowires of 2,5-(Bis-2-thienyl)-pyrrole. *Chem. Europ. J.*, 2012, **18**, 12008-12019.
16. S. Pruneanu, L. Dong, T. A. Hollis, N. G. Wright, M. A. Galindo, A. R. Pike, B. A. Connolly, B. R. Horrocks and A. Houlton., *AIP Conf. Proc.*, Jena (Germany) 2008.
17. R. Nagarajan, S. Roy, J. Kumar, S. K. Tripathy, T. Dolukhanyan, C. M. Sung, F. Bruno and L. A. Samuelson, Enzymatic synthesis of molecular complexes of polyaniline with DNA and synthetic oligonucleotides: Thermal and morphological characterization. *J. Macro. molec. Scie.*, 2001, **38**, 1519-1537.
18. S. Pruneanu, S. A. Al-Said, L. Dong, T. A. Hollis, M. A. Galindo, N. G. Wright, A. Houlton and B. R. Horrocks, Self-Assembly of DNA-Templated Polypyrrole Nanowires: Spontaneous Formation of Conductive Nanoropes. *Adv. Funct. Mater.*, 2008, **18**, 2444- 2454.
19. C. M. Hangarter, M. Bangar, A. Mulchandani and N. V. Myung, Conducting polymer nanowires for chemiresistive and FET-based bio/chemical sensors. *J. Mat. Chem.*, 2010, **20**, 3131-3140.
20. C. P. McCarthy, N. B. McGuinness, B. E. Alcock-Earley, C. B. Breslin and A. D. Rooney, Facile template-free electrochemical preparation of poly N-(2-cyanoethyl)pyrrole nanowires. *Elect. chem. Commun.*, 2012, **20**, 79-82.
21. Z. Deng and C. Mao, DNA-Templated Fabrication of 1D Parallel and 2D Crossed Metallic Nanowire Arrays. *Nano Lett.*, 2003, **3**, 1545-1548.
22. L. Dong, T. Hollis, S. Fishwick, B. A. Connolly, N. G. Wright, B. R. Horrocks and A. Houlton, Synthesis, Manipulation and Conductivity of Supramolecular Polymer Nanowires. *Chem. Eur. J.*, 2007, **13**, 822-828.
23. S. M. D. Watson, N. G. Wright, B. R. Horrocks and A. Houlton., Preparation, Characterization and Scanned Conductance Microscopy Studies of DNA-Templated One-Dimensional Copper Nanostructures. *Langmuir* 2010, **26**, 2068-2075.
24. J. W. Li, C. L. Bai, C. Wang, C. F. Zhu, Q. L. Z. Lin and E. H. Cao., A convenient method of aligning large DNA molecules on bare mica surfaces for atomic force microscopy *Nucl. Acids Res.* , 1998, **26**, 4785-4786.

25. Z. X. Deng and C. D. Mao, DNA-templated fabrication of 1D parallel and 2D crossed metallic nanowire arrays *Nano Lett.*, 2003, **3**, 1545-1548.
26. S. A. Al-Said, R. Hassanien, J. Hannant, M. A. Galindo, S. Pruneanu, A. R. Pike, A. Houlton and B. R. Horrocks, Templating Ag on DNA/polymer hybrid nanowires: Control of the metal growth morphology using functional monomers. *Elect. chem. Comm.*, 2009, **11**, 550-553.
27. M. Omastova, M. Trchova, J. Kovarova and J. Stejskal., Synthesis and structural study of polypyrroles prepared in the presence of surfactants. *Synth. Met.*, 2003, **138**, 447-455.
28. A. Bae, T. Hatano, M. Numata, M. Takeuchi and S. Shinkai, Superstructural Poly(pyrrole) Assemblies Created by a DNA Templating Method. *Macromol.*, 2005, **38**, 1609-1615.
29. E. Taillandier and J. Liquier, *Infrared spectroscopy of DNA.* , Academic Press, Inc., California, USA, 1992.
30. H. Arakawa, R. Ahmad, M. Naoui and H. A. Tajmir-Riahi, A Comparative Study of Calf Thymus DNA Binding to Cr(III) and Cr(VI) Ions. *J. Bio. Chem.* , 2000, **275**, 10150-10153.
31. E. Taillandier, J. A. Taboury, S. Adam and J. Liquier, Left-Handed Helical Structure of Poly[d(A-C)]ePoly[d(G-T)] Studied by Infrared Spectroscopy. *Biochemistry*, 1984, **23**, 5703-5706.
32. S. Alex and P. Dupuis, FT-IR AND Raman Investigation of cadmium binding by DNA. *Inorg. Chimica Acta*, 1989, **157**, 271-281.
33. A. A. Ouameur and H. A. Tajmir-Riahi, Structural analysis of DNA interactions with biogenic polyamines and cobalt(III) hexamine studied by Fourier transform infrared and capillary electrophoresis. *J. Bio. Chem.*, 2004, **279**, 42041-42054.
34. G. I. Dovbeshko, N. Y. Gridina, E. B. Kruglova and O. P. Pashchuk, FTIR spectroscopy studies of nucleic acid damage. *Talanta*, 2000, **53**, 233-246.
35. L.Tong, J. Lou, Z. Ye, G.T. Svacha and E. Mazur, Self-modulated taper drawing of silica nanowires. *Nanotech.*, 2005, **16**, 1445-1448.
36. B. Saoudi, N. Jammul, M. Abel, M. Chehimi and G. Dodin, DNA adsorption onto conducting polypyrrole. *Synthetic Metals*, 1997, **87**, 97-103.
37. V. Velusamy, K. Arshak, C. F. Yang, L. Yu, O. Korostynska and C. Adley, Comparison Between DNA Immobilization Techniques on a Redox Polymer Matrix. *Am. J. Analy. Chem.*, 2011, **2**, 392-400.

38. M. Bockrath, N. Markovic, A. Shepard and M. Tinkham, Scanned Conductance Microscopy of Carbon Nanotubes and DNA. *Nano Lett.*, 2002, **2**, 187-190.
39. J. Cristian Staii and Alan T. Johnson, Quantitative Analysis of Scanning Conductance Microscopy. *Nano Lett.*, 2004, **4**, 859-862.
40. C. Staii, A. T. Johnson and N. J. Pinto, Quantitative analysis of scanning conductance microscopy. *Nano Letters*, 2004, **4**, 859-862.
41. Y. Zhou, M. Freitag, J. Hone, C. Staii and A. T. Johnson, Fabrication and electrical characterization of polyaniline-based nanofibers with diameter below 30 nm. *Appl. Phys. Lett.*, 2003, **83**, 3800-3802.
42. R. Hassanien, S. A Al-Said, L. Siller, R. Little, N. G Wright, A. Houlton and B. R. Horrocks, Smooth and conductive DNA-templated Cu₂O nanowires: growth morphology, spectroscopic and electrical characterization. *Nanotech.* , 2012, **23**, 075601-075613.
43. Y. X. Zhou, M. Freitag, J. Hone, C. Staii, A. T. Johnson, N. J. Pinto and A. G. MacDiarmid, Fabrication and electrical characterization of polyaniline-based nanofibers with diameter below 30 nm. *App. Phys. Lett.*, 2003, **83**, 3800-3802.
44. T. S. Jespersen and J. Nygard, Charge trapping in carbon nanotube loops demonstrated by electrostatic force microscopy. *Nano Lett.*, 2005, **5**, 1838-1841.
45. Cristian Staii and A. T. Johnson, Quantitative Analysis of Scanning Conductance Microscopy. *Nano Lett.*, 2004, **4**, 859-862.
46. F. Houze, R. Meyer, O. Schneegans and L. Boyer, Imaging the local electrical properties of metal surfaces by atomic force microscopy with conducting probes. *Appl. Phys. Lett.*, 1996, **69**, 1975-1977.
47. J. Alvarez, I. Ngo, Ma. Gueunier-Farret, J. Kleider, L. Yu, P. Cabarrocas, S. Perraud, E. Rouviere, C. Celle, C. Mouchet and J. Simonato, Conductive-probe atomic force microscopy characterization of silicon nanowire. *Nano. Res. Lett.*, 2011, **6**, 1-9.
48. D. Talukdar, U. N. Nandi, K. K. Bardhan, C. C. Bof Bufon, A. D. T. Heinzl and C. D. Mukherjee, Nonlinearity exponents in lightly doped conducting polymers. *Phys. Rev.*, 2011, **84**, 054205-054218.
49. G. Givaja, P. Amo-Ochoa, C. J. Gomez-Garcı and F. Zamora, Electrical conductive coordination polymers. *Chem. Soc. Rev.*, 2012, **41**, 115-147.
50. H. Narayan, A. M. Montaña, M. L. Hernández, J. A. Hernández, C. P. González and C. A. Ortiz, Synthesis, characterization and ac-conductivity measurements of

- polyaniline based composites with fly-ash and clinker. *J. Mater. Environ. Sci.*, 2012, **3**, 137-148.
51. R.S. Kohlman, T. Ishiguro, H. Kaneko and A.J. Epstein, Metallic state of polypyrrole: Effects of disorder. *Synth. Met.*, 1995, **69**, 325-328.
 52. J. P. Spatz, B. Lorenz, K. Weishaupt and H. D. Hochheimer, Observation of crossover from three- to two-dimensional variable-range hopping in template-synthesized polypyrrole and polyaniline. *Phys. Rev. B*, 1994, **50**, 14888-14892.
 53. S. J. Xie, L. M. Mei and D. L. Lin, Transition between bipolaron and polaron states in doped hetrocycle polymers. *Phys. Rev. B*, 1994, **50**, 13364-13370.
 54. D. Talukdar, U. N. Nandi, K. K. Bardhan, C. C. B. Bufon, T. Heinzl, A. De and C. D. Mukherjee, Nonlinearity exponents in lightly doped conducting polymers. *Phys. Revi. B.*, 2011, **84**, 1-8.
 55. L. Dong, T. Hollis, B. A. Connolly, N. G. Wright, B. R. Horrocks and A. Houlton, DNA-Templated Semiconductor Nanoparticle Chains and Wires. *Adv. Mater.*, 2007, **19**, 1748-1751.
 56. H. J. Lee and S. M. Park, Electrochemistry of conductive polymers. 30. Nanoscale measurements of doping distributions and current-voltage characteristics of electrochemically deposited polypyrrole films. *J. Phys. Chem. B*, 2004, **108**, 1590-1595.

5. Metallization of CPs/DNA Nanowires

5.1. Introduction

DNA has made a great contribution to the synthesis of low-dimensional nanostructures as a wet-chemical, bottom-up fabrication technique.[1] A wide range of material types have been templated as 1D nanostructures at DNA including metals,[2-6] inorganic compounds[2, 7, 8] and conducting polymers.[8-10] This method takes advantage of the well-defined architecture, small, 2nm, diameter and large persistence length[11-13] of duplex DNA along with its chemical functionalities that allow the binding of metal ions and cationic molecules.

One of the most technologically important metals to form at the nanoscale as nanowires is copper. This remains the material of choice for consumer electronics due to its favourable conductivity/cost ratio. Previous reports [4, 5, 14] have made claim to the formation of copper nanowires using on the DNA-templating. However, Woolley *et al.*[5] have fabricated copper/DNA nanowires and used AFM to investigate the process. They associated Cu^{2+} ions directly to DNA templates using an aqueous $\text{Cu}(\text{NO}_3)_2$ solution as a source of Cu^{2+} and ascorbic acid solution as a reductant. Kudo *et al.*[4] used the traditional deposition method used in the semiconductor industry for the preparation of copper nanowires by activation of DNA with palladium, then electroless plating of copper. This was in the effort to provide greater control over the metallization process in either of these reports, however the process resulted in deposition of material, stated to be Cu^0 , along the DNA with granular morphology and some non-coated regions between Cu^0 nanoparticles due to deposition taking place to differing extents along the DNA template. However no chemical or electrical characterisation performed.

More recently in our laboratories, Watson *et al.*[15] have explored a process similar to that of Woolley. Despite evidence for the metallic composition (Cu^0) of these Cu/DNA nanostructures, no evidence of electrical conductivity was observed. This was attributed to the beads-on-a-string morphology of the resulting nanostructures as shown in the figure 100.[15]

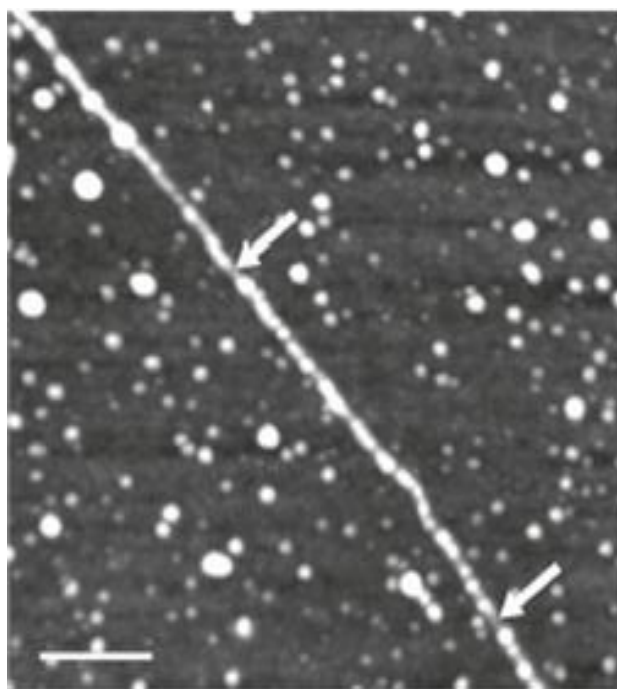
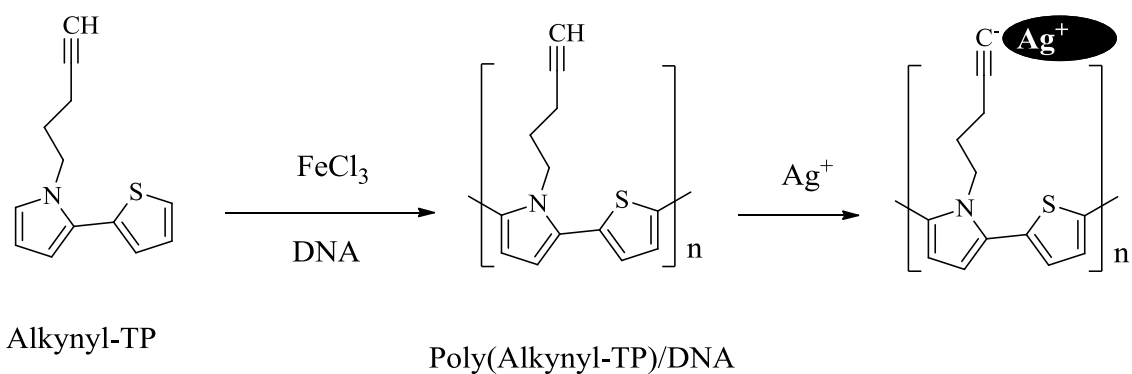


Figure 100. Tapping Mode AFM height image of a section of a λ -DNA molecule following solution treatments with $\text{Cu}(\text{NO}_3)_2$ and ascorbic acid, highlighting the “beads-on-a-string” morphology associated with Cu^0 material deposited along the DNA. The arrows highlight regions between Cu^0 nanoparticles on the DNA template, where less substantial Cu^0 deposition has taken place. Scale bar=200 nm, height scale=8 nm[15].

A possible approach to improve the growth of metals at DNA-based structures was recently reported by Al-Said *et al* (2009) for silver.[6] In this report the effect of growing silver at DNA/polymer nanowires was explored compared to bare DNA. It was found that the introduction of a functional, alkynyl-, group, into the polymer led to the formation of much smoother and more highly conductive nanowires than for DNA as template itself, or for DNA/polymer nanowires which did not bear an alkynyl group. This was explained by the alkynyl group providing site that facilitate nucleation and growth of silver on the CP/DNA nanowires. This group is well-known to bind soft metal ions such as Ag(I). The method of synthesis of these Ag/poly(Alkynyl-TP)/DNA hybrid nanowires is illustrated in scheme 18.



Scheme 18. DNA-templated synthesis of poly(alkynyl-TP) nanowires and deposition of Ag nanocrystals.[6]

Figure 101 shows EFM phase images of poly(alkynyl-TP)/DNA structures (b), Ag/DNA (c) and Ag/poly(alkynyl-TP)/DNA structures (e). Figure 101 b shows low phase shift corresponding to low conductivity of a regular and smooth poly(alkynyl-TP)/DNA nanowire. Ag/DNA nanowires, figure 101 c, shows large, unregularly and bright spots corresponding to Ag clusters which are apparently not in good electrical contact with the rest of the wire (dark shadow). Ag/poly(alkynyl-TP)/DNA nanowire, figure 101 e, shows a much more uniform structure than the pure Ag/DNA nanowires and a negative phase shift corresponding to higher conductivity[6].

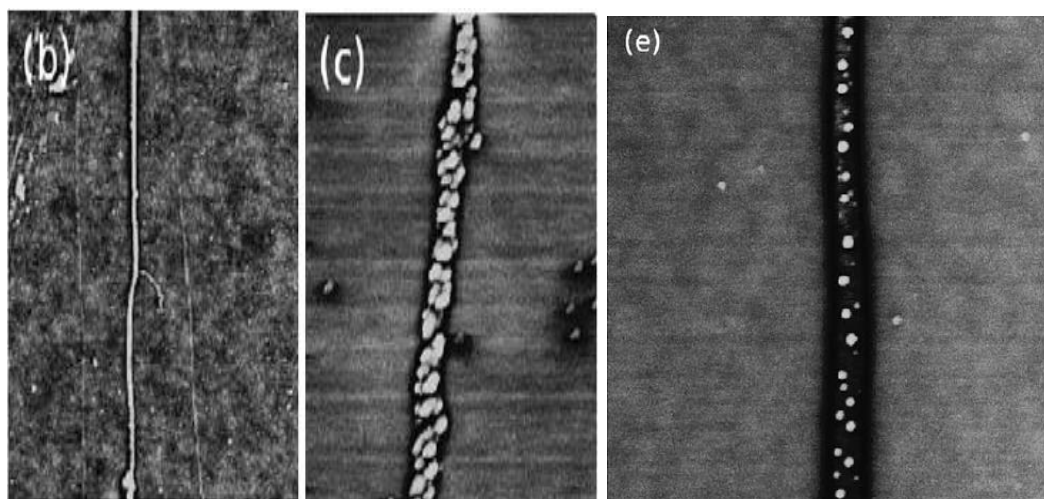
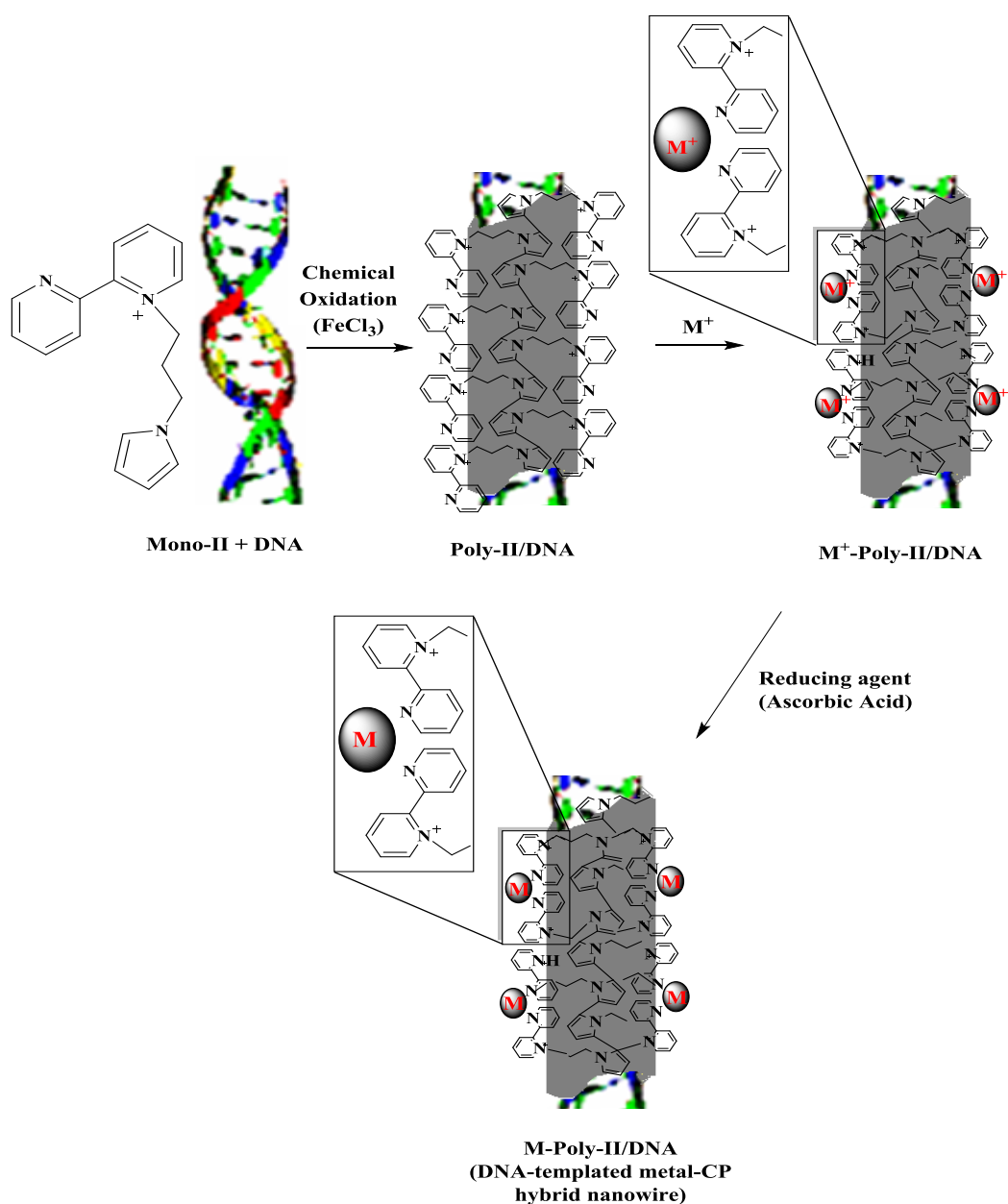


Figure 101. EFM phase images. (b) poly(alkynyl-TP)/DNA; (c) Ag/DNA and (e) Ag/poly(alkynyl-TP)/DNA.[6]

However, the alkynyl group is not so versatile for metal ions binding. Accordingly, in this work, we are interested in incorporating alternative metal ion binding sites suitable for metals ions, particularly Cu and Pd. As mentioned previously, Cu nanowires are important as electrical interconnects and Pd wires show use in gas sensing and catalysis as well as being used as seeds in deposition of Cu. The pyridine group is highly suitable for binding these divalent metal ions (Cu, Pd).[16] And in this chapter, the ability of the pyridyl-functionalized DNA-templated polymers nanowires prepared earlier in chapter 4 to enhance the formation of metal nanowires was explored, scheme 19.



Scheme 19. Synthesis of DNA-templated nanowires functionalised for enhanced deposition of metals.

5.2. Experimental

5.2.1. Materials

All general chemical reagents were obtained from Sigma-Aldrich unless otherwise stated, and were of Analar grade or equivalent. Monomers II and III are prepared as in chapter 3. Lambda (λ)-DNA was from New England Biolabs, cat no. N3011S (New England Biolabs (UK) Ltd. Hitchin, Herts, United Kingdom). Silicon <p-100>wafers, 3 in. diameter, 525 ± 50 μm thickness, 1-10 Ω cm resistance were purchased from Compant Technology Ltd. (Peterborough, Cambridgeshire, United Kingdom)

5.2.2. *Templating Copper nanoparticles on Poly-II/DNA and poly-III/DNA hybrids nanowires*

40 μL of λ -DNA-templated CP solution, prepared 24 hours ago, (as prepared in chapter 4) was mixed with 5 μL of a 0.5 M aqueous solution $\text{Cu}(\text{NO}_3)_2$. The solution was thoroughly mixed and allowed to react 10 minutes. Ascorbic acid (5 μL , 1.0 M) was added, and thoroughly mixed and the mixture was then allowed to react for at least 1h at room temperature prior to analysis. Cu-poly-II/DNA or Cu-poly-III/DNA solution was deposited on Si/SiO₂ and oriented by the molecular combing technique. In order to facilitate the alignment of nanowires on the substrates for analysis by AFM, the hydrophobicity of the SiO₂ was increased by treating the substrates with Me₃SiCl vapour, as described earlier (section 4.2.3), for about 2 minutes. Typically, 3 μL of Cu-CP/DNA solution was dropped on the silanized Si/SiO₂ surface and combed, then removed with a micropipette or by wicking with filter paper.

5.2.3. *Templating Pd nanoparticles on Poly-II/DNA hybrids nanowires*

40 μL of polymer-templated DNA (Poly-II/DNA) solution prepared 24 hours ago, as described in section 4.3.1, was mixed with 5 μL of 3.0 mM aqueous solution

PdCl₂. The solution was stirred for 10 minutes at room temperature. An aqueous solution of NaBH₄ (5 μL, 10 mM) was added and thoroughly mixed then allowed to react for 2 hours at room temperature prior to analysis. 3 μL of Pd-CP/DNA solution was dropped on a silicon chip, prepared as above, and combed as described earlier.

5.2.4. FTIR spectroscopy:

For FTIR measurements, about 10 μL of Cu-poly-II/DNA, Cu-poly-III/DNA or Pd-poly-II/DNA solution was deposited on a clean Si(100) substrate and left to dry in the Laminar flow cabinet for 1 h prior to measurements. FTIR spectra in the range from 600 to 4000 cm⁻¹ were recorded in absorbance mode by using a Biorad FTS-40 spectrometer operating with 4 cm⁻¹ spectral resolution and equipped with a liquid-nitrogen-cooled MCT detector. A clean Si(100) chip served as the background.

5.2.5. Uv-Vis Absorption spectroscopy:

The UV-vis absorption spectra (wavelength range from 250 to 900 nm) were recorded on a VARIAN-CARY 100 Bio spectrophotometer at room temperature. For UV-vis measurements, Cu-polymer/DNA or Pd-polymer/DNA solution was made using calf thymus DNA (CT-DNA). Typically, 0.6 mL of 3.0 mM freshly prepared monomer solution was added to 2.0 mL of CT-DNA solution (100 ng μL⁻¹) in the presence of 0.5 mM MgCl₂. Then, 0.6 mL of FeCl₃ (1 mM) was added dropwise to the solution. The mixture was stirred and allowed to react at room temperature for 2 hours.

In the case of copper metallization; Cu(NO₃)₂ (0.6 ml, 0.5 M) aqueous solution was added to the CP/DNA solution followed by the Uv-Vis measurement. Then 0.6 ml, 1.0 M of ascorbic acid was added as the final reduction step.

For metallization with Pd; 0.6 mL, 5.0 mM aqueous solution of PdCl₂ was added to the CP/DNA solution followed by the Uv-Vis measurement. Pd²⁺ was then reduced by the addition of NaBH₄ (0.6 ml, 15.0 mM) aqueous solution.

The mixtures were stirred and Uv-Vis measurements were taken after 1 hour. Polymer solutions were prepared by the same process without CT-DNA as a control.

5.2.6. X-ray Photoelectron Spectroscopy (XPS):

XPS spectra were acquired on a Thermo-Fisher Scientific K-Alpha instrument. This uses monochromated Al X-rays, with a selectable spot size between 30 and 400 micrometres. Typically 200 eV pass energy was used for survey scans. 50 eV or 20 eV for narrow scans. The pass energy used for each spectrum is contained in the data files and viewable from CasaXPS. The binding energies and intensities obtained in the XPS analysis were calibrated using Au_{4f} (84.0 eV) as a reference. A charge neutralisation gun was used for insulating samples that delivers low energy electrons and argon ions to the sample surface. The samples were prepared for XPS by depositing 5 μ L of solution on a clean Si(100) substrate and left to dry. The samples were rinsed three times with DI water then left to dry again in air at room temperature in a laminar flow hood to minimize contamination (Model VLF 4B, Envair, Haslingden, Lancs, U.K.) before being tested.

5.2.7. Atomic Force Microscopy (AFM) and Electrostatic Force Microscopy (EFM):

Tapping mode AFM images were acquired in air using a Dimension Nanoscope V system (Veeco Inc.) with NanoProbe tips (Veeco Inc.). The cantilever was 200–250 μ m long, with 1–5 N m^{-1} spring constant and 252 kHz resonant frequency. EFM measurements were carried out in air on a Dimension Nanoscope V system following the procedure as described in chapter 4.

5.2.8. Conductive AFM (c-AFM):

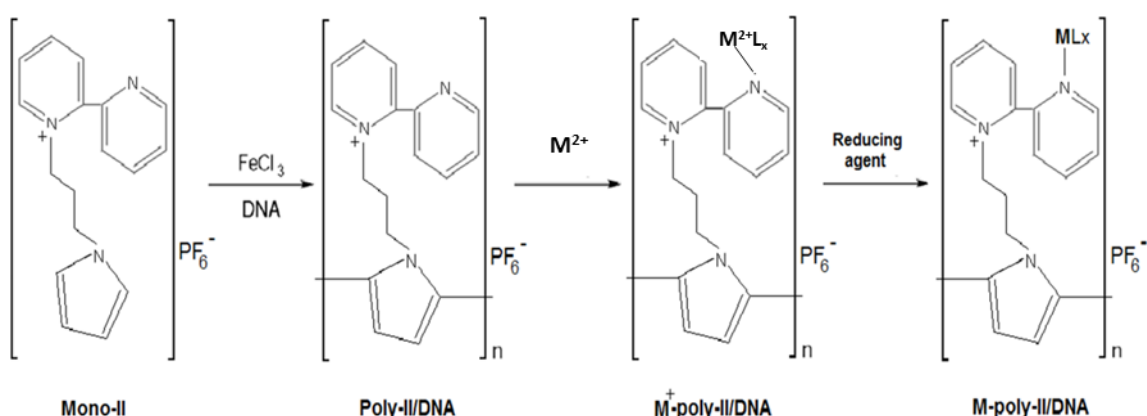
For c-AFM measurements, the same method that described in chapter 4 was applied with a constant bias between the tip and the sample (the tip was grounded).

Electrical contact was made by applying a drop of In/Ga eutectic to one corner of the chip and to the metallic chuck. C-AFM imaging was performed in contact mode, with an applied bias of 7.0 V. The imaged area was about 1 mm away from the In/Ga contact. The closed loop system of the Dimension V instrument makes it possible to reproducibly position the tip at a point of interest identified in the image of the nanowire and to record I-V measurements at that point. The resistance was estimated from the reciprocal of the slope of the I-V curve at zero bias.

5.3. Results and discussion

5.3.1. Templating Copper nanostructures on Poly-II/DNA and poly-III/DNA hybrids nanowires

This approach uses individual strands of DNA to template the growth of the CPs (poly-II and poly-III). The resulting functionalised poly-II and poly-III/DNA hybrid materials are formed as nanowires which were then studied for their ability to undergo metallisation using aqueous solution of $\text{Cu}(\text{NO}_3)_2$ as a source of Cu^{2+} ions and ascorbic acid was added to reduce the Cu(II) ions to metallic Cu^0 . [5] Scheme 20 illustrates the approach for the preparation of Cu-Poly-II/DNA hybrid nanostructures.



Scheme 20. DNA-templated synthesis of poly-II nanowires and deposition of metal on these nanostructures, where M= the targeted metal and L= Ligand.

Cu-Poly-II/DNA and Cu-Poly-III/DNA nanowires were synthesised in three steps: CP/DNA nanowires were formed using an aqueous solution of FeCl_3 (1 mM) as oxidant as described in chapter 4. These were then treated with an aqueous solution of $\text{Cu}(\text{NO}_3)_2$ with thorough mixing and allowed to react for 10 minutes. Finally, ascorbic acid was added and again thoroughly mixed. Then the reaction solution was allowed to stand for at least 1 hour at room temperature prior to spectroscopic analysis. Nanowire formation was investigated using different microscopic techniques after 1 hour and 24 hours of reaction time.

5.3.2. FTIR spectroscopy:

FTIR spectroscopy was used to investigate copper deposition on poly-II and poly-III/DNA templated nanowires employing an aqueous $\text{Cu}(\text{NO}_3)_2$ solution as a source of Cu^{2+} and ascorbic acid solution as a reductant. Figure 102 shows the infrared spectra for ct-DNA (a), poly-II/DNA (b) and Cu-poly-II/DNA after addition of ascorbic acid (c). The relevant bands and their assignments are shown in Table 8.

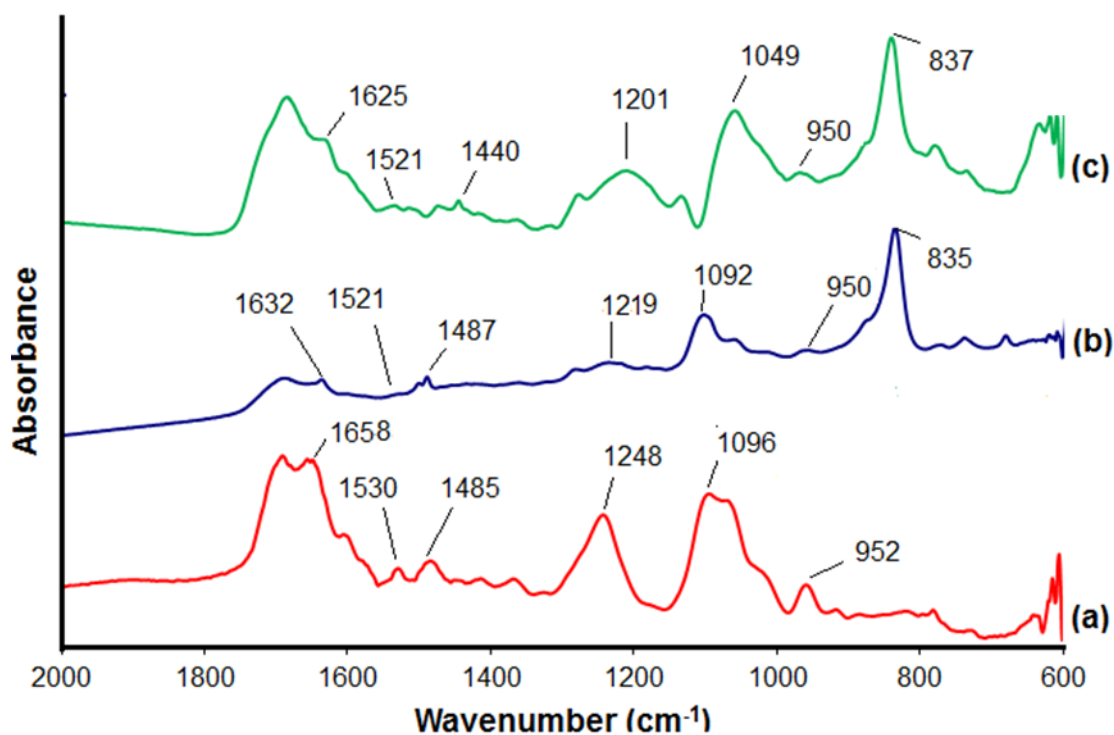


Figure 102. FTIR spectra of ct-DNA (a) poly-II/DNA (b) and Cu-poly-II/DNA hybrid (c).

Wavenumber (cm ⁻¹) in Ct-DNA	Wavenumber (cm ⁻¹) in poly-II/DNA	Wavenumber (cm ⁻¹) in Cu-poly-II/DNA	Assignment*
1658	1632	1625	C-N stretch, Adenine (C=N stretch of the guanine)
1530	1521	1521	in-plane C=N vibration of cytosine and guanine
1248	1219	1201	PO ₂ ⁻ asymmetric stretch,
1096	1092	1049	PO ₂ ⁻ symmetric stretch,
952	950	950	C-O deoxyribose, C-C
-	835	837	PF ₆ ⁻

*Assignments of DNA vibration bands reference to [17-21].

Table 7. The main bands observed in the FTIR spectra of ct-DNA, Poly-II/DNA and Cu-Poly-II/DNA in the region of 2000-600 cm⁻¹.

The FTIR spectra of the poly-II/DNA (b) and Cu-poly-II/DNA (c) samples show the same general features with some shifts compared with the spectrum of free DNA (a). Changes in band positions and intensities are apparent for the nucleobase vibrations in the 1400-1800 cm⁻¹ region of the spectra. Additionally, the DNA spectrum shows a broad feature at 1096 cm⁻¹ from PO₂⁻ symmetric stretches whereas a narrower band arising from it at 1092 cm⁻¹ for poly-II/DNA which is shifted to lower frequency at 1049 cm⁻¹ in Cu-poly-II/DNA after metallisation.

The presence of absorption bands located in the 600 to 650 cm⁻¹ region in the FTIR spectrum of pure DNA makes it difficult to assign if any peak corresponding to Cu(I)-O vibrations in the Cu-poly-II/DNA sample spectrum, which is expected at ~ 620 cm⁻¹. [7, 22]

The expected band of Cu(II)-O in Cu-poly-II/DNA should be at 480 and 530 cm⁻¹. [22] These bands are located in a range which is not accessible on the instrument. Also intense IR band at 835 cm⁻¹ and 837 cm⁻¹ for poly-II/DNA and Cu-poly-II/DNA samples respectively are characteristics of the PF₆⁻ anion. [23]

The FTIR spectra of poly-III/DNA before and after metallisation are presented in figure 103. The relevant bands and their assignments are tabulated in table 9.

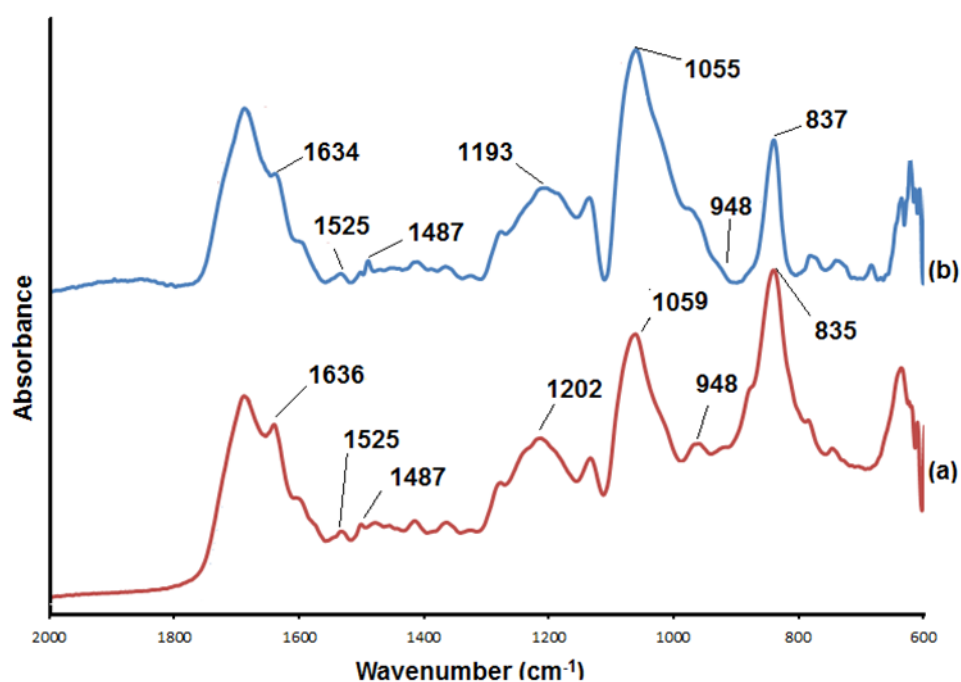


Figure 103. FTIR spectra of poly-III/DNA (a) and Cu-poly-III/DNA hybrid (b).

Wavenumber (cm ⁻¹) in Ct-DNA	Wavenumber (cm ⁻¹) in poly-III/DNA	Wavenumber (cm ⁻¹) in Cu-poly-III/DNA	Assignment
1658	1636	1634	C-N stretch, Adenine (C=N stretch of the guanine)
1530	1525	1525	in-plane C=N vibration of cytosine and guanine
1248	1202	1193	PO ₂ ⁻ asymmetric stretch,
1096	1059	1055	PO ₂ ⁻ symmetric stretch,
952	948	948	C-O deoxyribose, C-C
-	835	837	PF ₆ ⁻

Table 8. The main bands observed in the FTIR spectra of ct-DNA, Poly-III/DNA and Cu-Poly-III/DNA in the region of 2000-600 cm⁻¹

Generally, the spectra related to poly-III/DNA (a) and Cu-poly-III/DNA (b) show similar features and changes as described for poly-II/DNA before and after metallisation, especially those due to the phosphate backbone. The intense band at 1059 cm^{-1} for poly-II/DNA arising from PO_2^- symmetric stretches was shifted to lower frequency at (1055 cm^{-1}) in Cu-poly-II/DNA after metallisation.

Again, infrared absorption bands which are located in the $600\text{ to }650\text{ cm}^{-1}$ region of pure DNA makes it difficult to assign the absorption bands of Cu–O vibration of the Cu_2O here. The intense bands at 835 cm^{-1} and 837 cm^{-1} for poly-III/DNA and Cu-poly-III/DNA samples respectively are characteristics of the PF_6^- vibrations.

5.3.3. UV-Vis Absorption Spectroscopy

The UV-Vis absorption spectra of mono-II, poly-II, calf thymus (CT) DNA, and Cu-poly-II/DNA are recorded at room temperature in aqueous solution as shown in figure 104. CT-DNA solution and mono-II solution (CT-DNA and MII lines respectively) do not exhibit any characteristic absorption bands at wavelengths higher than 400 nm. The spectra of poly-II(PII), poly-II/DNA (PII/DNA), Cu(II)-poly-II/DNA (Cu(II)-PII/DNA) and Cu^0 -poly-II/DNA (Cu-PII/DNA/AA) indicate the absorption band at 350 nm due to π - π^* transition peak of poly-II. The two peaks which are shown at 480 and 530 nm are assigned to the bipolaron state formed during the polymerisation process. The spectrum of Cu(II)-poly-II/DNA (C(II)-PII/DNA) shows a strong broad absorption in the 700–900 nm range characteristic of aqueous Cu^{2+} . This peak disappears upon addition of the ascorbic acid (Cu-PII/DNA/AA) indicating the chemical reduction of Cu^{2+} ions. A new absorption band appears in the spectrum at 550 nm. This absorption band is consistent with the formation of copper nanoparticles which are known to absorb in this region due to surface plasmon resonance effect.[24, 25]

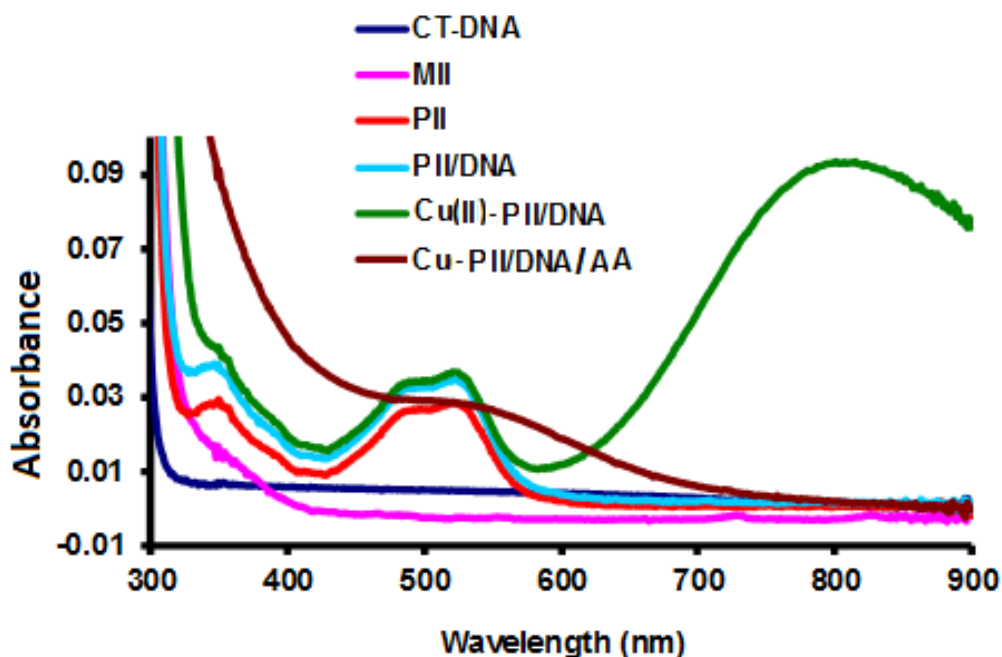


Figure 104. UV-Vis absorption spectra of 3.0 mM mono-II (MII), poly-II (PII), CT-DNA (CT-DNA), poly-II/DNA (PII/DNA), Cu(II)-poly-II/DNA (Cu(II)-PII/DNA) and Cu⁰-poly-II/DNA (Cu-PII/DNA/AA).

The UV-Vis absorption of poly-III/DNA, Cu²⁺-poly-III/DNA and Cu-poly-III/DNA was also recorded at room temperature in aqueous solution and these are shown in figure 105. The absorption band at 350 nm which is assigned to π - π^* transition peak of poly-III is observed in all the samples. The two peaks at 480-530 nm which also due to the bipolaron state formed during the polymerisation process. The spectrum of Cu(II)-poly-III/DNA (Cu(II)-PIII/DNA) shows a broad absorption band in the range 700–900 nm characteristic of aqueous Cu²⁺ as well as the double peak band assigned to bipolaron state. Upon addition of ascorbic acid the former is decreased significantly (~50%) indicating in this case partially reduction of Cu²⁺ ions. Additionally, the bipolaron band is lost and a new feature appears at ~ 470 nm (Cu-PIII/DNA/AA). This indicates the formation of copper nanoparticles that are either smaller in size than the case with poly-II or that there is CuO formed as well.[25-27]

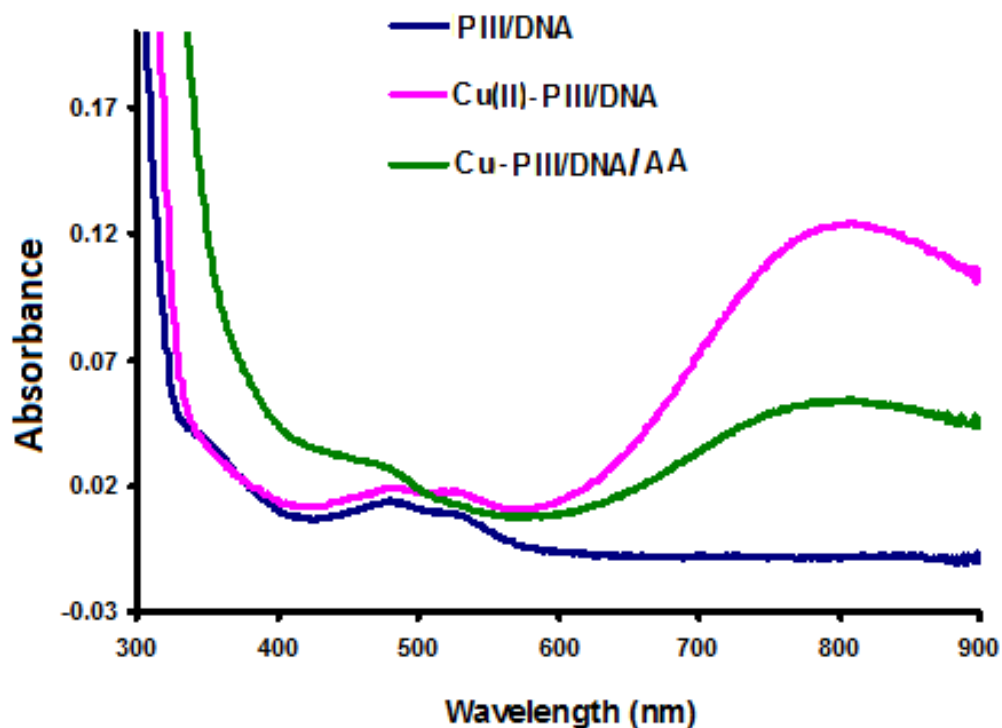


Figure 105. UV-Vis absorption spectra of poly-III/DNA(PIII/DNA), Cu(II)-poly-III/DNA (Cu(II)-PIII/DNA) and Cu⁰-poly-III/DNA (Cu-PIII/DNA/AA).

5.3.4. X-ray Photoelectron Spectroscopy

Poly-II and poly-III samples prepared using FeCl₃ as an oxidizing agent were analysed by XPS before and after washing the sample with DI water. Figure 106a shows the Fe 2p spectra of poly-II sample before washing. The peaks at 711.0 and 724.5 eV correspond to the binding energies of Fe 2p 3/2 and Fe 2p 1/2, respectively, which are attributed to the Fe³⁺ states.[28, 29] These features were not observed for the same sample after washing with DI water (figure 106b). This suggests that the Fe containing species incorporated during the polymer formation is not tightly bound (eg. coordinated to pyridyl groups). This is clear evidence that there is no chemically bonded Fe with the free nitrogen atom of the bipyridine molecules.

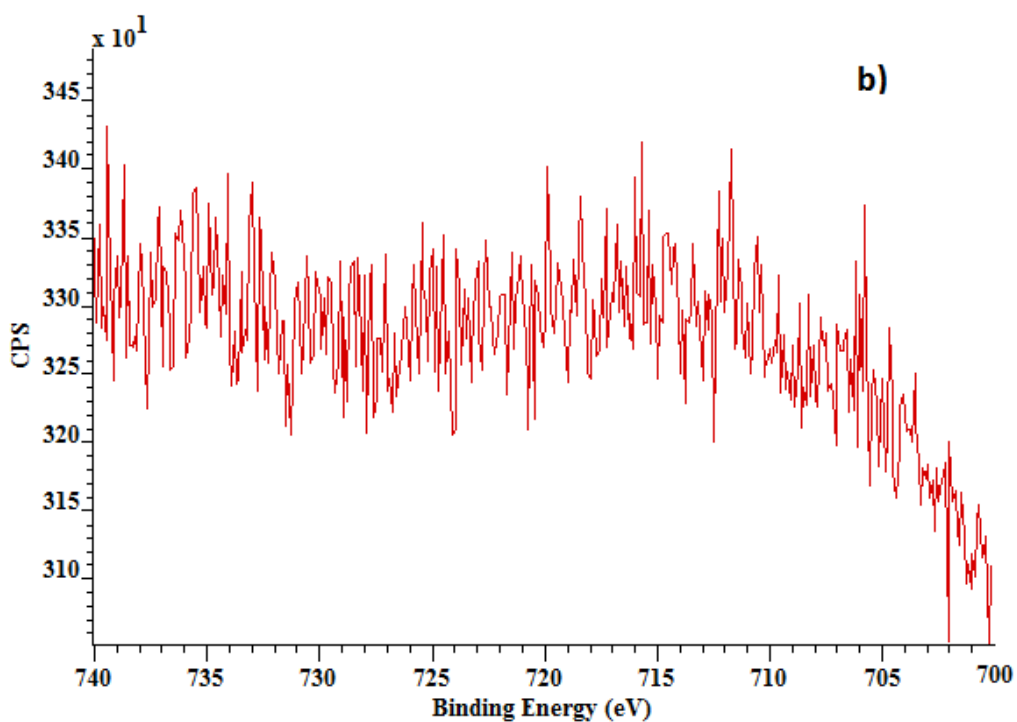
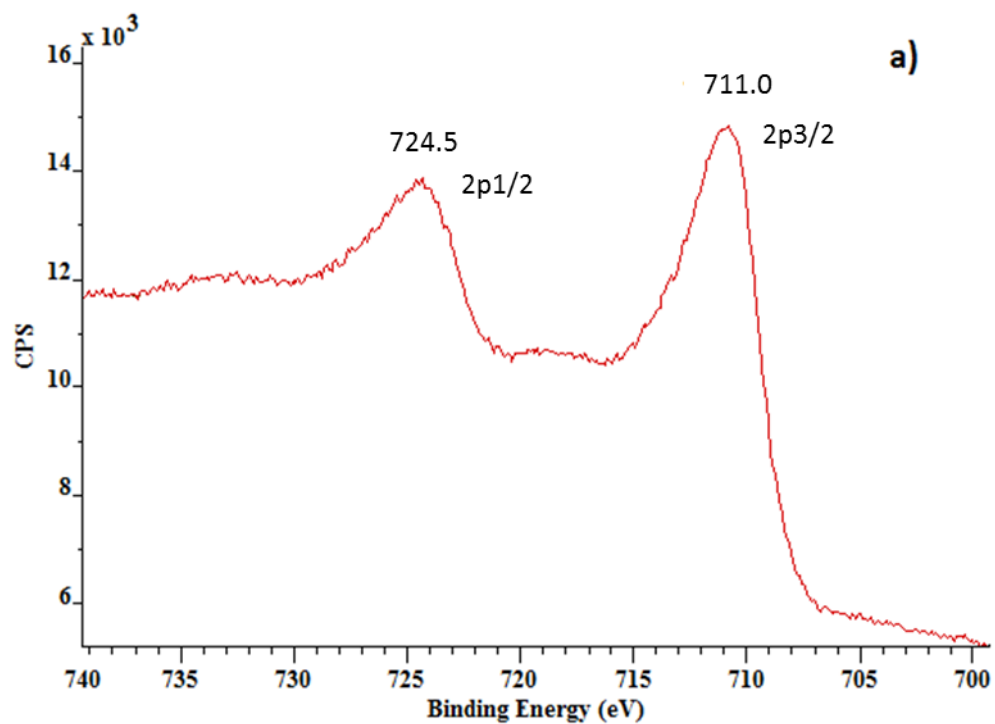


Figure 106. XPS Fe 2p spectra of poly-II sample on Si/SiO₂ substrate, prepared using FeCl₃ as oxidising agent (a) before washing with DI water, (b) after washing with DI water.

XPS survey scan spectra of Cu-poly-II/DNA (figure 107) and Cu-poly-III/DNA (appendix I) revealed the presence of the elements C, N, O, Cu, F, P and Si. In addition, they indicated the absence of iron, which confirm that the FeCl₃ was used only to drive the polymerisation and was not bound by the pyridyl groups of the CP or DNA.

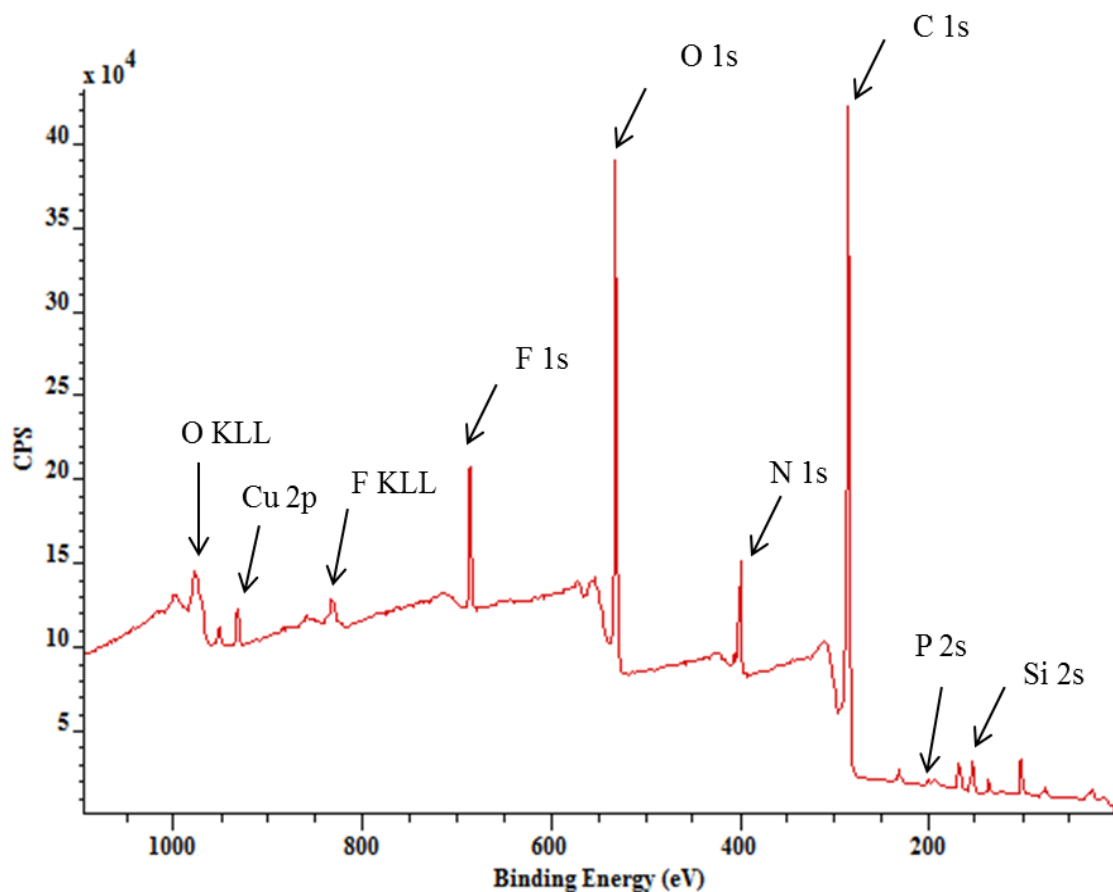


Figure 107. XPS survey spectrum of Cu-poly-II/DNA nanowires sample.

The C1s spectra are presented in figure 108. C1s of Cu-poly-II/DNA, figure 108a, can be resolved into four main peaks at 284.6, 286.2, 288.1, and 289.0 eV. Similar features are observed in the C1s spectrum for Cu-poly-III/DNA (figure 108b) at 284.6, 286.3, 288.2, and 289.1 eV. Four components have also been observed in C1s spectra of pure DNA by previous workers,[9, 30, 31] although the peak at 284.4 eV is dominant in pure DNA. The two components at the lowest binding energy are assigned to C-H, C-C, and C-N species from poly-II, poly-III and DNA.[9, 31] The third peak at 288.1 and 288.2 eV for Cu-poly-II/DNA and Cu-poly-III/DNA respectively is attributed to carbons in

functional group of the type, C=N, mainly from pyrrole and bipyridyle molecules, because this feature is more intense than in pure DNA.[30] The fourth, weak, peak at 289.0 and 289.1 eV for Cu-poly-II/DNA and Cu-poly-III/DNA respectively is may be assigned to C=N⁺ carbons in bipyridyl molecules,[9, 32] and/or to carbon adjacent to N that is bonded to copper (C=N-Cu), due to the formation of a Cu-N bond.[33, 34]

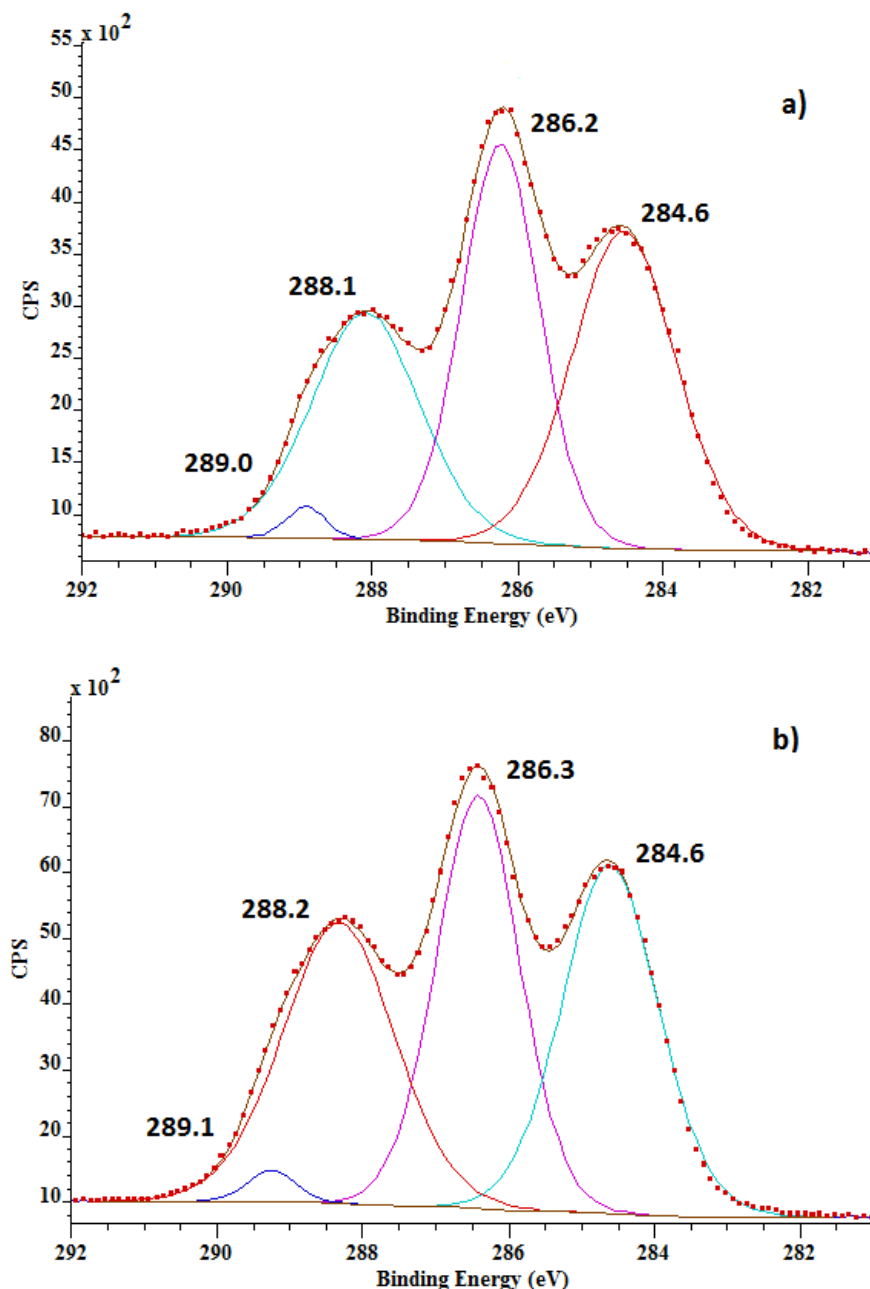


Figure 108. XPS spectra of (a) C1s spectrum of Cu-poly-II/DNA and (b) C1s spectrum of Cu-poly-III/DNA. Peak positions of the fitted components are indicated. The binding energies are reported after calibration of the energy scale so that the main C 1s binding energy is 284.6 eV.

X-ray photoelectron spectroscopy (XPS), which is very sensitive to the oxidation state of copper (e.g., Cu^{2+} , Cu^+ and Cu^0), has been used to study the composition of the Cu-CPs/DNA nanostructures samples. The reference peak for C1s was set at 284.6 eV. Figure 109 shows the Cu 2p region of the XPS spectra of Cu-poly-II/DNA nanostructures which features the Cu 2p_{3/2} and 2p_{1/2} binding energies located at 932.3 and 952.1 eV, respectively and fall within the expected range for metallic Cu^0 . [15, 35] These two peaks are located with a separation of 19.8 eV which is in good agreement with the established values for the 2p_{1/2}-2p_{3/2} splitting in metallic Cu^0 [15, 36]. Additional main and satellite peaks of Cu-poly-II/DNA were also detected. Two main broad peaks located at 933.6 eV (Cu 2p_{3/2}) and 953.6 eV (Cu 2p_{1/2}) respectively are in agreement with previous reports on copper oxide. [37] Copper can form oxides as both, cupric (CuO) and cuprous (Cu₂O) oxide. These can be distinguishable from each other, as the main peak of cupric form, CuO, is accompanied by the presence of intense shake-up satellites at ca. 8 eV higher binding energy, whereas these “shake-up” satellites are almost absent for Cu(I) materials. [22, 37] In addition, the Cu 2p_{3/2} spectrum of CuO is relatively broad (~3.4 eV), where the spectrum of Cu₂O is significantly narrower (~1.9 eV). [37] These facts indicate the presence of CuO in the sample of Cu-poly-II/DNA in addition to metallic Cu^0 .

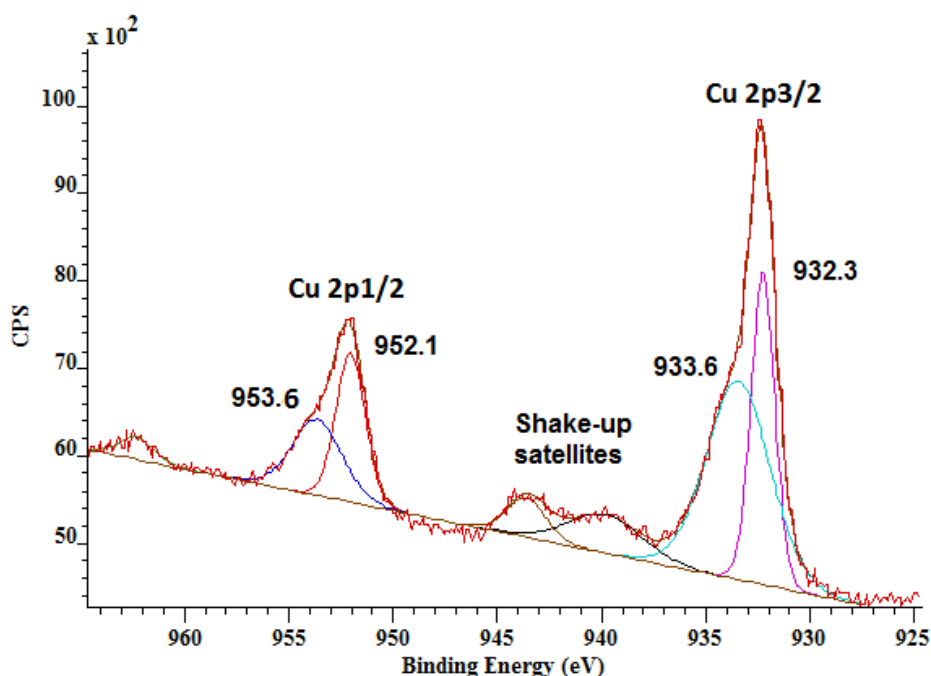


Figure 109. A representative fit of copper (2p_{3/2} and 2p_{1/2}) spectra for Cu-poly-II/DNA nanowires. The binding energies are reported after calibration of the energy scale so that the main C1s binding energy is 284.6 eV.

The Cu 2p region of the XPS spectrum of Cu-poly-III/DNA nanowires, figure 110, shows peaks at binding energies of 932.9 and 952.7 eV for Cu 2p_{3/2} and 2p_{1/2} respectively which again fall within the expected range for metallic Cu⁰[15, 29, 38, 39]. These two peaks are located with a separation of 19.8 eV which is again in good agreement with the established values for the 2p_{1/2}-2p_{3/2} splitting in metallic Cu⁰. [36] Other peaks detected at 933.6 and 953.5 for Cu 2p_{3/2} and Cu 2p_{1/2} respectively are in agreement with previous reports on cupric oxide (CuO). [37] The Cu 2p_{3/2}-Cu 2p_{1/2} peak separation of 19.9 eV is typical of the CuO state. [37] In addition, the main peak of CuO is relatively broad (3.4 eV) and accompanied with a satellite peak at about 9 eV higher binding energies which is absent in the case of Cu₂O. [37, 40] However, due to the small satellite peak, there is obviously much less Cu²⁺ apparent in the Cu-poly-III/DNA samples than observed in the Cu-poly-II/DNA samples.

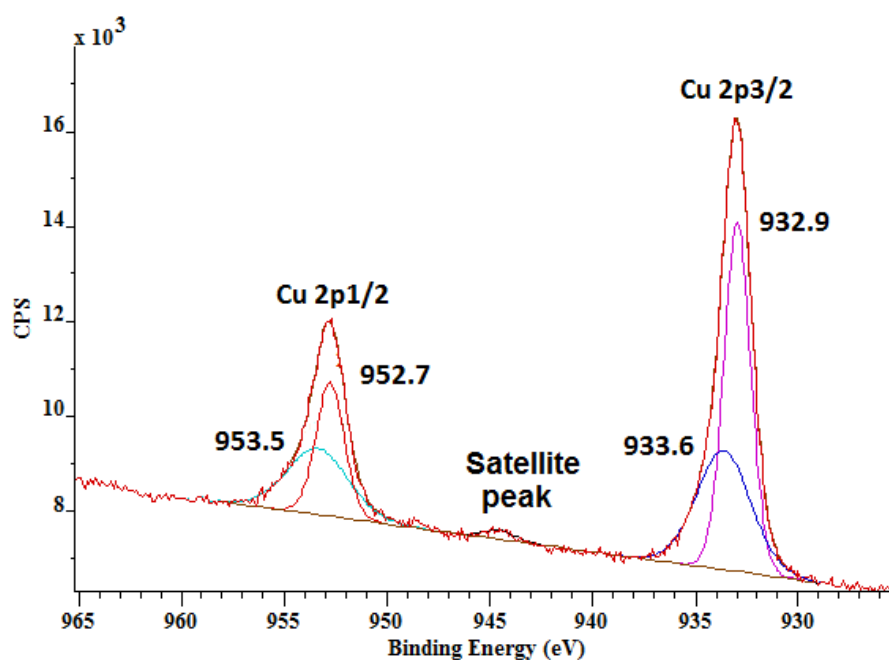


Figure 110. A representative fit of copper (2p_{3/2} and 2p_{1/2}) spectra for Cu-poly-III/DNA nanowires. The binding energies are reported after calibration of the energy scale so that the main C 1s binding energy is 284.6 eV.

These XPS results of Cu-poly-II/DNA and Cu-poly-III/DNA samples are consistent with the presence of metallic Cu⁰ in addition to CuO due to the presence of a small CuO layer around the nanoparticles. The presence of Cu⁰ metal and CuO would be expected

for structures containing a copper core with a surficial oxide. This oxide layer is a result of the unavoidable exposure of the samples to air and the necessity of being in a dried form for the XPS measurement.[41] In summary, although the FTIR spectra of Cu-poly-II/DNA and Cu-poly-III/DNA show absorption bands which may be attributed to the possible presence of Cu₂O, the XPS results together with in combination with the UV-Vis absorption spectra suggest the formation of Cu⁰ core structure with CuO upon CPs/DNA nanowires.

5.3.5. AFM characterisation of Cu-poly-II/DNA and Cu-poly-III/DNA nanowires

The morphology of Cu-poly-II/DNA nanostructures was investigated using AFM in tapping mode. Samples for AFM were prepared by molecular combing onto oxidized Si wafers (Si/SiO₂) which had been silanized by exposure to trimethylchlorosilane vapour as described earlier. Figure 111 shows AFM image of Cu-poly-II/DNA nanostructures 1 hour after preparation. Continuous but uneven coverage of the template is apparent with a great variation in structure height indicating the non-uniform deposition of Cu⁰ along the length of the poly-II/DNA template. Regions of the template exhibit extensive Cu⁰ deposition, up to ca. 25 nm in height. Values as low as ca. 5 nm are also observed where less significant levels of metallisation have taken place (e.g. wire A). Some strands show a granular morphology attributed to the “nucleation and growth” mechanism of Cu⁰ deposition along the polymer/DNA templates yielding small metallic clusters of Cu⁰ along the template. These Cu⁰ clusters act as seed particles for further reduction of Cu²⁺ at their surface, resulting in Cu⁰ growth upon poly-II/DNA templates.[15, 42, 43] Other nanostructures can also be seen with lower packing density of the Cu⁰ nanoparticles along them, where less substantial Cu⁰ deposition has taken place. The heights of these regions however (ca. 2.0-5.0 nm), suggest that Cu⁰ deposition has still taken place upon these templates (e.g. wire B). A high level of non-specific deposition of Cu⁰ particles with a large variety in height, typically ca. 1.0 - 20 nm, are also observed across the substrate surface. This non-specific deposition of Cu⁰ occurred because of free Cu(II) ions in solution being

reduced by ascorbic acid and being deposited on the substrate during the alignment process.[5]

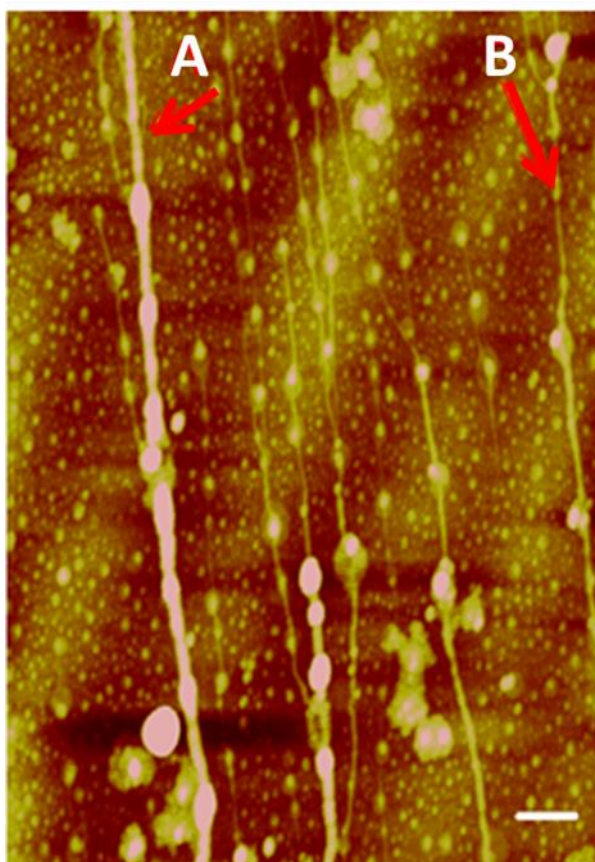


Figure 111. Tapping Mode AFM height image of Cu-poly-II/DNA nanowires aligned on Si/SiO₂ substrate, observed 1 hour after preparation. Scale bar = 500 nm, height scale = 20 nm.

Different incubation times lead to different types of Cu nanostructures. When the duration of the reaction is extended, the small particles redeposit onto larger crystals or particles to form thicker nanostructures and also driven towards the formation of smooth and continuous nanowires.[7, 44, 45] Figure 112 shows the resulted nanowires After 24 hours of reaction time. Continuous coverage was achieved resulted in relatively smooth metal-coated nanowires (e.g. indicated by blue arrows) with 10 - 30 nm in size. Some gaps along the metallised segments (indicated by red arrows) did not have noticeable metal deposition with heights ranging from 2 to 5 nm. These are

attributed to non-metallised polymer/DNA regions. Again lot of nonspecific Cu^0 deposition can be also clearly seen (e.g. the areas that circled by the blue circles)

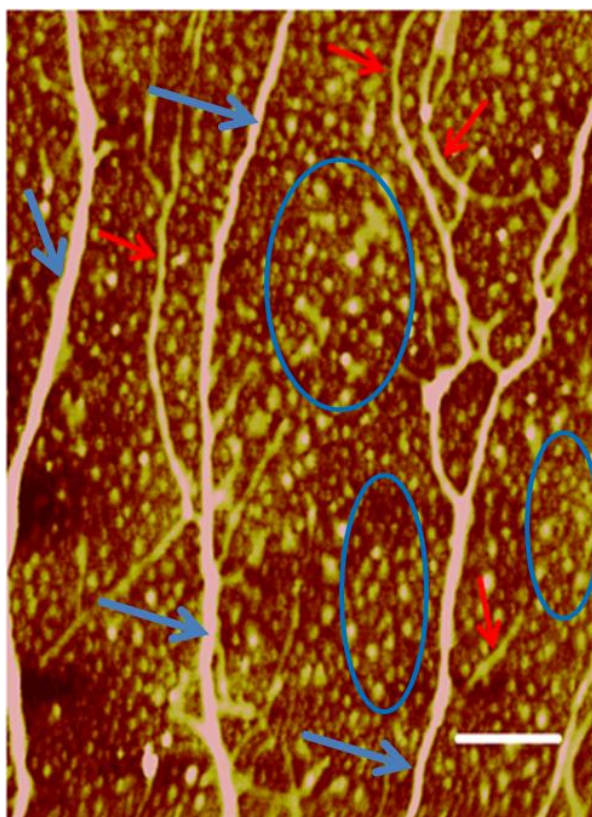


Figure 112. Tapping Mode AFM height image of Cu-poly-II/DNA nanowires aligned on Si/SiO₂ substrate, observed 24 hours after preparation. Scale bar = 1 μm , height scale = 20 nm.

Even longer incubation times resulted in thicker wires with diameters up to ~ 50 nm. Figure 113 show a thick nanowire, with an average diameter ~ 45 nm, deposited 48 hours after preparation.

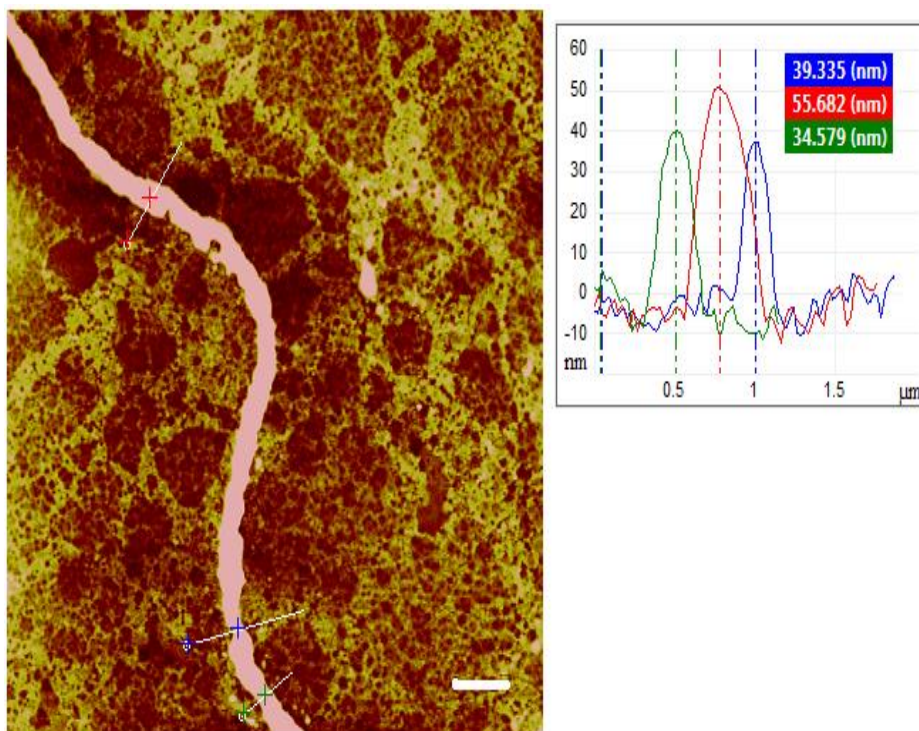


Figure 113. Tapping Mode AFM height image of Cu-poly-II/DNA nanowires deposited on Si/SiO₂ substrate, observed 48 hours after preparation. Scale bar = 1 μm, height scale = 20 nm.

From further analysis, figure 114 shows line traces along Cu-poly-II/DNA nanowires referenced against the substrate at different stages of reaction times; 2 hours (a) and 48 hours (b). This clearly shows the effect of reaction time upon the thickness and regularity of the nanowires. Material isolated 2 hours after the start of reaction showed diameter range from 3 to 15 nm with a variation of about 5 orders of magnitude in the diameter along the length. At longer reaction times (48 hours) the particles are densely packed on the CP/DNA template forming thicker continuous structure with diameter range from ~ 40 to ~ 65 nm with a variation of about 50% in the diameter was observed. This could describe the formation of these continuous metal-nanostructures as it occurs upon standing by gradual deposition of the metal upon the template. By time, the structures become thicker, smoother and their thickness appears more uniform along the length of the nanowire.

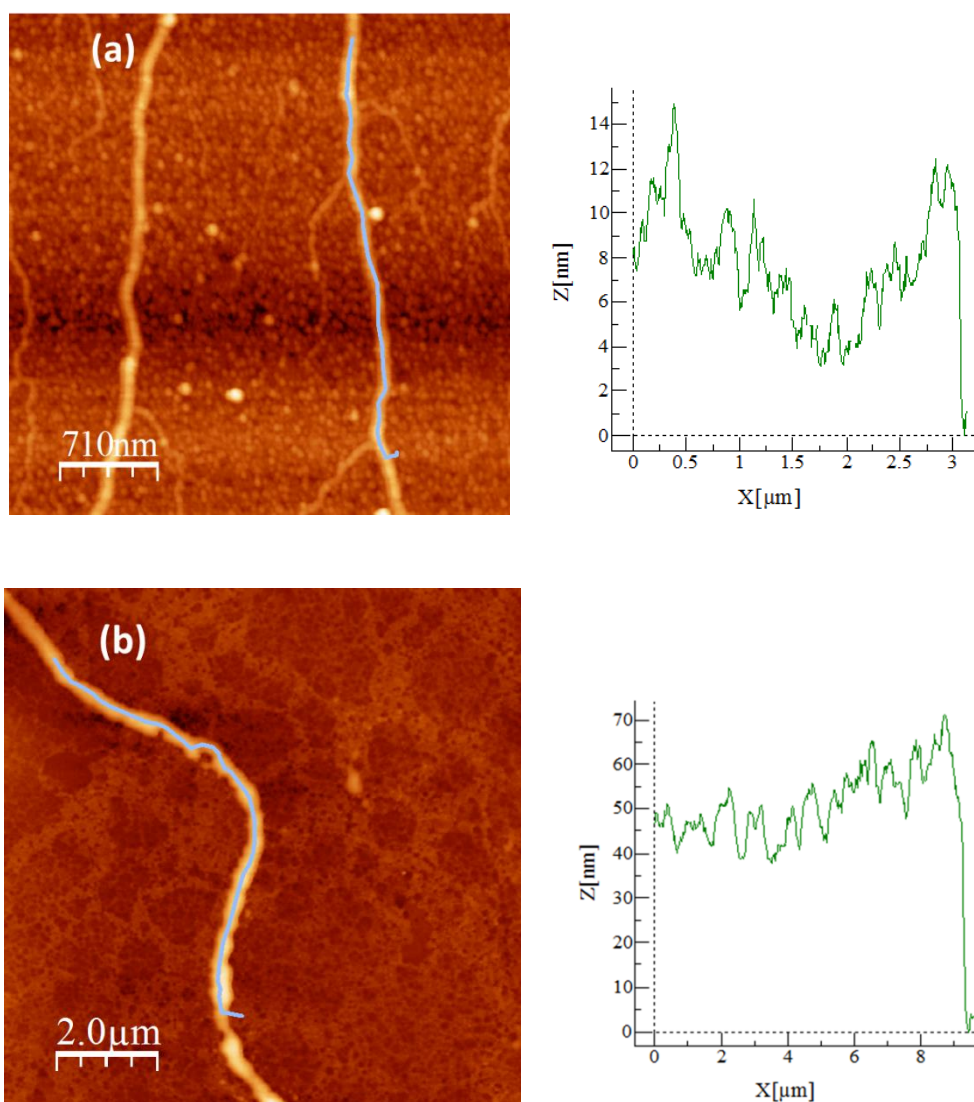


Figure 114. Tapping Mode AFM height images of Cu-poly-II/DNA nanowires deposited on Si/SiO₂ substrate, observed 2 hours (a) and 48 hours (b) after preparation combined with their line traces referenced against the substrate.

Similar analysis has performed on samples of Cu-poly-III/DNA nanowires which were prepared and deposited after 24 hours of reaction time. These showed in continuous morphology structures similar to those described in Cu-poly-II/DNA nanostructures. Figure 115 shows an AFM image of Cu-poly-III/DNA nanowires deposited on Si/SiO₂ substrate. The nanowires formed appear quite continues but irregular in shape. This could be due to deposition taking place to different extents along poly-III/DNA templates. The nanowire heights vary from ca. 10 to 30 nm in diameter. Some parts of the structures indicate non-metallised regions (e.g. indicated by red arrows) with heights

ranging from 2 to 5 nm consistent with the polymer/DNA nanowires. Along bare DNA strands also exist as evidence from thinner diameters (e.g. indicated by blue arrows) with heights ranging from 0.5 to 2 nm. This is consistent with other studies of single duplex DNA molecules by AFM.[46] That means not all the template DNA is modified during the initial templating reaction to form polymer nanowires. Nonspecific Cu^0 deposition can also be seen in some extent (e.g. the area which is red circulated).

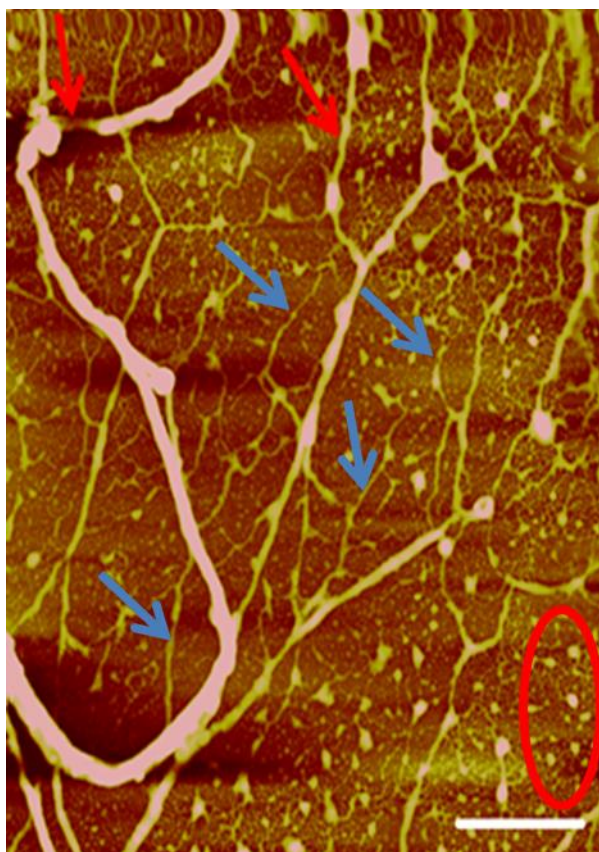


Figure 115. Tapping Mode AFM height image of Cu-poly-III/DNA nanowires deposited on Si/SiO₂ substrate, observed 24 hours after preparation. Scale bar = 1 μm , height scale = 20 nm.

We have previously shown (chapter 4) that conductive polymers (poly-I, poly-II, and poly-III) produce regular and smooth nanowires when templated on λ -DNA by oxidative chemical polymerisation of the monomer in a solution of λ -DNA. The Cu^0 metallized nanowires (Cu-poly-II/DNA and Cu-poly-III/DNA) are less uniform compared with the case before metallisation. Figure 116 shows a comparison between AFM height images of poly-II/DNA nanowires before metallisation (A-a) and

Cu-poly-II/DNA nanowires after metallisation (B-a). The line trace along several microns of Cu-poly-II/DNA nanowires after metallisation (B-b) shows a greater variation in structure height than the line trace corresponding to the non-metallized poly-II/DNA nanostructure (A-b). This indicates the non-uniform deposition of Cu^0 along the length of poly-II/DNA nanowire. The surface plot of poly-II/DNA before metallisation (A-c) shows a smooth and uniform height of the nanowire along its length, which is rather different compared to the rough and variable height of the nanowire after metallization (B-c).

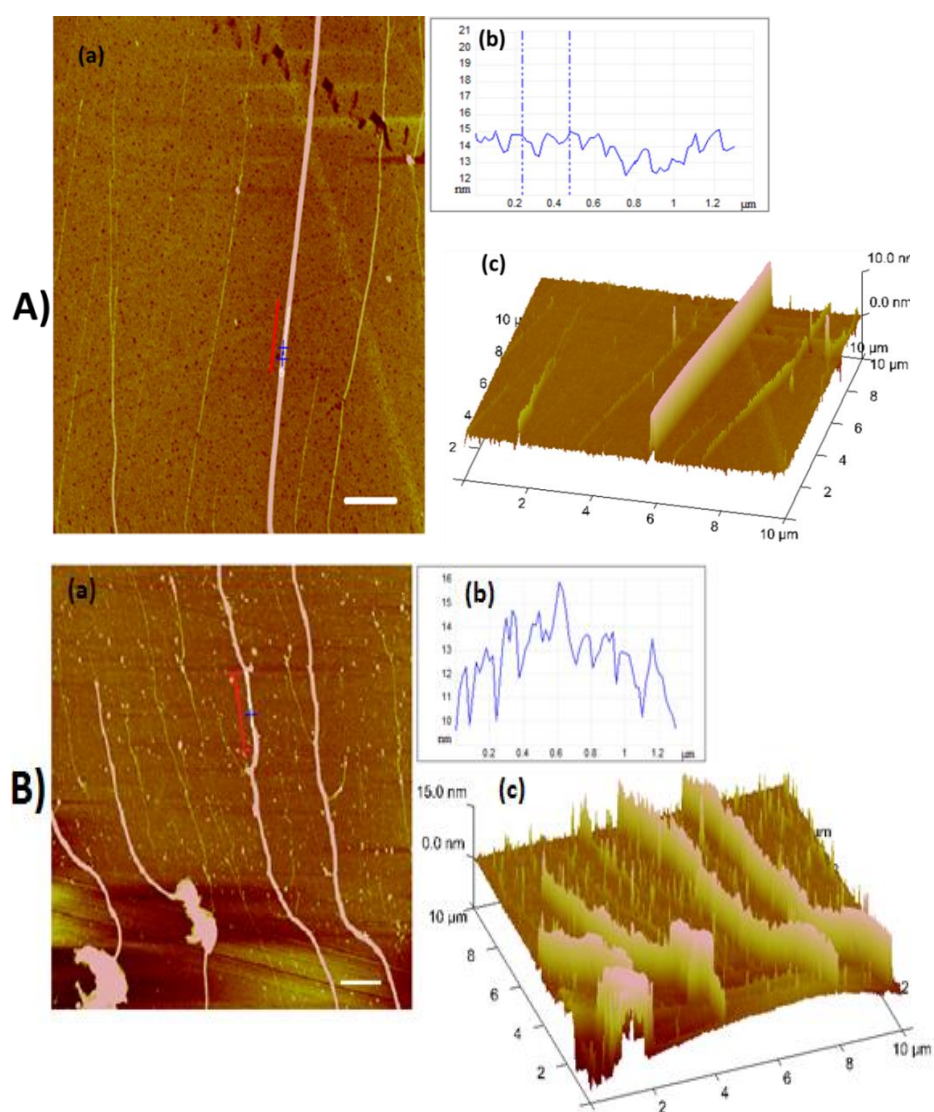


Figure 116. Tapping Mode AFM height images of (A-a) poly-II/DNA nanowires before metallisation immobilized upon a Si/SiO₂ substrate, modified with a TMS, (B-a) Cu-poly-II/DNA nanowires after Cu^0 metallisation, with (A-b) and (B-b) showing the corresponding line trace of (A-a) and (B-a) respectively. (A-c) and (B-c) showing the corresponding surface plot of (A-a) and (B-a) respectively. Scale bar= 1 μm , height scale=20 nm.

However in comparison with copper nanowires prepared using the templating method directly onto DNA, this approach with functionalised polymer/DNA templates, resulted in more continuous morphologies with the nanostructures appearing to be less granular. This provides more regular nanowire structures, with largely continuous metal coatings (figure 117b). In comparison, the growth of copper nanostructures on DNA itself exhibited more discontinuities forming more granular metal coating (white arrows, figure 117a).[2, 8, 15, 45]

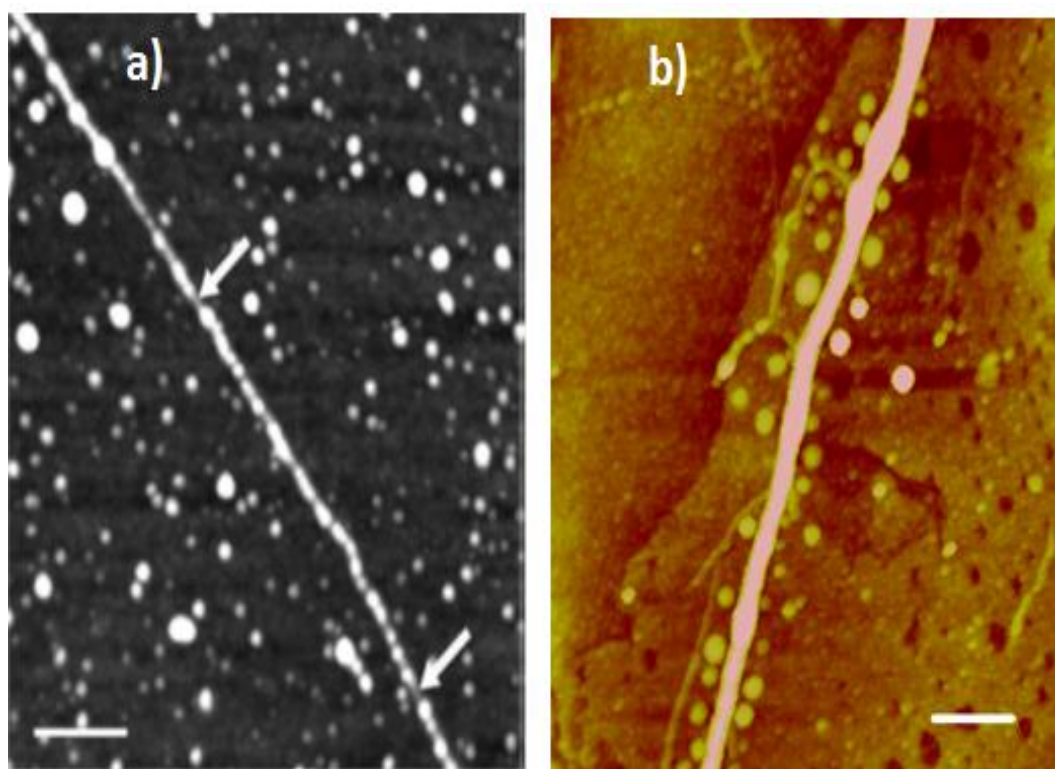


Figure 117. Tapping Mode AFM height images showing a comparison between the morphology of : (a) Cu/DNA nanowire, scale bar=200 nm, height scale=8 nm, with permission from reference[15]. And (b) Cu-poly-II/DNA nanowire, 48 hours after preparation, scale bar=200 nm, height scale=20 nm, using $\text{Cu}(\text{NO}_3)_2$ as a source of Cu^{2+} and ascorbic acid as a reducing agent in both methods.

5.3.6. EFM characterisation of Cu-poly-II/DNA and Cu-poly-III/DNA nanowires

The electrical conductivity of the resulting nanostructures was probed by imaging the phase shift using the EFM technique. Figure 118 shows AFM and EFM images of Cu-poly-II/DNA nanowires taken after 1 hour of reduction on SiO_2/Si surface with a SiO_2 thickness of 200 nm. AFM image shows Cu-poly-II/DNA nanowires with

various morphologies and diameters as described above. The continuous nanostructures attributed to Cu-poly-II/DNA nanowires (heights: 10 – 25 nm) give rise to a negative phase shift when imaged using EFM (red arrows) on figure 118(b), which is indicative of conducting materials.[15] In contrast, structures with “beads-on-a-string” morphology show a positive phase shift (e.g. the area within the blue square) indicating a lack of electrical conductivity along the length of the structures; this lack of conductivity could be due to tunneling barriers at various points along the nanostructure preventing efficient charge transport.[15, 47] The size effect also contributes to the total resistivity of the nanostructure. The small grain sizes increase the electrical resistivity by means of grain-boundary scattering.[48, 49]

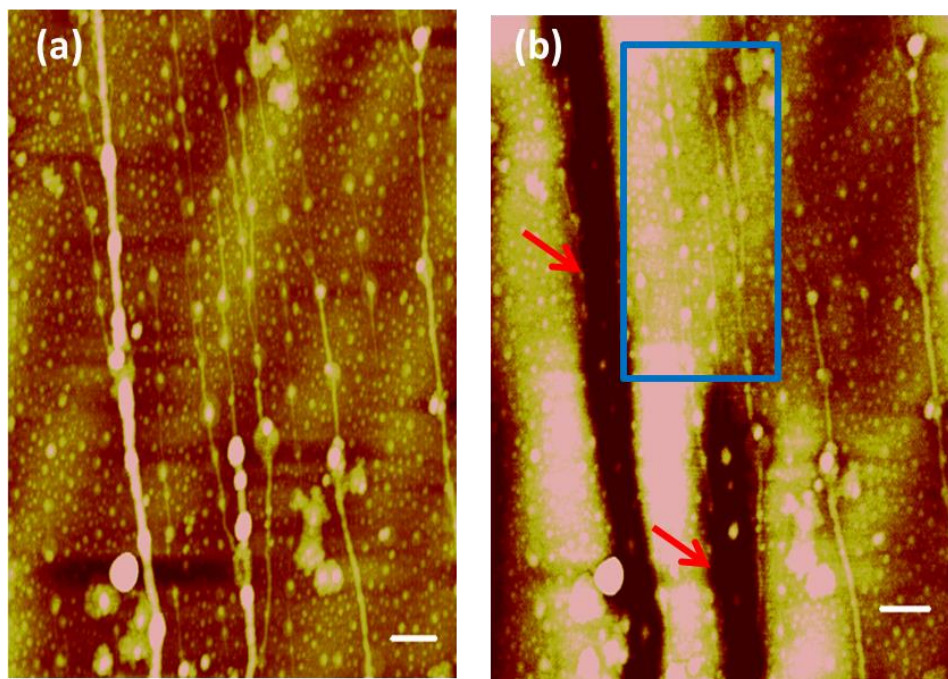


Figure 118. (a) AFM image of Cu-poly-II/DNA nanowires observed 1 hour after preparation on SiO₂/Si surface with a SiO₂ thickness of 200 nm with various nanostructures morphologies and diameters, grayscale 20 nm. (b) Correspondent EFM Phase image of the same nanowires at a tip/sample bias of +6 V and lift height of 60 nm. Scale bar of both images = 500 nm.

Figure 119 presents an AFM image (a) of Cu-poly-II/DNA nanowire after 24 hours reduction on SiO₂/Si surface, and its corresponding EFM image (b) which been taken at a tip/sample bias of +6 V and lift height of 60 nm. The nanowire with a thickness of around 17 nm (c) appears as a dark line as shown in the EFM image (b); this corresponds to a negative phase shift as the tip crosses the nanowire and demonstrates

the existence of charge conduction in the wire. The inset on the figure shows the corresponding profile of the phase shift along a cross section of the nanowire. The W-shape observed is characteristic for polymer nanowires. [50, 51]

The expected parabolic dependence of phase shift on bias for voltages between -10 and +10 V was also observed (figure 119(d)); this confirms the phase is due to the scanned conductance effect rather than the trapped charge effect, which produce phase shifts that depend linearly on bias voltage.[52-54] All these findings indicate a conductive object. Interestingly the non-specific Cu^0 depositions seen on the substrate as small particles, show a positive phase shift indicating a lack of electrical conductivity. Indicating that they are not well connected to form a conduction pathway.

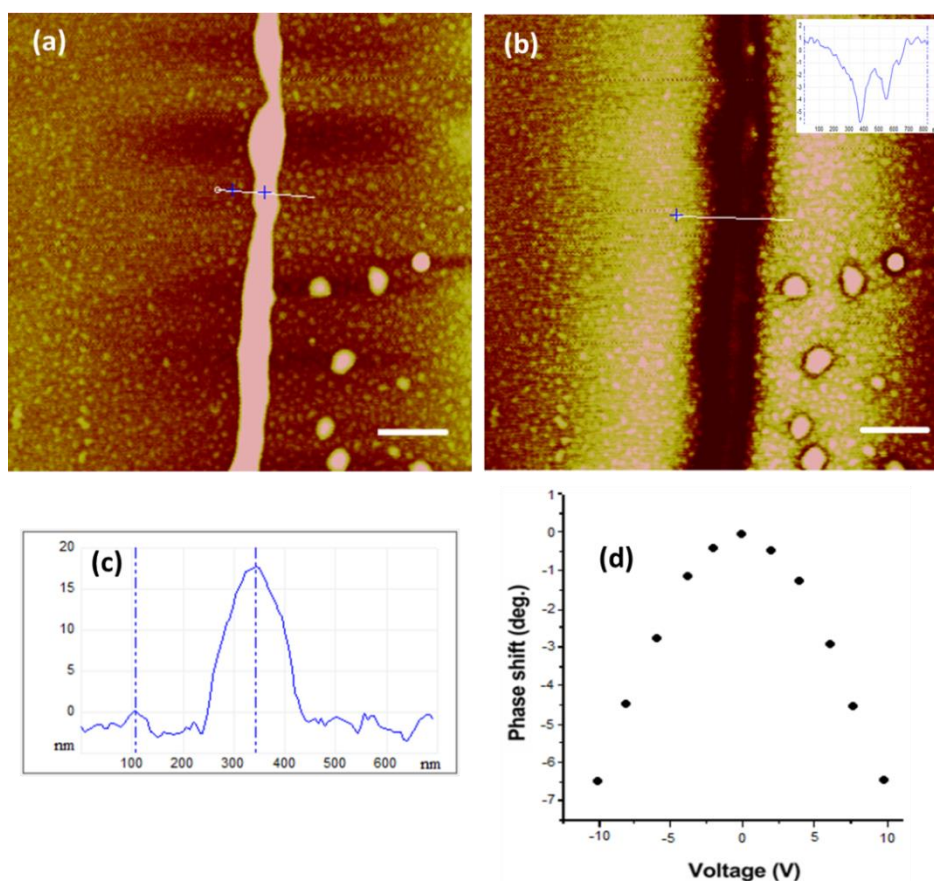


Figure 119. (a) AFM phase image of Cu-poly-II/DNA nanowire on SiO_2/Si surface with a SiO_2 thickness of 200 nm observed 24 hours after preparation. (b) The correspondent EFM phase image at a tip/sample bias of +6 V and lift height of 60 nm. The inset shows the corresponding profile of the phase shift along a cross section of the nanowire. (c) inset of the AFM image shows the height cross section of the nanowire at a diameter of ~17 nm, (d) shows the phase shift as a function of applied voltage of the same nanowire at a diameter of 17 nm, scale bar of both images = 500 nm.

Figures 120(a) shows AFM-phase image for Cu-poly-III/DNA nanowire which been taken 24 hours after addition of the ascorbic acid reducing agent. This nanowire has a diameter around 16 nm, figures 120(c). This nanowire appears as dark line in the EFM image, figures 120(b), which corresponds to a negative phase shift and demonstrates the existence of conductivity in the nanostructure.

The inset on the image, Figures 120(d), shows corresponding profile of phase shift along a cross section of the nanowire at a diameter of ~16 nm. The W-shape observed indicates polymer behaviour, as stated previously. The phase shift exhibits a parabolic dependence upon the sample bias, figure 120(e), but slight asymmetry associated with the parabola which attributed to the probability of some trapped charges being present.[52]

Much thinner strands segments, (indicated by red arrows), show a positive phase shift as seen by EFM, figures 120(b), indicating a lack of electrical conductivity. These strands did not have noticeable polymer or metal deposition. Their heights range from 0.5 – 2 nm attributed to free DNA, which consistent with other studies on DNA molecules,[10] and indicate that not all of template is modified during reaction. The non-specific Cu⁰ depositions (e.g. blue circulated particles) also show a positive phase shift indicating a lack of conductivity.

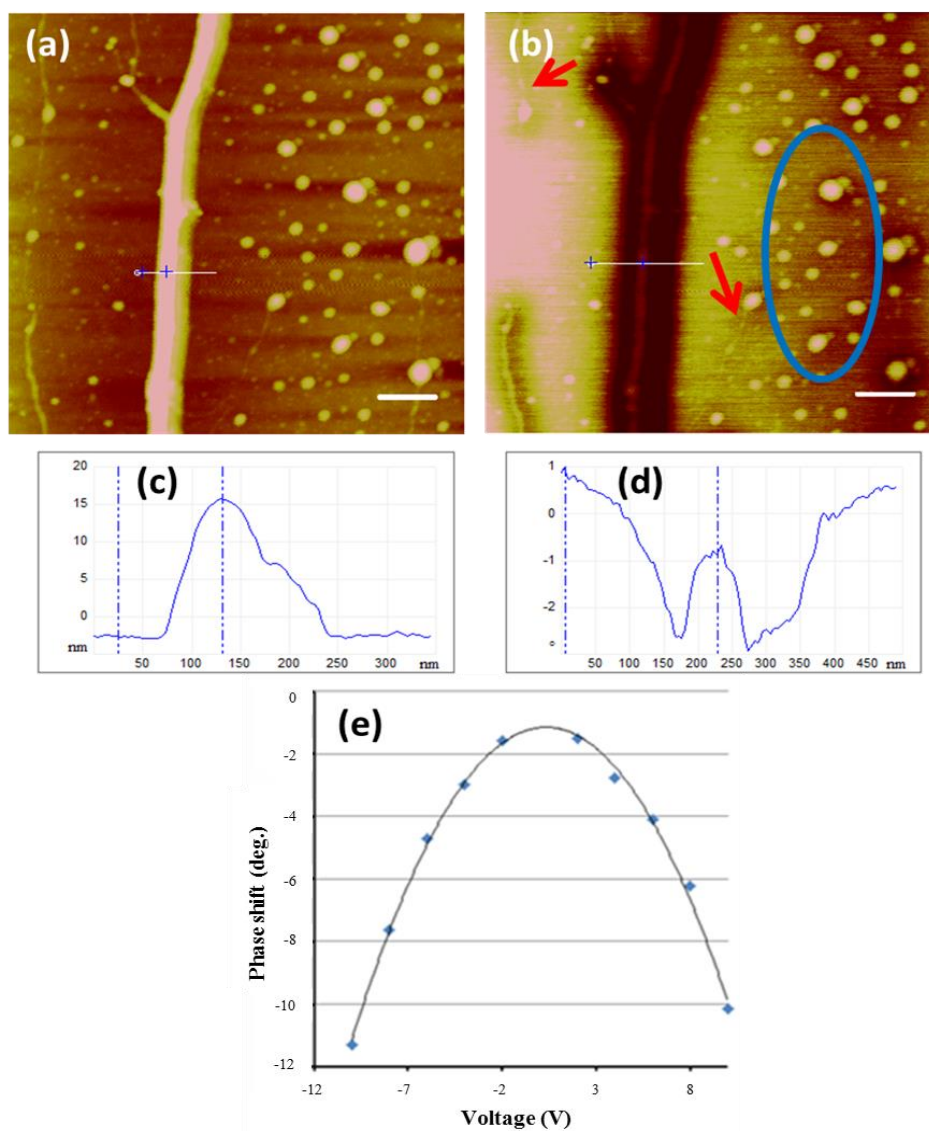


Figure 120. (a): AFM image of Cu-poly-III/DNA nanowires on SiO₂/Si surface with a SiO₂ thickness of 200 nm observed 24 hours after preparation. (b): The correspondent EFM Phase image at a tip/sample bias of +6 V and lift height of 60 nm Scale bar of both images= 500 nm. (c): Inset of the AFM image shows the height cross section of the nanowire at a diameter of ~16 nm, (d): shows the inset of the corresponding profile of the phase shift along a cross section of the nanowire at a diameter of 16 nm. (e): The phase shift as a function of applied voltage of the same nanowire on bias between -10V and +10V.

5.3.7. Conductive AFM of Cu-poly-II/DNA and Cu-poly-III/DNA nanowires

For c-AFM experiments, 2 μ L of Cu-poly-II/DNA solution was drop-cast from the reaction solution onto a SiO₂/Si substrate treated with TMS to control the hydrophobicity. By dragging the drop of solution to the edge of the substrate and

allowing it to dry, a dense network of nanowires was obtained. The edge of the network was connected with a few individual nanowires stretched out along the Si/SiO₂ surface.

Electrical contact between the network and the external circuit was made by applying a drop of In/Ga eutectic. Figure 121 shows c-AFM measurements of Cu-poly-II/DNA nanowires aligned on a SiO₂/Si substrate. The usual contact mode height image, figure 121(a), shows the presence of about 3 main nanowires. The mean diameter of the measured nanowire (indicated by red arrow) was 50 nm. Figure 121(b) provides a slightly clearer deflection error image, which is the difference between the measured deflection and the setpoint. The current image, figure 121(c), shows the associated current on the nanowires with a bias of 7.0 V applied between the cantilever and the metallic chuck. The imaged area was about 1.0 mm away from the In/Ga eutectic contact and the position of the tip along the nanowire was 1.5 μm. No measurable current was observed when the tip was above a clean area of SiO₂/Si, but currents were observed when the tip was in contact with the nanowire, which demonstrates that the current path from the tip to the In/Ga contact is through the nanowires lying on the surface and that charge does not reach the contact by leak and transport through the SiO₂/Si substrate.

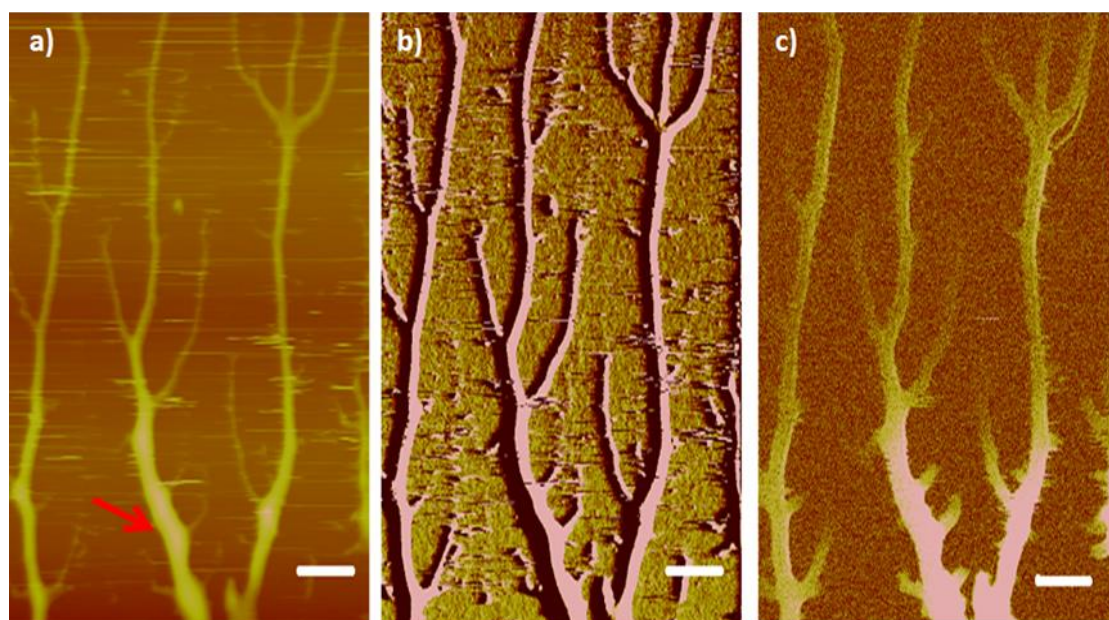


Figure 121. C-AFM measurements of Cu-poly-II/DNA nanowires aligned on a 200 nm SiO₂/Si substrate. a) Contact mode image the grayscale corresponds to a height of 13 nm; b) Deflection error image (the grayscale corresponds to a height of 10 nm) and c) c-AFM current image (the grayscale corresponds to a current of 100 nA). The tip-sample bias was 0.5V; the images (a)-(c) were acquired simultaneously. Scale bars (a-c)=1.5 μm.

Figure 122 shows a plot of the circuit resistance as a function of the relative distance, d , of the tip along the nanowire in the direction away from the massive deposit of Cu-poly-II/DNA. The resistance increases with d because the current must flow through a longer portion of the nanowire. The measured circuit resistance comprises three resistances: The resistance between the nanowire and the external circuit (R_{ext}), the tip/nanowire contact resistance (R_{tip}) and the resistance of the measured nanowire (R_{wire}).[9] The intercept on the resistance axis is clearly decreased with increasing deflection setpoint (higher applied force), Because the tip/nanowire contact (R_{tip}) has the most significant contribution to this intercept rather than the other resistances (R_{ext} and R_{wire}).[7]

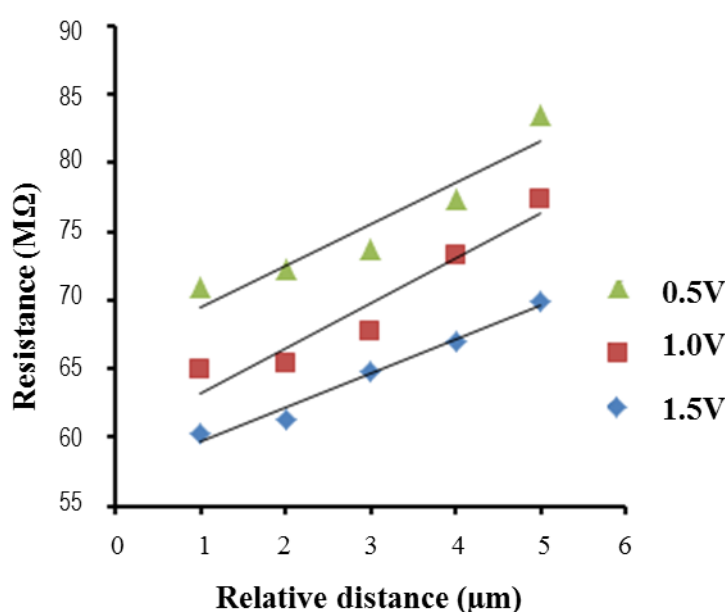


Figure 122. Cu-poly-II/DNA nanowire resistance at zero bias as a function of tip-contact relative distance for different applied forces in single-point c-AFM I-V measurements.

Based on the measured diameter (15nm), length (1.5 μm) and width (230 nm), the conductivity of Cu-poly-II/DNA nanowire was estimated to lie in a range from 3.1×10^{-2} to $7.1 \times 10^{-2} \text{ S cm}^{-1}$. This conductivity is higher than that have been estimated previously for poly-II/DNA nanowires ($5.0 \times 10^{-3} \text{ S cm}^{-1}$), and slightly less than the conductivity of PPy/DNA nanowires ($2.1 \times 10^{-1} \text{ S cm}^{-1}$) measured by the same technique (chapter 4).

The C-AFM measurements of Cu-poly-III/DNA nanowires were also run using the same procedure. Figure 123 shows the contact mode height image (a), deflection error image (b) and the current image (c). As shown in figure 123(a), using the contact mode AFM for nanowire imaging affects the quality of the height image and could cut the structure as can be seen at the upper half of the nanowire. This effect was controlled by decreasing the set point which decreases the force of the tip on the nanowire. The current image (figure 123c) shows the associated current on the nanowires with a current of 7.0 V which once the nanowire is broken the current flow through the wire is stopped which further confirms that the observed current flow is through the nanowire under investigation. The imaged area was again about 1.0 mm away from the In/Ga eutectic contact. The mean diameter of the measured nanowire was 20 nm and the position of the tip along the nanowire was 1.5 μm .

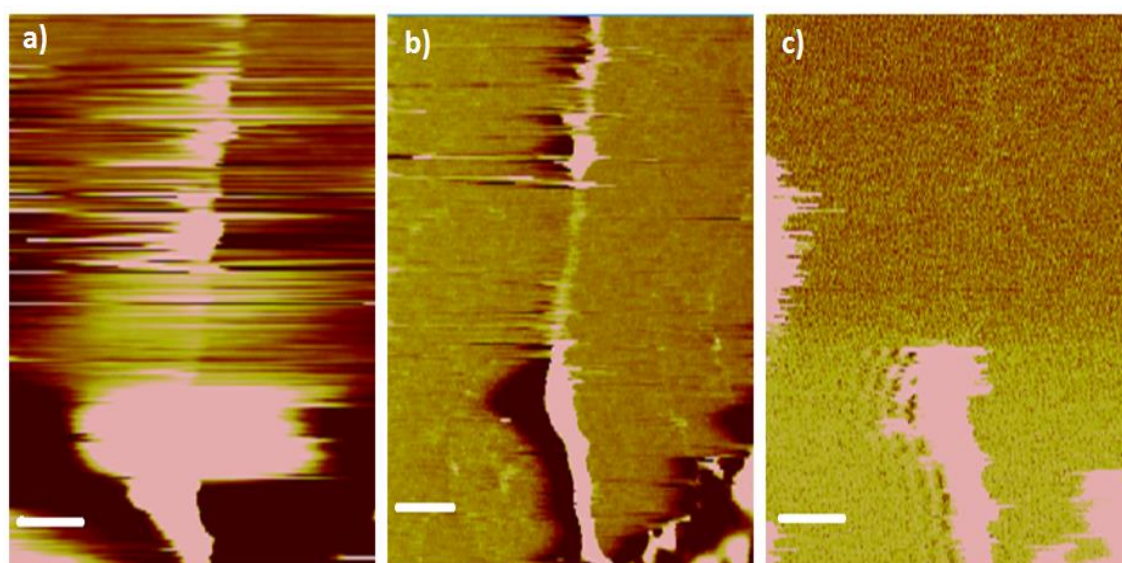


Figure 123. C-AFM measurements of Cu-poly-III/DNA nanowires aligned on a 200 nm SiO_2/Si substrate. a) Contact mode image the grayscale corresponds to a height of 13 nm; b) Deflection error image (the grayscale corresponds to a height of 10 nm) and c) cAFM current image (the grayscale corresponds to a current of 100 nA). The tip-sample bias was 0.5V; the images (a-c) were acquired simultaneously. Scale bars (a-c)=1.0 μm .

The plot of the circuit resistance as a function of the relative distance, d , of Cu-poly-III/DNA nanowire is shown in figure 124. As described earlier, the resistance increases with “ d ” because the current must flow through a longer portion of the nanowire and the intercept on the resistance axis decreased with increasing the deflection set point.

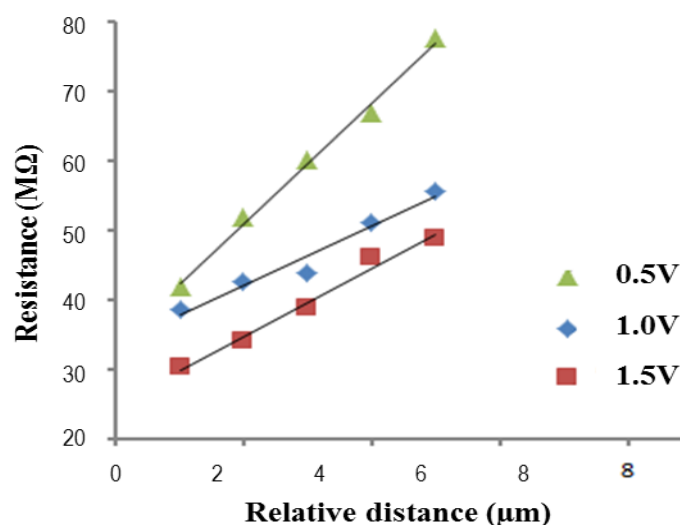


Figure 124. Cu-poly-III/DNA nanowire resistance at zero bias as a function of tip-contact relative distance for different applied forces in single-point c-AFM I-V measurements.

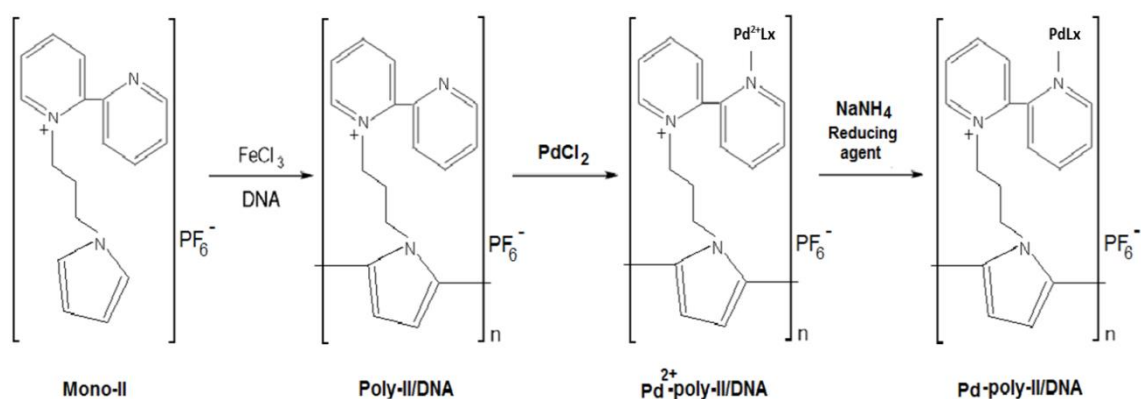
The conductivity of Cu-poly-III/DNA nanowires was estimated to be around 4.2×10^{-2} to $6.4 \times 10^{-2} \text{ S cm}^{-1}$. These values increased with increasing the deflection set point. This conductivity is about the same of the previously estimated measurements for Cu-poly-II/DNA ($7.1 \times 10^{-2} \text{ S cm}^{-1}$) and higher than the conductivity of poly-III/DNA nanowires ($9.0 \times 10^{-3} \text{ S cm}^{-1}$), but again however it is lower than the measurements for ppy/DNA nanowires ($2.1 \times 10^{-1} \text{ S cm}^{-1}$) measured by the same technique (chapter 4).

However, despite the small improvement in the conductivity of Cu-poly-II/DNA and Cu-poly-III/DNA nanowires compared to poly-II/DNA and poly-III/DNA nanowires respectively, these conductivity values are much lower than that of bulk copper ($6.0 \times 10^5 \text{ S cm}^{-1}$).^[55] The possible reason for this is probably due to the structure morphology and reduced dimensions of the Cu^0 architectures produced.

Although the AFM images show relatively regular metal coverage of the CPs/DNA templates, the presence of discontinuities or voids along the length of the nanostructure are highly likely. Such voids in the metal structure would introduce significant tunneling barriers at various points along the Cu^0 architectures, preventing efficient charge transport along the entire length of the nanostructures.

5.4. Templating palladium nanoparticles on Poly-II/DNA hybrids nanowires

Poly-II/DNA nanostructures were also used as templates to direct Pd nanowires formation. The method reported here is similar to that has been used for the templating of Cu metal nanowires. An aqueous solution of PdCl_2 (5 μL , 3.0 mM) as a source of Pd^{2+} ions was drop-wise added into 40 μL of the, 24 hours incubated, poly-II/DNA solution. The reaction mixture was stirred for 10 minutes to allow coordination to the free nitrogen atom of the 2-2,bipyridyl group, before being reduced to Pd^0 by drop-wisely addition of 5 μL , 10 mM NaBH_4 solution, as shown in scheme 21. The reaction mixture was kept at room temperature for 24 hours.



Scheme 21. DNA-templated synthesis of poly-II/DNA nanowires and deposition of Pd nanocrystals. Where L= Ligand, x= number of ligands.

5.4.1. UV-Vis absorption spectra of Pd-poly-II/DNA nanostructures

The UV-Vis absorption results of poly-II/DNA and Pd-poly-II/DNA (ie. after addition of NaBH_4) solutions were recorded at room temperature. Figure 125 shows the UV-Vis absorption spectra of poly-II/DNA solution (poly-II/DNA) which exhibits the characteristic absorption band of π - π^* transition at 350 nm and the peak at 530 nm of the bipolaron state formed during the polymerisation process. These bands were absent

in the spectrum of (Mono-II) before polymerisation. The UV-Vis spectrum of Pd-poly-II/DNA solution (Pd-poly-II/DNA) displays a broad continuous band in the range 300–600 nm. This is consistent with the peak of metallic Pd nanowires which indicates the Pd metallisation of poly-II/DNA nanowires.[56, 57]

The XPS technique was used to confirm the metallisation and the chemical state of Pd on the resulting Pd-poly-II/DNA nanowires.

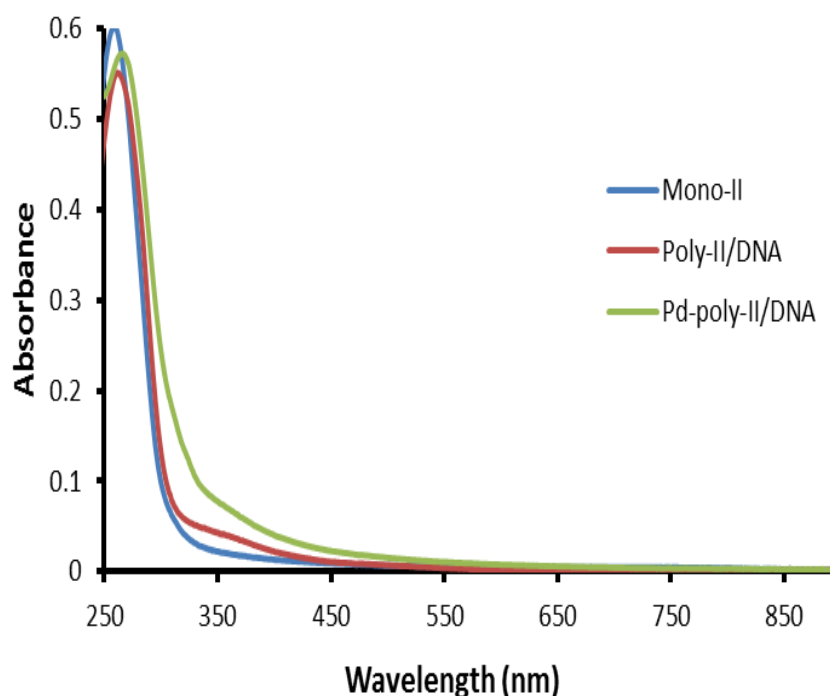


Figure 125. UV-Vis absorption spectra of mono-II (Mono-II), poly-II/DNA (Poly-II/DNA) and Pd-poly-II/DNA (Pd-poly-II/DNA).

5.4.2. X-ray photoelectron spectroscopy (XPS) of Pd-poly-II/DNA nanostructures

XPS has been used to study samples of Pd-poly/DNA and to identify the different oxidation states of Pd. The binding energies are calculated with the reference of C1s binding energy 284.6 eV. Previous studies indicated that Pd-3d bands are observed within three distinct ranges.[58, 59] 3d_{5/2} peaks between 334.8-335.5 eV have been assigned to metallic Pd. Peaks lying between 336.5-337.2 eV are assigned to PdO. Binding energies in the range 337.9-338.4 eV imply the presence of Pd²⁺ ions which are much more cationic than PdO.

The corresponding XPS core-level spectra of Pd 3d region acquired for Pd-poly-II/DNA sample is depicted in figure 126. The Pd 3d spectra, characterized by the spin-orbit splitting (Pd 3d_{5/2} and Pd 3d_{3/2}), decomposed into two doublet components. These spectra reveal the low-binding-energy doublet at 335.5 eV (Pd 3d_{5/2}) and 341.2 eV (Pd 3d_{3/2}). These peaks attributed to the Pd⁰ species that indicate the presence of Pd metal in Pd-poly-II/DNA samples. Simultaneous the presence of other significant peaks (Pd 3d_{5/2} and Pd 3d_{3/2}) located at slightly higher energies ca. 336.4 eV and 343.2 eV respectively which assigned to PdO. The other small peak at 341.5 eV attributed to Pd⁰ plasmons. These peaks are consistent with previous spectra reported in literatures.[58-62] These results indicate the complete reduction of Pd(II) to Pd(0) by the treatment with NaBH₄ as a reducing agent. This is in a good agreement with previous finding[63] which revealed the action of strong reducing agents, like borohydride (BH₄⁻), on Pd(II) leads to Pd(0), while reduction by a weak reagent, e.g. hydrazine, gives a mixture of Pd-species of different oxidation states. The presence of PdO on the surface was due to the unavoidable exposure of the samples to air.

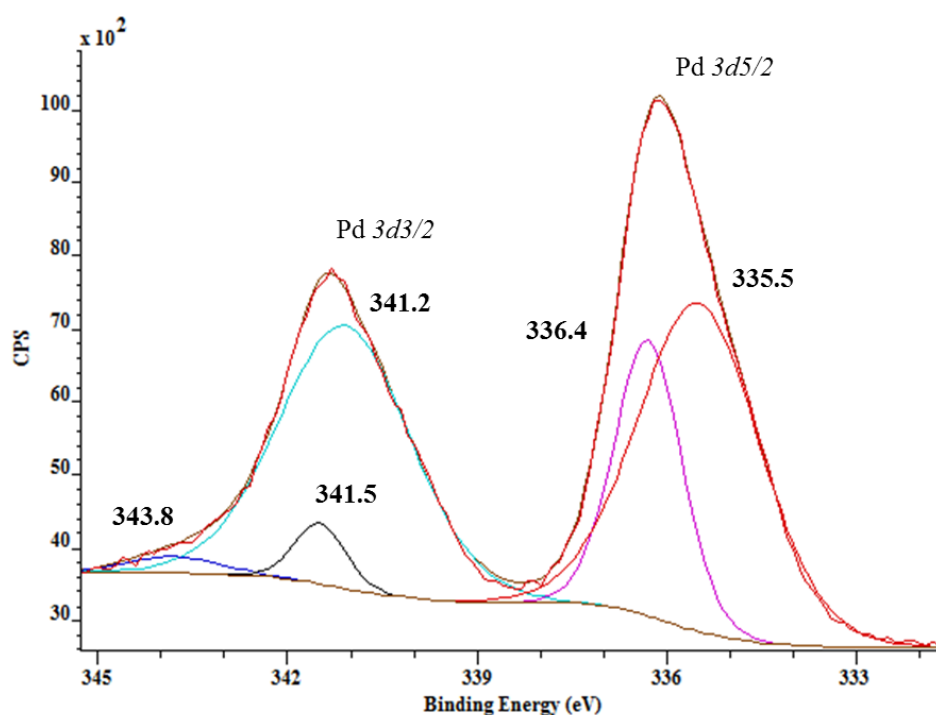


Figure 126. A representative fit of Pd 3d_{5/2} and Pd 3d_{3/2} spectra for Pd-poly-II/DNA nanowires. The binding energies are reported after calibration of the energy scale so that the main C 1s binding energy is 284.6 eV.

5.4.3. *Pd-poly-II/DNA nanowires assembly: AFM characterization*

As described before, tapping mode AFM was used to record the morphology of the Pd-poly-II/DNA nanowires. Figure 127 shows tapping mode AFM images of the template nanostructures before and after metallisation. Figure 127(a) is a typical AFM image for poly-II/DNA which prepared on λ -DNA as described in chapter 5; these nanowires are continuous, relatively regular and rather smooth. The line trace along several microns of a particular nanowire, figure 127(c), shows same variation in structure height, *ca.* ~9 - 15 nm.

Figure 127(b) shows Pd-poly-II/DNA nanostructures formed by the addition of PdCl₂ to the previous solution and reduced with NaBH₄. This sample was imaged 24 hours after reduction. The growth of Pd along the poly-II/DNA template is indicated by an increase in height from an average of 15 nm before metallization to an average height of 20 - 25 nm after metallization. These nanowires are continuous and vary in size (up to ~45 nm) but are less regular and uniform compared with the case before metallisation. The line trace along several microns of a particular Pd-poly-II/DNA nanowire after metallisation shows a greater variation in structure height, *ca.* ~15 - 45 nm, as shown in figure 127(d).

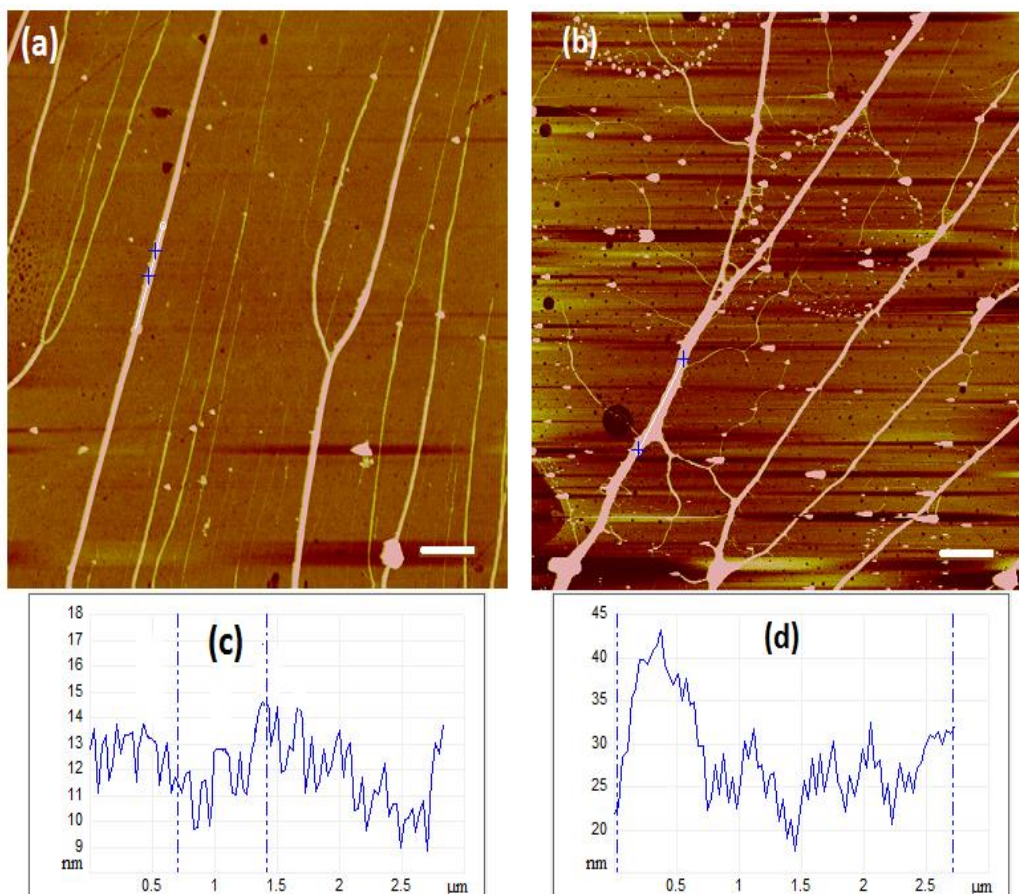


Figure 127. Tapping Mode AFM height images of (a) poly-II/DNA nanowires before metallisation immobilized upon a Si/SiO₂ substrate, modified with a TMS, (b) Pd-poly-II/DNA nanowires after metallisation. (c) and (d) are the corresponding line trace of (a) and (b) respectively. Scale bar= 1 μm, height scale=20 nm.

The statistical analysis of the size distribution of Pd-poly-II/DNA nanowires was performed by observing ~100 nanowires of poly-II/DNA before and after metallization. The parameters were extracted from the AFM images (the height of the nanowires). Figure 128(a) shows a histogram of the average wire height for ~100 different wires of poly-II/DNA before metallization which are isolated 2 hours after preparation. The distribution of heights of poly-II/DNA shows a spread of structure heights within the range 3.0 - 8.0 nm, with an average diameter of ~5.0 nm. The structure heights observed at 1.0-2.0 nm are considered to be for bare DNA strands. The common sized structures of poly-II/DNA are 3.0-4.0 nm, where some larger structure were also observed in much lower frequency with diameters up to 18 nm.

Figure 128(b) shows a histogram of the Pd-poly-II/DNA nanowires which were randomly selected out of the test group after 24 hours of incubation time. The thickness profile was averaged along a linear portion of the wire ($\sim 3 \mu\text{m}$ long). It is clear that the diameter range of nanowires was increased after metallization. The common sized structures of Pd-poly-II/DNA, after metallization, are 3.0-16.0 nm, with an average diameter of ~ 7.0 nm. Larger heights (up to 39 nm) also observed in much lower frequency.

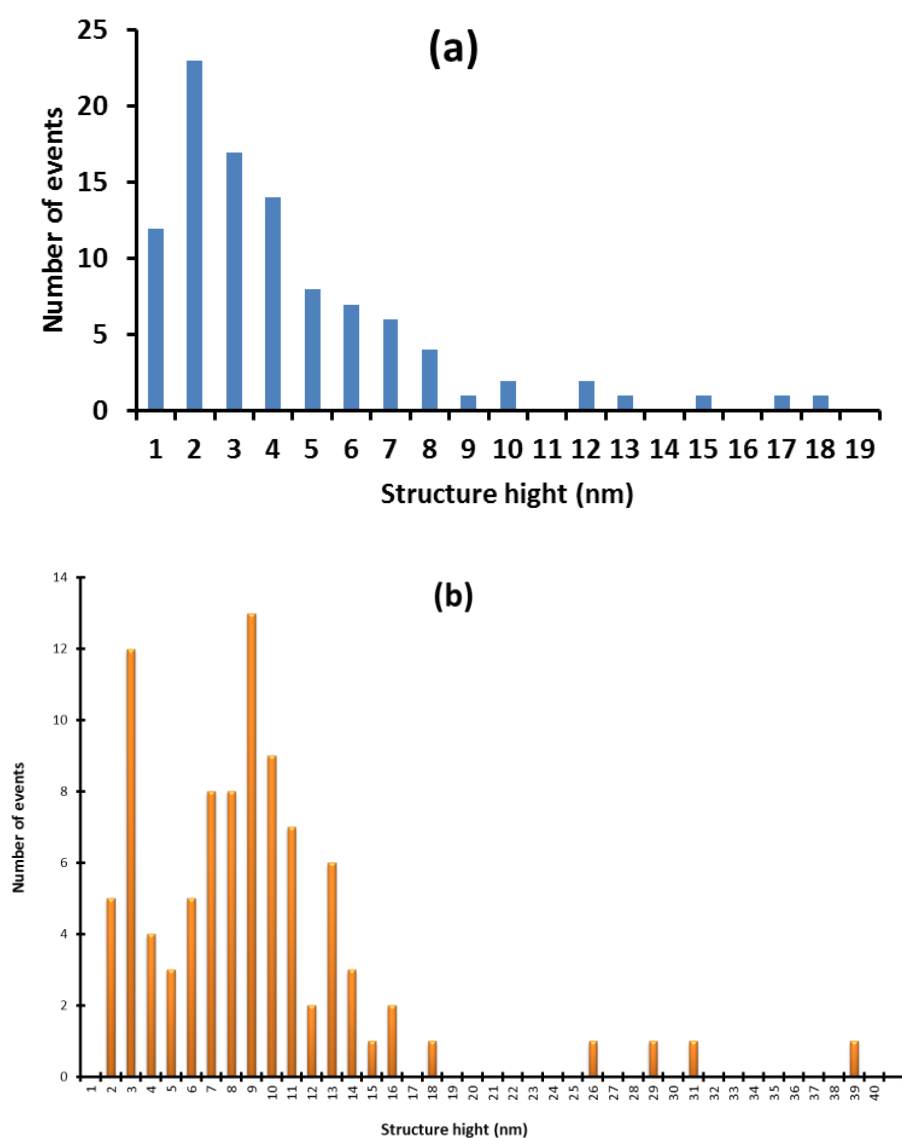


Figure 128. (a): Height distribution of ~ 100 poly-II/DNA templates before metallization, determined from Tapping Mode AFM images 2 hours after preparation. (b): The height distribution of ~ 100 Pd-poly-II/DNA nanowires determined from Tapping Mode AFM images after 24 hours of reaction time.

5.4.4. Electrical characterisation of Pd-poly-II/DNA nanowires by Electrostatic Force Microscopy (EFM)

As discussed before, EFM is an effective tool to trace the nanowires conductivity. Conducting 1D nanostructures show a negative phase shift with respect to the background (SiO_2). In contrast, insulating materials have a positive phase shift. Figure 129(a) shows the AFM image for Pd-poly-II/DNA nanowire with a thickness of ~ 25 nm, and 129(b) shows the correspondent EFM image (applied bias = +6V, lift height 60 nm). As the tip crossed the nanowire a negative-positive-negative phase variation was observed 129(d). This behaviour is same as that reported for Cu-poly-II/DNA nanowires as well as for other polymer nanowires.[50, 51] Upon varying the applied bias and measuring the phase shift at the most negative point along a cross section of the nanowire at a diameter of 25 nm, the expected parabolic dependence of phase shift on bias for voltages between -10V and +10V was observed, figure 129(e).

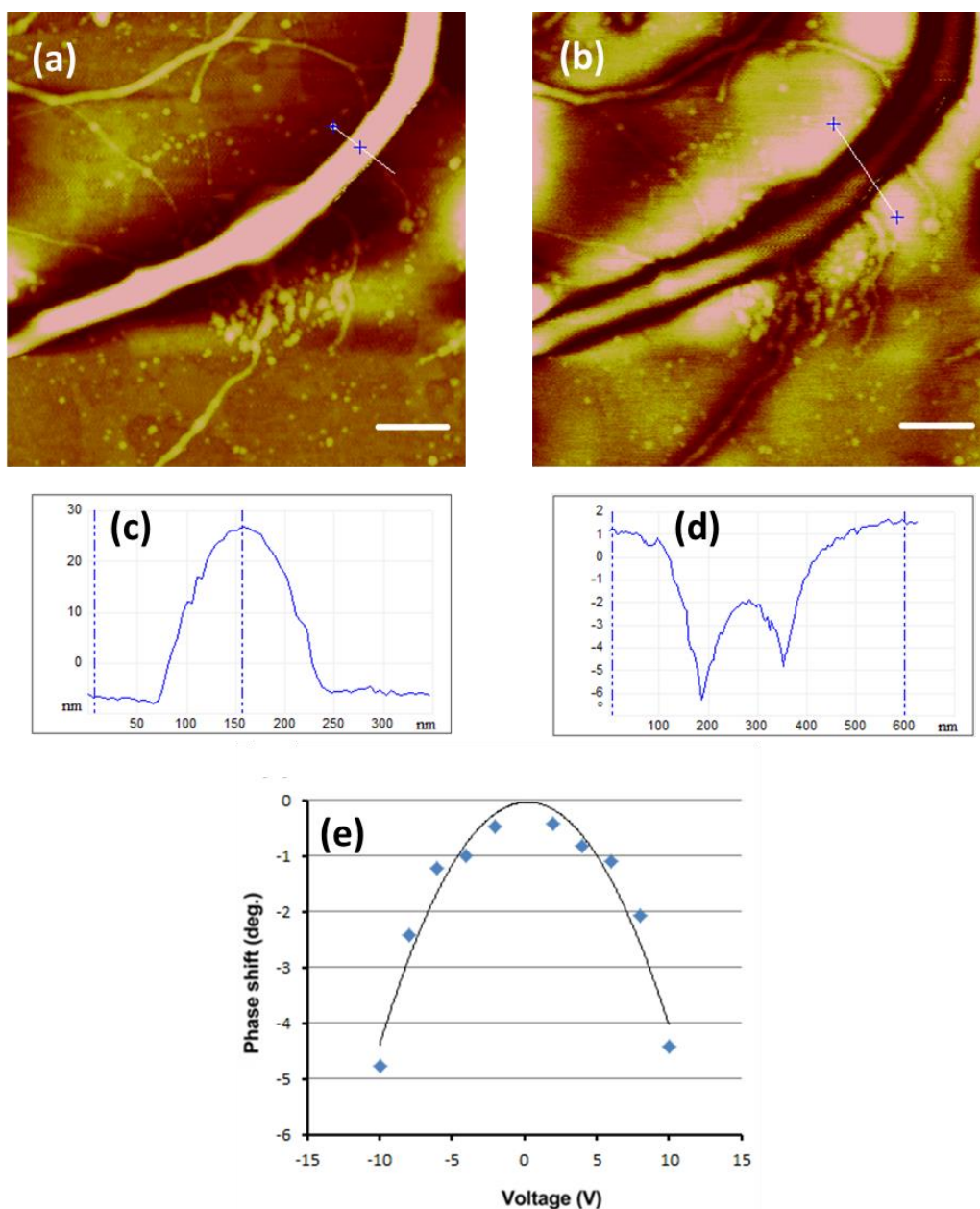


Figure 129. (a): AFM image of Pd-poly-II/DNA nanowires, with a thickness of ~ 25 nm, on SiO_2/Si surface with a SiO_2 thickness of 200 nm observed 24 hours after preparation. (b): The correspondent EFM Phase image at a tip/sample bias of +6 V and lift height of 60 nm Scale bar of both images= 300 nm. (c): Inset of the AFM image shows the height cross section of the nanowire at a diameter of ~ 25 nm, (d): shows the inset of the corresponding profile of the phase shift along a cross section of the nanowire at a diameter of 25 nm. (e): The phase shift as a function of applied voltage of the same nanowire on bias between -10V and +10V.

5.5. Summary

In this approach, an effort to increase the conductivity of the as prepared CP/DNA nanowires was employed. DNA-templated poly-II and poly-III nanostructures were metallized using copper and palladium to produce conducting polymer nanowires. The formation of these nanowires was characterized through spectroscopic and microscopic techniques. The obtained nanostructures were less regular in shape compared with poly-II/DNA and poly-III/DNA nanostructures before metallization, but they were continuous and less granular compared with metal nanowires prepared using templating method directly onto DNA. The electrical properties of the resulted Cu-poly-II/DNA and Cu-poly-III/DNA nanowires were evaluated by C-AFM and compared by the conductivity of their corresponding polymer/DNA nanostructures before metallisation. Importantly, their conductivity was slightly improved after metallisation.

Poly-II/DNA nanostructures were also used as templates to direct the formation of Pd nanowires by a similar preparation method. AFM studies show that the resulting Pd poly-II/DNA nanowires exhibit continuous and smooth morphology. EFM showed that these nanowires are electrically conductive.

5.6. References

1. J. Richter, Metallization of DNA. *Physica E* 2003, **16**, 157-173.
2. A. Houlton, A. R. Pike, M. A. Galindo and B. R. Horrocks, DNA-based routes to semiconducting nanomaterials. *Chem. Commun.*, 2009, 1797-1806.
3. J. Richter, M. Mertig and W. Pompe, Construction of highly conductive nanowires on a DNA template. *Appl. Phys. Lett.*, 2001, **78**, 536-538.
4. H. Kudo and M. Fujihira, DNA-Templated Copper Nanowire Fabrication by a Two-Step Process Involving Electroless Metallization. *IEEE Trans. on Nanotech.*, 2006, **5**, 90-92.
5. C. F. Monson and A. T. Woolley, DNA-Templated Construction of Copper Nanowires. *Nano Lett.*, 2003, **3**, 359-363.
6. S. A. F. Al-Said, R. Hassanien, J Hannant, M. A. Galindo, S. Pruneanu, A. R. Pike, A. Houlton and B. R. Horrocks, Templating Ag on DNA/polymer hybrid nanowires: Control of the metal growth morphology using functional monomers. *Electrochem. Comm.*, 2009, **11**, 550-553.
7. R. Hassanien, S. A. F. Al-Said, L. Siller, R. Little, N. G Wright, A. Houlton and B. R. Horrocks, Smooth and conductive DNA-templated Cu₂O nanowires: growth morphology, spectroscopic and electrical characterization. *Nanotech.*, 2012, **23**, 075601-075613.
8. A. Houlton and S. M. Watson, DNA-based nanowires. Towards bottom-up nanoscale electronics. *Annu. Rep. Prog. Chem., Sect. A.*, 2011, **107**, 21-42.
9. R. Hassanien, M. Al-Hinai, S. A. F. Al-Said, R. Little, L. Siller, N. G. Wright, A. Houlton and B. R. Horrocks, Preparation and Characterization of Conductive and Photoluminescent DNA Templated Polyindole Nanowires. *J. Am. Chem. Soc.*, 2010, **4**, 2149-2159.
10. S. Pruneanu, S. A. F. Al-Said, L. Dong, T. A. Hollis, M. A. Galindo, N. G. Wright, A. Houlton and B. R. Horrocks., Self-Assembly of DNA-Templated Polypyrrole Nanowires: Spontaneous Formation of Conductive Nanoropes. . *Adv. Funct. Mater.*, 2008, **18**, 2444-2454.
11. E. Braun, From DNA to transistors. *Adv. in Phys.*, 2004, **53**, 441-496.
12. X. D. Liu, H.Y. Diaob and N. Nishic, Applied chemistry of natural DNA. *Chem. Soc. Rev.*, 2008, **37**, 2745-2757.

13. A. Lebrun and R. Lavery, Modelling extreme stretching of DNA. *Nucl. Acids Res.*, 1996, **24**, 2260-2267.
14. R. M. Stoltenberg and A. T. Woolley, DNA-Templated Nanowire Fabrication. *Biomed. Microdev.*, 2004, **6**, 105-111.
15. S. M. D. Watson, N. G. Wright, B. R. Horrocks and A. Houlton, Preparation, Characterization and Scanned Conductance Microscopy Studies of DNA-Templated One-Dimensional Copper Nanostructures. *Langmuir*, 2010, **26**, 2068-2075.
16. P. Tomasik, Z. Ratajewicz, G. R. Newkome and L. Strekowski, *The Chemistry of Heterocyclic Compounds; Pyridine-Metal Complexes* John Wiley & Sons, Inc., New York, 1985.
17. H. Arakawa, R. Ahmad, M. Naoui and H. A. Tajmir-Riahi, A Comparative Study of Calf Thymus DNA Binding to Cr(III) and Cr(VI) Ions. *J. biological chem.*, 2000, **275**, 10150-10153.
18. S. Alex and P. Dupuis, FT-IR AND Raman Investigation of cadmium binding by DNA. *Inorg. Chimica Acta*, 1989, **157**, 271-281.
19. A. A. Ouameur and H. A. Tajmir-Riahi, Structural analysis of DNA interactions with biogenic polyamines and cobalt(III) hexamine studied by Fourier transform infrared and capillary electrophoresis. *J. Biolog. Chem.*, 2004, **279**, 42041-42054.
20. G. I. Dovbeshko, N. Y. Gridina, E. B. Kruglova and O. P. Pashchuk, FTIR spectroscopy studies of nucleic acid damage. *Talanta*, 2000, **53**, 233-246.
21. S. Higuchi, M. Tsuboi and Y. Iitaka, Infrared spectrum of a DNA-RNA hybrid. *Biopoly.*, 1969, **7**, 909-916.
22. D. Barreca, A. Gasparotto, C. Maccato, E. Tondello, O. I. Lebedev and G. V. Tendeloo, CVD of Copper Oxides from a β -Diketonate Diamine Precursor: Tailoring the Nano-Organization. *Crystal Growth & Design.*, 2009, **9**, 2470-2480.
23. P.W. Hansen and P. W. Jensen, Vibrational studies on bis-terpyridine-ruthenium(II) complexes. *Spectrochimica Acta Part A: Molec. Spect.*, 1994, **50**, 169-183.
24. K. Mallicka, M. J. Witcomb and M. S. Scurrrell, In situ synthesis of copper nanoparticles and poly(o-toluidine): A metal-polymer composite material. *Euro. Poly. J.*, 2006, **42**, 670-675.

25. T. Dang, T. T. Le, E. F. Blanc and M. C. Dang, The influence of solvents and surfactants on the preparation of copper nanoparticles by a chemical reduction method. *Adv. Nat. Sci.: Nanosci. Nanotech.*, 2011, **2**, 025004-025011.
26. M. S. Niasaria and F. Davar, Synthesis of copper and copper(I) oxide nanoparticles by thermal decomposition of a new precursor. *Mat. Lett.*, 2009, **63**, 441-443.
27. W. Yu, H. Xie, L. Chen, Y. Li and C. Zhang, Synthesis and Characterization of Monodispersed Copper Colloids in Polar Solvents. *Nanoscale Res. Lett.*, 2009, **4**, 465-470.
28. Z. Yan, Z. Zhuxia, L. Tianbao, L. Xuguang and X. Bingshe, XPS and XRD study of FeCl₃-graphite intercalation compounds prepared by arc discharge in aqueous solution. *Spectrochimica acta. Part A, Mol. and biomol. spect.*, 2008, **70**, 1060-1064.
29. C.D. Wagner, W.M. Riggs, L.E. Davis, J.F. Moulder and G. E. Muilenberg, *Handbook of X-Ray Photoelectron Spectroscopy*, Physical Electronics Division, Perkin-Elmer Corporation, Eden Prairie, Minn. 55344, 1979.
30. C. Y. Lee, P. Gong, G. M. Harbers, D. W. Grainger, D. G. Castner and L. J. Gamble, Surface Coverage and Structure of Mixed DNA/Alkylthiol Monolayers on Gold: Characterization by XPS, NEXAFS, and Fluorescence Intensity Measurements. *Anal. Chem.*, 2006, **78**, 3316-3325.
31. S. Ptasinska, A. Stypczynska, T. Nixon, N. J. Mason, D. V. Klyachko and L. Sanche, X-ray induced damage in DNA monitored by X-ray photoelectron spectroscopy. *J. Chem. Phy.*, 2008, **129**, 065102- 065107
32. M. Gervais, A. Douy and B. Gallot, Surface-analysis of lipopeptides using x-ray photoelectron-spectroscopy .1. lipopeptides with polysarcosine peptidic chains. *J. Coll. and Interf. Sci.*, 1988, **125**, 146-154.
33. T. Yoshida, K. Yamasaki and S. Sawada, X-ray photoelectron spectroscopic study of biuret metal-complexes. *Bull. Chem. Soc. Jap.*, 1978, **51**, 1561-1562.
34. U. B. Steiner, W. R. Caseri, U. W. Suter, M. Rehahn and L. Schmitz, Ultrathin layers of low and high-molecular-weight imides on gold and copper. *Langmuir*, 1993, **9**, 3245-3254.
35. L. D. E. Strohmeier B.R., Field R.S., Hercules D.M. , *J. Catal.*, 1985, **94**, 514-519.

36. J. C. Fuggle, E. Kallne, L. M. Watson and D. J. Fabian, Electronic structure of aluminum and aluminum-noble-metal alloys studied by soft-x-ray and x-ray photoelectron spectroscopies. *Phys. Rev. B.* , 1977, **16**, 750-761.
37. J. Ghijsen, L. H. Tjeng, J. van Elp, H. Eskes, J. Westerink and G. A. Sawatzky, Electronic structure of Cu₂O and CuO. *Phys. Rev. B* 1988, **38**, 11322- 11330.
38. T.Y. Chen, S.F. Chen, H.S. Sheu and C. S. Yeh, *J. Chem. Phys.* 2002, **106**, 9717-9723.
39. F. M. Capece, V. D. Castro, C. Furlani, G. Mattogno, C. Fragale, M. Gargano and M. Rossi, “Copper chromite” Catalysts: XPS structure elucidation and correlation with catalytic activity. *Elec. Spectrosc. Relat. Phenom.*, 1982, **27**, 119-128.
40. T. Ghodselahi, M. A. Vesaghi, A. Shafiekhani, A. Baghizadeh and M. Lameii, XPS study of the Cu@Cu₂O core-shell nanoparticles. *Appl. Surf. Sci.*, 2008, **255**, 2730-2734.
41. Y. Wang, A. V. Biradar, G. Wang, K. K. Sharma, C. T. Duncan, S. Rangan and T. Asefa, Controlled Synthesis of Water-Dispersible Faceted Crystalline Copper Nanoparticles and Their Catalytic Properties. *Chem. Eur. J.*, 2010, **16**, 10735-10743.
42. A. Henglein, Formation and Absorption Spectrum of Copper Nanoparticles from the Radiolytic Reduction of Cu(CN)₂⁻. *J. Phys. Chem. B.*, 2000, **104**, 1206-1211.
43. A. Henglein, Reduction of Ag(CN)₂⁻ on Silver and Platinum Colloidal Nanoparticles. *Langmuir*, 2001, **17**, 2329-2333.
44. J. Aleman, A. V. Chandwick, J. He, M. Hess, K. Horie, R. G. Jones, P. Kratochvil, I. Meisel, I. Mita, G. Moad, S. Penczek and R. F. T. Stepto, Definations of terms relating to the structure and processing of sols, gels, networks, and inorganic-organic hybrid materials . *Pure and Appl. Chem.*, 2007, **79**, 1801-1829.
45. S. Pruneanu, L. Dong, T. A. Hollis, N. G. Wright, M. A. Galindo, A. R. Pike, B. A. Connolly, B. R. Horrocks and A. Houlton, DNA-based Inorganic and Polymer Nanowires: Synthesis, Characterization and Electrical Properties of Nanoelectronic Components. *Am. Inst. of Phys.*, 2008, 33-41.
46. Z. X. Deng and C. D. Mao, DNA-templated fabrication of 1D parallel and 2D crossed metallic nanowire arrays. *Nano Lett.*, 2003, **3**, 1545-1548.

47. C. Staii and A. T. Johnson, Quantitative Analysis of Scanning Conductance Microscopy. *J. Nano Lett.*, 2004, **4**, 859-862.
48. W. Steinhögl, G. Schindler, G. Steinlesberger, M. Traving and M. Engelhardt, Comprehensive study of the resistivity of copper wires with lateral dimensions of 100 nm and smaller. *J. Appl. Phys.*, 2005, **97**, 023706-023713.
49. W. Wu, S. H. Brongersma, M. V. Hove and K. Maex, Influence of surface and grain-boundary scattering on the resistivity of copper in reduced dimensions. *Appl. Phys. Lett.*, 2004, **84**, 2838-2840.
50. M. Bockrath, N. Markovic, A. Shepard and M. Tinkham, Scanned Conductance Microscopy of Carbon Nanotubes and DNA. *Nano Lett.*, 2002, **2**, 187-190.
51. Y. X. Zhou, M. Freitag, J. Hone, C. Staii, A. T. Johnson, N. J. Pinto and A. G. MacDiarmid, Fabrication and electrical characterization of polyaniline-based nanofibers with diameter below 30 nm. *Appl. Phys. Lett.*, 2003, **83**, 3800-3802.
52. T. S. Jespersen and J. Nygård, Charge Trapping in Carbon Nanotube Loops Demonstrated by Electrostatic Force Microscopy. *Nano Lett.*, 2005, **5**, 1838-1841.
53. B. D. Terris, J. E. Stern, D. Rugar and H. J. Mamin, Contact Electrification Using Force Microscopy. *Phys. Rev. Lett.*, 1989, **63**, 2669-2672.
54. R. M. Nyffenegger, R. M. Penner and R. Schierle, Electrostatic force microscopy of silver nanocrystals with nanometer-scale resolution. *Appl. Phys. Lett.*, 1997, **71**, 1878-1880.
55. C. R. Hammond, *The Elements, in Handbook of Chemistry and Physics*, 81st edn., CRC press, 2004.
56. S. Kundu, K. Wang, D. Huitink and H. Liang, Photoinduced formation of electrically conductive thin palladium nanowires on DNA scaffolds. *Langmuir*, 2009., **25**, 10146-10152.
57. J.A. Creighton and D. G. Eadon, Ultraviolet-visible absorption spectra of the colloidal metallic elements. *J. Chem. Soc.*, 1991, **87**, 3881-3891.
58. K. S. Kim, A. F. Gossmann and N. Winograd, X-Ray Photoelectron Spectroscopic Studies of Palladium Oxides and the Palladium-Oxygen Electrode. *Anal. Chem.*, 1974, **46**, 197-200.
59. L. S. Kibis, A. I. Titkov, A. I. Stadnichenko, S. V. Koscheev and A. I. Boronin, X-ray photoelectron spectroscopy study of Pd oxidation by RF discharge in oxygen. *App. Surf. Sci.*, 2009, **255**, 9248-9254.

60. A. Tompos, J. L. Margitfalvi, M. Hegedus, Á. Szegedi, J. G. Fierro and S. Rojas., Characterization of Trimetallic Pt-Pd-Au/CeO₂ Catalysts Combinatorial Designed for Methane Total Oxidation. *Comb. Chem. & High Throughput Screening.*, 2007, **10**, 71-82.
61. F. Bozon-Verduraz, A. Omar, J. Escard and B. Pontivanne, Chemical State and Reactivity of Supported Palladium. I. Characterization by XPS and Uv-Visible Spectroscopy. *J. cat.*, 1978, **53**, 126-134.
62. J. C. Zhou, C. M. Soto, M.-S. Chen, M. A. Bruckman, M. H. Moore, E. Barry, B. R. Ratna, P. E. Pehrsson, B. R. Spies and T. S. Confer, Biotemplating rod-like viruses for the synthesis of copper nanorods and nanowires. *J. Nanobio Tech.*, 2012, **10**, 10-18.
63. J. P. Mathew and M. Srinivasan, Photoelectron doestrosopy (XPS) studies on some palladium catalysts *Eur. Polym. J.*, 1995, **31**, 835-839.

6. Overall Conclusion and Future Work

6.1. Achievements

In this thesis, different pyrrole-pyridine based nanowires formed by templating on DNA were fabricated and their spectroscopic and microscopic characteristics investigated using different methods. These were then used as templates themselves for the templation of metals. This work will help in developing new methods and techniques for the fabrication of smooth and uniform conductive nanowires. In addition, it may lead to the development of new ways to reduce the cost and difficulties now facing the methods to fabricate 1-D nanostructures for particular materials.

In chapter 3, the monomers (mono-I, mono-II and mono-III) were synthesized, characterized and chemically polymerised in the bulk scale to form poly-I, poly-II and poly-III respectively. Those polymers were characterized by different spectroscopic techniques such as Uv-Vis, FTIR and XPS spectroscopy. As described in section 3.3.7, based on cyclic voltammetric studies and the XPS N1s spectrum of poly-II and poly-III the non-quaternised pyridyl nitrogen atom in mono-II and mono-III becomes involved in the polymerisation reaction, acting as a nucleophile attacking the α -position of pyrrolyl groups, as shown in scheme 13 (page109). This fraction of pyridyl nitrogen atoms involved in this was estimated to be 49% in poly-II and 58% in poly-III. As a result, the electrical conductivity at room temperature of the resulted polymers which was measured using the two-terminal technique was dramatically reduced compared with that of PPy film prepared by the same method, see table 3 (section 3.3.7). The effect of *N*-substitution on decreasing the conductivity of the polymer has also been reflected in table 9 below. More importantly however, this reduces the available coordination sites for metal ions and will have a detrimental effect on their effectiveness as templates for metals.

In chapter 4, PPy, poly-I, poly-II and poly-III were used for the fabrication of nanowires using DNA as a template. The AFM studies show that the obtained nanowires have a

uniform diameter and smooth morphology. Over longer periods of time, these individual nanowires further assembled into large rope-like structures as indicated, in particular, by frayed ends of thicker structures. Conductivity measurements of PPy/DNA and poly-I/DNA, poly-II/DNA and poly-III/DNA as nanowires, table 9, were obtained from the c-AFM and two terminal I-V measurements. The conductivity of PPy/DNA and poly-I/DNA nanowire at room temperature obtained from the two terminal I-V measurements is lower compared with their conductivity using c-AFM technique. This difference in conductivity obtained by the two methods may be attributed to the variations in doping level and possible changes in the structural order of polymer/DNA nanowires.[1] In addition, two terminal I-V measurements are less straightforward to implement than c-AFM, due to the difficulties of locating and aligning the nanowires across the Au microelectrode gap.

<i>CP/DNA nanowire</i>	σ ($S\ cm^{-1}$) @ RT <i>measured by C-AFM</i>	σ ($S\ cm^{-1}$) @ RT <i>by two terminal I-V</i>	σ ($S\ cm^{-1}$) @ RT <i>of corresponding bulk polymers films by two terminal I-V</i>
PPy/DNA	2.1×10^{-1}	1.1×10^{-2}	86.2
Poly-I/DNA	2.0×10^{-2}	3.3×10^{-5}	4.5×10^{-8}
Poly-II/DNA	5.0×10^{-3}	-	2.0×10^{-12}
Poly-III/DNA	9.0×10^{-3}	-	1.0×10^{-12}

Table 9. Electrical conductivity at room temperature of DNA template polymers nanowires and their corresponding bulk polymer films.

As shown in table 9, the conductivities of PPy/DNA nanowires at room temperature, which were determined using both methods, are significantly lower than the conductivity of the corresponding bulk PPy film ($86.2\ S\ cm^{-1}$) prepared by chemical polymerisation method. In the case of other types of nanowires (poly-I/DNA, poly-II/DNA and poly-III/DNA) the conductivities of these nanowires, although they are generally lower than PPy/DNA nanowires, they are relatively higher than the conductivity of their corresponding bulk films which were chemically prepared using the same method and measured using two terminal I-V measurement. These results, as

described in chapter 3, obviously reflect the variation in conductivity between PPy and the *N*-substituted derivatives. The large effect of *N*-alkylation on decreasing the conductivity has been explained as being due to the presence of the alkyl side chain in the polymer backbone which induces a loss of co-planarity of the aromatic rings due to steric hindrance.

Using c-AFM the following sequence for the conductivity of different types of polymer nanowire is found: PPy/DNA > poly-I/DNA > poly-II/DNA \approx poly-III/DNA. This order is consistent with the known trends of: (i) decreasing conductivity upon *N*-alkylation, PPy vs poly-I, II and III, and (ii) the involvement of pyridine in the chain extension of poly-II/III. The two terminal nanowire device data for PPy and poly-I confirm this trend though the magnitude of the difference here is larger. In all the cases of poly-I, II and III a significant increase in the conductivity is observed of 6 orders of magnitude between the nanowires and their correspondent bulk polymers.

While there is literature precedence for increased conductivity of CP in nanowire form compared to bulk,[2, 3] the observed increases are dramatic. Previous explanations have been based on improved ordering of the polymer chains during the templating process as being a major factor responsible for the enhancements. For poly-II/III, where the most dramatic increases are seen, a possible explanation would be that the DNA templating reduces dramatically the extent of pyridine being involved in the chain-extension mechanism of polymerisation resulting in more highly conjugated and hence more conductive polymer chains.

Chapter 5 showed the attempted formation of Cu nanowires templated by the poly-II/DNA and poly-III/DNA 1-D nanowires using $\text{Cu}(\text{NO}_3)_2$ solution as a source of Cu^{2+} and ascorbic acid as reducing agent. In addition, attempts were also made to prepare palladium nanowires with poly-II/DNA nanowires as templates and PdCl_2 solution as a source of Pd^{2+} and NaBH_4 as reducing agent. The advantage of this method lies in its simplicity and mild reaction conditions, as well as short synthesis time. AFM imaging showed that although the obtained Cu-CP/DNA and Pd-CP/DNA nanowires were less regular in shape compared with poly-II/DNA and poly-III/DNA nanostructures before metallization, but they were continuous and less granular compared with similar attempts to form metal nanowires directly at DNA.

The conductivity of those nanostructures before and after metallisation is shown in table 10.

<i>Cp/DNA nanostructures</i>	σ ($S\ cm^{-1}$) @ RT <i>using c-AFM, before metallisation</i>	σ ($S\ cm^{-1}$) @ RT <i>using c-AFM, after metallisation (Cu metallised- Cp/DNA)</i>
PPy/DNA	2.1×10^{-1}	-
Poly-I/DNA	2.0×10^{-2}	-
Poly-II/DNA	5.0×10^{-3}	7.1×10^{-2}
Poly-III/DNA	9.0×10^{-3}	6.4×10^{-2}

Table 10. Electrical conductivity at room temperature, using c-AFM, of DNA templated polymers nanostructures and their corresponding copper metallised nanowires.

While the resulting metallized wires show some increase in conductivity compared to the parent nanowire, this is still low compared with some previously reported nanowires.[4] However, this slight improvement indicates that this approach of synthesising 1D nanostructures holds promise for the future development. This may open the prospects for these materials to be used in various applications such as interconnects or as a chemical or biological sensor elements.

6.2. Further work

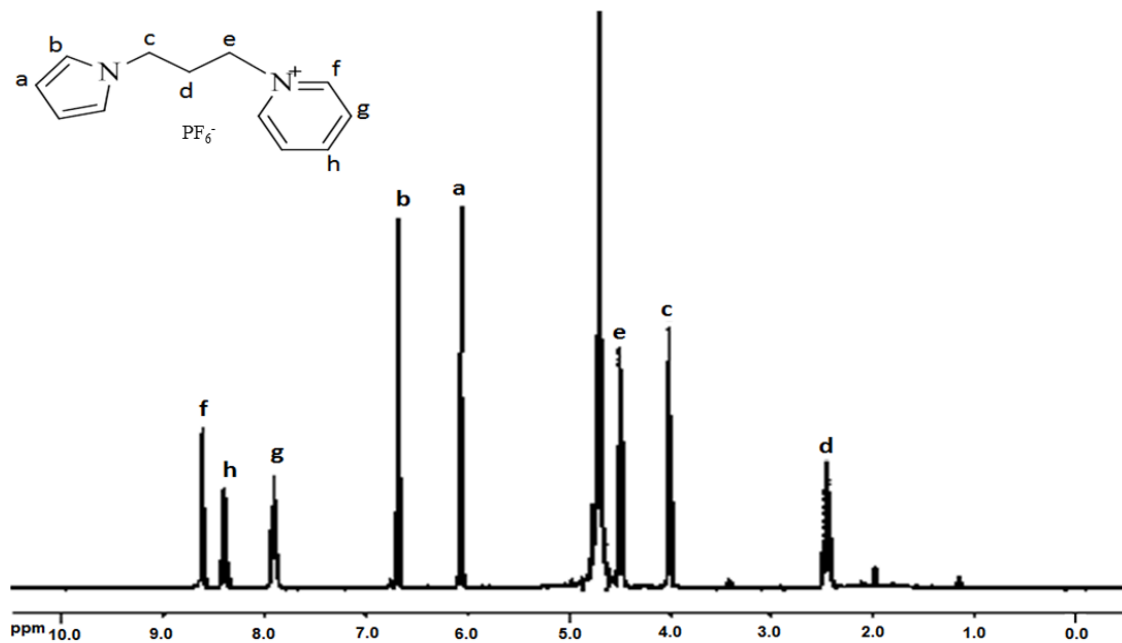
In the conclusion of this research, areas for further investigation on the fabrication of nanowires have been identified. The main problem arises from the fact that the pyridyl nitrogen groups may become involved in polymerization, so are therefore no longer available for metal binding. One approach to avoid this problem would be to use suitable protecting group chemistry so as to allow polymerisation without the involvement of the ligating group. Protected thiols would be one possibility. In addition to this, another area for further study could be to explore using this type of CP/DNA nanowires as sensing elements for metal ions in the natural and industrial environment.

6.3. References

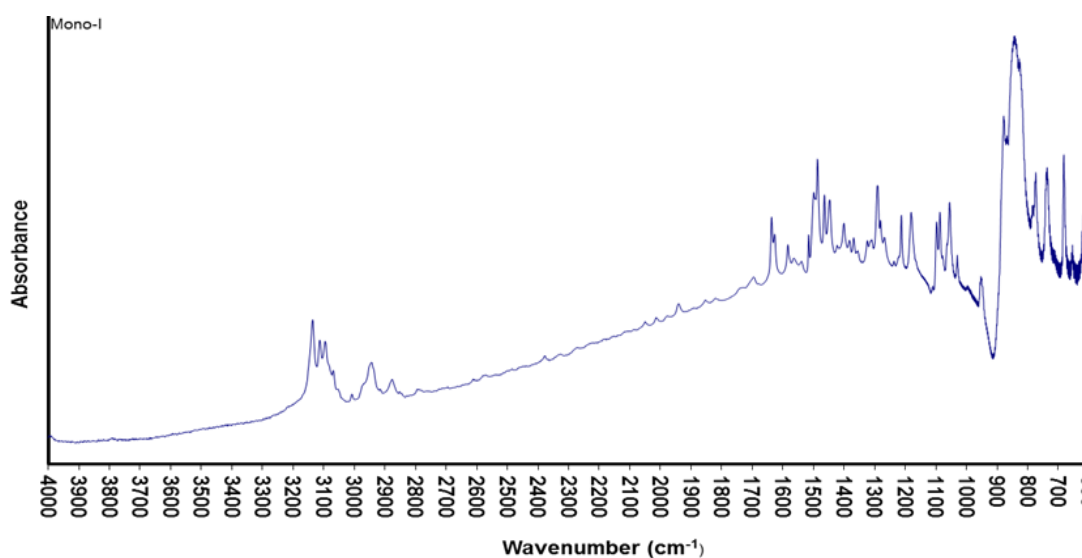
1. R. Hassanien, M. Al-Hinai, S. Al-Said, R. Little, L. Siller, N. Wright, A. Houlton and B. Horrocks, Preparation and Characterization of Conductive and Photoluminescent DNATemplated Polyindole Nanowires. *J. Am. Chem. Soc.*, 2010, **4**, 2149-2159.
2. S. J. Choi and S. M. Park, Electrochemical growth of nanosized conducting polymer wires on gold using molecular templates. *Adv.Mat.*, 2000, **12**, 1547-1549.
3. V. P. Menon, J. T. Lei and C. R. Martin, Investigation of molecular and supermolecular structure in template-synthesized polypyrrole tubules and fibrils. *Chem. of Mat.*, 1996, **8**, 2382-2390.
4. R. Hassanien, S. A. F. Al-Said, L. Siller, R. Little, N. G Wright, A. Houlton and B. R. Horrocks, Smooth and conductive DNA-templated Cu₂O nanowires: growth morphology, spectroscopic and electrical characterization. *Nano tech.*, 2012, **23**, 075601-075613.

7. Appendixes:

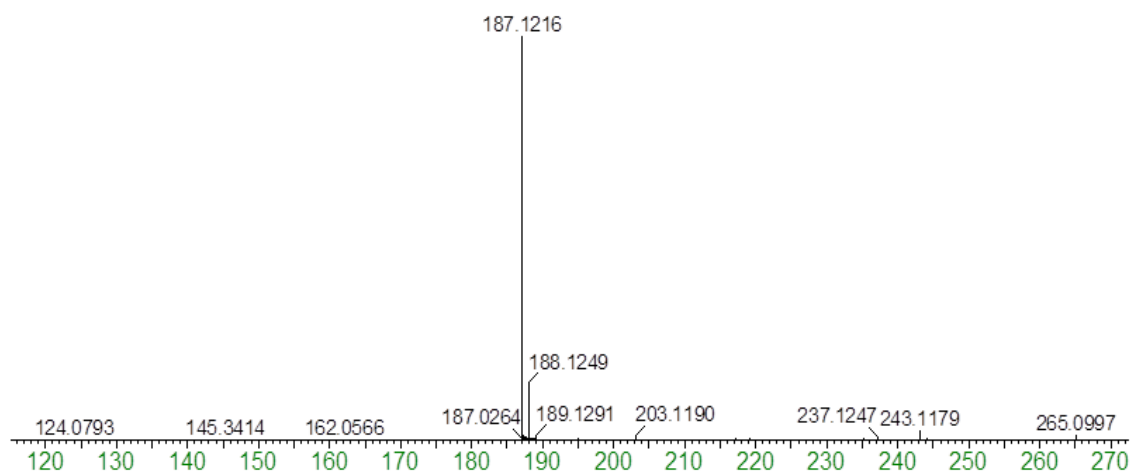
Appendix A: Spectroscopic data of mono-I



Appendix A1. ¹H NMR spectrum of N-(3-Pyrrol-1-yl-propyl)pyridinium (Mono-I).

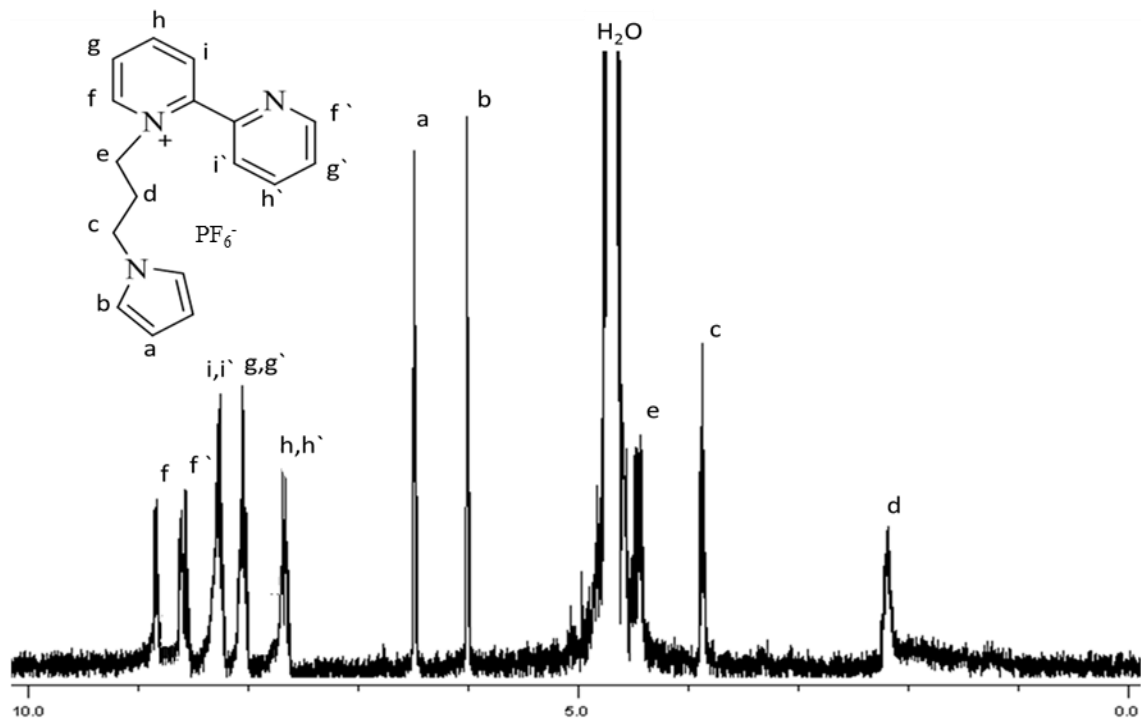


Appendix A2. FTIR spectrum of Mono-I.

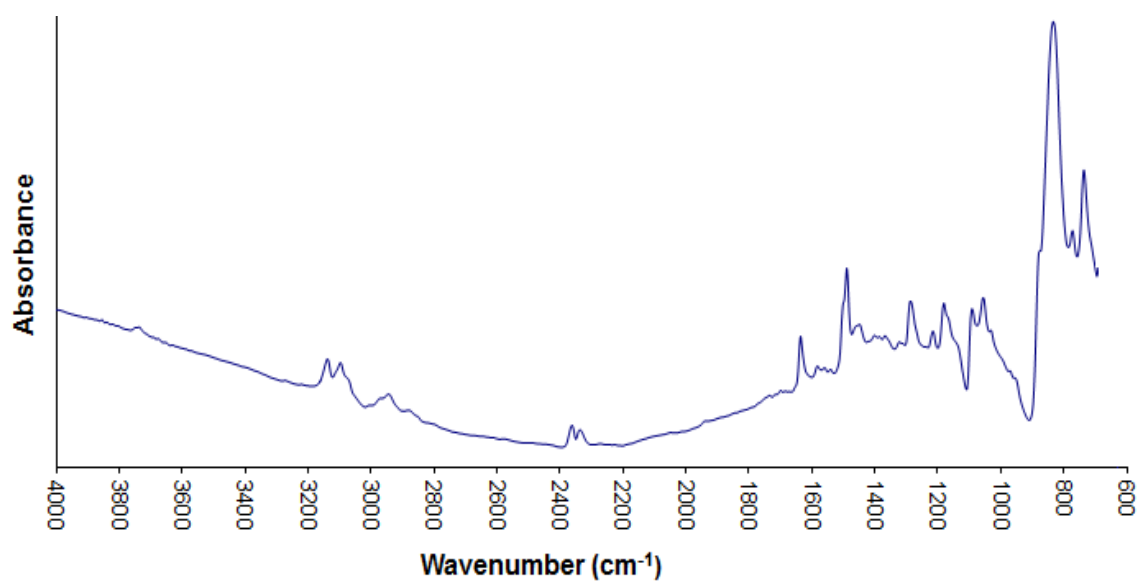


Appendix A3: Mass spectrum of Mono-I

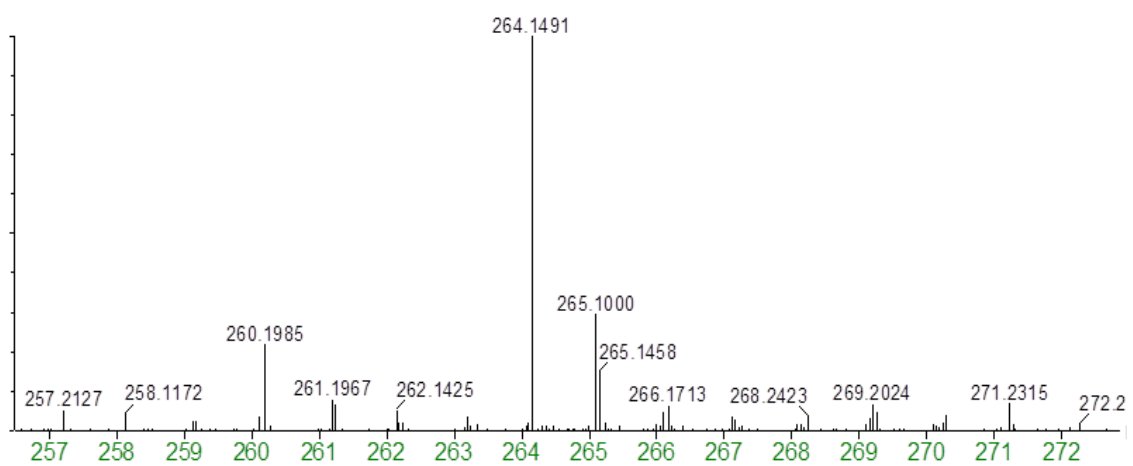
Appendix B: Spectroscopic data of mono-II



Appendix B1: ¹H NMR spectrum of Mono-II.



Appendix B2: FTIR spectrum of mono-II.



Appendix B3: Mass spectrum of mono-II.

Appendix C: Spectroscopic data of mono-III

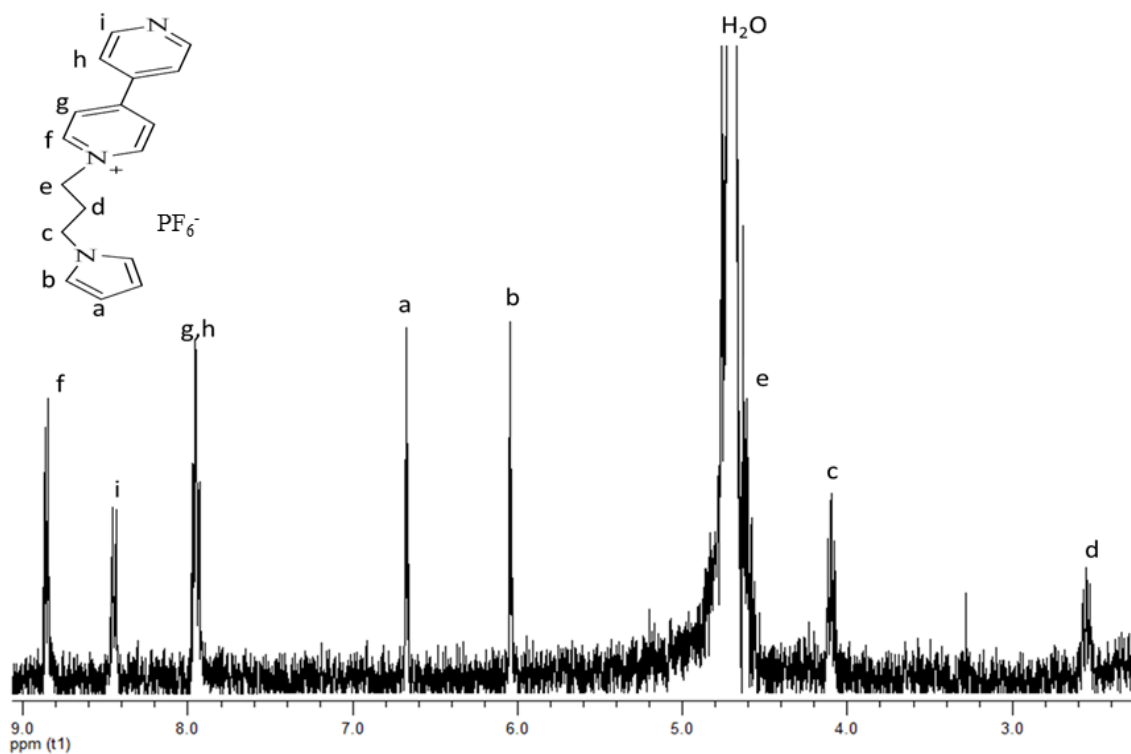
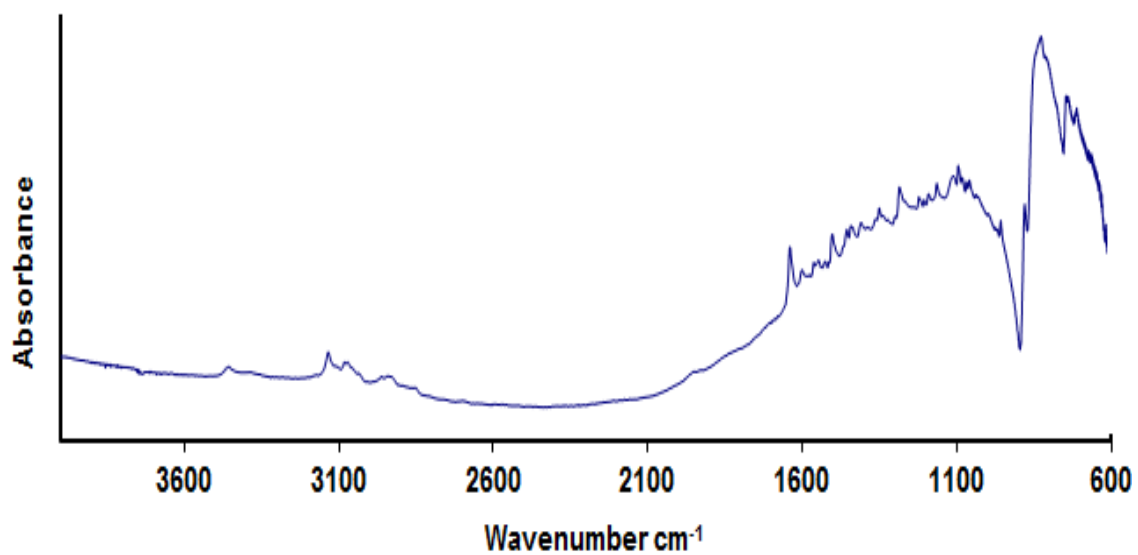
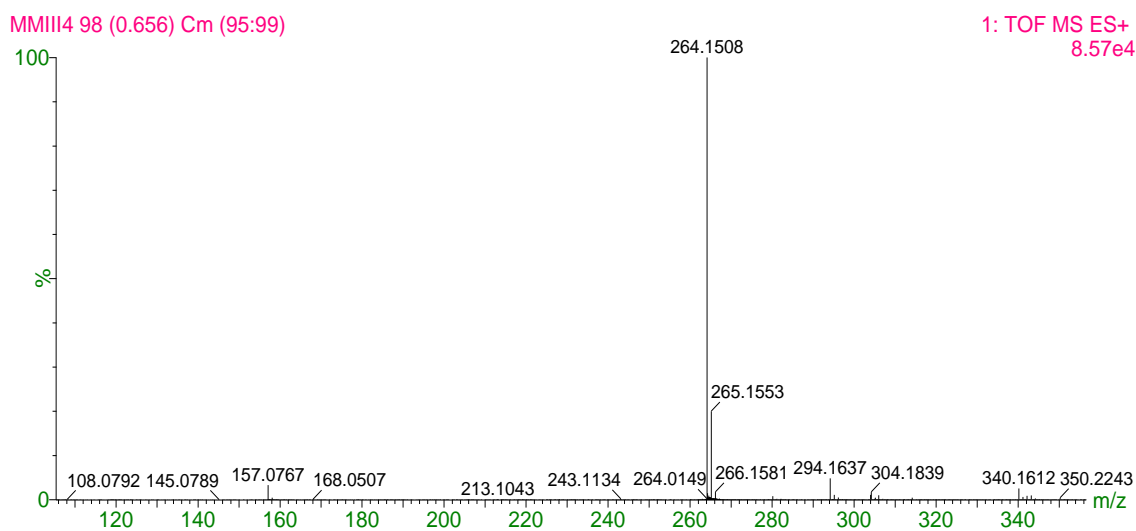


Figure C1: ¹H NMR spectrum of Mono-III.

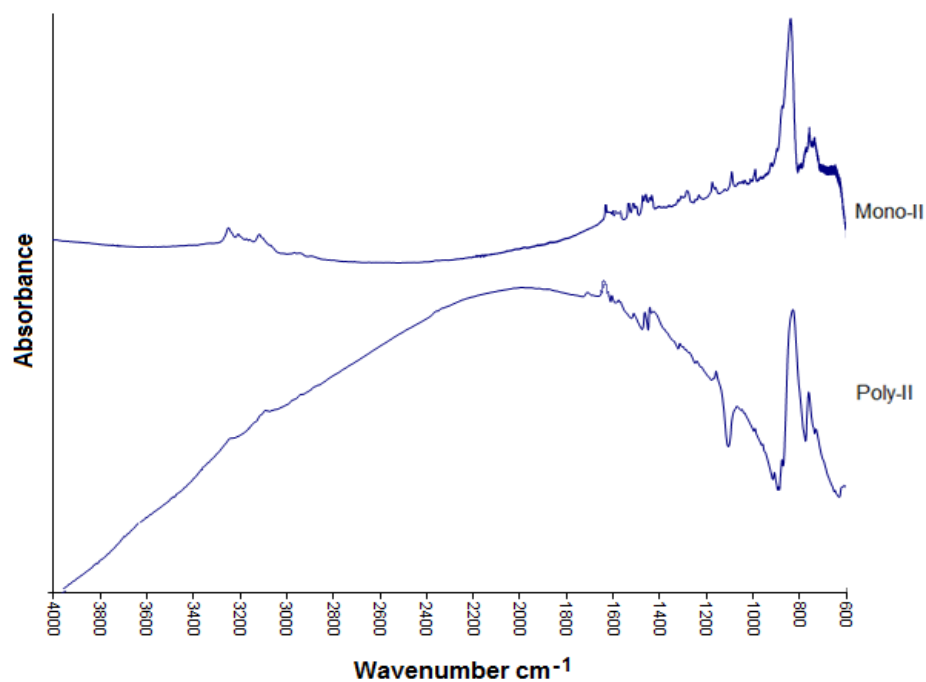


Appendix C2: FTIR spectrum of mono-III.

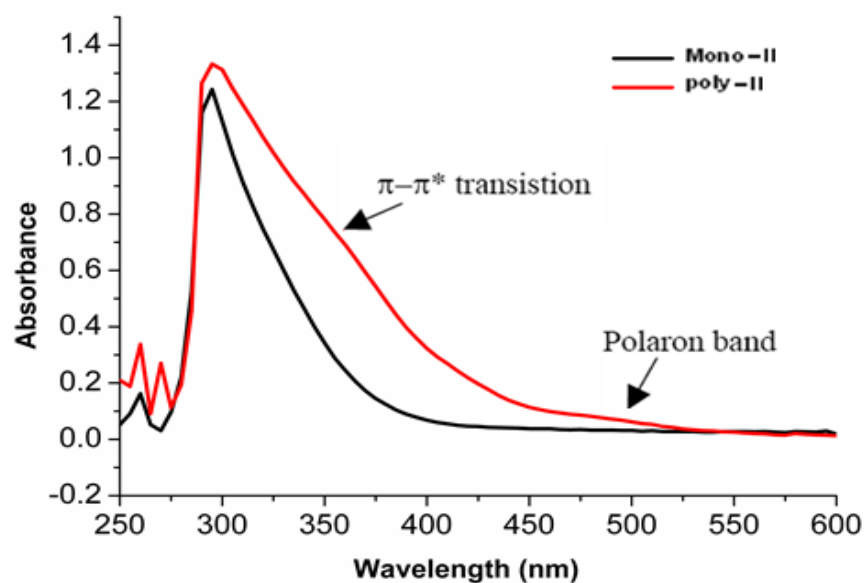


Appendix C3: Mass spectrum of mono-III.

Appendix D: Spectroscopic data of poly-II

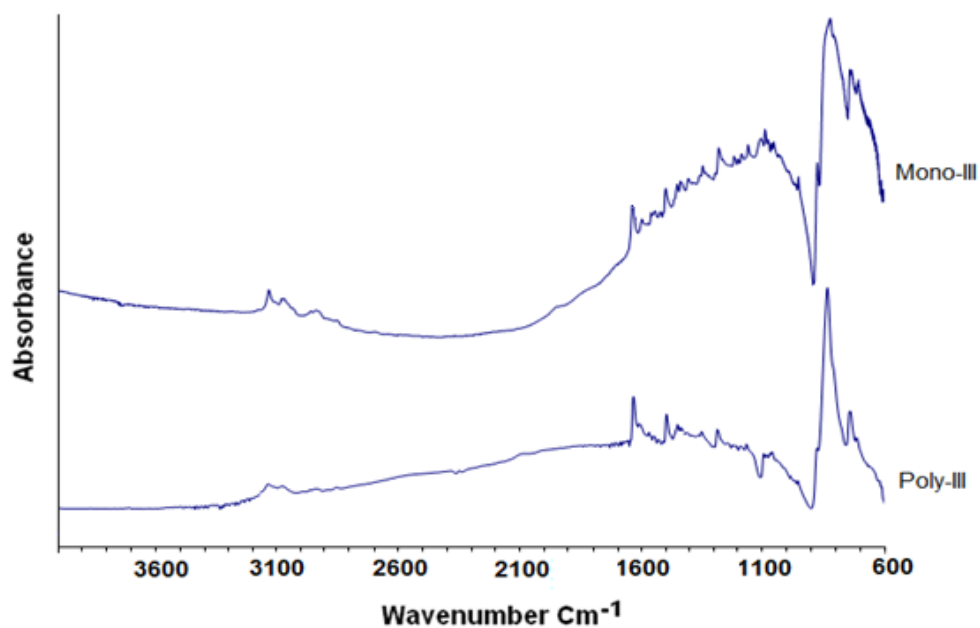


Appendix D1: FTIR spectra in the range (600 cm^{-1} - 4000 cm^{-1}) for mono-II and the chemically prepared poly-II.

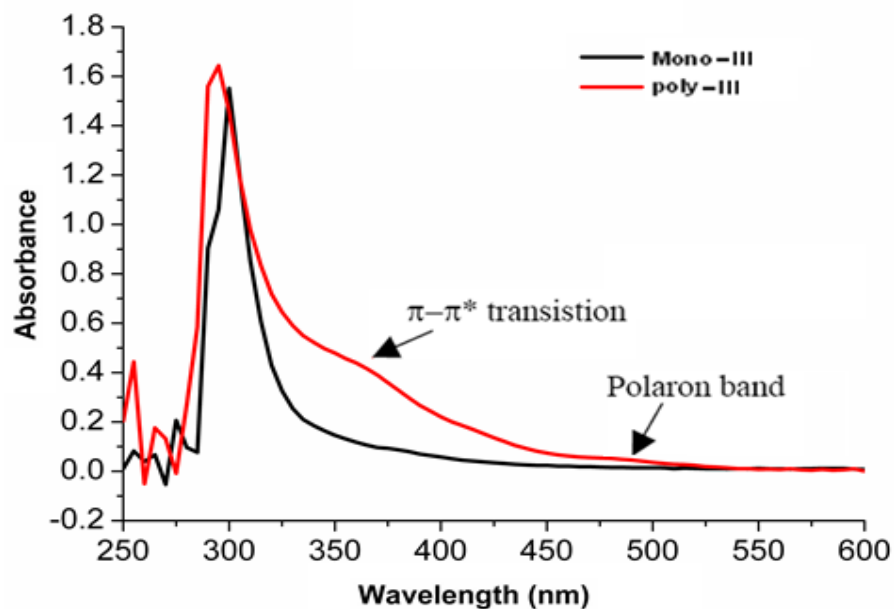


Appendix D2: Uv-Vis spectra of poly-II prepared by chemical polymerisation using FeCl_3 as oxidising agent.

Appendix E: Spectroscopic data of poly-III

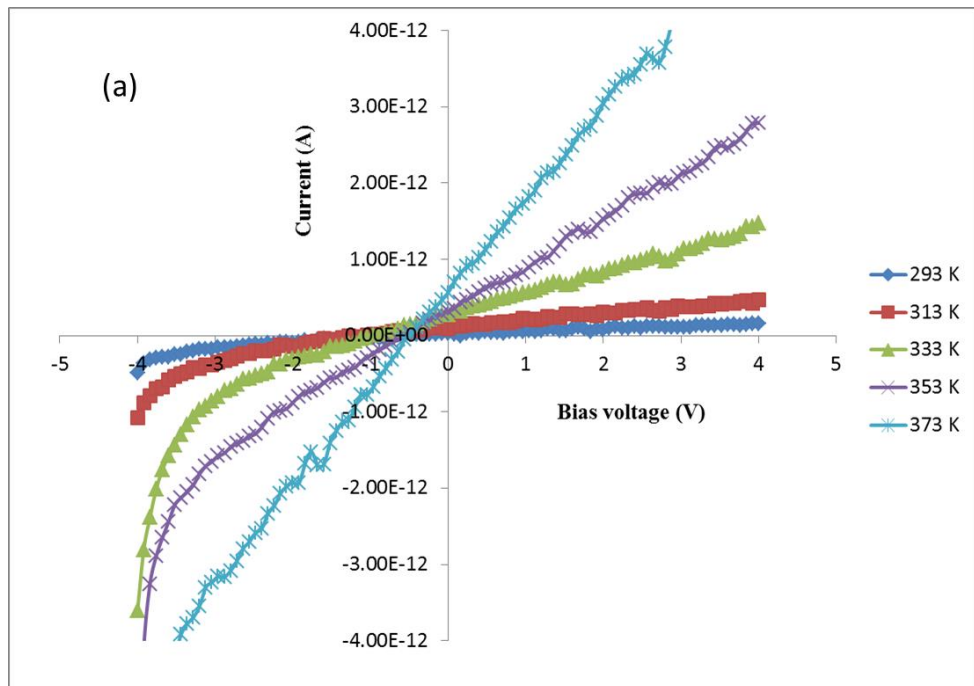


Appendix E1: FTIR spectra in the range (600 cm⁻¹ - 4000 cm⁻¹) for mono-III and the chemically prepared poly-III.

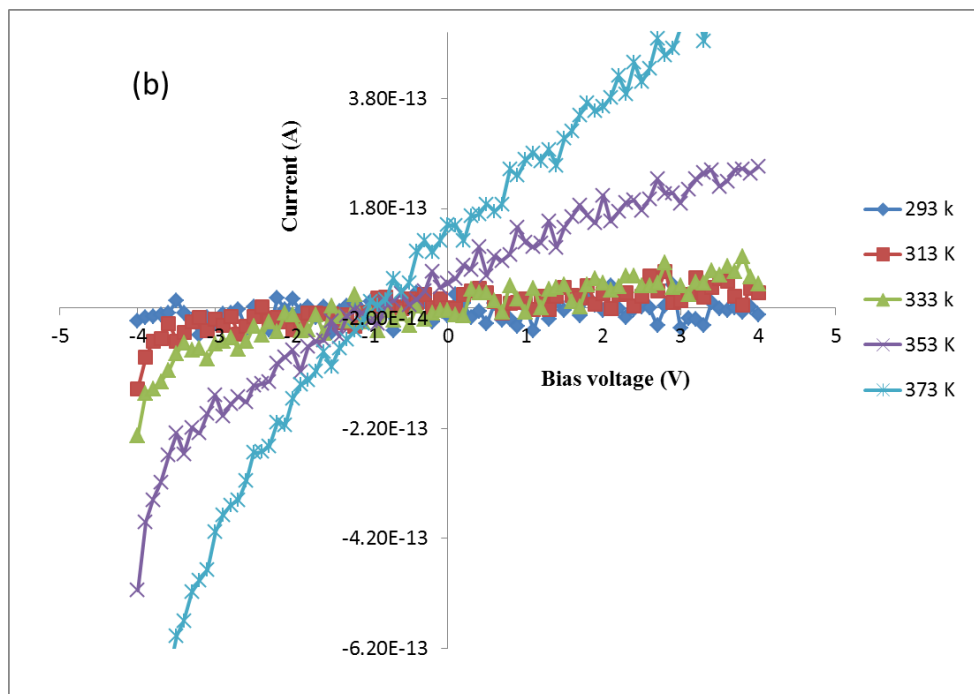


Appendix E2: Uv-Vis spectra of poly-III prepared by chemical polymerisation using FeCl₃ as oxidising agent.

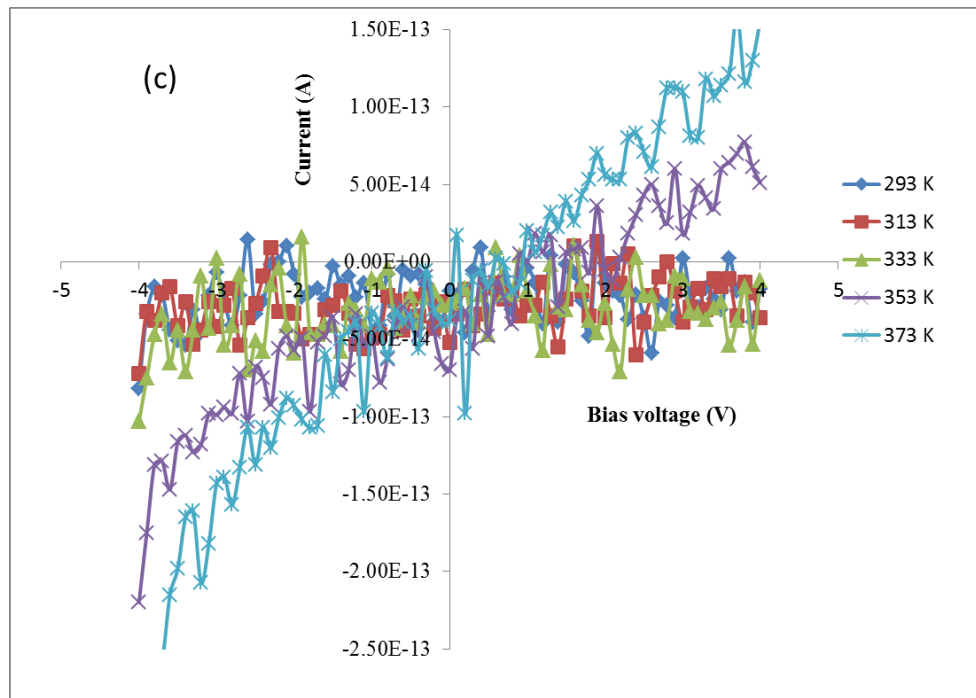
Appendix F: I-V curves of: (a) poly-I, (b) poly-II and (c) poly-III



Appendix F1: the I-V curves of poly-I



Appendix F2: the I-V curves of poly-II



Appendix F3: the I-V curves of poly-III

Appendix G: Crystallographic, Bond Length and Angle Data for Mono-I

Table 1. Crystal data and structure refinement for Mono-I, chapter 3.

Identification code	ah160	
Chemical formula (moiety)	$C_{12}H_{15}F_6N_2P$	
Chemical formula (total)	$C_{12}H_{15}F_6N_2P$	
Formula weight	332.23	
Temperature	150(2) K	
Radiation, wavelength	MoK α , 0.71073 Å	
Crystal system, space group	monoclinic, $P2_1/n$	
Unit cell parameters	$a = 9.034(7)$ Å	$\alpha = 90^\circ$
	$b = 10.648(7)$ Å	$\beta = 94.65(6)^\circ$
	$c = 14.901(10)$ Å	$\gamma = 90^\circ$
Cell volume	$1428.6(17)$ Å ³	
Z	4	
Calculated density	1.545 g/cm ³	
Absorption coefficient μ	0.254 mm ⁻¹	
F(000)	680	
Crystal colour and size	colourless, $0.20 \times 0.20 \times 0.15$ mm ³	
Reflections for cell refinement	86 (θ range 2.5 to 27.5°)	
Data collection method	Nonius KappaCCD diffractometer ϕ and ω scans	
θ range for data collection	3.9 to 22.5°	
Index ranges	$h -9$ to 9, $k -11$ to 11, $l -16$ to 16	
Completeness to $\theta = 22.5^\circ$	99.5 %	
Reflections collected	9932	
Independent reflections	1856 ($R_{int} = 0.1193$)	
Reflections with $F^2 > 2\sigma$	1186	
Absorption correction	semi-empirical from equivalents	
Min. and max. transmission	0.9510 and 0.9630	
Structure solution	direct methods	
Refinement method	Full-matrix least-squares on F^2	
Weighting parameters a, b	0.1552, 20.0735	
Data / restraints / parameters	1856 / 0 / 190	
Final R indices ($F^2 > 2\sigma$)	$R1 = 0.1127$, $wR2 = 0.3504$	
R indices (all data)	$R1 = 0.1578$, $wR2 = 0.3776$	
Goodness-of-fit on F^2	1.159	
Largest and mean shift/su	0.000 and 0.000	
Largest diff. peak and hole	0.73 and -0.54 e Å ⁻³	

Table 2. Atomic coordinates and equivalent isotropic displacement parameters (\AA^2) for Mono-I, chapter 3.

	x	y	z	U_{eq}
P(1)	0.1651(4)	0.2501(3)	0.4554(2)	0.0315(10)
F(1)	0.2197(10)	0.2962(8)	0.3607(5)	0.061(3)
F(2)	0.3287(9)	0.2699(10)	0.5017(7)	0.078(3)
F(3)	0.1118(9)	0.2083(8)	0.5513(5)	0.059(2)
F(4)	0.2027(10)	0.1098(7)	0.4328(6)	0.065(3)
F(5)	0.0006(8)	0.2348(8)	0.4107(5)	0.058(2)
F(6)	0.1269(9)	0.3939(7)	0.4803(5)	0.053(2)
N(1)	0.1815(11)	0.5039(9)	0.7596(6)	0.036(3)
N(2)	0.5862(11)	0.3528(11)	0.6670(7)	0.044(3)
C(1)	0.1829(14)	0.4683(12)	0.8478(8)	0.040(3)
C(2)	0.0720(14)	0.3850(12)	0.8581(10)	0.045(4)
C(3)	-0.0029(13)	0.3693(12)	0.7728(8)	0.037(3)
C(4)	0.0671(15)	0.4426(12)	0.7129(9)	0.042(3)
C(5)	0.2848(14)	0.5882(13)	0.7213(9)	0.046(4)
C(6)	0.3921(15)	0.5235(13)	0.6645(10)	0.051(4)
C(7)	0.4987(16)	0.4401(14)	0.7220(9)	0.052(4)
C(8)	0.5695(14)	0.2310(13)	0.6730(9)	0.041(3)
C(9)	0.6578(15)	0.1486(13)	0.6225(9)	0.046(4)
C(10)	0.7590(14)	0.1973(11)	0.5713(8)	0.037(3)
C(11)	0.7710(14)	0.3265(12)	0.5652(8)	0.038(3)
C(12)	0.6826(14)	0.4012(12)	0.6116(8)	0.040(3)

Table 3. Bond lengths (\AA) and angles (9°) for Mono-I, chapter 3.

P(1)–F(1)	1.608(8)	P(1)–F(2)	1.594(9)
P(1)–F(3)	1.607(8)	P(1)–F(4)	1.574(8)
P(1)–F(5)	1.586(8)	P(1)–F(6)	1.619(8)
N(1)–C(1)	1.367(15)	N(1)–C(4)	1.364(16)
N(1)–C(5)	1.446(16)	N(2)–C(7)	1.506(17)
N(2)–C(8)	1.309(16)	N(2)–C(12)	1.350(15)
C(1)–H(1A)	0.950	C(1)–C(2)	1.356(18)
C(2)–H(2A)	0.950	C(2)–C(3)	1.400(18)
C(3)–H(3A)	0.950	C(3)–C(4)	1.377(17)
C(4)–H(4A)	0.950	C(5)–H(5A)	0.990
C(5)–H(5B)	0.990	C(5)–C(6)	1.505(18)
C(6)–H(6A)	0.990	C(6)–H(6B)	0.990
C(6)–C(7)	1.522(18)	C(7)–H(7A)	0.990
C(7)–H(7B)	0.990	C(8)–H(8A)	0.950
C(8)–C(9)	1.439(19)	C(9)–H(9A)	0.950
C(9)–C(10)	1.341(17)	C(10)–H(10A)	0.950
C(10)–C(11)	1.384(17)	C(11)–H(11A)	0.950
C(11)–C(12)	1.356(17)	C(12)–H(12A)	0.950
F(1)–P(1)–F(2)	90.0(5)	F(1)–P(1)–F(3)	178.2(5)
F(1)–P(1)–F(4)	90.9(5)	F(1)–P(1)–F(5)	90.4(5)
F(1)–P(1)–F(6)	89.9(4)	F(2)–P(1)–F(3)	89.2(5)
F(2)–P(1)–F(4)	90.6(5)	F(2)–P(1)–F(5)	178.0(5)

F(2)–P(1)–F(6)	89.0(5)	F(3)–P(1)–F(4)	90.7(4)
F(3)–P(1)–F(5)	90.4(5)	F(3)–P(1)–F(6)	88.4(4)
F(4)–P(1)–F(5)	91.4(5)	F(4)–P(1)–F(6)	179.1(5)
F(5)–P(1)–F(6)	89.1(4)	C(1)–N(1)–C(4)	107.8(10)
C(1)–N(1)–C(5)	126.6(11)	C(4)–N(1)–C(5)	125.6(11)
C(7)–N(2)–C(8)	120.4(11)	C(7)–N(2)–C(12)	119.3(11)
C(8)–N(2)–C(12)	120.3(11)	N(1)–C(1)–H(1A)	125.1
N(1)–C(1)–C(2)	109.9(12)	H(1A)–C(1)–C(2)	125.1
C(1)–C(2)–H(2A)	126.8	C(1)–C(2)–C(3)	106.4(12)
H(2A)–C(2)–C(3)	126.8	C(2)–C(3)–H(3A)	126.1
C(2)–C(3)–C(4)	107.9(11)	H(3A)–C(3)–C(4)	126.1
N(1)–C(4)–C(3)	108.0(11)	N(1)–C(4)–H(4A)	126.0
C(3)–C(4)–H(4A)	126.0	N(1)–C(5)–H(5A)	108.8
N(1)–C(5)–H(5B)	108.8	N(1)–C(5)–C(6)	113.8(11)
H(5A)–C(5)–H(5B)	107.7	H(5A)–C(5)–C(6)	108.8
H(5B)–C(5)–C(6)	108.8	C(5)–C(6)–H(6A)	109.4
C(5)–C(6)–H(6B)	109.4	C(5)–C(6)–C(7)	111.0(12)
H(6A)–C(6)–H(6B)	108.0	H(6A)–C(6)–C(7)	109.4
H(6B)–C(6)–C(7)	109.4	N(2)–C(7)–C(6)	113.0(11)
N(2)–C(7)–H(7A)	109.0	N(2)–C(7)–H(7B)	109.0
C(6)–C(7)–H(7A)	109.0	C(6)–C(7)–H(7B)	109.0
H(7A)–C(7)–H(7B)	107.8	N(2)–C(8)–H(8A)	120.1
N(2)–C(8)–C(9)	119.7(12)	H(8A)–C(8)–C(9)	120.1
C(8)–C(9)–H(9A)	120.2	C(8)–C(9)–C(10)	119.6(12)
H(9A)–C(9)–C(10)	120.2	C(9)–C(10)–H(10A)	120.6
C(9)–C(10)–C(11)	118.8(12)	H(10A)–C(10)–C(11)	120.6
C(10)–C(11)–H(11A)	120.1	C(10)–C(11)–C(12)	119.8(12)
H(11A)–C(11)–C(12)	120.1	N(2)–C(12)–C(11)	121.5(12)
N(2)–C(12)–H(12A)	119.2	C(11)–C(12)–H(12A)	119.2

Table 4. Anisotropic displacement parameters (\AA^2) for Mono-I, chapter 3.

	U^{11}	U^{22}	U^{33}	U^{23}	U^{13}	U^{12}
P(1)	0.037(2) 0.0031(14)	0.0244(18)	0.0346(19)	0.0003(13)	0.0118(14)	
F(1)	0.081(6)	0.064(6)	0.044(5)	0.008(4)	0.030(4)	0.010(4)
F(2)	0.041(5)	0.105(8)	0.088(7)	–0.020(5)	–0.001(5)	0.005(5)
F(3)	0.077(6)	0.067(6)	0.035(4)	0.011(4)	0.018(4)	0.025(4)
F(4)	0.090(7)	0.031(5)	0.075(6)	–0.003(4)	0.019(5)	0.009(4)
F(5)	0.041(5)	0.072(6)	0.059(5)	–0.011(4)	–0.005(4)	–0.002(4)
F(6)	0.072(6)	0.026(4)	0.064(5)	–0.001(4)	0.022(4)	–0.002(4)
N(1)	0.046(7)	0.034(6)	0.030(6)	–0.002(5)	0.008(5)	0.003(5)
N(2)	0.041(7)	0.043(8)	0.051(7)	0.007(5)	0.015(5)	0.009(5)
C(1)	0.046(8)	0.039(8)	0.034(8)	–0.005(6)	–0.001(6)	0.000(7)
C(2)	0.040(8)	0.031(8)	0.065(10)	0.001(7)	0.011(7)	0.008(6)
C(3)	0.032(7)	0.038(8)	0.041(8)	–0.005(6)	0.003(6)	–0.007(6)
C(4)	0.051(9)	0.039(8)	0.035(7)	–0.005(6)	0.004(6)	–0.003(7)
C(5)	0.044(8)	0.041(8)	0.056(9)	–0.010(7)	0.013(7)	–0.008(7)
C(6)	0.053(9)	0.047(9)	0.054(9)	0.008(7)	0.014(7)	–0.001(7)

C(7)	0.057(10)	0.066(10)	0.032(7)	0.002(7)	-0.004(7)	0.001(8)
C(8)	0.032(7)	0.044(10)	0.047(8)	0.008(6)	-0.001(6)	-0.001(6)
C(9)	0.048(9)	0.032(8)	0.057(9)	-0.002(7)	-0.001(7)	-0.013(7)
C(10)	0.040(8)	0.029(7)	0.044(8)	-0.001(6)	0.014(6)	-0.001(6)
C(11)	0.043(8)	0.039(8)	0.033(7)	-0.011(6)	0.009(6)	-0.006(6)
C(12)	0.043(8)	0.032(7)	0.047(8)	0.003(6)	0.019(7)	-0.001(6)

Table 5. Hydrogen coordinates and isotropic displacement parameters (\AA^2) for Mono-I, chapter 3.

	x	y	z	U
H(1A)	0.2515	0.4976	0.8949	0.048
H(2A)	0.0495	0.3452	0.9124	0.054
H(3A)	-0.0871	0.3173	0.7588	0.044
H(4A)	0.0404	0.4493	0.6501	0.050
H(5A)	0.3418	0.6336	0.7707	0.056
H(5B)	0.2279	0.6513	0.6838	0.056
H(6A)	0.4492	0.5872	0.6334	0.061
H(6B)	0.3362	0.4718	0.6180	0.061
H(7A)	0.5685	0.4939	0.7595	0.062
H(7B)	0.4414	0.3898	0.7630	0.062
H(8A)	0.4993	0.1972	0.7106	0.050
H(9A)	0.6445	0.0602	0.6254	0.055
H(10A)	0.8213	0.1440	0.5398	0.044
H(11A)	0.8411	0.3627	0.5286	0.046
H(12A)	0.6885	0.4898	0.6049	0.048

Table 6. Torsion angles ($^\circ$) for Mono-I, chapter 3.

C(4)–N(1)–C(1)–C(2)	0.3(14)	C(5)–N(1)–C(1)–C(2)	-178.0(11)
N(1)–C(1)–C(2)–C(3)	-0.8(14)	C(1)–C(2)–C(3)–C(4)	1.0(14)
C(1)–N(1)–C(4)–C(3)	0.3(14)	C(5)–N(1)–C(4)–C(3)	178.6(11)
C(2)–C(3)–C(4)–N(1)	-0.8(14)	C(1)–N(1)–C(5)–C(6)	107.2(14)
C(4)–N(1)–C(5)–C(6)	-70.8(17)	N(1)–C(5)–C(6)–C(7)	-67.3(16)
C(8)–N(2)–C(7)–C(6)	-116.0(14)	C(12)–N(2)–C(7)–C(6)	64.2(16)
C(5)–C(6)–C(7)–N(2)	167.8(11)	C(7)–N(2)–C(8)–C(9)	-177.8(11)
C(12)–N(2)–C(8)–C(9)	2.0(19)	N(2)–C(8)–C(9)–C(10)	2(2)
C(8)–C(9)–C(10)–C(11)	-3(2)	C(9)–C(10)–C(11)–C(12)	0.9(19)
C(7)–N(2)–C(12)–C(11)	175.6(12)	C(8)–N(2)–C(12)–C(11)	-4(2)
C(10)–C(11)–C(12)–N(2)	3(2)		

Appendix H: Crystallographic, Bond Length and Angle Data for Mono-II

Table 1. Crystal data and structure refinement for Mono-II, Chapter 3.

Identification code	ah172	
Chemical formula (moiety)	$C_{17}H_{18}F_6N_3P$	
Chemical formula (total)	$C_{17}H_{18}F_6N_3P$	
Formula weight	409.31	
Temperature	150(2) K	
Radiation, wavelength	MoK α , 0.71073 Å	
Crystal system, space group	monoclinic, C2/c	
Unit cell parameters	a = 29.316(6) Å	$\alpha = 90^\circ$
	b = 8.040(3) Å	$\beta = 126.448(11)^\circ$
	c = 19.658(5) Å	$\gamma = 90^\circ$
Cell volume	3727.2(19) Å ³	
Z	8	
Calculated density	1.459 g/cm ³	
Absorption coefficient μ	0.211 mm ⁻¹	
F(000)	1680	
Crystal colour and size	colourless, 0.32 × 0.20 × 0.20 mm ³	
Reflections for cell refinement	125 (θ range 2.5 to 27.5°)	
Data collection method	Nonius KappaCCD diffractometer ϕ and ω scans	
θ range for data collection	4.0 to 25.0°	
Index ranges	h -34 to 34, k -9 to 9, l -23 to 23	
Completeness to $\theta = 25.0^\circ$	99.5 %	
Reflections collected	18471	
Independent reflections	3266 ($R_{int} = 0.0444$)	
Reflections with $F^2 > 2\sigma$	2463	
Absorption correction	semi-empirical from equivalents	
Min. and max. transmission	0.9355 and 0.9590	
Structure solution	direct methods	
Refinement method	Full-matrix least-squares on F^2	
Weighting parameters a, b	0.0445, 5.6022	
Data / restraints / parameters	3266 / 0 / 247	
Final R indices ($F^2 > 2\sigma$)	R1 = 0.0454, wR2 = 0.1020	
R indices (all data)	R1 = 0.0693, wR2 = 0.1156	
Goodness-of-fit on F^2	1.081	
Largest and mean shift/su	0.000 and 0.000	
Largest diff. peak and hole	0.45 and -0.30 e Å ⁻³	

Table 2. Atomic coordinates and equivalent isotropic displacement parameters (\AA^2) for Mono-II, Chapter 3.

	x	y	z	U_{eq}
P(1)	0.5000	0.52772(12)	0.2500	0.0334(2)
P(2)	0.7500	0.2500	0.0000	0.0398(3)
F(1)	0.5000	0.3313(3)	0.2500	0.1102(12)
F(2)	0.5000	0.7246(3)	0.2500	0.0833(9)
F(3)	0.52616(7)	0.5264(3)	0.19937(11)	0.0843(7)
F(4)	0.56278(6)	0.5304(2)	0.33617(10)	0.0612(5)
F(5)	0.69834(7)	0.2308(2)	0.00593(12)	0.0687(5)
F(6)	0.76269(7)	0.0551(2)	0.01934(11)	0.0692(5)
F(7)	0.79158(7)	0.2908(2)	0.09893(10)	0.0616(5)
N(1)	0.61889(9)	0.8327(3)	0.62963(13)	0.0461(6)
N(2)	0.63196(8)	0.7298(2)	0.79176(11)	0.0295(4)
N(3)	0.69882(8)	0.3895(2)	0.69660(13)	0.0368(5)
C(1)	0.60420(12)	0.8056(4)	0.55161(18)	0.0542(8)
C(2)	0.55159(13)	0.7540(4)	0.48449(18)	0.0551(8)
C(3)	0.51047(13)	0.7302(4)	0.49680(18)	0.0640(9)
C(4)	0.52409(11)	0.7576(4)	0.57688(16)	0.0518(8)
C(5)	0.57874(10)	0.8065(3)	0.64061(14)	0.0329(5)
C(6)	0.59658(9)	0.8388(3)	0.72848(14)	0.0310(5)
C(7)	0.57905(11)	0.9796(3)	0.74794(16)	0.0407(6)
C(8)	0.59809(11)	1.0102(3)	0.83038(17)	0.0442(6)
C(9)	0.63367(11)	0.8970(3)	0.89273(16)	0.0418(6)
C(10)	0.64994(10)	0.7575(3)	0.87202(15)	0.0363(6)
C(11)	0.65256(9)	0.5742(3)	0.77579(15)	0.0309(5)
C(12)	0.71195(10)	0.5990(3)	0.80018(16)	0.0359(6)
C(13)	0.73393(10)	0.4406(3)	0.78531(16)	0.0398(6)
C(14)	0.66136(11)	0.2606(4)	0.66298(19)	0.0501(7)
C(15)	0.63466(14)	0.2581(5)	0.5775(2)	0.0687(10)
C(16)	0.65656(17)	0.3909(5)	0.5589(2)	0.0751(11)
C(17)	0.69642(15)	0.4692(4)	0.63312(19)	0.0575(8)

Table 3. Bond lengths (Å) and angles (°) for Mono-II, Chapter 3.

P(1)–F(1)	1.579(3)	P(1)–F(2)	1.583(3)
P(1)–F(3)	1.5767(16)	P(1)–F(3A)	1.5767(16)
P(1)–F(4)	1.5978(15)	P(1)–F(4A)	1.5978(15)
P(2)–F(5)	1.5939(16)	P(2)–F(5B)	1.5939(16)
P(2)–F(6)	1.6037(18)	P(2)–F(6B)	1.6036(18)
P(2)–F(7)	1.5996(16)	P(2)–F(7B)	1.5996(16)
N(1)–C(1)	1.342(3)	N(1)–C(5)	1.333(3)
N(2)–C(6)	1.363(3)	N(2)–C(10)	1.352(3)
N(2)–C(11)	1.501(3)	N(3)–C(13)	1.462(3)
N(3)–C(14)	1.362(3)	N(3)–C(17)	1.367(3)
C(1)–H(1A)	0.950	C(1)–C(2)	1.369(4)
C(2)–H(2A)	0.950	C(2)–C(3)	1.377(4)
C(3)–H(3A)	0.950	C(3)–C(4)	1.393(4)
C(4)–H(4A)	0.950	C(4)–C(5)	1.381(3)
C(5)–C(6)	1.500(3)	C(6)–C(7)	1.388(3)
C(7)–H(7A)	0.950	C(7)–C(8)	1.387(4)
C(8)–H(8A)	0.950	C(8)–C(9)	1.378(4)
C(9)–H(9A)	0.950	C(9)–C(10)	1.372(3)
C(10)–H(10A)	0.950	C(11)–H(11A)	0.990
C(11)–H(11B)	0.990	C(11)–C(12)	1.520(3)
C(12)–H(12A)	0.990	C(12)–H(12B)	0.990
C(12)–C(13)	1.532(3)	C(13)–H(13A)	0.990
C(13)–H(13B)	0.990	C(14)–H(14A)	0.950
C(14)–C(15)	1.369(4)	C(15)–H(15A)	0.950
C(15)–C(16)	1.401(5)	C(16)–H(16A)	0.950
C(16)–C(17)	1.365(5)	C(17)–H(17A)	0.950
F(1)–P(1)–F(2)	180.000(1)	F(1)–P(1)–F(3)	89.62(10)
F(1)–P(1)–F(3A)	89.62(10)	F(1)–P(1)–F(4)	90.76(8)
F(1)–P(1)–F(4A)	90.76(8)	F(2)–P(1)–F(3)	90.38(10)
F(2)–P(1)–F(3A)	90.38(10)	F(2)–P(1)–F(4)	89.24(8)
F(2)–P(1)–F(4A)	89.24(8)	F(3)–P(1)–F(3A)	179.25(19)
F(3)–P(1)–F(4)	89.05(9)	F(3A)–P(1)–F(4)	90.96(9)
F(3)–P(1)–F(4A)	90.96(9)	F(3A)–P(1)–F(4A)	89.05(9)
F(4)–P(1)–F(4A)	178.48(15)	F(5)–P(2)–F(5B)	180.00(12)
F(5)–P(2)–F(6)	89.13(10)	F(5B)–P(2)–F(6B)	89.13(10)
F(5)–P(2)–F(6B)	90.87(10)	F(5B)–P(2)–F(6)	90.87(10)
F(5)–P(2)–F(7)	90.10(9)	F(5B)–P(2)–F(7)	89.90(9)
F(5B)–P(2)–F(7B)	90.10(9)	F(5)–P(2)–F(7B)	89.90(9)
F(6)–P(2)–F(6B)	180.00(16)	F(6)–P(2)–F(7)	90.58(9)
F(6B)–P(2)–F(7)	89.42(9)	F(6B)–P(2)–F(7B)	90.58(9)
F(6)–P(2)–F(7B)	89.42(9)	F(7)–P(2)–F(7B)	180.00(15)
C(1)–N(1)–C(5)	116.4(2)	C(6)–N(2)–C(10)	121.1(2)
C(6)–N(2)–C(11)	121.83(18)	C(10)–N(2)–C(11)	117.06(19)
C(13)–N(3)–C(14)	125.9(2)	C(13)–N(3)–C(17)	125.1(2)
C(14)–N(3)–C(17)	108.9(2)	N(1)–C(1)–H(1A)	117.8
N(1)–C(1)–C(2)	124.3(3)	H(1A)–C(1)–C(2)	117.8
C(1)–C(2)–H(2A)	120.8	C(1)–C(2)–C(3)	118.4(3)
H(2A)–C(2)–C(3)	120.8	C(2)–C(3)–H(3A)	120.5
C(2)–C(3)–C(4)	118.9(3)	H(3A)–C(3)–C(4)	120.5
C(3)–C(4)–H(4A)	121.0	C(3)–C(4)–C(5)	118.0(3)
H(4A)–C(4)–C(5)	121.0	N(1)–C(5)–C(4)	123.9(2)
N(1)–C(5)–C(6)	114.9(2)	C(4)–C(5)–C(6)	121.1(2)

N(2)–C(6)–C(5)	119.7(2)	N(2)–C(6)–C(7)	118.6(2)
C(5)–C(6)–C(7)	121.7(2)	C(6)–C(7)–H(7A)	119.7
C(6)–C(7)–C(8)	120.6(2)	H(7A)–C(7)–C(8)	119.7
C(7)–C(8)–H(8A)	120.4	C(7)–C(8)–C(9)	119.2(2)
H(8A)–C(8)–C(9)	120.4	C(8)–C(9)–H(9A)	120.4
C(8)–C(9)–C(10)	119.3(2)	H(9A)–C(9)–C(10)	120.4
N(2)–C(10)–C(9)	121.2(2)	N(2)–C(10)–H(10A)	119.4
C(9)–C(10)–H(10A)	119.4	N(2)–C(11)–H(11A)	109.5
N(2)–C(11)–H(11B)	109.5	N(2)–C(11)–C(12)	110.63(19)
H(11A)–C(11)–H(11B)	108.1	H(11A)–C(11)–C(12)	109.5
H(11B)–C(11)–C(12)	109.5	C(11)–C(12)–H(12A)	109.4
C(11)–C(12)–H(12B)	109.4	C(11)–C(12)–C(13)	111.3(2)
H(12A)–C(12)–H(12B)	108.0	H(12A)–C(12)–C(13)	109.4
H(12B)–C(12)–C(13)	109.4	N(3)–C(13)–C(12)	112.55(19)
N(3)–C(13)–H(13A)	109.1	N(3)–C(13)–H(13B)	109.1
C(12)–C(13)–H(13A)	109.1	C(12)–C(13)–H(13B)	109.1
H(13A)–C(13)–H(13B)	107.8	N(3)–C(14)–H(14A)	125.8
N(3)–C(14)–C(15)	108.4(3)	H(14A)–C(14)–C(15)	125.8
C(14)–C(15)–H(15A)	126.5	C(14)–C(15)–C(16)	107.0(3)
H(15A)–C(15)–C(16)	126.5	C(15)–C(16)–H(16A)	126.1
C(15)–C(16)–C(17)	107.9(3)	H(16A)–C(16)–C(17)	126.1
N(3)–C(17)–C(16)	107.8(3)	N(3)–C(17)–H(17A)	126.1
C(16)–C(17)–H(17A)	126.1		

Table 4. Anisotropic displacement parameters (\AA^2) for Mono-II, Chapter 3.

	U^{11}	U^{22}	U^{33}	U^{23}	U^{13}	U^{12}
P(1)	0.0272(4)	0.0384(5)	0.0329(5)	0.000	0.0169(4)	0.000
P(2)	0.0344(5)	0.0445(6)	0.0422(5)	0.0167(4)	0.0237(5)	0.0072(4)
F(1)	0.091(2)	0.0428(17)	0.152(3)	0.000	0.049(2)	0.000
F(2)	0.0490(14)	0.0374(14)	0.138(3)	0.000	0.0419(17)	0.000
F(3)	0.0503(10)	0.162(2)	0.0531(11)	–0.0012(12)	0.0373(9)	0.0134(12)
F(4)	0.0328(8)	0.0933(14)	0.0403(9)	0.0042(9)	0.0124(7)	0.0068(8)
F(5)	0.0543(10)	0.0873(14)	0.0828(13)	–0.0079(10)	0.0507(10)	
–0.0102(9)						
F(6)	0.0658(11)	0.0491(11)	0.0730(12)	0.0215(9)	0.0305(10)	0.0127(8)
F(7)	0.0597(10)	0.0740(12)	0.0427(9)	0.0103(8)	0.0259(8)	–0.0110(9)
N(1)	0.0371(12)	0.0656(16)	0.0402(13)	0.0058(11)	0.0254(11)	
	0.0011(11)					
N(2)	0.0279(10)	0.0298(11)	0.0315(11)	0.0028(8)	0.0180(9)	0.0013(8)
N(3)	0.0412(12)	0.0323(12)	0.0442(12)	0.0041(9)	0.0293(11)	0.0068(9)
C(1)	0.0501(17)	0.077(2)	0.0474(17)	0.0099(15)	0.0356(15)	
	0.0093(15)					
C(2)	0.067(2)	0.064(2)	0.0375(15)	0.0017(14)	0.0327(16)	
	0.0041(16)					
C(3)	0.0516(18)	0.090(3)	0.0384(16)	–0.0052(16)	0.0202(15)	
–0.0162(17)						
C(4)	0.0387(15)	0.076(2)	0.0405(16)	0.0032(14)	0.0234(13)	
–0.0072(14)						
C(5)	0.0339(13)	0.0315(13)	0.0340(13)	0.0071(10)	0.0205(11)	

	0.0049(10)					
C(6)	0.0263(11)	0.0334(13)	0.0331(13)	0.0040(10)	0.0176(11)	
	0.0000(10)					
C(7)	0.0406(14)	0.0377(15)	0.0418(15)	0.0069(12)	0.0234(13)	
	0.0097(11)					
C(8)	0.0507(16)	0.0364(15)	0.0487(16)	-0.0023(12)	0.0313(14)	
	0.0076(12)					
C(9)	0.0483(15)	0.0419(15)	0.0352(14)	-0.0041(12)	0.0248(13)	
	0.0009(12)					
C(10)	0.0353(13)	0.0392(15)	0.0297(13)	0.0057(11)	0.0166(11)	
	0.0030(11)					
C(11)	0.0309(12)	0.0285(13)	0.0361(13)	0.0040(10)	0.0213(11)	
	0.0031(10)					
C(12)	0.0298(12)	0.0381(14)	0.0394(14)	0.0019(11)	0.0204(11)	
	0.0005(10)					
C(13)	0.0310(13)	0.0442(16)	0.0461(15)	0.0079(12)	0.0240(12)	
	0.0072(11)					
C(14)	0.0409(15)	0.0477(17)	0.0649(19)	-0.0045(14)	0.0331(15)	
	-0.0009(13)					
C(15)	0.0552(19)	0.069(2)	0.061(2)	-0.0173(18)	0.0231(17)	
	0.0105(17)					
C(16)	0.114(3)	0.058(2)	0.051(2)	0.0083(17)	0.047(2)	0.036(2)
C(17)	0.097(2)	0.0381(16)	0.0592(19)	0.0086(15)	0.059(2)	0.0124(16)

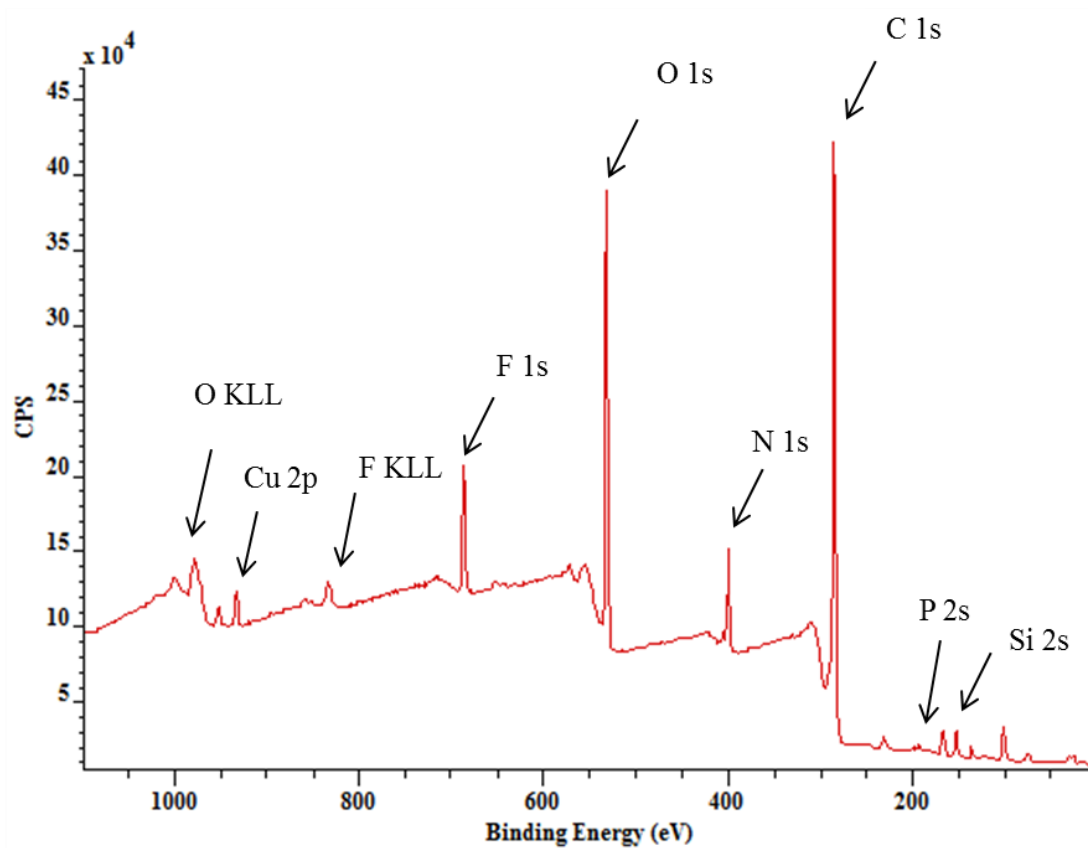
Table 5. Hydrogen coordinates and isotropic displacement parameters (\AA^2) for Mono-II, Chapter 3.

	x	y	z	U
H(1A)	0.6322	0.8234	0.5423	0.065
H(2A)	0.5436	0.7352	0.4307	0.066
H(3A)	0.4734	0.6955	0.4514	0.077
H(4A)	0.4966	0.7431	0.5873	0.062
H(7A)	0.5538	1.0557	0.7044	0.049
H(8A)	0.5867	1.1080	0.8437	0.053
H(9A)	0.6468	0.9154	0.9494	0.050
H(10A)	0.6743	0.6789	0.9148	0.044
H(11A)	0.6264	0.5443	0.7152	0.037
H(11B)	0.6528	0.4815	0.8091	0.037
H(12A)	0.7379	0.6306	0.8606	0.043
H(12B)	0.7115	0.6910	0.7663	0.043
H(13A)	0.7732	0.4598	0.8041	0.048
H(13B)	0.7350	0.3495	0.8201	0.048
H(14A)	0.6549	0.1852	0.6936	0.060
H(15A)	0.6066	0.1810	0.5382	0.082
H(16A)	0.6456	0.4212	0.5044	0.090
H(17A)	0.7186	0.5625	0.6395	0.069

Table 6. Torsion angles (°) for Mono-II, Chapter 3.

C(5)–N(1)–C(1)–C(2)	0.1(4)	N(1)–C(1)–C(2)–C(3)	0.9(5)
C(1)–C(2)–C(3)–C(4)	–0.7(5)	C(2)–C(3)–C(4)–C(5)	–0.5(5)
C(1)–N(1)–C(5)–C(4)	–1.4(4)	C(1)–N(1)–C(5)–C(6)	–179.7(2)
C(3)–C(4)–C(5)–N(1)	1.6(4)	C(3)–C(4)–C(5)–C(6)	179.9(3)
C(10)–N(2)–C(6)–C(5)	178.3(2)	C(10)–N(2)–C(6)–C(7)	–0.2(3)
C(11)–N(2)–C(6)–C(5)	–1.8(3)	C(11)–N(2)–C(6)–C(7)	179.7(2)
N(1)–C(5)–C(6)–N(2)	–73.3(3)	N(1)–C(5)–C(6)–C(7)	105.1(3)
C(4)–C(5)–C(6)–N(2)	108.2(3)	C(4)–C(5)–C(6)–C(7)	–73.3(3)
N(2)–C(6)–C(7)–C(8)	1.3(4)	C(5)–C(6)–C(7)–C(8)	–177.2(2)
C(6)–C(7)–C(8)–C(9)	–1.5(4)	C(7)–C(8)–C(9)–C(10)	0.7(4)
C(6)–N(2)–C(10)–C(9)	–0.6(3)	C(11)–N(2)–C(10)–C(9)	179.5(2)
C(8)–C(9)–C(10)–N(2)	0.4(4)	C(6)–N(2)–C(11)–C(12)	99.1(2)
C(10)–N(2)–C(11)–C(12)	–81.1(2)	N(2)–C(11)–C(12)–C(13)	179.28(18)
C(14)–N(3)–C(13)–C(12)	–104.8(3)	C(17)–N(3)–C(13)–C(12)	71.8(3)
C(11)–C(12)–C(13)–N(3)	61.1(3)	C(13)–N(3)–C(14)–C(15)	176.8(2)
C(17)–N(3)–C(14)–C(15)	–0.2(3)	N(3)–C(14)–C(15)–C(16)	–0.4(3)
C(14)–C(15)–C(16)–C(17)	0.9(4)	C(15)–C(16)–C(17)–N(3)	–1.1(4)
C(13)–N(3)–C(17)–C(16)	–176.3(2)	C(14)–N(3)–C(17)–C(16)	0.8(3)

Appendix I: XPS survey spectrum of Cu-poly-III/DNA nanowires sample.



Appendix I: XPS survey spectrum of Cu-poly-III/DNA nanowires sample.